5-2013

Enabling Sum Frequency Spectroscopy and Fluorescence Correlation Spectroscopy of Model Cellular Membranes

Sarah M. Sterling

ENABLING SUM FREQUENCY SPECTROSCOPY AND FLUORESCENCE CORRELATION SPECTROSCOPY OF MODEL CELLULAR MEMBRANES

By

Sarah M. Sterling

B.S. Russell Sage College, 2005

A DISSERTATION

Submitted in Partial Fulfillment of the

Requirements for the Degree of

Doctor of Philosophy

(in Biomedical Sciences and Chemical Engineering)

The Graduate School

The University of Maine

May 2013

Advisory Committee:

David Neivandt, Associate Professor of Chemical & Biological Engineering, Co-Advisor

Igor Prudovsky, Principle Investigator at Maine Medical Center Research Institute, Co-Advisor

Michael Mason, Associate Professor of Chemical & Biological Engineering

Paul Millard, Associate Professor of Chemical & Biological Engineering and Laboratory for Surface Science and Technology

Sharon Ashworth, Assistant Research Professor of Biological Sciences

DISSERTATION ACCEPTANCE STATEMENT

On behalf of the Graduate Committee for Sarah M. Sterling, we affirm that this manuscript is the final and accepted dissertation. Signatures of all committee members are on file with the Graduate School at the University of Maine, 42 Stodder Hall, Orono, Maine.

David Neivandt, Associate Professor of Chemical & Biological Engineering (Date)

Igor Prudovsky, Principle Investigator at Maine Medical Center Research Institute (Date)

LIBRARY RIGHTS STATEMENT

In presenting this dissertation in partial fulfillment of the requirements for an advanced degree at The University of Maine, I agree that the Library shall make it freely available for inspection. I further agree that permission for "fair use" copying of this thesis for scholarly purposes may be granted by the Librarian. It is understood that any copying or publication of this dissertation for financial gain shall not be allowed without my written permission.

Sarah M. Sterling (Date)

ENABLING SUM FREQUENCY SPECTROSCOPY AND FLUORESCENCE CORRELATION SPECTROSCOPY OF MODEL CELLULAR MEMBRANES

By Sarah M. Sterling

Dissertation Co-Advisors: Dr. David Neivandt

Dr. Igor Prudovsky

An Abstract of the Dissertation Presented
in Partial Fulfillment of the Requirements for the
Degree of Doctor of Philosophy
(in Biomedical Sciences and Chemical Engineering)
May 2013

The majority of proteins secreted from cells contain a signal peptide sequence that is required for secretion mediated by the endoplasmic reticulum and Golgi apparatus. However, many proteins lack the essential signal peptide sequence, yet still undergo secretion. Such proteins are known to regulate cell proliferation, differentiation, and migration. Fibroblast growth factor 1 (FGF-1) is one protein which undergoes non-classical protein transport. The role of its interactions with the cellular membrane during non-classical protein transport is not fully understood, although FGF-1 has shown preferential destabilizing effects on artificial membranes composed of acidic phospholipids. In the present work, physiologically relevant model membrane systems have been developed and characterized in order to investigate the role of phospholipid:FGF-1 interactions in translocation of the protein across the membrane. In addition, a confocal z-scan fluorescence correlation spectrometer (z-scan FCS) and a sum frequency spectrometer (SFS) have been assembled, and

temperature controlled liquid sample holders have been designed and fabricated. Z-scan FCS and SFS have been employed to characterize the model membrane systems and have been shown to be suitable tools for elucidating the role of specific phospholipid:FGF-1 interactions in transmembrane translocation.

DEDICATION

"I admire you for what you are doing and for what you have completed. I just wanted to try and tell you that I am extremely thankful that God has blessed me with such a great daughter."

In memory of my dad

ACKNOWLEDGEMENTS

The research presented in this thesis was made possible by contributions of several individuals. The author would like to thank her advisers David Neivandt and Igor Prudovsky for their guidance, support and patience. Their conversations and advice provided valuable direction and enabled a deeper understand of this research area. Additionally, they provided many hours of review and comments that helped refine and polish the presentation of this research. Committee members, Sharon Ashworth, Michael Mason, and Paul Millard have also provided valuable reviews and comments regarding the research presented, and have additionally been excellent collaborators on the present work and other programs at the University of Maine. Their collective expertise and generous contribution of time is greatly appreciated.

Experiments conducted in the present work required sophisticated equipment and diligent maintenance, both of which were made possible by several individuals. The author would like to thank Amos Cline for fabricating the temperature controlled liquid flow cell and designing and fabricating new substrate holders for the LB trough and spin coater, both of which were essential to this body of work. Additionally, Keith Hodgins, the Pilot Plant staff, and Nick Hill provided excellent assistance and tools for resolving the various laboratory issues and maintaining the equipment. Cathy Dunn and Angel Hildreth in the Department of Chemical and Biological Engineering, and Laura Hall in the Graduate School of Biomedical Science and Engineering provided support with handling orders and other required paperwork. Several individuals external to the University of Maine provided additional assistance that expedited the construction and configuration of various laboratory components. Fred Gonzales from Spectra-Physics was a valuable resource with regard to laser maintenance and optimization. Resolution of issues with the LB

trough, including creation of a custom LB trough control program, was provided by Chris Harling, resulting in reducing our fabrication time by half. The author is very thankful for time spent at Hokkaido University with Shen Ye and his students, Yujin Tong and Na Li, learning sum frequency spectroscopy techniques and instrumentation.

Funding for this research was graciously provided by several organizations. The author would like to recognize and thank the financial support provided by the University of Maine Pulp & Paper Foundation, the University of Maine Graduate School of Biomedical Science and Engineering, the Institute for Molecular Biophysics, and the Rosen Foundation. Additionally, the Japan Society for the Promotion of Science funded the author's research experience at Hokkaido University in Sapporo, Japan.

Some help is not as easily quantifiable but is equally important in handling the day to day issues of graduate work. The author is appreciative of the academic and personal support provided through conversations, brainstorms, whiteboards, explanations, corrections, debates, and extracurricular social interactions by fellow University of Maine Neivandt Lab members James Beaupré, Lei Li, Alex Demers, and Ryan Dawes; Prudovsky Lab members Doreen Kacer and Aleksandr Kirov; Hokkaido University professor Shen Ye and his students, Yujin Tong and Na Li. The author also would like to give her profound and deep appreciation to Edward Allgeyer for his pivotal assistance with preparing, configuring, conducting and analyzing experiments; scrawling, compiling, drafting and composing the resulting papers; wandering, eating, shopping, and jesting, with the author. The rubberbands will never be forgotten.

Graduate work is typically a long, tiresome, and repetitive process and the present work was no exception. While the results presented here are a sweet fruit, the process requires the support and encouragement of family and friends. The author would like to thank her friends at University of Maine and Russell Sage College

for their support over the years. There are too many to name, but the author would like to specifically acknowledge Jess Wilson, Eleni Dedovich, Daesha More and Tim Beaucage, Gary Craig, Danielle Beaupré, the members of the First Congregation Church in Milford, ME, the Chemical Engineering crew, the GSBSE crew, and the members of the First Presbyterian Church in San Mateo, CA. Also, the love and support of the author's long time friend, and now husband, Jonathan Purnell has been invaluable over the many years.

The author is proud to be a part of the Sterling family. Based out of Endicott, NY and spanning northern New York and north-central Pennsylvania, the Sterling family is a shining example of devotion, support, community service, and humility. The author wishes to express her deepest gratitude for their role in raising her to be a humble, driven, competitive, not-too-serious, grounded, and well loved daughter/sister/niece/cousin. The holiday and non-holiday meals and heart-to-hearts formed the author in ways immeasurable and uncountable. Love and thanks to: Randy, Joanne, Tom, Lisa, Beth, Josh, Chelsea, Andrew, and Rachel. Inexpressible love and gratitude goes to her brother, Adam, for being a life-long friend, confidante, and source of relaxation and rock 'n roll. The author especially thanks her parents for their tremendous support, love, and guidance in her life. Extra special thanks are extended to her mother, Annie, for being her continuous role model and for her loving friendship, which has been a linchpin in the author's life.

TABLE OF CONTENTS

LIST OF FIGURES

Chapter 1
INTRODUCTION

A subset of proteins have been identified that lack the classical signal peptide sequence required for secretion mediated by the endoplasmic reticulum and Golgi apparatus. Despite lacking a signal peptide sequence, these proteins are secreted to the extracellular compartment where they regulate cell proliferation, differentiation, and migration by binding to specific cell receptors or occasionally by penetrating the membranes of neighboring cells. Two ubiquitously expressed fibroblast growth factors (FGF), FGF-1 and FGF-2, are signal peptide-less, non-classically released proteins. FGF-1 and FGF-2 regulate angiogenesis, restenosis, muscle repair, and play key roles in certain types of cancer. The mechanisms used by these proteins to traverse the plasma membrane remain largely unknown.

This thesis details the development, construction, and characterization of model membrane systems for elucidating the role of interactions with specific phospholipids in FGF-1 transmembrane translocation. Model membrane systems provide a controlled environment for spectroscopic and microscopic investigations of the mechanisms of non-classical protein export, specifically, the penetration of proteins into phospholipid bilayers. A model membrane is an artificial lipid bilayer that is either spherical or planar and may be freely suspended or supported on a solid substrate, (either directly or via a cushion), and many have been shown to allow proteins to be incorporated into the bilayer structure. The present work details the development of model membrane systems potentially amenable to protein transport studies, specifically the aforementioned FGF-1 transmembrane translocation. In addition, construction, fabrication, and optimization of a custom confocal z-scan fluorescence

correlation spectrometer and a sum frequency spectrometer, both capable of probing the model membrane systems, are described.

1.1 Classical Protein Secretion

Proteins are produced in the cytoplasm as a result of mRNA translation. A targeting sequence on the protein determines its destination, whether it will be transported to specific organelles within the cell, or secreted to the extracellular compartment.[1] Figure 1.1 presents the various processes requiring a signal sequence for protein transport, each process having its own characteristic targeting (signal) sequence. Proteins transporting into the mitochondrion and chloroplast have signal sequences on the N-terminus, while proteins bound for peroxisomes have a signal sequence on the C-terminus.[1] Nuclear bound proteins have an internal signal sequence that forms a three-dimensional signal patch recognized by importins, which transport these proteins through the nuclear pores.[1]

For the majority of secreted proteins and proteins of the cell membrane, the translation process occurs on ribosomes attached to the surface of the endoplas-

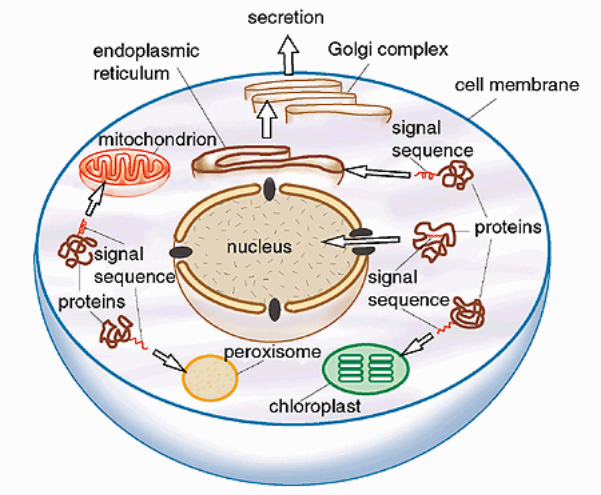

Figure 1.1. Signal sequence mediated pathways inside the cell.[2] Transport of proteins with specific signal sequences are mediated through various classical pathways.

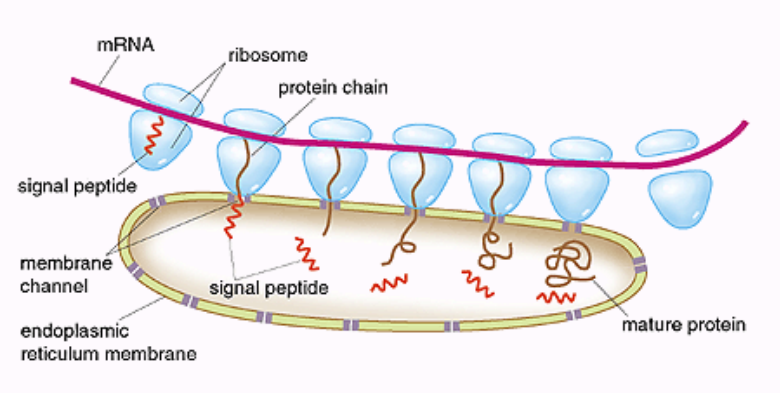

Figure 1.2. Co-translational translocation of a polypeptide into the endoplasmic reticulum.[2]

mic reticulum (ER). Proteins being translated are directed toward the ER via a hydrophobic signal sequence on the N-terminus of the peptide chain. The signal sequence is recognized by a signal-recognition particle (SRP) which binds and leads the signal sequence toward a SRP receptor on the ER membrane. Once the ribosome containing the protein being translated is bound to the SRP receptor, translocation across the ER membrane occurs while translation continues.[1,3] Translocation of the nascent polypeptide into the ER during the course of translation is known as co-translational translocation, and it proceeds through a narrow channel in the ER membrane (Figure 1.2).

After proteins bound for secretion have entered the ER, they are transported to the Golgi apparatus (Figure 1.1) via vesicles that bud from the ER. The vesicles are received by the *cis* Golgi network where they fuse with the membranes of the Golgi. The Golgi is a series of plate-like vesicles (cisternae) that transport molecules through to the *trans* Golgi network. The molecules being transported, including proteins, undergo various covalent modifications which facilitate sorting for their intended destination, whether it be lysosomes or secretory (exocytotic) vesicles.[1]

1.2 Non-Classical Protein Secretion

There is a significant subset of secreted proteins that do not employ the classical protein transport pathway due to their lack of a signal peptide sequence. Among these signal peptide-less proteins are some members of the Fibroblast Growth Factor (FGF) gene family, which play roles in a variety of developmental processes and in angiogenesis, tissue regeneration, and tumor formation.[4,5] Of the 23 members of the gene family, two members, FGF-1 and FGF-2, lack the signal sequence required for utilization of the classical protein secretion mechanism.[5,6] It is hoped that a greater understanding of the mechanisms by which these proteins are released from cells, specifically their means of translocating through the plasma membrane, will eventually aid in the development of therapeutics to fight cardiovascular, oncologic, and inflammatory disorders involving FGF-1 and FGF-2.

FGF-1 is released through a non-classical mechanism in response to cellular stress (Figure 1.3). Cellular stress can be caused *in vitro* by heat shock,[7] serum deprivation,[8] hypoxia,[9] or an oxidized low-density lipoprotein treatment,[10] all of which have been shown to induce FGF-1 export. Release of FGF-1 occurs as part of a multiprotein complex that forms at the proximal leaflet of the cell membrane. The components of this complex migrate to the cell membrane using actin filaments.[11] FGF-1 forms a homodimer mediated by its cysteine 30 residue. The FGF-1 homodimer, in turn, non-covalently binds a homodimer of S100A13 and the p40 form of Synaptotagmin 1 (Syt1).[12–15] p40 Syt1 is produced as a result of alternative initiation of translation of the Syt1 mRNA.[16] In common with FGF-1, both p40 Syt1 and S100A13 lack a signal sequence for utilization of the ER and Golgi apparatus, however, they may be secreted individually (independent of FGF-1) in a non-stress environment.[13] The FGF-1 export complex is dependent on intracellular copper ions (Cu^{2+}), which mediate both the formation of the covalent homodimer of FGF-1 and

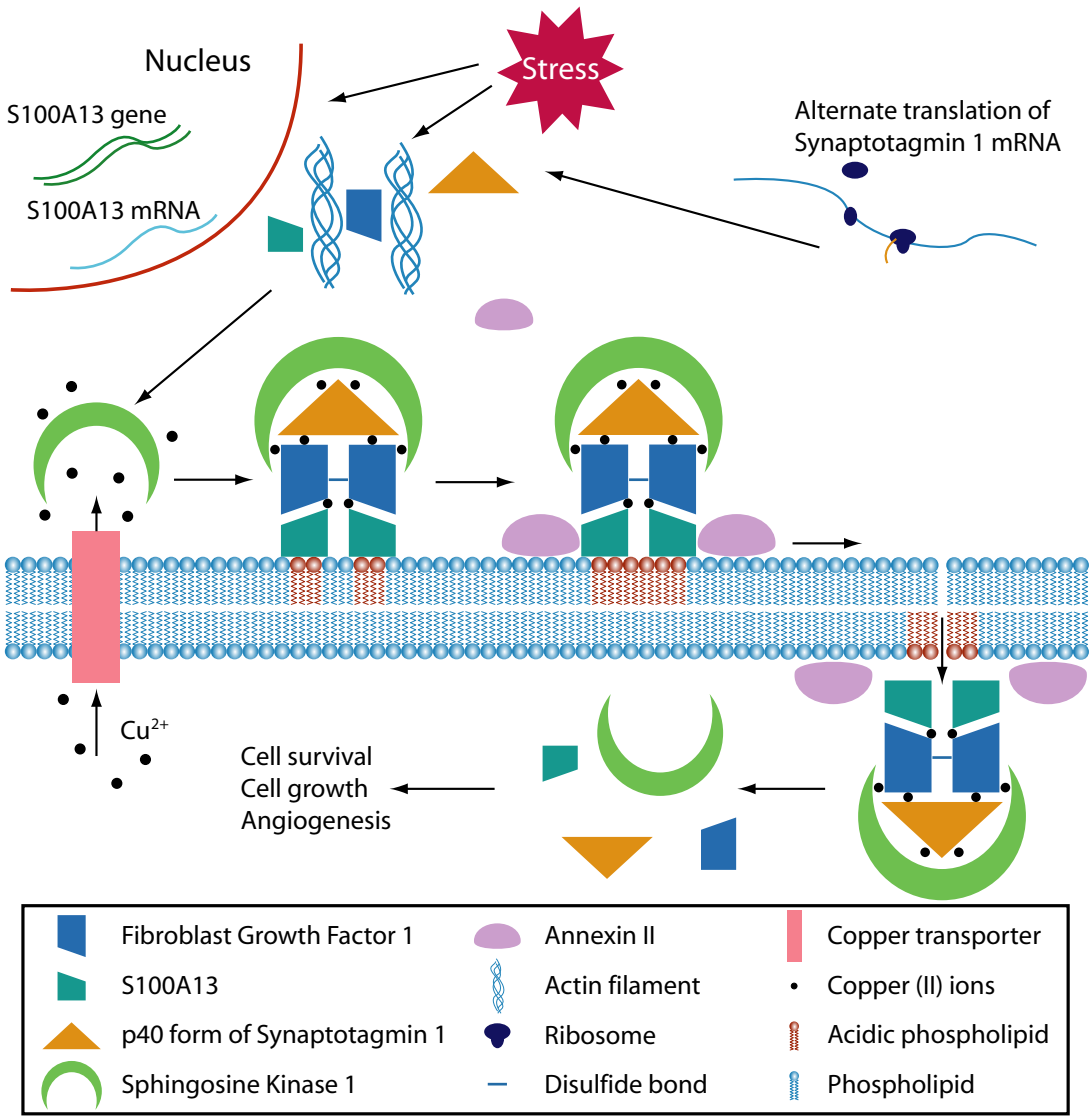

Figure 1.3. Current proposed mechanism for non-classical release of the multiprotein complex.

the non-covalent binding of S100A13 and FGF-1.[17–19] Another member of the complex is Sphingosine kinase 1 (SK1), a non-classically secreted, signal peptide-less enzyme that catalyzes the production of sphingosine 1-phosphate, a positive regulator of angiogenesis.[20,21] Similarly to p40 Syt1 and S100A13, SK1 can be secreted independently of FGF-1 in a spontaneous, stress-independent manner. SK1 is characterized by a very high copper affinity and it is thought to be the donor of the Cu^{2+} necessary for the formation of the FGF-1 release complex.[20] It has also been

hypothesized that the export complex may involve annexin II, a protein known to bind to S100A family members, and which exhibits transmembrane flipping as a result of various stresses.[22]

Currently, the mechanism of the FGF-1 export complex's translocation across the cell membrane is not well understood. Plasma membranes are composed of a variety of phospholipids; zwitterionic phosphatidylcholine (PC) and glycosphingolipids dominate the distal leaflet, while acidic phosphatidylserine (PS), acidic phosphatidylglycerol (PG), acidic phosphatidylinositol (PI), phosphatidylethanolamine (PE), and aminophospholipids are primarily found in the proximal leaflet (adjacent to the cytosol).[13,23] It has been demonstrated that FGF-1 has a domain that associates with PS,[24] and further, that PS flips from the proximal to the distal leaflet of cell membranes as a function of stress.[25] Thus, since FGF-1 binds acidic phospholipids, it has been hypothesized that secretion of the FGF-1 complex may be mediated by the flipping of PS.[13] It has been recently demonstrated that under stress, FGF-1 is released through limited domains of the cell membrane characterized by PS externalization.[26] Moreover, chemical compounds, which suppressed PS externalization, inhibited FGF-1 release.[26] Additionally, the ability of FGF-1, S100A13, and p40 Syt1 to destabilize membranes comprised of acidic phospholipids has been shown using liposomes of various phospholipid compositions.[27] Since S100A13 and p40 Syt1 interact with acidic phospholipids, they may play a chaperone role for FGF-1 during transport.[5] FGF-1 has a tertiary structure dominated by β-sheets, and as such, has a structure with an open core (Figure 1.4).[5] FGF-1 tertiary structure may partially unfold into a molten globular state at elevated temperatures (e.g. during heat shock),[28] potentially aiding transfer across the hydrophobic core of the phospholipid bilayer.[5] Interestingly, while FGF-1 exhibits a molten globular state as a function of temperature, S100A13 and p40 Syt1 do not.[5,28] However, a recent study by the author and co-workers has shown that both

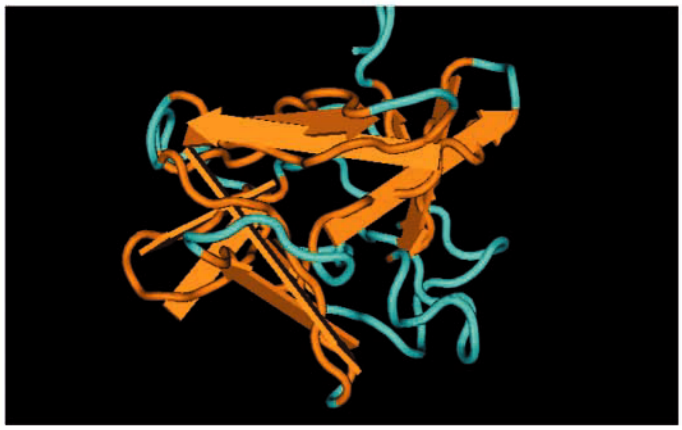

Figure 1.4. 3D rendering of FGF-1 structure.[5]

FGF-1 and S100A13 are able to traverse the cell membrane in their folded form.[29] In this work, dihydrofolate reductase (DHFR)-containing chimeras, which can be locked in a folded conformation by aminopterin, were employed, and FGF-1 and S100A13 secretion was studied *in vitro* by examining cell lysates and conditioned media as well as via immunofluorescence.[29]

1.3 Sum Frequency Generation Vibrational Spectroscopy

To further understand the process of FGF-1 complex translocation across the plasma membrane, information regarding the phospholipid conformational order and orientation is required. A spectroscopic technique uniquely capable of elucidating both conformational order and molecular orientation is sum frequency generation vibrational spectroscopy (SFS). Unlike typical spectroscopic methods, SFS records vibrational spectra of interfacial molecules exclusively.[30,31] SFS utilizes the nonlinear optical phenomenon of sum frequency generation (SFG). SFG occurs when light interacts at an interface under certain symmetry and phase matching conditions.[30] SFG, when employed in spectroscopic investigations, is typically generated by two pulsed, high energy lasers that are temporally and spatially overlapped at an

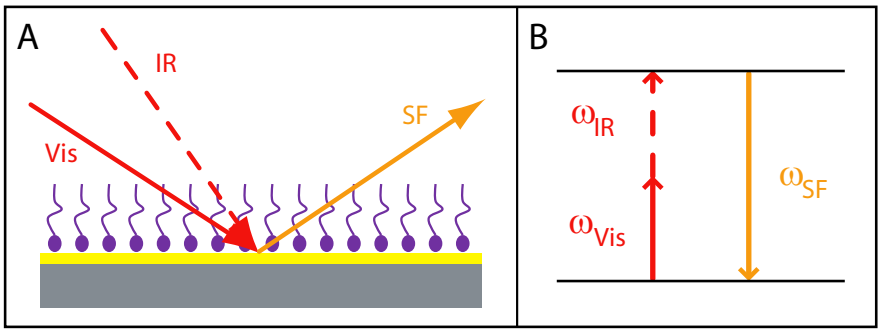

Figure 1.5. Sum frequency generation scheme. **A** Sum frequency generation occurs at an interface when two laser beams interact. **B** The frequency of the beam emitted is at the sum of the high-energy, pulsed incident frequencies ($\omega_{Vis} + \omega_{IR} = \omega_{SF}$).

interface. The pump beam has a fixed visible frequency, while the probe beam has a tunable infrared frequency (Figure 1.5A). As the two incident laser beams interact at an interface, light is generated and emitted from the interface at the sum of the two incident frequencies such that $\omega_1 + \omega_2 = \omega_3$ (Figures 1.5A and 1.5B). Typically, molecules in the bulk do not produce an SF signal since they are isotropically distributed and possess inversion symmetry. Generally, only molecules at an interface may lack inversion symmetry and therefore produce an SF signal. Consequently, interfacial molecules may be probed via SFS without spectral contributions from the bulk.[32] The emitted SF signal is resonantly enhanced when the frequency of the infrared beam matches a vibrational mode of the interfacial molecules. Thus, the vibrational spectrum of the interfacial molecules is measured as a function of the infrared frequency; however, SFG inherently up-shifts the emitted signal to visible wavelengths.[30]

SF spectra provide two forms of molecular information: the degree of conformational order and orientation of the molecules at the interface, (however, the latter requires a non-resonant background signal from the substrate). The conformational order of the interfacial molecules may be determined by the relative strength of var-

ious vibrational modes. For example, if a highly ordered, fully *trans* monolayer of phospholipid at an interface was probed, methyl group resonances would be present in the spectrum since the methyl groups that terminate the alkyl chain tails of the phospholipids break inversion symmetry and are SF active. However, the methylene groups in the phospholipid tails possess inversion symmetry and therefore are SF inactive. Should alkyl chain disorder be introduced, producing *gauche* defects in the phospholipid tails, the methylene group resonances would lose inversion symmetry and become SF active. Comparison of the methyl and methylene resonance intensity ratios for the fully ordered monolayer and the disordered monolayer provides the degree of conformational order of the interfacial molecules.[33] Further, the orientation of the interfacial molecules may be determined from the phase of the SF spectrum ('peaks' vs. 'dips' relative to the baseline), provided that the substrate supporting the molecules produces a non-resonant background as a reference.

The first SF spectra were recorded in 1987 by Shen et al. and shortly after by Harris et al..[34–36] Since this pioneering work, SFS has been applied to many synthetic and biological systems.[30] Current biological applications vary widely, but include applications of SFS to model membrane systems, and protein transport studies. The Richmond group has extensively studied surfactant adsorption at the water/oil interface and phospholipids at both the water/oil and air/water interfaces, probing both the conformation of the various lipids and their effect on solvent structure.[33,37–43] Further, Wolfrum and co-workers have combined SFS studies on phospholipids with Fourier transform infrared spectroscopy to probe the fluidity of drop cast lipids on solid substrates, specifically assessing the order of the hydrocarbon chains.[44,45] The Bonn group has performed numerous SFS studies on various phospholipid monolayers at the air/water interface, specifically exploring the effect of surface pressure,[46,47] the presence of calcium and sodium ions in the subphase,[48] and separately, DNA in the subphase[49] on phospholipid ordering. Bonn et al. have

also probed the interaction of the phospholipid monolayer with duramycin, a peptide.[50] These and other studies have also yielded information regarding the structure of water in proximity to phospholipids.[51–55] Bonn has also investigated the effect of including cholesterol in the monolayer, probing the ordering of the monolayer via SFS.[56] Cholesterol-induced phospholipid condensation has been explored by Itoh et al..[57] Furthermore, Itoh and co-workers performed SFS studies on mixed phospholipid monolayers, monitoring phase transitions of the monolayers with increased surface pressure, and separately, the interaction of the monolayer with polymyxin B, an antibiotic.[58,59] The Yan group has probed PG monolayers at the air/water interface[60] and studied the interaction of human islet amyloid polypeptide with the lipid monolayer.[61,62] Recently, Viswanath et al. studied the interaction of thiocyanate ions with zwitterionic phospholipid monolayers,[63] and Hill et al. assessed an isoniazide peptide conjugate's affinity for zwitterionic phospholipid monolayers;[64] both studies were performed at the air/water interface. The Rutland group has probed the conformational order of phospholipids as a function of the degree of unsaturation as well as on variations in headgroup and deuteration at the air/aqueous solution interface.[65,66] Simulations of lung phospholipid and surfactant distribution have been studied by Ma and Allen, specifically investigating the conformation of PC monolayers as a function of lateral pressure at the air/water interface.[67–69] Ma and Allen demonstrated for the first time that SFS could be employed to study the hydration state of phospholipid head groups,[70,71] and further have studied the hydration and orientation of the phosphate group in PC monolayers,[72] in addition to the interaction of PC monolayers with dimethylsulfoxide.[73] The Allen group, as well as the Walker group, have examined the interaction of anionic[74,75] and cationic surfactants[75] with PC monolayers at the air/water interface. Similarly, the conformation of mixed lipid and surfactant monolayers at the air/water interface has been probed by the Miller group, and the conformational information correlated with

interfacial water structure.[76] Other studies have employed various phospholipids at the air/water interface to study the structure of interfacial water.[77,78]

In addition to the air/water monolayer studies described above, many SF studies have been performed on phospholipid bilayer systems. The Conboy group has studied the conformation of phospholipids comprising each leaflet of bilayers supported on solid structures.[79] In addition, Conboy and co-workers have assessed the phase transition temperature,[80] phase segregation behavior,[81,82] the binding affinity of various drugs to phospholipid membranes,[83] and transbilayer movement, or 'flip-flop', of phospholipids in lipid systems.[84–88] Conboy et al. also studied phospholipid systems in the presence of various membrane-spanning peptides such as gramicidin A,[89] WALP and melittin,[90] and separately, external electrostatic forces.[91] Tong et al. has employed solid supported membranes to study the effect of phospholipase A_1 on membrane hydrolysis.[92] Kim et al. studied the structure of interfacial water in relation to solid supported membranes.[93] Hybrid bilayer membranes (HBMs) have been investigated by SFS. Specifically, Petralli-Mallow and Briggman et al. have studied vesicle fusion and Langmuir-Blodgett deposition of phospholipids onto self-assembled alkanethiol monolayers, probing the phase transition temperature of the resultant membranes, and investigating the interaction between cholesterol and phospholipids in the HBM.[94–97] Davies and co-workers have explored the effect of phospholipid deposition surface pressure on the ordering of phospholipids and alkanethiol monolayers comprising HBMs, with and without cholesterol present.[98,99] Lis et al. has probed vibrations in the head group of phospholipids deposited by the Langmuir Schaefer technique on self-assembled monolayers (SAMs).[100] SFS has also been employed to study the conformational changes that occur in membranes in the presence of proteins or polysaccharides. A study by the Neivandt group was the first to demonstrate protein-induced deformation of a phospholipid membrane (a HBM) via SFS utilizing FGF-1 as the protein.[101] The Chen group has examined membrane

perturbations of solid supported bilayers induced by antimicrobial peptides,[102–105] membrane-active polymers,[106] melittin,[107] and magainin 2.[108] Recently, Chen and co-workers have expanded to cushioned supported bilayers, specifically looking at poly(*L*-lactic acid) (PLLA) (100 nm thickness) supported PG bilayers and their interaction with Cecropin P_1, an antimicrobial peptide.[109] Chen and co-workers have further probed the orientation of the G protein $\beta\gamma$ subunit,[110] melittin,[111] antimicrobial peptides,[105,112,113] alamethicin,[114] tachyplesin I,[115] and cytochrome b_5,[116] embedded within various bilayers. Additionally, the Miranda group studied the interaction of polysaccharides with phosphatidic acids,[117,118] and separately, with phospholipids.[119]

The review presented above details work utilizing SFS to study phospholipid membranes, an area of interest that continues to expand in the growing SF community. While fundamental membrane questions are being addressed, it is noteworthy that these studies do not involve live cells. The high power, pulsed lasers required for SFS are likely to irreversibly damage cells. Additionally, interpretation of a live cell SF spectrum would be complicated due to the various components found in the cellular membrane that could contribute to a measured spectrum. However, Inoue et al. have constructed a non-scanning vibrational sum frequency generation microscope capable of collecting SF signal from an onion root cell.[120] While they were successful in collecting spectra, they were not able to clearly assign spectral resonances to cellular constituents.[120] As such, it is necessary to employ model membrane systems in SFS studies, and it is critical that the systems be physiologically relevant. While the model membrane systems utilized previously have given new insight into membrane function, they are not amenable to protein transport studies. Membranes on solid substrates clearly do not allow for protein transport, while membranes at the air/water or oil/water interface are not at the aqueous/aqueous interface necessary for physiological relevance. Consequently, there exists a pressing

need for an alternative model membrane system that allows for protein transport and is physiologically relevant.

1.4 Fluorescence Correlation Spectroscopy

Developing a model membrane system as a platform for studying protein transport across membranes requires characterization of the diffusion coefficient of component phospholipids to ensure physiologic relevance. The lateral diffusion of lipids comprising a membrane may be measured by a variety of techniques: fluorescence recovery after photobleaching (FRAP), fluorescence correlation spectroscopy (FCS), or single particle tracking (SPT).[121,122] In a FRAP experiment, the membrane is doped with high fluorophore concentrations (0.5 - 2 mol%[123]) during fabrication. With the sample mounted on an optical microscope, high intensity laser light is employed to bleach the fluorophores in a small region of the membrane. Immediately following, a lower intensity laser is used to monitor the recovery of fluorescence in the bleached area as unbleached fluorophores diffuse into it. For a SPT measurement, the membrane is doped with a low concentration of fluorophores, typically 10^{-6} mol%.[121] The substrate is mounted on an optical microscope where single molecule trajectories from the membrane may be monitored with a CCD camera and widefield illumination. FCS[124] is also a single molecule technique that requires a low concentration of fluorophores (0.001 - 0.01 mol%[123]). As the probe molecules, typically fluorophores, diffuse through an observation volume, most often created by a tightly focused laser beam, they emit fluorescence (Figure 1.6). Fluorescence emission is collected as a function of time to produce a time course. A correlator card receives the time course and auto or cross correlates the data collected.[125] The correlation curve is then fit to a known diffusion model.[126] A calibration standard must be measured and compared to membrane correlation data in order to determine diffusion

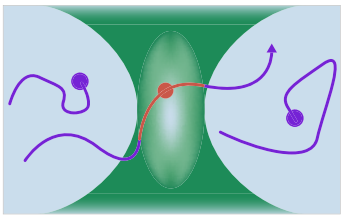

Figure 1.6. Fluorescence correlation spectroscopy scheme. The scheme depicts diffusion of fluorophores through the observation volume.

coefficients of the species of interest, in addition to chemical rate conversions and photophysical information.[126–128] Of these techniques, FCS would likely provide the greatest detail regarding the interaction of phospholipid membranes and the FGF-1 transport complex.

The instrumentation required for FCS measurements may be as simple as an excitation laser source, a confocal microscope with appropriate filters and collection optics, and an avalanche photodiode (APD) or photomultiplier tube (PMT) for detection. Measurements are facilitated by the use of automated hardware that converts the intensity time course into a correlation curve (a correlator card).[129]

The use of FCS for membrane characterization has been extensive, with studies on live cells, vesicles, and planar membranes.[123,130,131] Typically when fabricating a phospholipid bilayer, a fluorescent phospholipid analog, such as 1,1'-dioctadecyl-3,3,3',3'-tetramethylindocarbocyanine perchlorate (DiI C_{18}) or a fluorescently tagged phospholipid, such as *N*-(7-nitrobenz-2-oxa-1,3-diazol-4-yl)-1,2-dihexadecanoyl-*sn*-glycero-3-phosphoethanolamine, triethylammonium salt (NBD-PE), is added to the phospholipid mixture. Incorporation may be achieved by incubating cells or membranes with the fluorophore, or by mixing the phospholipids and fluorophore in solution prior to model membrane fabrication.[130,131] As stated above, the concentration of fluorophore required for FCS membrane measurements is on the order of 0.001 - 0.01 mol% of fluorophore to phospholipid, which is considerably lower than

for other fluorescence techniques, e.g. fluorescence recovery after photobleaching (FRAP).[123] Reducing the amount of fluorophore in the model membrane decreases the potential for perturbation of the membrane, thereby increasing the physiological relevance of the measurement. Ideally, the fluorophore chosen for membrane studies should have a high quantum efficiency, a high fluorescence quantum yield, low triplet activity (an intermediate transition during relaxation occurring on fast time scales), and should not photobleach readily, in addition to being a lipid analog.[128,132]

Chiantia et al. provides an excellent review covering the breadth of FCS studies on live cells, vesicles, and planar membranes,[133] and therefore such material will not be covered in detail in this review. However, several studies pertinent to phospholipid diffusion within model membrane systems and live cells will be discussed. Briefly, Elliot et al. spread phospholipid monolayers on polystyrene films, and studied phospholipid lateral diffusion via FCS.[134] Both the Webb and Schwille groups, independently and collaboratively, have performed a variety of FCS studies on live cells and vesicles. Comparisons were made of fluorophore diffusion in live cell membranes and model membrane vesicles. Separately, fluorophore diffusion in model membranes has been employed to probe the effect of phase separation and cholesterol addition.[130,135–139] Additionally, both groups utilized supported phospholipid bilayers to study membrane phospholipid distribution and dynamics via FCS.[125,133,140] Zhang and Granick have employed FCS to investigate the diffusion in each leaflet of solid supported membranes, and separately, monitored the effect of an adsorbed polymer on lipid diffusion.[123,141]

Further, FCS has been used to probe membrane-protein interactions, with an emphasis on lipid domains (rafts) in supported bilayers.[125,131] Proteins are involved in raft formation, and therefore tracking protein movement optically, in addition to monitoring the movement of the lipid domains via a fluorescent lipid analog, provides a powerful methodology to study raft formation.[137] Vesicle model membranes and

fluorescently tagged proteins have been utilized to study protein diffusion in model membranes with FCS. For example, the Schwille group studied the raft-associated protein, human placental alkaline phosphatase, monitoring its change in diffusion rate as it associated with domains in the model membrane.[137] The Kinjo group employed PS liposomes to study the binding interaction of lipids with a rhodamine-labeled protein known as protein 4.1.[142] FCS measurements of rhodamine 6G, protein 4.1, and protein 4.1-liposome complexes formed either by contact with PS or with PC liposomes, were performed. The resulting correlation curves had significantly different shapes with variation in molecular weight and interaction between the protein and lipids.[142] As a result, the protein of interest was shown to only interact with PS liposomes and not with PC liposomes.[142] A study by Campbell et al. of polychlorinated biphenyl (PCB) interactions with model membranes further demonstrated the power and capabilities of FCS.[143] Specifically, supported bilayers with fluorescently tagged lipid molecules were fabricated, and the diffusion of the lipids determined via FCS. Subsequently, two different fluorescently active PCBs were brought into contact with the tagged and non-tagged bilayers, and each PCB's correlation curve was measured. Fitting of each PCB's correlation curve resulted in two diffusion coefficients, one value within error of the phospholipid diffusion coefficient, and one value an order of magnitude slower, indicating two potential interactions of each PCB and the membrane.[143]

The studies presented above are a small sampling of the many calibration-dependent FCS studies to date. Calibration-dependent FCS requires the use of a fluorophore with a previously determined diffusion coefficient, relying either on a separate measurement technique or previously reported diffusion coefficients in literature. Unfortunately, many groups have found FCS to be highly sensitive to experimental conditions and in addition, diffusion coefficients of well-known fluorophores reported in the literature often do not agree.[121,144] Recently, a derivative of confocal

FCS has been developed that requires no calibration standard.[145] Termed 'z-scan' FCS, the technique utilizes the parabolic dependence of the characteristic diffusion time and effective particle number (as determined in standard FCS measurements) on the z-axis position of the sample in the observation volume to determine the diffusion coefficient and concentration. It is uniquely suited to planar systems, such as model membrane systems, and has been employed to study solid and cushion supported membranes formed by vesicle fusion,[145–152] giant unilamellar vesicles (GUVs),[121,125,153–155] and probing the plasma membrane and membrane-protein interactions of live cells.[156,157] Since z-scan FCS is ideally suited to, and limited to, planar systems, it is an excellent complementary technique to SFS for the study of non-classical protein secretion employing model membrane systems.

1.5 Model Membrane Systems

Model membranes are artificial lipid bilayers that are either spherical or planar, and may be freely suspended or supported on a solid substrate (either directly or via a cushion). Select membranes potentially allow proteins to be incorporated into, or translocated through, the bilayer. A model membrane provides a simplified version of a cell membrane and is often more amenable to microscopy and/or spectroscopy. The following sections provide a review of the various model membrane systems, noting their potential for the study of FGF-1 non-classical secretion via SFS and/or FCS.

1.5.1 Vesicles and Liposomes

Most cytoplasmic organelles may be considered membrane vesicles of various sizes. For example, Golgi-derived exocytotic vesicles are key elements of the classical secretion pathway and have an approximate radius of 100 nm.[1] Artificial membrane vesicles are spherical structures comprising a phospholipid bilayer membrane

surrounding an aqueous core, and are stable in aqueous solution. Artificial vesicles are also termed liposomes, indeed, the terminology for vesicles and liposomes is often used interchangeably. However, it should be noted that vesicles may also be formed from surfactants. Phospholipid vesicles or liposomes are often characterized according to their diameters, for example small unilamellar vesicles (SUVs), large unilamellar vesicles (LUVs), and giant unilamellar vesicles (GUVs) with radii of 4 nm - 20 nm, 50 nm - 10 μm, and $>$ 10 μm, respectively, are named for their sizes.[158] Additionally, liposomes may be described by the number of phospholipid bilayers they are composed of (uni- or multilamellar vesicles) and the charge of the outer surface (anionic, cationic, or neutral).[158] Due to the enclosed bilayer structure of vesicles, they represent an excellent model of the plasma membrane of a cell, providing a means of studying membrane properties as well as membrane-protein interaction.[19,27,159] Additionally, vesicles and liposomes often serve as intermediates for producing other model membrane systems.[33,94,160] Due to the breadth of research utilizing this particular model membrane system, a selection of studies directly related to non-classical protein transport is reviewed below.

A novel assay utilizing 'inside-out' vesicles formed from reconstituted plasma membranes of cells was developed by Schäfer et al..[161] The assay established a method for membrane extraction as well as characterization by affinity purification of the 'inside-out' and 'right side-out' vesicles formed.[161] For an 'inside-out' vesicle, the cytosolic plasma membrane leaflet components serve as the distal (outer) leaflet of the vesicle membrane system. The cytosolic plasma membrane leaflet components serve as the proximal (inner) leaflet of a 'right side-out' vesicle. The transport of FGF-2 was studied by incubating the vesicles with the protein at 37°C for 4 hours. After removing excess protein by rinsing, a protection study was performed using a protease and/or detergent. Results were visualized by Western blotting after running SDS-PAGE. It was demonstrated that FGF-2 was capable of entering the membrane

vesicles as evidenced by protection from the protease.[161] Other researchers have since assessed the transport behavior of additional proteins including somatostatin,[162] HASPB lipoprotein,[163] and FGF-1 (discussed in Chapter 3),[13,29,164] as well as Na^+ transport across the membranes of the reconstituted vesicles.[165]

Non-reconstituted, or artificial, liposomes have been used to study the ability of non-classical transport complex members to destabilize phospholipid membranes by Prudovsky and co-workers.[27] Unilamellar liposomes were prepared from a variety of synthetic phospholipids (PS, PI, PG, and PC) resuspended in an aqueous solution containing carboxyfluorescein, a fluorescent dye. After removing the excess dye using a dextran desalting column, the dye-enclosed liposomes were monitored via a spectrofluorimeter.[19,27] At a temperature representative of heat shock (50°C), FGF-1, p40 Syt1, and S100A13 were added to the liposome solution, and the change in fluorescence intensity was monitored as the proteins interacted with the membrane. It was demonstrated that FGF-1 most efficiently destabilized membranes comprising acidic phospholipids (PI, PG, PS), but not zwitterionic PC liposomes. S100A13 behaved in a similar manner to FGF-1, however, p40 Syt1 only destabilized the PI liposomes, indicating a level of selectivity.[27] The results reported by Prudovsky and coworkers reinforce the importance of determining the role of the phospholipid bilayer in secretion of signal peptide-less proteins.

While vesicles and liposomes are physiologically relevant due to their shape and ability to incorporate or translocate proteins, they are not amenable for use in SFS studies. As described earlier, SFS is typically restricted to planar interfaces; a sphere of lipids would likely provide multiple interfaces and not maintain a stationary position during spectral acquisition. Although SFS studies have been performed in a scattering geometry from spheres in a solvent, the signal was extremely weak and the experiment was limited to a carefully selected sphere/solvent pair.[166,167] To date, SFS in the scattering geometry has only been applied to polymer spheres, and

not to lipid vesicles. Since commonly employed SFS geometries, such as reflection and total internal reflection, have been readily applied to planar lipid membranes as discussed in Section 1.3, the following sections review planar model membrane systems.

1.5.2 Black Lipid Membranes

An early generation model membrane system, in use since the 1960's, is the black lipid membrane (BLM).[168,169] A BLM is a phospholipid bilayer formed across an aperture maintained in aqueous solution. This type of membrane was first formed for use in patch clamp experiments. The ease of forming planar bilayers across small holes has greatly improved with the development, over the past two decades, of microfabrication techniques.[170] Various studies have been performed on BLMs including ion channel investigations by monitoring electric potential, monitoring of chemicals binding to receptors maintained in the membrane, and studying the interaction of DNA with membranes.[168] However, the stability of BLMs is problematic. Indeed, the membranes typically only last for a few hours.[170] To combat this issue, agarose, a hydrated polymer, has been used to support and stabilize BLMs with minimal detrimental effects observed on the membrane properties.[171]

The instability of BLMs does not make them an attractive choice for studying non-classical protein translocation via SFS. Since it has been shown that FGF-1, S100A13, and p40 Syt1 are capable of destabilizing phospholipid membranes,[27] it would be experimentally impossible to differentiate bilayer rupture due to protein interaction from spontaneous destabilization. Additionally, the cross-sectional area of the SF beams at the surface would likely be larger than the area of the hole required to maintain the membrane, resulting in signal aberrations and decreased signal intensity.

1.5.3 Hybrid Bilayer Membranes

A more stable alternative to BLMs are hybrid bilayer membranes (HBMs). HBMs consist of a solid support functionalized with an alkanethiol monolayer, with a second monolayer composed of phospholipid deposited on the alkanethiol layer (Figure 1.7).[172,173] The substrate is most often a metal surface, e.g. a gold coated silicon wafer, on which an alkanethiol can covalently bind. The quality of the monolayer may be assessed by contact angle measurements.[174] The alkanethiol is dissolved in a solvent, e.g. methanol or ethanol, and the substrate placed in solution, allowing self-assembly to take place. Subsequent formation of the phospholipid monolayer may be achieved via vesicle fusion, Langmuir-Blodgett (LB) deposition, or Langmuir Schaefer (LS) deposition. Vesicle fusion occurs via spontaneous rupture and spreading of phospholipid vesicles on the hydrophobic alkanethiol monolayer. Alternatively, LB and LS deposition employ a trough containing an aqueous subphase on which a monolayer of phospholipid is spread, drop-wise, from a volatile, non-aqueous solvent. The phospholipids spontaneously orient such that their hydrophilic head groups are immersed in the water subphase, while their hydrophobic tails are positioned in the air.[172,175,176] After the solvent evaporates, the phospholipids are compacted via a closing barrier system on the trough to a specified surface pressure, (measured by a Wilhelmy film balance). Finally, the substrate of the HBM containing the thiol monolayer is passed vertically for LB deposition or horizontally for LS deposition into the subphase, through the phospholipid monolayer, resulting in an alkanethiol-supported lipid leaflet.

HBMs provide an experimentally amenable system in various ways. Due to the metallic surface, electrochemical techniques and surface plasmon resonance may be used to characterize the membrane.[173] Additionally, the use of various spectroscopic and microscopic techniques such as atomic force microscopy, ellipsometry, and SFS

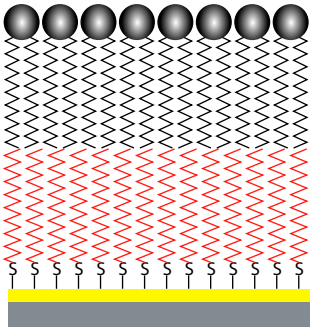

Figure 1.7. Hybrid bilayer membrane. The lower layer (red) is the alkanethiol, while the upper layer (black) is the phospholipid. The gold coating and support are represented by the yellow and gray, respectively.

are greatly facilitated by the planar and stable nature of the membrane.[173] Two SFS studies detailed below exemplify the use of HBMs, the first a membrane characterization study, the second, a non-classical protein transport study.

The Petralli-Mallow group and later, the Briggman group have been leaders in the use of HBMs, particularly in SFS studies.[94–97] In one particular study, the formation of a HBM via vesicle fusion onto an alkanethiol functionalized gold surface was monitored by SFS.[94] Due to the inversion symmetry required for an interface to be SF active, a HBM had to be constructed that would facilitate spectral differentiation between the alkanethiol layer and the fused vesicle layer. This was achieved through use of a perdeuterated octadecanethiol (d-ODT), and a PC phospholipid with a perdeuterated headgroup but perprotonated tails. The broadband IR pulses were tuned to the C-H stretching region (2800-3100 cm^{-1}). Thus, the resonances detected were from the perprotonated terminal methyl and the methylene groups composing the phospholipid tails. SF spectra revealed that as vesicles were flown through the liquid cell, into contact with the d-ODT monolayer on the substrate, there was an increase in the intensity of the methyl resonances from the phospholipids with time. The contribution of methylene resonances to the SF spectra was minimal. Further, the intensity of the methyl resonances increased after rinsing ex-

cess and partially fused vesicles from the system, indicating that the phospholipid layer was very well ordered. This provided a new method for others to study HBMs *in situ* via SFS.[94]

Building upon this study, an investigation of the interaction between FGF-1 and a HBM, as probed via SFS, was performed by Doyle et al..[101] Specifically, the degree of lipid conformational order was measured *in situ* at 60°C in the presence of FGF-1. The HBM consisted of d-ODT self-assembled on titanium primed, gold coated silicon wafers. After mounting the sample in a liquid cell, SF spectra were collected in the C-H stretching region as PG vesicles were flown through the system (Figure 1.8a). As in the previous study, the only source of SF signal was from the phospholipids. An SF spectrum collected after vesicle fusion to the surface clearly showed strong methyl resonances at 2881 cm^{-1}, 2943 cm^{-1}, and 2973 cm^{-1}, implying that the fused vesicles had created a very highly ordered phospholipid monolayer. Spectral fitting revealed the presence of very weak methylene resonances present at 2860 cm^{-1} and from 2890 to 2930 cm^{-1}. The weakness of the methylene resonances in comparison to the methyl resonances indicated that the PG possessed almost complete inversion symmetry, meaning that the phospholipid tails were in a nearly fully *trans* conformation. Additionally, the use of gold as the substrate facilitated the determination of the orientation of the phospholipids from the spectral phase; the phospholipids were found to be oriented with their alkyl chain tails toward the d-ODT surface.

Subsequently, any partially fused vesicles and remaining whole vesicles were removed via rinsing, and a second SF spectrum recorded (Figure 1.8b). A similar increase in the intensity of the methyl resonances and decrease in the intensity of the methylene resonances was observed by Petralli-Mallow et al.,[94] implying a further increase in the order of the HBM.[101] FGF-1 was subsequently introduced to the liquid cell containing the PG membrane and permitted to equilibrate prior to an-

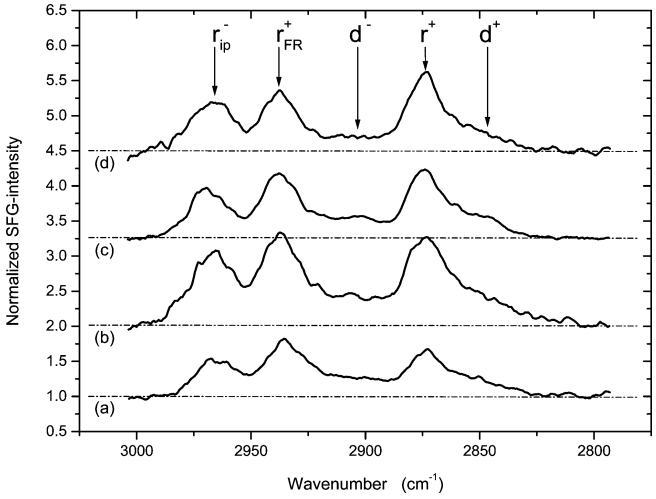

Figure 1.8. HBM-FGF-1 interaction as determined by SFS.[101] *In situ* SF spectra of (a) PG vesicle fusion, (b) rinsing of excess lipids, (c) equilibration with FGF-1, (d) removal of FGF-1, where r^+ is the symmetric methyl stretch, r^+_{FR} is the Fermi resonance of the symmetric methyl stretch, r^-_{ip} is the in-plane methyl asymmetric stretch, d^+ is the symmetric methylene stretch, and d^- is the asymmetric methylene stretch.[101]

other SF spectrum being recorded (Figure 1.8c). Comparison of the new spectrum with those previously recorded revealed a decrease in the intensity of the methyl resonances and a concurrent increase in the methylene resonance intensities. This result was attributed to FGF-1 interacting with the membrane and causing the phospholipid methyl groups to lose symmetry and become more disordered and therefore less SF active. In addition, the methylene groups, which previously were in a nearly fully *trans* conformation, had more *gauche* defects present in the phospholipid tails as a result of FGF-1 interaction, thereby breaking inversion symmetry and resulting in increased SF activity. It was concluded that FGF-1 induced conformational disorder in the phospholipid membrane.[101] The last component of the experiment was to rinse away the FGF-1, and record an SF spectrum (Figure 1.8d). The final spectrum was comparable to that of the HBM prior to FGF-1 addition, implying that the PG phospholipid returned to a highly ordered, near fully *trans* conformation, indicating reversibility in membrane deformation.[101] These findings were consistent

with the liposome study discussed in Section 1.5.1, where it was demonstrated that FGF-1 destabilizes acidic phospholipid membranes.[27] The SFS study detailed in this section was the first to show reversible deformation of membranes by FGF-1. As a control, α-chymotrypsin, a protein secreted through the classical pathway and unable to permeabilize membranes composed of acidic phospholipids[6] was employed. Unlike FGF-1, it did not induce any significant changes in the membrane as reported by the SF spectra.

It may be concluded from the work of Doyle et al. that the use of HBMs provides an amenable membrane model for studies utilizing SFS. However, HBMs possess several limitations. First, the use of an alkanethiol monolayer does not make the HBM a true phospholipid bilayer. Second, since the alkanethiol molecules are covalently bound to the surface, protein transport across the membrane is not possible. As such, the result of membrane-protein interactions can only be assessed from the perturbation of the distal leaflet as described above.[101] The ability to create a model membrane in which both leaflets contain phospholipids addresses the first of these limitations and is discussed in the following section.

1.5.4 Solid Supported Membranes

A phospholipid bilayer supported on a hydrophilic substrate is a very satisfactory and widely used model membrane system. Such membranes have been employed extensively for studies not limited to but including; channel formation, energy conversion, molecular recognition, and antibody-antigen binding.[177–184] As with the HBM, the planar bilayer facilitates the use of spectroscopic and microscopic techniques (e.g. SFS and FCS), and a greater degree of stability is achieved over BLMs due to the proximity of the solid support. The membrane is separated from the substrate by a 10-20 Å water layer, permitting lateral movement of lipids in the proximal (lower) leaflet.[185] While a solid supported membrane is a step closer to mimicking

the cell membrane, the thin water layer (10-20 Å[185]) still prevents incorporation of transmembrane proteins containing intracellular components and transport of proteins across the bilayer. In only a few studies have researchers retained protein activity after incorporation into a planar bilayer system, where typically the protein is immobile due to interaction with the solid surface.[185–187] Despite the limitations regarding protein incorporation and transport, SFS has been used to characterize this type of model membrane, in particular the 'flip-flop' of phospholipids between leaflets, as well as membrane-protein interactions (reviewed in Section 1.3).

Planar supported phospholipid bilayers are primarily formed by two methods: vesicle fusion and the Langmuir-Blodgett/Langmuir Schaefer (LB/LS) technique.[188] Vesicle fusion, as described previously, employs liposome rupture to create phospholipid films on solid surfaces. In order to create a bilayer on a hydrophilic surface (rather than a monolayer on a hydrophobic surface for a HBM), liposomes are simply brought into contact with the substrate and allowed to fuse. While simple, vesicle fusion does not allow for independent control of the phospholipid content of each leaflet of the bilayer or lipid density. Conversely, the LB/LS technique provides great control over the content and conformation of each lipid bilayer leaflet.[79] Specifically, the first layer is deposited by the LB technique, described in Section 1.5.3, but with the substrate initially immersed in the subphase. The second leaflet is deposited by holding the sample above the subphase horizontally, and passing it through into the subphase (Figure 1.9). The two separate phospholipid depositions allow the monolayer composition of the two leaflets to be varied by replacing the phospholipid monolayer at the air/water interface between the two depositions. Thus, asymmetric bilayers may be readily created, for example, membranes may contain perdeuterated phospholipids in one leaflet and perprotonated phospholipids in the other leaflet; such membranes are amenable to SFS studies.[84,102]

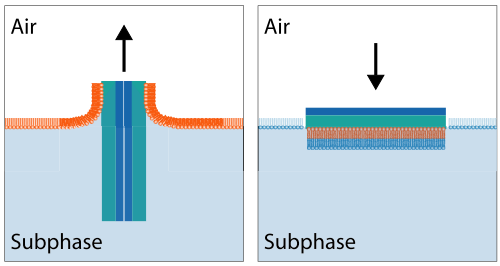

Figure 1.9. Langmuir-Blodgett/Langmuir Schaefer deposition. The LB/LS technique is employed for lipid bilayer deposition. Note the asymmetric bilayer (represented by orange, and separately blue lipids) is readily formed.

1.5.5 Cushioned Membranes

To combat the limitations regarding protein incorporation and protein transport that occur with solid supported bilayer membranes, cushioned model membranes have been developed. Cushioned model membranes are constructed such that the phospholipid bilayer is separated from the solid substrate by a lipopolymer tether or a hydrated polymer/hydrogel layer (Figure 1.10). This provides space beneath the membrane for incorporation of transmembrane proteins, or to permit protein transport. Many researchers have developed different versions of these cushioned bilayers, notably, Ringsdorf,[189] Sackmann,[190,191] Israelachivili,[160] Offenhausser,[171] Tanaka,[191,192] Cremer,[193–196] Wirth,[197] Knoll,[198–203] and Frank,[202,204,205] among others. As these model membranes have been created to facilitate many kinds of studies, the size of the space created by the tether, or the more commonly used hydrated polymer, must be considered for protein incorporation or transport. Knowing the size of the intracellular domains of the transmembrane protein of interest is essential, and it is beneficial to have flexibility in cushion thickness. The hydrated polymers and hydrogels used thus far have included polyethyleneimine,[160,189,206] polyacrylamide,[197,207,208] and polysaccharides such as dextran, cellulose, and chitosan.[171,209–212]

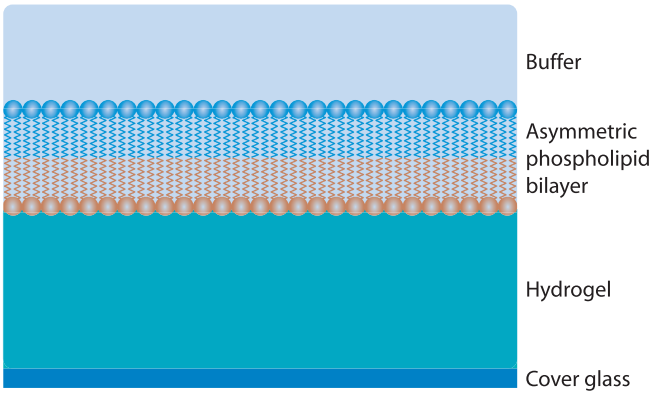

Figure 1.10. Cushioned model membrane. The hydrated polymer/hydrogel cushion supports an asymmetric phospholipid membrane.

A variety of techniques have been utilized to apply the hydrated polymer/hydrogel to the solid support. Adsorption of a variety of polyelectrolytes has been effective on substrates such as quartz, mica, and silica, however this method has an inherent lack of control over the thickness of the polymer layer.[160,177,189] Another method employed to form the hydrated polymer layer is LB deposition. Films formed via this technique have well controlled thickness as the substrate may make multiple passes through a hydrophobic polymer at the air/water interface. Once deposited on the substrate, the polymer must be chemically modified to produce a hydrophilic hydrated layer on which the lipid membrane may be formed.[213] In this particular method, the hydrophobically modified polymer must be synthesized, therefore limiting the application of the technique. One last method that has been used in many applications is spin coating. Briefly, the solid substrate is held, most often by vacuum, on a spinning chuck. The polymer solution of interest is dispensed onto the surface either prior to spinning or during spinning, and after spinning has commenced, the polymer solution is spread across and off the surface, leaving a thin film. It is noted that the spin parameters can be adjusted to change the thickness of the polymer film. Poly(ethoxaline) and poly(ethoxaline-co-ethylenimine) have both been spin cast onto benzophenone-silane modified silicon surfaces, followed

by development under ultraviolet light to covalently bind the polymer to the surface.[202] Most noteworthy, relevant cushioned systems have been fabricated with the polysaccharide chitosan.[171] Chitosan is easily prepared to a liquid state and has been demonstrated to make highly controllable thin films via spin coating.[214]

Once the hydrated polymer film has been formed, either LB/LS deposition or vesicle fusion methods may be used to fabricate the phospholipid bilayer. The relative advantages of the two techniques for bilayer formation on hydrated polymer films have been explored using polyethylenimine coated substrates and PC lipids.[160] While vesicle fusion was established as the simplest method to deposit a bilayer on a cushion,[160] LB/LS deposition, due to increased control over the bilayer constituents, has since proven to be the most successful bilayer deposition method for a variety of cushions.[171,215,216] Wong et al. showed that successful bilayer membrane depositions depended heavily on the supporting substrate's degree of swelling.[160] Smith et al. determined that a lack of roughness of the polymer layer is critical in maintaining membrane fluidity and the mobility of transmembrane proteins.[197] Additionally, polymer/lipid electrostatic interactions, steric forces from polymer chains extending into solution, and vesicle osmotic stress contribute to the success of deposition and the stability of the bilayer.[206]

It is evident from the review provided in this chapter that a cushioned model membrane would be an excellent platform to pursue detailed studies of the role of the phospholipid membrane in FGF-1 translocation. The HBM utilized by Doyle et al.[101] was a good starting point and provided critical information regarding FGF-1:membrane interactions, however, it was limited in that it was not a true phospholipid bilayer, and did not facilitate protein transport. Rather, by employing a cushioned model membrane, with its inherent two phospholipid leaflets and a suitable cushion material, the membrane would be far more physiologically relevant, and provide the capability of potential protein translocation. Separately, there is

a precedence for utilizing cushioned membranes in SFS studies and in z-scan FCS studies as detailed in Sections 1.3 and 1.4. Thus, the efforts made to develop and characterize a cushioned model membrane system, and to develop the instrumentation and methodologies required to make SFS and z-scan FCS measurements of it possible, will be detailed in the subsequent chapters.

Chapter 2
EXPERIMENTAL DETAILS

2.1 Cushioned Model Membrane

The model membrane system selected for development in order to investigate the role of the plasma membrane in non-classical protein secretion was the cushioned system. This choice was driven by the need for a stable, planar membrane with sufficient thickness between the substrate and the bilayer to accommodate protein transport.

Spin casting is the preferable method for creating the hydrated polymer/hydrogel film since it is reproducible and provides excellent control over the polymer layer thickness. One such polymer hydrogel is chitosan, which is the deacetylated form of chitin, a polymer derived from shellfish and some fungi (Figure 2.1).[217] Baumgart and Offenhäusser[171] demonstrated that chitosan hydrogel films spin cast on glass substrates provide suitable supports for PC bilayers deposited via the LB/LS method. The model membranes were shown to be fluid, have self healing abilities, and be stable for extended periods of time.[171]

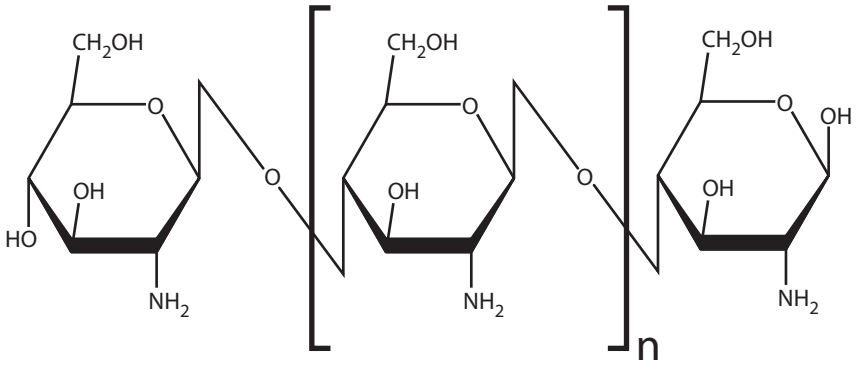

Figure 2.1. Molecular structure of chitosan.

2.1.1 Substrate Preparation

Initially, spin cast chitosan films were created on gold coated silicon wafers to facilitate the use of several film characterization methods. Optically polished silicon wafers were primed with an adhesive titanium or chromium layer, then coated with 100 - 300 nm of gold (root mean square (rms) roughness of ~1 nm) (Platypus Technologies, Madison, WI and provided by Dr. Scott Collins of LASST, University of Maine, Orono, ME). Prior to use, a gold coated silicon wafer was diced and the ~1.5 cm square pieces were cleaned in a 2-5% v/v Contrad 70 detergent/18.2 MΩ·cm water solution overnight (Decon Labs, King of Prussia, PA) followed by copious rinsing in 18.2 MΩ·cm water (Milli-Q, Millipore, Billerica, MA). It was found that the gold surface required functionalization with a carboxylic acid terminated thiol (3-mercaptoproprionic acid)[177,218] to compatibilize the gold with the chitosan film. A 5 mM solution of 3-mercaptoproprionic acid (Sigma-Aldrich, St. Louis, MO) in absolute ethanol (Fisher Scientific, Suwanee, GA) (degassed by bubbling N_2 through it for an hour), was prepared and substrates submerged for at least 18 hours. The substrates were then rinsed in ethanol and dried with N_2. Subsequent chitosan films were prepared on No. 1.5 square cover glass (22 mm, Corning, Corning, NY) and bare silicon wafer pieces (provided by Dr. Scott Collins of LASST, University of Maine, Orono, ME), both of which were cleaned via the following standard cleaning procedure utilized for all glass and stainless steel components in the Neivandt laboratory. The procedure consisted of a rinse in 18.2 MΩ·cm water followed by an overnight soak in a 2-5% v/v Contrad 70 detergent/18.2 MΩ·cm water solution. The soak was followed by rinsing with copious amounts of 18.2 MΩ·cm water and an overnight soak in 70% nitric acid (Fisher Scientific, Suwanee, GA). A final rinse with copious amounts of 18.2 MΩ·cm water was performed; final storage before use was in 18.2 MΩ·cm water.

A final substrate employed for chitosan film preparation was a CaF_2 hemicylinder prism (25.4 mm length, 12.7 mm radius, Red Optronics, Mountain View, CA). Initial use of a given CaF_2 prism required a specific cleaning protocol to remove the polishing oil. The procedure developed was as follows: rinse in acetone ($\geq$ 99.5%, ACS Certified, Fisher Scientific, Suwanee, GA), wipe with lens tissue soaked in acetone, rinse in a 2-5% v/v Contrad 70 detergent/18.2 MΩ·cm water solution, copious rinsing in 18.2 MΩ·cm water, dry with N_2, soak in chloroform in a Teflon beaker for 1 hour, dry with N_2, wipe with lens tissue soaked in acetone, and place in a UVO Cleaner Unit 342 box (Jelight Company Inc., Irvine, CA) for 30 minutes to render the surface hydrophillic. Subsequent cleanings were not as extensive and varied according to whether or not a chitosan film had been spin cast on the surface. For a prism with a chitosan film, the following procedure was employed: an overnight soak in a 2-5% v/v Contrad 70 detergent/18.2 MΩ·cm water solution, copious rinsing in 18.2 MΩ·cm water, minimal polishing with 0.05 μm aluminum oxide (CH Instruments, Inc., Austin, TX), soaking in a 2-5% v/v Contrad 70 detergent/18.2 MΩ·cm water solution, and a final copious rinse with 18.2 MΩ·cm water was sufficient to clean the surface. For a prism supporting solely a phospholipid bilayer, the following procedure was employed: wiping with lens tissue soaked in chloroform and rinse in chloroform (HPLC grade, Fisher Scientific, Suwanee, GA) to remove the lipid, rinsing in acetone and soaking in acetone overnight, and copious rinsing in 18.2 MΩ·cm water. If the surface was rendered hydrophobic after this procedure, 30 minutes in the UVO box followed by more rinsing with 18.2 MΩ·cm water was utilized.

2.1.2 Chitosan Film Preparation and Characterization

Based on previously published work by Baumgart et al.,[171] medium molecular weight chitosan was purchased from Sigma-Aldrich (Product number 448877, St.

Louis, MO) and used without further purification. A 1% w/w chitosan solution was prepared in a 1% v/v glacial acetic acid solution (Certified ACS, Fisher Scientific, Suwanee, GA) in 18.2 MΩ·cm water. The solution was stirred for 2 days with a magnetic stirrer to allow the chitosan to dissolve completely. The resulting solution was filtered through a 5 μm pore size syringe filter (Millipore, Billerica, MA) for storage. Prior to spin casting, 1-2 mL of the stock chitosan solution was centrifuged at 11400 rpm for 30 minutes. Approximately 60 μL of the centrifuge supernatant was dispensed onto the substrate, which was resident on the stationary spin chuck of a Specialty Coating Systems (Indianapolis, IN) spin coater with a programmable spin cycle. The programmed cycle consisted of three steps, each with a ramp time, a spin time and a set speed, and a separate, final ramp down time. To complete chitosan coverage on substrates, steps one and two were programmed to a ramp time and spin time each of 1 second at 100 rpm. Step three was optimized to a ramp time of 1 second and a spin time of 8 seconds at 5000 rpm. The final ramp down time was 5 seconds. The film-coated substrate was subsequently immersed in a borate buffer solution for 1.5 hours (Product number 1470953, Hach, Loveland, CO) to neutralize the chitosan film, and finally rinsed with 18.2 MΩ·cm water.

Spin cast chitosan films were characterized to assess spatial uniformity, thickness, and surface roughness. Fluorescence images of chitosan films doped with 1 mM fluorescein (Sigma-Aldrich, St. Louis, MO) were collected by a custom built sample scanning confocal microscope.[219] The images (Figure 2.2A and 2.2B) indicated that the fluorophore was uniformly distributed throughout the film, and further, that the films were relatively featureless. The thickness of the films, and the uniformity of their thickness as a function of spatial position, were determined by ellipsometry of films on functionalized gold coated silicon wafers. All ellipsometry (J.A. Woollam M-2000V spectroscopic ellipsometer, Lincoln, NE) measurements were performed at an incident angle of 75° and *in situ* measurements were facilitated by a 5 mL liquid

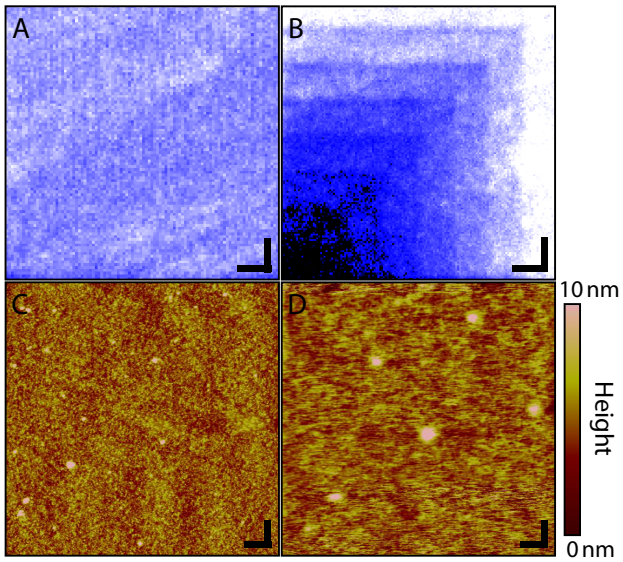

Figure 2.2. Images of chitosan films. **A** presents the uniformity of fluorescein within the spin cast chitosan, scale bar is 5 μm. **B** presents step-wise photobleaching of the chitosan film doped with 1 mM fluorescein, scale bar is 5 μm. **C** presents *ex situ* AFM micrograph of a spin cast chitosan film with rms roughness of 1.1 nm, scale bar is 1 μm. **D** presents *in situ* AFM micrograph of a spin cast chitosan film with rms roughness of 1.2 nm, scale bar is 1 μm.

cell. Thickness measurements from the center of a given film were routinely within 1 nm of the thickness measured at the periphery. *Ex situ* and *in situ* ellipsometry were employed to determine the extent of swelling of the chitosan films when equilibrated in both water and a buffer solution (10 mM HEPES, pH 7.4). Film thickness was demonstrated to increase by a factor of 2.3 with a standard deviation of 0.1, from the dry to the fully hydrated state, independent of the solution employed. Indeed, employing the spin coating parameters provided above, film thicknesses ranged from 55-60 nm in the dry state to 125-140 nm in the fully hydrated state. Atomic force microscopy (AFM) (Digital Instruments Nanoscope IIIa controller with a Multimode Atomic Force Microscope, Veeco Instruments, Plainview, NY) in tapping mode was utilized to determine the surface roughness of mica supported chitosan films both *ex situ* and *in-situ*. Root mean square roughness (rms) values of 1.1 nm and 1.2 nm respectively, were determined, as evident in Figure 2.2C and 2.2D. It is noted that

the rms roughness values of the chitosan films were significantly smaller than the thickness of the phospholipid bilayers to be deposited upon them (∼5 nm[220]). In accordance with the work Brisson,[221] and separately, Wirth,[197] it was therefore not anticipated that the chitosan hydrogel film would propagate defects or roughness to the bilayer.

2.1.3 Bilayer Preparation

During the course of the present work, a variety of phospholipids were employed to fabricate monolayers and bilayers. A generic methodology for the preparation of a bilayer on a flat substrate (e.g. gold coated silicon wafers, cover glass) is provided below. Details specific to individual phospholipids will be presented in their respective sections. All phospholipids were purchased from Avanti Polar Lipids (Alabaster, AL) and used without further purification. All phospholipids were stored at -20°C. Stock solutions (∼4-10 mg/mL) were prepared with HPLC grade chloroform (Fisher Scientific, Suwanee, GA) which were diluted to a concentration of 1 mg/mL on the day of use. For fluorescence measurements, a fluorescent lipid analog, 1,1'-dioctadecyl-3,3,3',3'-tetramethylindocarbocyanine perchlorate, (DiI C_{18}) or a fluorescently tagged lipid, 1,2-dimyristoyl-*sn*-glycero-3-phosphoethanolamine-N-(lissamine rhodamine B sulfonyl) (ammonium salt) (RhoPE) were employed at various concentrations. DiI C_{18} stock solutions (∼10 mg/mL) in chloroform were prepared (stored at 4°C) and RhoPE stock solutions were received from Avanti Polar Lipids at concentrations of 1 mg/mL in chloroform (stored at -20°C). All subsequent fluorophore dilutions, as well as creation of specific phospholipid:fluorophore solutions were performed on the day of use. In some cases (indicated where appropriate), stock solutions and subsequent dilutions were sonicated for 15 minutes prior to use. Due to the requirement of asymmetric bilayers for SF activity, the deposition method selected for bilayer fabrication was the LB/LS technique described

in Section 1.5.4. Utilizing a dual compartment Langmuir-Blodgett trough (Model 1232D1D2, Nima, Coventry, England) containing two Wilhelmy balance sensors, a mechanical dipper, a custom user interface and a custom fixed center barrier, two chitosan-coated substrates were submerged back-to-back in a subphase of either 18.2 MΩ·cm water or various buffers maintained at 15°C (unless otherwise noted). The phospholipid solution and the phospholipid:fluorophore solution were spread in a drop-wise manner on the subphase on the appropriate side of the trough. The chloroform was allowed to evaporate for a period of 30 minutes prior to the monolayers being compressed to a specified surface pressure (e.g. 35 mN/m). The monolayers were subsequently decompressed, and finally recompressed to the final pressure and held for 30 minutes. The LB deposition was performed at a dipper speed of 4 mm/min in one of the two trough compartments. Using a custom vacuum sample holder, the LS deposition was performed on one substrate utilizing the second trough compartment. The resultant bilayer was maintained in the subphase solution while it was mounted in the appropriate sample holder.

Successful LB depositions on chitosan films were performed with zwitterionic PC, and separately, with anionic PG. The degree of success of a given deposition was quantified by the transfer ratio, that is the area of the lipid monolayer that was removed from the subphase, divided by the area of the substrate immersed in the subphase.[222] Transfer ratios for each of the phospholipid depositions were routinely unity (within error) as reported by the trough software.

2.2 Sum Frequency Generation Vibrational Spectroscopy

2.2.1 Theory

As detailed in Section 1.3, sum frequency generation vibrational spectroscopy (SFS) is a surface-specific technique that records vibrational spectra of molecules at

an interface. It is derived from the non-linear optical phenomenon of sum frequency generation (SFG). SFG, as applied to SFS, is typically generated by two pulsed, high energy lasers that are temporally and spatially overlapped at the surface of interest. The pump beam has a fixed visible (Vis) frequency, while the probe beam has a tunable infrared (IR) frequency. When the two beams interact at the surface, with the appropriate phase matching condition and symmetry considerations, light is coherently emitted from the surface at the sum of the two incident frequencies (see Figure 1.5).

The origin of SFG may be demonstrated employing the total surface electric field of the two incident beams;

$$E = E_{Vis}\cos(\omega_{Vis}t) + E_{IR}\cos(\omega_{IR}t) \tag{2.1}$$

where E_{Vis} and E_{IR} are the incident electric fields and ω is the angular frequency of the respective electric fields. The second order non-linear polarization induced at the surface ($P_{SF}^{(2)}$) may be written as

$$P_{SF}^{(2)} = \chi^{(2)}E_{Vis}E_{IR} \tag{2.2}$$

where $\chi^{(2)}$ is the second order non-linear susceptibility of the surface. Substitution of the total surface electric field defined in Equation 2.1 into Equation 2.2 yields

$$P_{SF}^{(2)} = \chi^{(2)}(E_{Vis}\cos(\omega_{Vis}t) + E_{IR}\cos(\omega_{IR}t))^2 \tag{2.3}$$

Expansion of Equation 2.3 yields a DC term (no frequency dependence), second harmonic generation terms for each frequency ($2\omega_{Vis}$ and $2\omega_{IR}$), a difference frequency generation term ($\omega_{Vis} - \omega_{IR}$), and a sum frequency generation term ($\omega_{Vis} + \omega_{IR}$).[223,224] Focusing solely on the sum frequency term, the resultant SF signal may be expressed as:

$$\omega_{SF} = \omega_{Vis} + \omega_{IR} \tag{2.4}$$

It is evident from Equations 2.2 and 2.3 that $P_{SF}^{(2)}$ is proportional to $\chi^{(2)}$. As such, in order to assess the molecular structure and orientation at an interface, the components of $\chi^{(2)}$ must be determined. Providing that the substrate employed is SF active (e.g. metallic), $\chi^{(2)}$ consists of both a resonant (arising from interfacial molecules) and a non-resonant component (arising from the substrate), that is,

$$\chi^{(2)} = \chi_R^{(2)} + \chi_{NR}^{(2)} \tag{2.5}$$

The resonant component is a third rank tensor, and may be represented as

$$\chi_{R,ijk}^{(2)} \propto \frac{M_{ij} A_k}{\omega_{IR} - \omega_\nu + i\Gamma} \tag{2.6}$$

where ω_ν and ω_{IR} are the frequencies of the relevant vibrational resonance of the interfacial molecule, and the infrared beam, respectively. Γ is the linewidth of the vibrationally excited state, and M_{ij} and A_k are the Raman and IR transition moments, respectively. It is evident from Equation 2.6 that in order for SFG to arise from a given vibrational mode, both the Raman and IR transitions must be non-zero.[224] An SFG response is observed when the IR frequency is equivalent to the surface molecule's vibrational mode.[223,224] The non-resonant component of Equation 2.5, $\chi_{NR}^{(2)}$, is determined experimentally since its magnitude is not typically dependent on the infrared frequency over the narrow range probed in a given measurement, but rather on material properties.[30] $\chi_{NR}^{(2)}$, being a third rank tensor, is better represented as $\chi_{NR,ijk}^{(2)}$ where ijk symbolizes all possible combinations of the Cartesian axis system (x, y, z). The nature of the substrate determines the relative contribution of $\chi_{NR,ijk}^{(2)}$ to an SF spectrum. For example, for a dielectric substrate, such as calcium fluoride, the non-resonant contribution is essentially zero, whereas for a metallic substrate, such as gold, a large non-resonant component is typically present in an SF spectrum as a result of surface plasmon resonance.[223] In order to

assess the phase of $\chi^{(2)}$, Equation 2.5 may be written in polar coordinates,

$$\chi^{(2)}_{ijk} = |\chi^{(2)}_{R,ijk}|e^{i\delta} + |\chi^{(2)}_{NR,ijk}|e^{i\varepsilon} \tag{2.7}$$

where $|\chi^{(2)}_{R,ijk}|$ is the absolute magnitude of the resonant contribution, δ is the phase of the resonant contribution, $|\chi^{(2)}_{NR,ijk}|$ is the fixed, absolute magnitude of the non-resonant contribution, and ε is the fixed, non-resonant phase of the substrate.[223] The magnitude ($|\chi^{(2)}_{R,ijk}|$) and phase (δ) of the resonant contribution are dependent upon the infrared frequency (ω_{IR}) as observed in Equation 2.6.[223] Equation 2.7 may be written as

$$\chi^{(2)}_{ijk} = \Sigma|\chi^{(2)}_{R,ijk}|e^{i\delta} + |\chi^{(2)}_{NR,ijk}|e^{i\varepsilon} \tag{2.8}$$

when more than one resonant contribution is present in the SF spectrum.[224]

With the components of $\chi^{(2)}_{ijk}$ described and the dependence of $P^{(2)}_{SF}$ on $\chi^{(2)}_{ijk}$ established (Equation 2.2), the relationship of these parameters to the intensity of the SF beam generated will be addressed. To connect $P^{(2)}_{SF}$ at the surface with the intensity of the SF light emitted (I_{SF}), it is necessary to employ the appropriate Fresnel factors, or L factors. The six L factors are non-linear SF optical coefficients that account for phase matching and have been reported extensively in the literature.[225] The intensity of the SF signal may be described generically as

$$I_{SF} \propto |LP^{(2)}_{SF}|^2 \tag{2.9}$$

The dependency of I_{SF} upon the plane of incidence, the SF emission angle, and polarization of the SF light is accounted for by employing the appropriate L factor.[30,225] Assuming a single resonant contribution, and employing the dependence of $P^{(2)}_{SF}$ on $\chi^{(2)}_{ijk}$, the intensity of the SF signal may be written via substitution of Equation 2.7 into Equation 2.9 as

$$I_{SF} \propto ||\chi^{(2)}_{R,ijk}|e^{i\delta} + |\chi^{(2)}_{NR,ijk}|e^{i\varepsilon}|^2 \tag{2.10}$$

and hence,

$$I_{SF} \propto |\chi^{(2)}_{R,ijk}|^2 + |\chi^{(2)}_{NR,ijk}|^2 + 2|\chi^{(2)}_{R,ijk}||\chi^{(2)}_{NR,ijk}| \cos[\varepsilon - \delta] \tag{2.11}$$

It is noted that the squares of the resonant and non-resonant components of the susceptibility are always positive terms. The cross product of the resonant and non-resonant terms in Equation 2.11 gives rise to amplification and a phase change of the resonant term of the SF signal.[30] Additionally, Equation 2.11 may serve as a starting point for modeling the SF spectra.

As stated above, $\chi^{(2)}_{ijk}$ is a third rank tensor and as such, has 27 contributing elements. The elements are defined by all possible combinations of the Cartesian axis system (x, y, z), and therefore may be written as $\chi^{(2)}_{xyz}$. In order to be SF active, a given combination must satisfy the following two criteria:

$$\chi^{(2)}_{xyz} = \chi^{(2)}_{-x-y-z} \tag{2.12}$$

$$\chi^{(2)}_{xyz} = -\chi^{(2)}_{-x-y-z} \tag{2.13}$$

The sign change in Equations 2.12 and 2.13 denotes a reverse in the axis system for a planar surface where x and y are parallel to the plane and z is perpendicular. It is evident that $\chi^{(2)}_{xyz}$ must equal zero in order to satisfy both equations, the implication of this observation is that no SF emission arises from a centrosymmetric medium. For example, given a surface where the x and y directions are in the plane of the surface and may freely rotate around a perpendicular z axis, it may be deduced that x is equivalent to $-x$ and y is equivalent to $-y$, whereas z does not equal $-z$. When the tensor rule (Equation 2.13) is applied to the 27 elements of $\chi^{(2)}_{xyz}$, given the surface described above, only four unique non-zero elements remain,

$$\chi^{(2)}_{zxx} \equiv \chi^{(2)}_{zyy} \qquad \chi^{(2)}_{xzx} \equiv \chi^{(2)}_{yzy} \qquad \chi^{(2)}_{xxz} \equiv \chi^{(2)}_{yyz} \qquad \chi^{(2)}_{zzz}$$

each of which may be SF active.[223] The differing $\chi^{(2)}$ elements may be probed by changing the polarization of the incident electric fields (p vs. s polarization), where

a p polarized electric field is parallel to, and an s polarized electric field is perpendicular to the plane of incidence. Clearly, the polarization of the incident electric fields determines the polarization of the resultant SF signal. Since a p polarized beam comprises both x and z components, and an s polarized beam comprises solely a y component, the four tensor elements above may be written with respect to polarization. Thus,

$$pss \qquad sps \qquad ssp \qquad ppp$$

are the four polarization combinations from which an SF signal may be collected, listed by decreasing frequency (SF, visible, and infrared). The SF signal derived from *pss*, *sps*, and *ssp* polarizations each have one contributing $\chi^{(2)}_{xyz}$ tensor element, whereas the *ppp* polarization has four contributing $\chi^{(2)}_{xyz}$ elements, and is therefore, a more complicated spectrum to resolve. By probing a surface with various excitation and emission beam polarization combinations, the parallel and perpendicular transition moments of a given vibrational mode are selectively enhanced, allowing for deduction of molecular orientation and tilt angle information.[30] Specifically, the *ssp* beam polarization combination probes components within the transition moments of vibrational modes that are parallel to the plane of incidence, where the *sps* and *pss* beam polarization combinations probe components that are perpendicular to the plane of incidence.[226] The *pss* and *sps* beam polarization combinations probe the same vibrational modes, differing only by a constant within the Fresnel factors.[66,226] The *pss* beam polarization combination is not often employed due to a lower SF signal level than typically achieved for the *sps* beam polarization combination.[226]

In summary, sum frequency spectroscopy (SFS) is governed by selection rules that are more complex than for linear vibrational spectroscopies, such as infrared or Raman spectroscopy. Vibrational resonances of molecules of interest are SF active only if the vibrational mode is both infrared and Raman active (Equation 2.6), and

if there is a lack of inversion symmetry in the sample (Equation 2.13). Application of SFS may reveal orientational and conformational information of interfacial species.

2.2.2 Instrumentation

The Neivandt SF spectrometer is a custom built broadband spectrometer consisting of a tunable (nominally 800 nm), pulsed, 800 mW seed beam produced by a Ti:Sapphire oscillator (Mai Tai, Spectra Physics, Mountain View, CA) and a fixed, 527 nm, pulsed, 30 W pump beam produced by a frequency doubled Nd:YLF laser (Empower 30, Spectra Physics, Mountain View, CA). Both beams enter a regenerative amplifier (Spitfire, Spectra-Physics, Mountain View, CA) that produces a pulsed (pulse width of approximately 150 fs), $\sim$2.5 W beam at 1 kHz repetition rate. The output of the amplifier is split such that 30% is sent to a spectral shaper (Symphotic TII Corporation, Camarillo, CA) that narrows the linewidth of the visible (800 nm) beam (Vis) from approximately 15 nm to 1 nm or less and increases the pulse width to 1.6 - 3 ps. The remaining 70% is directed to a tunable optical parametric amplifier (OPA) (Topas-C, Light Conversion, Vilnius, Lithuania) where it is converted to a tunable infrared beam (IR) (in the range of 2.4 to 11 μm). The IR and Vis beams are temporally and spatially overlapped at a sample stage consisting of a metal base, x, y, and z translation stages, and a goniometer (Melles Griot, Albuquerque, NM). The emitted SF signal is focused into a spectrograph (2300i, Princeton Instruments, Trenton, NJ) and imaged on a CCD camera (PI-Max, Princeton Instruments, Trenton, NJ). Figure 2.3 is a basic schematic of the Neivandt spectrometer.

It is necessary here to expand upon the base SF equation (Equation 2.4) presented in Section 2.2.1 to enable prediction of the angle of emission of the SF beam by accounting for conservation of momentum of the Vis and IR beams. Specifically, the angle of emission of the SF beam depends on the angle of incidence of the incom-

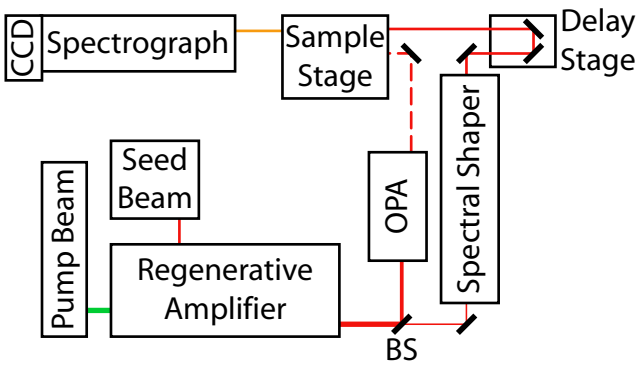

Figure 2.3. Schematic of the Neivandt spectrometer. BS indicates the 70/30 beamsplitter.

ing beams as well as the refractive index of the medium through which the beams propagate.

$$\mathrm{n}_{SF}\omega_{SF}\sin\theta_{SF} = \mathrm{n}_{Vis}\omega_{Vis}\sin\theta_{Vis} \pm \mathrm{n}_{IR}\omega_{IR}\sin\theta_{IR} \tag{2.14}$$

The sign indicates whether the beams are co-propagating (positive, i.e. both beams incident from the same side as shown in Figure 1.5) or counter-propagating (negative, i.e. beams incident from different sides). The Neivandt sample stage is set in a co-propagating geometry as shown in Figure 2.4 with the incident angles measured from the sample surface normal. Halfwave plates are employed to control the polarization of the incoming beams (s or p) while polarizers ensure the quality of each beam polarization. A shortpass filter (750 nm) is employed to remove excess 800 nm light from the resultant SF signal prior to detection.

SF measurements of bilayers were performed in a total internal reflection (TIR) geometry,[227,228] where the incident lasers were set just beyond the critical angle of the TIR crystal/ solution interface as determined by Snell's law:

$$n_1 \sin\theta_1 = n_2 \sin\theta_2 \tag{2.15}$$

where n_1 and n_2 are the refractive indices of the two media, and θ_1 and θ_2 are the angles of the incident and reflected laser beam from the normal. The critical angle

(θ_C) is determined when θ_2 is set to 90° such that

$$\theta_C = \arcsin \frac{n_2}{n_1} \tag{2.16}$$

Since the refractive index of a given medium depends on the wavelength of light propagating through it, Equation 2.16 was applied separately to the Vis and IR beams to determine the respective critical angles based on each beam passing from a CaF_2 TIR prism to solution. SF measurements were taken with the incident angles set beyond their respective critical angles; specific angles are given in Chapter 5. By employing the hemicylinder prism discussed in Section 2.1.1, the incident beams pass through the CaF_2 prism without refraction and impinge on the planar surface at the angles set. In the TIR geometry, an evanescent wave (a bound electric field) is generated at the surface that extends into the less dense medium (water). The intensity of the evanescent wave in the CaF_2/water system employed in the present work may be represented by

$$I(z) = I_0 e^{-z/d_p} \tag{2.17}$$

where $I(z)$ is the intensity of the evanescent wave with respect to its distance from the surface, z. The penetration depth, d_p, at the incident wavelength (λ), is defined as

$$d_p = \frac{\lambda}{2\pi}[n_1^2 \sin^2\theta - n_2^2]^{-\frac{1}{2}} \tag{2.18}$$

As such, d_p is the depth at which I has decayed to $1/e$ of the initial value, I_0.[229] Use of the TIR geometry for SFS yields an enhancement of the 800 nm and infrared interfacial electric fields, when compared to the electric fields produced in the externally reflected geometry.[230] The intensity of the SF signal may consequently be increased several orders of magnitude, provided certain beam polarizations and appropriate incident angles are employed.[228,230,231] An additional advantage to the TIR geometry is that the intensity of the incident beams (in particular the IR beam) are not attenuated by the bulk solution.

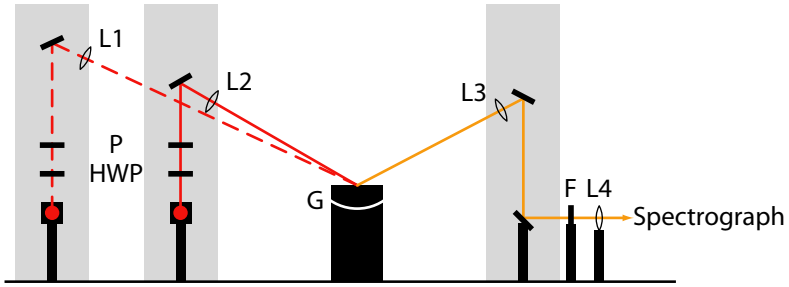

Figure 2.4. Schematic of the Neivandt spectrometer sample stage. HWP is the halfwave plate and P is the polarizer for each of the incident beams. L1, L2, and L4 are focusing lenses for the Vis, IR, and SF beams, respectively, and L3 is a columnating lens for the SF beam. F is a 750 shortpass filter, and G is a goniometer mounted on separate x, y and z translation stages.

2.2.3 Spectral Analysis

The SF signal imaged on the CCD camera is stored on a laboratory computer. Analysis of a single raw SF spectrum from a sample of interest involves acquisition and processing of multiple SF spectra. The SF spectrum is generally normalized by the energy profile of the IR beam. The energy profile may be obtained by collecting a SF spectrum of a gold-coated prism, a flat gold-coated substrate, or a nonlinear crystal in the same wavelength region as the sample of interest spectrum. Additionally, recalling from Section 1.3 that SFG up-shifts the emitted SF signal to visible wavelengths, it is necessary to affirm the position of the vibrational resonances with respect to the infrared frequency. By inserting a standard Fourier Transform infrared spectroscopy (FTIR) polystyrene film in the IR beam path and collecting a SF spectrum with the same substrate and alignment employed for the IR beam energy profile, the absorption of polystyrene may be utilized to calibrate the SF signal (a $\pm$ cm^{-1}/ nm shift). An infrared spectrum of the Neivandt polystyrene film is given in Appendix A for reference. The peak at 2923.32 cm^{-1} was employed for calibration by members of the Ye lab at Hokkaido University (verbal communication) while Ma et al.[60] employed the peak ca. 2849.64 cm^{-1}. To account for extraneous signal collected by the CCD camera, such as scattered laser light, collection of a

background spectrum is necessary. The background spectrum may be collected by blocking the IR beam or adjusting the delay stage while measuring the sample of interest, thereby removing the spatial and/or temporal overlap required for SFG.

Subsequently, the raw SF spectrum may be processed in the following order: subtraction of the background spectrum to create a difference spectrum, correction of the wavelength of both the IR beam energy profile and the difference SF spectrum based upon the polystyrene spectrum, and division of the calibrated difference spectrum by the calibrated IR beam energy profile spectrum (normalization). The normalized SF spectrum of the sample of interest, which is reported in units of wavelength (nominally nm), is subsequently converted to wavenumber (cm^{-1}). The conversion is best accomplished by employing the base sum frequency equation, $\omega_{Vis} + \omega_{IR} = \omega_{SF}$, as presented in Figure 1.5. Analysis of the resultant spectra was performed utilizing a custom LabView program employing a Levenberg-Marquardt fit routine. The program was originally written by Dr. Alex Lambert[223] and updated by Dr. Edward Allgeyer.[232]

2.3 Z-Scan Fluorescence Correlation Spectroscopy

2.3.1 Theory

As described in Section 1.4, fluorescence correlation spectroscopy (FCS) is a single molecule technique yielding molecular diffusion coefficients, chemical conversion rates, and photophysical information.[126–128] FCS inherently requires a low concentration of probe molecules in the sample of interest. In the confocal geometry, passage of fluorophores through the observation volume (most often created by a tightly focused laser beam) results in their excitation and subsequent relaxation. The fluorescence emission is collected, often by a single photon sensitive avalanche photodiode (APD) or photomultiplier tube (PMT) detector. The result is fluo-

rescence emission, $F(t)$, that fluctuates as a function of time ($\delta F(t)$) around the average fluorescence emission, $\langle F(t)\rangle$.[128]

$$\delta F(t) = F(t) - \langle F(t)\rangle \tag{2.19}$$

where the brackets denote an average over time. An autocorrelation function may be computed from the recorded fluctuating fluorescence signal as:

$$G(\tau) = \frac{\langle \delta F(t) \cdot \delta F(t+\tau)\rangle}{\langle F(t)\rangle^2} + G_\infty \tag{2.20}$$

where τ is the lag time, G_∞ is an asymptotic offset, and $G(\tau)$ is the autocorrelation function normalized by the average fluorescence signal squared.[133] The autocorrelation curve obtained from a given experimental dataset may be fit to an appropriate diffusion model.[133] For example, the diffusion model for a single, freely diffusing species in solution is given as

$$G(\tau)_{3D} = \frac{1}{N}\left(1 + \frac{\tau}{\tau_D}\right)^{-1}\left(1 + \frac{\tau}{\omega^2\tau_D}\right)^{-0.5} \tag{2.21}$$

where N is the effective concentration, ω, the structure factor, is the ratio of the axial to lateral dimension ($\omega = z_0/r_0$) of the confocal observation volume, τ_D is the characteristic diffusion time, and τ is time.[127,128] To determine the diffusion coefficient, D, of a given species, the observation volume requires calibration, often employing a fluorophore with a known diffusion coefficient.[233] In the present work, FCS measurements of 3 nM Alexa-Fluor 546 (Invitrogen, Carlsbad, CA) in 18.2 MΩ·cm water were taken and fit with Equation 2.21 to optimize the microscope setup and assess its performance. A basic scheme for the collection and analysis of an Alexa-Fluor 546 FCS measurement is presented in Figure 2.5. The characteristic diffusion time, τ_D, of the fluorophore may be determined experimentally, and subsequently, the lateral dimension, r_0, of the observation volume may be calculated via

$$\tau_D = \frac{r_0^2}{4D} \tag{2.22}$$

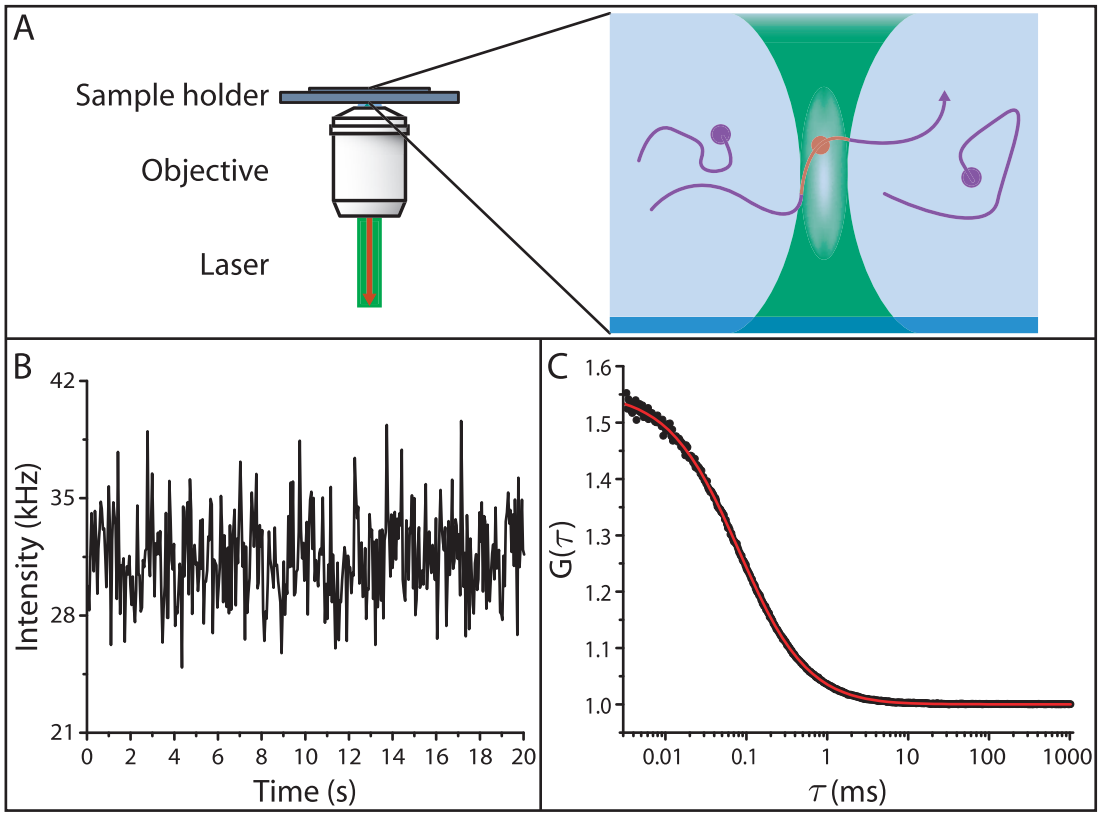

Figure 2.5. Schematic of a FCS measurement. **A** Fluorophores freely diffusing through the observation volume in a sample holder are excited by the incident laser beam. **B** As the fluorophores relax, they emit photons that are collected over time and recorded as a time course. **C** Application of Equation 2.20 to the time course yields a correlation curve (black line). This curve is then fit to the appropriate diffusion model (e.g. Equation 2.21) as shown by the red line.

The value of r_0 may be employed in later experiments to determine the relative diffusion coefficient of unknown species.[127,128] For FCS measurements of planar model membranes, such as those employed in the present work, it is appropriate to utilize a two dimensional (2D) diffusion model;

$$G(\tau)_{2D} = \frac{1}{N}\left(1 + \frac{\tau}{\tau_D}\right)^{-1} \tag{2.23}$$

Indeed, Equation 2.23 was utilized for fitting all membrane autocorrelation curves collected in the work presented in Chapter 4.

While the traditional FCS method described above has been widely employed, it is dependent upon calibration and is therefore susceptible to error.[234] As such,

an alternative, calibration-free method to collect diffusion coefficients for bilayers, z-scan FCS, was employed in the present work.[235] Z-scan FCS measurements are accomplished by collecting correlation curves at each of a series of axial positions, fitting each correlation curve to the appropriate diffusion model (Equation 2.23 for the present work), and plotting the diffusion time, τ_D, and the effective concentration, N, separately, as functions of the relative axial position.[145,235] The resulting parabolic dependence of τ_D and N on the axial position may be fit with

$$\tau_D = \frac{w_0^2}{4D}\left(1 + \frac{\lambda_0^2 \Delta z^2}{\pi^2 n^2 w_0^4}\right) \tag{2.24}$$

and

$$N = \pi c w_0^2 \left(1 + \frac{\lambda_0^2 \Delta z^2}{\pi^2 n^2 w_0^4}\right) \tag{2.25}$$

where w_0 is the radius of the beam in the focal plane, c is the average concentration of the fluorophores in the focal plane, λ_0 is the excitation laser wavelength, Δz is the distance axially of the sample from the focal plane, and n is the refractive index of the medium.[145,235] A scheme for conducting z-scan FCS measurements is presented in Figure 2.6. The method shown in Figure 2.6 was utilized for all work reported in Chapter 4.

2.3.2 Instrumentation and Data Analysis

The instrument employed for the z-scan FCS measurements outlined above has been described extensively by Allgeyer et al.[235] and in the Ph.D. thesis of Dr. Edward S. Allgeyer[232], therefore, only a brief summary will be given here.

Using an inverted microscope base (IX71, Olympus, USA), a custom stage, allowing for stable axial changes of the order of 0.5 μm, and an objective holder were constructed to replace the translation stage and objective turret supplied by the factory. The new stage consists of an aluminum plate with a hole to accommodate a brass mounting plate through which a threaded stainless steel rod passes, serving as

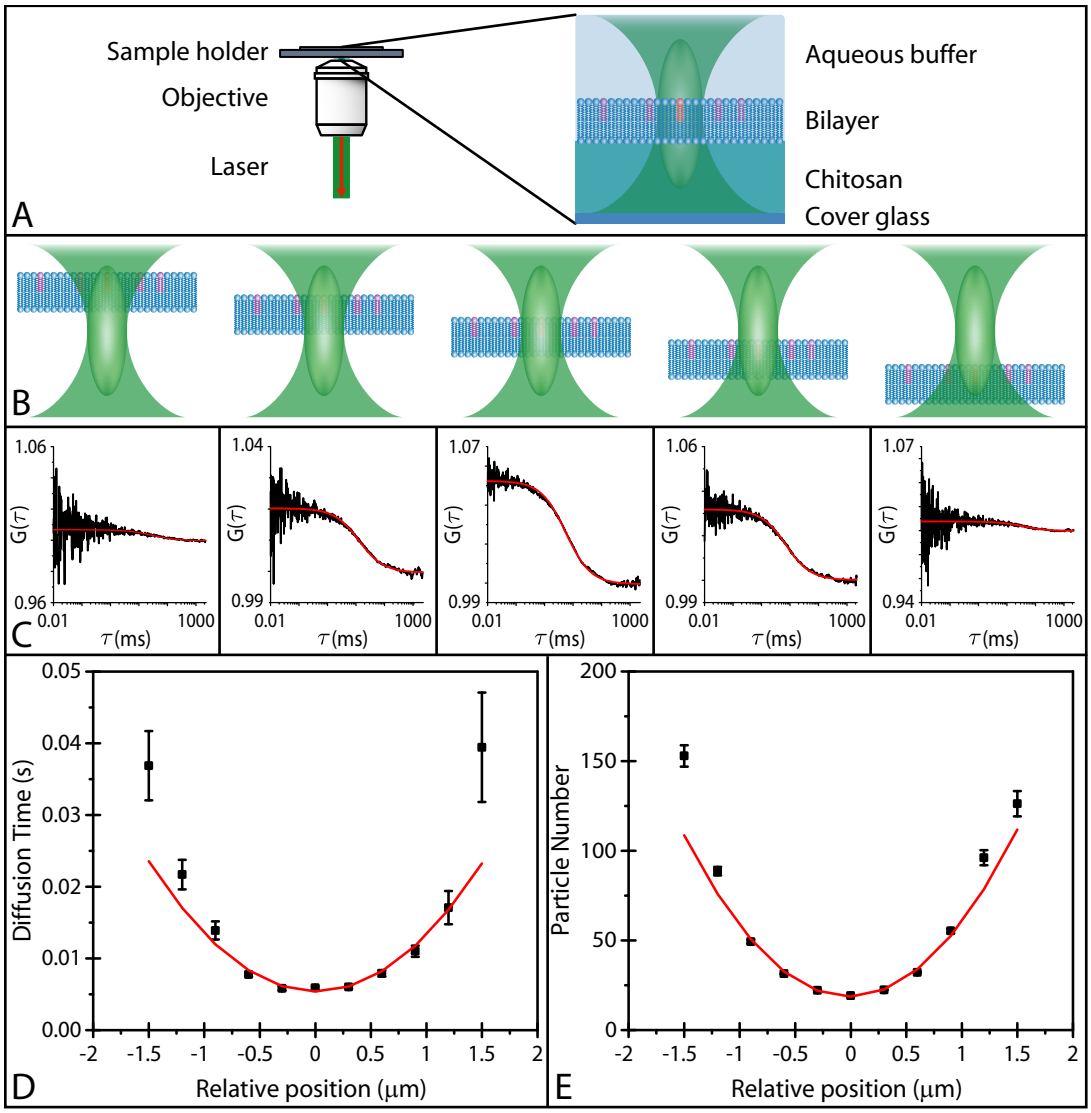

Figure 2.6. Schematic of z-scan FCS measurements and analysis. The schematic depicts from measurement to final analysis yielding the diffusion coefficient and particle number. **A** Fluorescent lipid analogs or fluorescently tagged lipids are included in the model membrane during fabrication. **B** The sample z_0 position is moved through the observation volume of the laser. **C** Time courses are collected and autocorrelated at each z_0 position as shown by the black line. Each correlation curve is fit with the 2D diffusion model (Equation 2.23) as shown by the red line. The diffusion time, τ_D, and the effective concentration, N, are each determined from the fit equation. **D** Z-scan FCS plot of τ_D with respect to the relative z_0 position as shown by the black data points. The red line is the fit of Equation 2.24 yielding the calibration-free diffusion coefficient. **E** Z-scan FCS plot of N with respect to the relative z_0 position as shown by the black data points. The red line is the fit of Equation 2.25 yielding the calibration-free particle number.

the objective holder. To allow for sample movement, a course XY translation stage with a large aperture (406, Newport Corporation, Irvine, CA) and a XYZ piezo scan stage (Nano-T115, Mad City Labs, Madison, WI) were mounted on top of the aluminum plate. An acrylic sample cell holder was mounted to insulate the piezo scan stage from the liquid sample cell and the temperature-control stage. Figure 2.7A shows the successive layers of the microscope stage.[235] Additionally, a custom liquid sample cell was designed and fabricated to maintain the model membranes in an aqueous environment. As shown in Figure 2.7B, two cover glass were sandwiched over a PTFE coated o-ring which is slightly compressed ($\sim$5%) between the two stainless steel portions of the holder. Additionally, a brass rod with a thermistor (MP-2444, TE Technology, Traverse City, MI) mounted internally was friction-fit in a hole in the side of the lower portion of the sample cell to monitor the temperature. Finally, to control the temperature of the sample cell, a TE heater/cooler (TE-127-1.0-0.8, TE Technology, Traverse City, MI) was mounted to an aluminum plate that was friction-fit to the upper portion of the sample cell. An aluminum reservoir was fabricated and attached to the other side of the TE heater/cooler to act as a heat sink (Figure 2.7C). A proportional-integral-derivative (PID) control system (TC-36-25-RS232, TE Technology, Traverse City, MI) was initially employed to maintain the temperature of the sample cell, however, it was determined that the power cycling required to maintain a steady temperature distorted the measured correlation curves. Thus, constant power was applied to the sample, and measurements were taken once a steady state temperature was attained.[235]

With the custom microscope stage mounted on the inverted geometry microscope base, fluorescence excitation was achieved employing a 543 nm Helium-Neon (HeNe) laser. The HeNe beam was adjusted such that it filled approximately 60% of the back aperture of the microscope objective (60X, 1.2 NA UPlanApo/IR water immersion, Olympus, USA). Emission was collected with a 50 μm diameter sil-

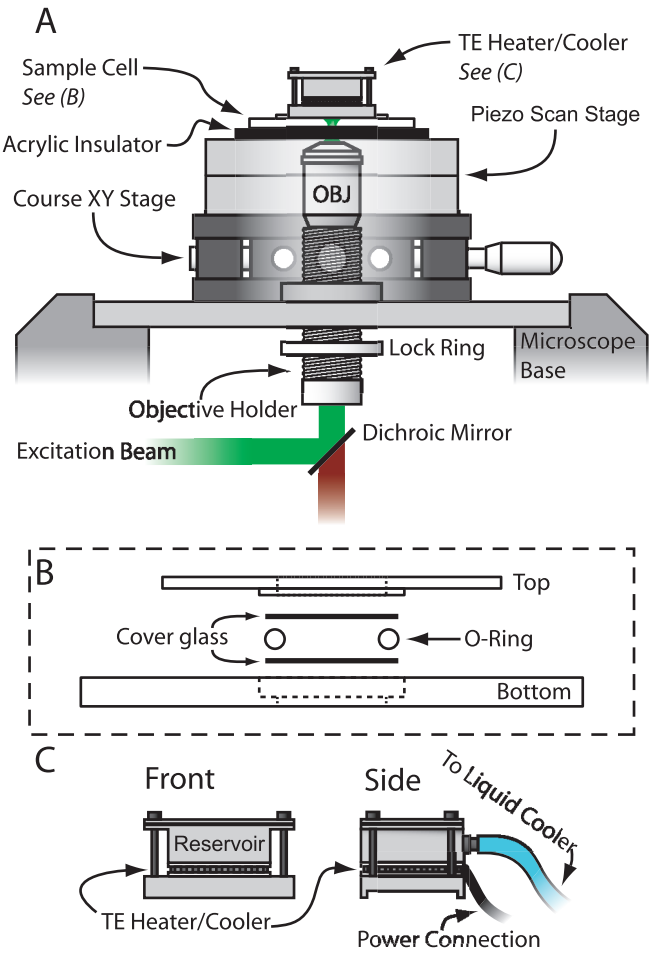

Figure 2.7. Custom FCS microscope schematic.[235] **A** The custom stage with the course translation stage and the piezo scan stage through which the custom objective holder is mounted. **B** The liquid sample cell sandwiches an o-ring between two cover glass; the model membrane system is present on the lower cover glass. **C** To control the temperature of the sample cell, a TE heater/cooler with a circulating liquid reservoir as a heat sink and an aluminum block friction fit to the sample cell is placed on top of the sample cell.

ica core fiber optic cable (visible-IR 1 m length step index multimode cable with 0.22 NA, Thorlabs, Newton, NJ) supported in an XY translation mount which is mounted on a second translation stage in the Z (axial) direction. The fiber was connected to an avalanche photodiode (APD) (SPCM-AQRH-13-FC, Perkin Elmer, Waltham, MA) which was connected to a correlator (Correlator.com, USA). As the count rate was received from the APD, the correlator autocorrelated the signal to

produce an autocorrelation curve (see Figure 2.5). Additionally, the objective correction collar was adjusted for the cover glass thickness and to minimize spherical aberrations (nominally $\sim$176 μm). With the sample cell containing the bilayer in place and the temperature control stage set, the sample was initially positioned to produce the maximum count rate utilizing less than $\sim$1.5 μW at the sample. Measurements were taken from 16°C to 44°C. At each temperature, 13 different axial positions (centered around the predetermined maximum count rate) were employed, with ten 3 second correlation curves generated at each position. A custom MatLab (MathWorks, Natick, MA) program[232] was employed to control the hardware and acquire the data. Correlation curves whose corresponding time courses showed events greater than three standard deviations above the mean were removed and the remaining curves were averaged.[236] Data were analyzed in two separate programs, Mathematica 7.0.1 (Wolfram Research, Champaign, IL) and Origin 7.0 (OriginLab Corporation, Northampton, MA), by two separate people and while the results were found to be the same, the analysis time required by each program was quite different. Results in the present work derive from Mathematica, which was chosen as the primary analysis tool since the required analysis time was far less than when employing Origin. For each program, a weighted non-linear Levenberg-Marquardt fit routine was applied to the mean correlation curve and the standard deviation served as the fitting weight. The mean correlation curve at each position was fit to Equation 2.23, and the resultant data plotted with respect to position to determine the z-scan FCS curve (see Figure 2.6). Finally, the z-scan FCS plots of diffusion time and particle number, each with respect to the relative position, were fit to Equations 2.24 and 2.25, respectively. For detailed notes regarding instrument setup and optimization, it is highly recommended that Dr. Edward Allgeyer's Ph.D. thesis be consulted.[232]

Chapter 3
FGF-1 TRANSLOCATION STUDIED VIA VESICLE AND CUSHIONED MODEL MEMBRANES

During the development of the FCS and SFS instrumentation, exploration of FGF-1 translocation across two varieties of model lipid membranes was performed. The ability of FGF-1 to destabilize artificial lipid membranes was shown by Graziani et al.[27], as described in Section 1.5.1. Building upon this work, a novel assay utilizing vesicles formed from reconstituted plasma membranes of cells[161] was employed to investigate FGF-1 translocation. Separately, cushioned model membranes were fabricated, as detailed in Section 2.1, and a similar assay was developed to perform preliminary FGF-1 translocation studies.

3.1 Vesicle Study of FGF-1 Translocation

3.1.1 Vesicle Preparation

The procedure of Schäfer et al. employed for isolating the membranes of cells, was modified for the present work.[161] Specifically, NIH 3T3 cells were grown to 100% confluency in 8-10 tissue culture dishes (15 cm diameter). After removing the media and washing with PBS (phosphate buffered saline), the cells were scraped off each dish surface in the presence of 5 mL of ice cold PBS. The suspended cells were spun down at 1500 rpm for 2 minutes, the supernatant was removed, and the cells were resuspended in 5-10 mL of ice cold PBS. The cells were washed two more times employing the same methodology, with final resuspension in hypotonic buffer (0.5 mM $NaPO_4$ buffer, pH 7.0, 0.1 mM EDTA (ethylenediaminetetraacetic acid)) with an appropriate amount of protease inhibitor cocktail (100 μL cocktail solution, Sigma-Aldrich, St. Louis, MO, per 10 mL cell lysate). The volume of the resus-

pension was dependent upon the volume of the pellet of the cells resulting from centrifugation, with a typical dilution being 8-12 fold. It is noted that a 40 fold dilution is recommended by Schäfer et al..[161] The final resuspension was incubated for 2 hours at 4°C, allowing the cells to fully lyse, thereby releasing the membranes. Following incubation, the lysed cell suspension was ultracentrifuged at 26000 rpm for 40 minutes at 4°C. The supernatant was removed and discarded, and the pellet was resuspended in 5-15 mL of hypotonic buffer with no protease inhibitor cocktail and homogenized with a glass/Teflon homogenizer. The homogenized solution was diluted with incubation buffer (10 mM Tris-HCl, 250 mM sucrose, pH 7.4) at a 1:1 by volume ratio, and then centrifuged at 12000 rpm for 10 minutes at 4°C. Post centrifugation, the membrane components were suspended in the supernatant, which was collected and stored at 4°C. The pellet was resuspended in 5-15 mL of hypotonic buffer with no protease inhibitor cocktail, homogenized with the glass/Teflon homogenizer, diluted with incubation buffer in a 1:1 by volume ratio, and finally centrifuged at 12000 rpm for 10 minutes at 4°C. The supernatant was collected and combined with the supernatant from the first centrifugation. It is noted that, schedule depending, the procedure may be halted overnight at this juncture.

The combined supernatants were subsequently either ultracentrifuged at 26000 rpm for 40 minutes at 4°C, or centrifuged at 24000 rpm for 1 hour at 4°C. While the supernatants were undergoing centrifugation, a 38% (w/v) sucrose solution (5 mM HEPES-KOH, pH 7.4) was prepared and evenly distributed in ultracentrifuge tubes (5-7 mL per tube). Upon completion of the centrifugation of supernatants, the resultant lipid pellet was resuspended in 5-15 mL of incubation buffer and homogenized for 50 strokes in a tight-fitting glass/Teflon homogenizer. The homogenized lipid suspension was very carefully pipetted on top of the 38% (w/v) sucrose solution in the ultracentrifuge tubes. The suspension/sucrose system was ultracentrifuged at 39000 rpm for 2 hours at 4°C. Following ultracentrifugation, the lipid residue was

visible as a translucent thin film at the sucrose/buffer interface. The lipid residue layer was carefully collected, diluted in 10-15 mL of incubation buffer, and homogenized for 30 strokes in the glass/Teflon homogenizer. The lipid suspension was subsequently ultracentrifuged at 26000 rpm for 40 minutes at 4°C. The supernatant was discarded, and the lipid pellet resuspended in 1 mL of incubation buffer. The final suspension was passed 5-10 times through a $26\frac{3}{8}$ gauge needle to break down the lipid aggregates and form vesicles. Finally, the vesicles were divided into 100 μL aliquots and stored at -80°C. The preparation performed by Schäfer et al.[161] took the purification of the resultant vesicles a step further by separating the 'inside-out' vesicles from the 'right side-out' vesicles. It is noted that for the results discussed in Section 3.1.3, the vesicles were not separated by orientation ('inside-out' vs. 'right side-out'), nor by size.

3.1.2 Translocation Assay

The vesicles prepared in Section 3.1.1 were thawed on ice and centrifuged at 15000 rpm for 30 minutes at 4°C. The incubation buffer was discarded, and the remaining lipid pellet was resuspended in transport assay buffer (2 mM $MgCl_2$, 2 mM $CaCl_2$, 50 mM NaCl, 25 mM sucrose, 10 mM dithiothreitol, 25 mM HEPES-KOH, pH 7.4). The lipid suspension was centrifuged at 15000 rpm for 30 minutes at 4°C and the supernatant discarded. The pellet was resuspended a final time in transport assay buffer and centrifuged under the same conditions. The supernatant was discarded, and the pellet resuspended in transport assay buffer containing 10 μM GTP (guanosine-5'-triphosphate) and protease inhibitor cocktail. The suspension was passed through a $26\frac{3}{8}$ gauge needle 20 times to ensure vesicle formation. At this point in the protocol, the vesicle suspension was apportioned into different reaction tubes allowing for variances in incubation conditions. An ATP-(adenosine-5'-triphosphate)regenerating system was selectively added to the vesicle solution in

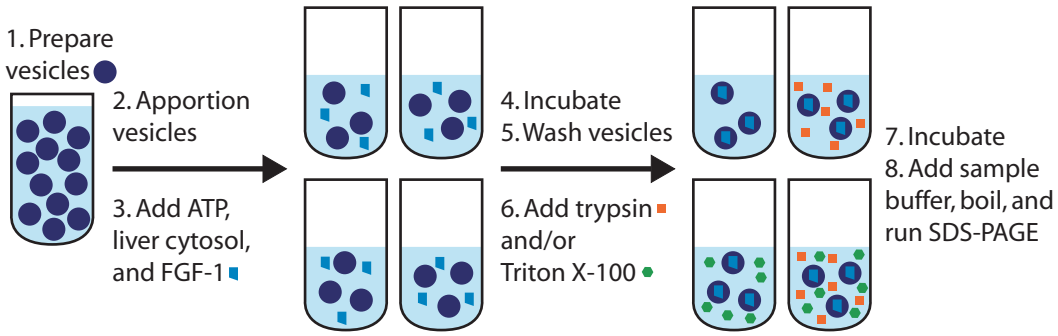

Figure 3.1. Schematic of the translocation assay. The assay was employed to study FGF-1 translocation with reconstituted plasma membrane vesicles.

order to supply ATP potentially required for transport of the protein. The ATP-regenerating system consisted of 8 units/mL creatine kinase, 5 mM creatine phosphate, and 50 μM ATP. Additionally, rat or human liver cytosol (1-5 mg/mL) was selectively added to restore the translocation activity of the vesicle membranes.[161] Finally, 1-5 μg of FGF-1 or other protein of interest was selectively added to the vesicle suspension, and each tube was brought to a volume of 100 μL with transport assay buffer.

With FGF-1 mixed with the reconstituted vesicles, the reaction tubes were incubated for 4 hours at 37°C (or other temperature of interest). Post incubation, the reaction tubes were centrifuged at 15000 rpm for 30 minutes at 4°C to facilitate removal of excess FGF-1 and the other reaction components utilized. The vesicle pellet was resuspended in transport assay buffer and centrifuged at 15000 rpm for 30 minutes at 4°C two additional times for thorough washing of the vesicles. Subsequently, the extent of protection of FGF-1 inside the vesicles was assessed by addition of the protease, trypsin, and/or the detergent, Triton X-100 (1% w/v in 50 mM Tris buffer), to the reaction tubes. Trypsin is known to degrade FGF-1 in solution.[4,237] Triton X-100 renders the lipids in the reconstituted vesicles soluble in the aqueous buffer, ultimately breaking down the vesicles and releasing their contents (if any) into the buffer.[161] The samples were treated with trypsin and/or Triton X-100 for

24 hours at 4°C, at which time any reactions were stopped by the addition of 100 μL of SDS-PAGE sample buffer and the boiling of the samples for 5 minutes. 100 μL of each boiled sample was then run on a 15% SDS-PAGE gel to separate the proteins present, and all protein components subsequently transferred from the gel to a nitrocellulose membrane (Hybond-C, Amersham Biosciences, Buckinghamshire, England). Employing an enhanced chemiluminescence (ECL) Western blotting system (Amersham, GE Healthcare Companies, Buckinghamshire, England), the nitrocellulose membrane was immunoblotted with a rabbit anti-FGF-1 antibody, followed by a goat anti-rabbit IgG, horseradish peroxidase (HRP)-linked antibody (Bio-Rad, Hercules, CA). HRP serves as a catalyst in a proprietary chemical reaction (performed in the presence of the nitrocellulose membrane) which results in chemiluminescence. The nitrocellulose membrane was subsequently exposed to light sensitive film, and the film was developed to visualize the results. Figure 3.1 depicts the translocation assay employed in the present work.

3.1.3 Results of Translocation Assay

Prior to assessing potential translocation of FGF-1 into reconstituted vesicles, the amount of trypsin required to breakdown FGF-1 was determined. Employing the same quantity of FGF-1 used in the translocation assay (2 μg), five reaction tubes were prepared with FGF-1 (2 μg/100 μL) and differing amounts of trypsin (0, 1, 10, 100, and 1000 ng/mL). The tubes were incubated for 2 hours at 4°C, after which time the reactions were stopped with the addition of SDS-PAGE sample buffer, the samples were boiled for 5 minutes, and then run on SDS-PAGE gel and analyzed by Western blotting. FGF-1, with a molecular weight of 18 kDa, was observed at the correct position on the SDS-PAGE gel based on the protein molecular weight standards. It was determined that FGF-1 was not fully degraded by any of the amounts of trypsin employed, therefore a second test was performed

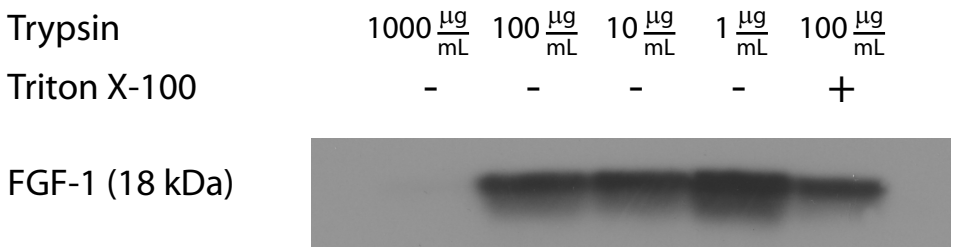

Figure 3.2. Western blot results of the trypsin requirement for FGF-1 degradation.

using higher amount of trypsin (1, 10, 100, and 1000 μg/mL). Additionally, Triton X-100 was added to 1 tube with 100 μg/mL trypsin to give an assessment of its effect on the reaction. After incubation under identical conditions, separation, and Western blot analysis (presented in Figure 3.2), the amount of trypsin required for full degradation of 2 μg/100 μL of FGF-1 was determined to be at least 1 mg/mL. It was also evident that Triton X-100 had no negative affect on the results. Consequently, for the translocation assays reported below, 2 mg/mL of trypsin was employed to ensure full FGF-1 degradation.

FGF-1 translocation assays were performed as detailed in Section 3.1.2 to assess whether FGF-1 translocated into the reconstituted vesicles at a physiologically relevant temperature. Specifically, FGF-1 was incubated with reconstituted vesicles for 4 hours at 37°C. Subsequently, the reaction mixture was separated into four vials, and experiments were performed to determine if FGF-1 had translocated into the vesicles. The first vial was treated with trypsin, the second vial was treated with Triton X-100, the third vial was treated with both trypsin and Triton X-100, and the final vial was not treated. The Western blot results are presented in Figure 3.3. It is evident that Column B (no trypsin or Triton X-100 treatment) contains significant FGF-1, however it is not possible to determine whether the protein is in solution, bound to the vesicles, or inside the vesicles. The presence of FGF-1 is also evident in Column D (Triton X-100 treatment only), although the result sheds no additional

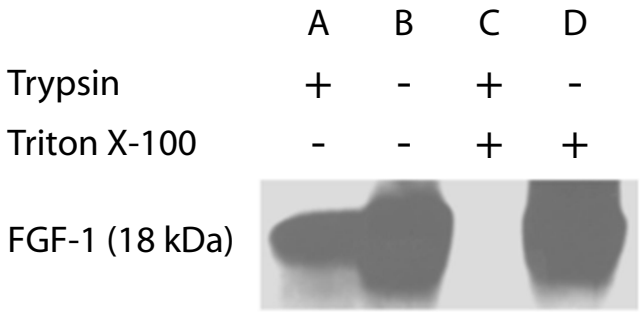

Figure 3.3. Western blot results of the FGF-1 translocation assay employing reconstituted vesicles.[164] FGF-1 was incubated with reconstituted vesicles for 4 hours at 37°C (the physiologic temperature of humans), followed by treatment with trypsin and/or Triton X-100. The "+" indicates the presence of trypsin or Triton X-100, while the "-" indicates the absence of trypsin or Triton X-100.

light on the location of the protein. Column A, however, (trypsin treatment only) provides evidence of the location of FGF-1. Indeed, despite the addition of trypsin, a protease known to degrade FGF-1, evidence of the protein is present in Column A; suggesting that a portion of FGF-1 translocated across the vesicle membranes and was subsequently protected from the action of trypsin in solution. Finally, Column C confirms the observation of Column A in that Triton X-100 treatment broke down the reconstituted vesicles, thereby releasing FGF-1 that had translocated and subsequently allowing its degradation by trypsin. It is concluded therefore, that FGF-1 is capable of translocating across reconstituted vesicle membranes in a cell-free system, and further, is protected within such vesicles from degradation by trypsin. It is noted that addition of the ATP-regenerating system, and/or the liver cytosol, was not necessary for FGF-1 translocation to occur.

To assess the temperature dependence of FGF-1 translocation into reconstituted vesicles, four separate vials containing FGF-1 and reconstituted vesicles were incubated, each at a different temperature: 42°C, 37°C, 20°C, and 4°C. Post incubation, trypsin was added to each vial to elucidate the extent of FGF-1 translocation and protection within the reconstituted vesicles. The Western blot results of the four

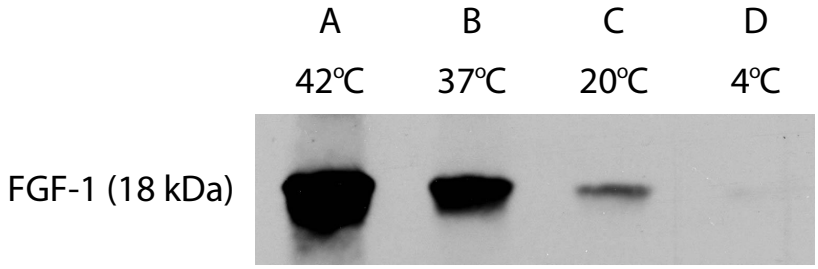

Figure 3.4. Temperature dependence of FGF-1 translocation.[164] Western blot results of the FGF-1 translocation assay employing reconstituted vesicles are presented. FGF-1 was incubated with reconstituted vesicles for 4 hours at four different temperatures: 42°C, 37°C, 20°C, and 4°C. The incubation was followed with trypsin treatment only. The Western blot results indicate that as the incubation temperature decreased (from Column A through Column D), the amount of protein protected in the vesicles decreased.

vials are presented in Figure 3.4. Investigation of Figure 3.4 reveals that the greatest amount of FGF-1 translocation and protection occurred within Column A, at an incubation temperature of 42°C. The concentration of FGF-1 decreased sequentially in Columns B through D, correlating with a progressive decrease in incubation temperature. The lower degree of FGF-1 protection at decreased temperatures may be a result of decreased fluidity of the lipid comprising the vesicle membranes. The decreased fluidity may yield a more solid-like membrane, which is less amenable to FGF-1 translocation. Additionally, conformational changes of FGF-1 with temperature may affect translocation into vesicles.[5]

The findings presented thus far indicate that FGF-1, a non-classically secreted protein, translocates into reconstituted vesicles. However, to provide physiologic relevance, a control experiment was performed with a classically secreted protein, osteopontin, (kindly supplied by Dr. Lucy Liaw's laboratory at MMCRI). Osteopontin (OPN) is a classically secreted protein found in the extracellular matrix of bone and teeth cells.[238,239] The OPN translocation assay was performed in an analogous manner to that executed with FGF-1, with immunoblotting of the results performed with a rabbit anti-OPN primary antibody and goat anti-rabbit IgG, HRP-

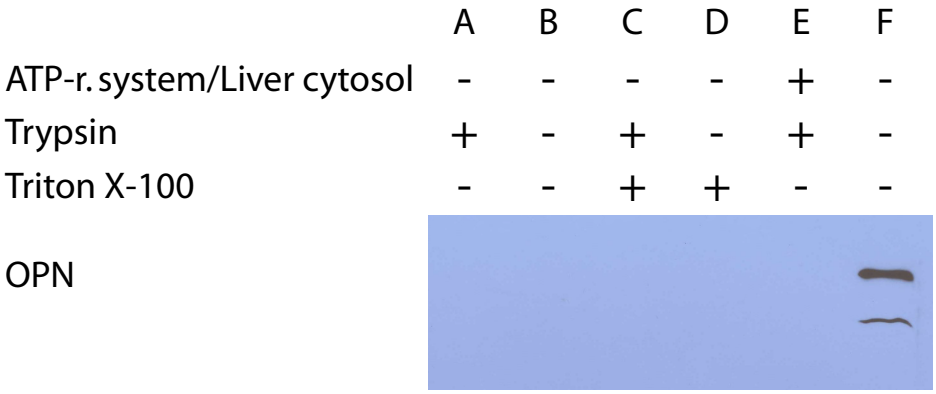

Figure 3.5. Western blot results of the control translocation assay. The assay utilized OPN, a classically secreted protein. The "+" indicates presence of the ATP-regenerating system and liver cytosol in the incubation, or trypsin or Triton X-100 in the treatment, while the "-" indicates no ATP-regenerating system and liver cytosol, trypsin or Triton X-100 was used in the experiment. OPN was incubated with reconstituted vesicles for 4 hours at 37°C, and the ATP-regenerating system and liver cytosol was added to a single vial (Column E). The incubation was followed with trypsin and/or Triton X-100 treatment. Separately, 1 μg of OPN was added directly to one of the lanes of the SDS-PAGE gel as a positive control (Column F).

linked secondary antibody. The resultant Western blot is presented in Figure 3.5. Examination of Figure 3.5 indicates that no OPN bands are visible in the Western blot other than for the positive control of 1 μg of OPN, which was added directly to Column F of the SDS-PAGE gel. It may therefore be concluded that no OPN translocated into the reconstituted vesicles and rather, it was removed during the washing step.

3.1.4 Summary

The results presented regarding translocation of FGF-1 into reconstituted membrane vesicles are an interesting first step in the study of translocation of the multi-protein FGF-1 export complex. Preliminary studies by the author of translocation of the other members of the non-classical FGF-1 release complex, specifically p40 Syt1 and S100A13, were performed, in addition to studies of translocation of combi-

nations of these proteins (FGF-1 and S100A13). Additionally, translocation assays have been performed with mutants of FGF-1, as well as FGF-1 proteins with altered 3D conformations. Finally, another non-classically secreted protein, Interleukin 1α (IL-1α), was studied employing the translocation assay. Unfortunately, no definitive results were obtained from these experiments and significantly more work should be dedicated to their pursuit.

3.2 Cushioned Model Membrane Study of FGF-1 Translocation

Building upon the FGF-1 translocation into reconstituted vesicle results presented in Section 3.1.3, FGF-1 translocation assays were performed employing the chitosan supported membranes described in Chapter 2. A significant advantage of the cushioned membranes is that unlike the reconstituted vesicle system, the composition of each leaflet of the membrane may be controlled via application of the LB/LS lipid deposition methodology. Indeed, the reconstituted vesicle membranes of Section 3.1.1 likely contained both zwitterionic and acidic lipids, amongst others, in unknown distributions in both leaflets. Conversely, the LB/LS method enables the fabrication of chitosan supported membranes with well defined leaflet composition. Given the hypothesis that FGF-1 membrane translocation may be mediated by FGF-1:acidic phospholipid interactions,[26,27,101] such membranes are likely to prove a highly valuable tool in evaluating the validity of the hypothesis.

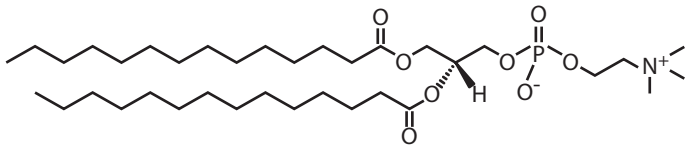

Figure 3.6. Molecular structure of 1,2-dimyristoyl-*sn*-glycero-3-phosphocholine (DMPC), a zwitterionic phospholipid.

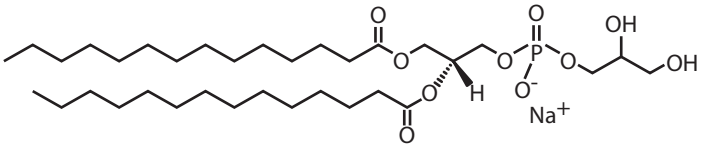

Figure 3.7. Molecular structure of 1,2-dimyristoyl-*sn*-glycero-3-phospho-(1'-rac-glycerol) (sodium salt) (DMPG), an acidic phospholipid.

Phospholipid bilayers were prepared with 1,2-dimyristoyl-*sn*-glycero-3-phosphocholine (DMPC), a zwitterionic lipid (molecular structure shown in Figure 3.6). Since DMPC is zwitterionic, it constitutes an excellent control bilayer for studying FGF-1 translocation, with minimal or no FGF-1 translocation expected to occur due to the proposed reliance of translocation upon acidic phospholipids. Phospholipid bilayers were also prepared with 1,2-dimyristoyl-*sn*-glycero-3-phospho-(1'-rac-glycerol) (sodium salt) (DMPG), an acidic phospholipid (molecular structure shown in Figure 3.7). According to the proposed reliance of the translocation process on acidic phospholipids, and the results of Graziani et al.[27], membranes comprising DMPG should facilitate FGF-1 translocation.

3.2.1 Cushioned Model Membrane Preparation

Preparation of chitosan supported membranes was accomplished as described in Section 2.1. Briefly, chitosan films were spin cast on cover glass, neutralized in borate buffer solution, and rinsed in 18.2 MΩ·cm water. The LB trough was cleaned and an 18.2 MΩ·cm water subphase introduced (maintained at 15°C), no center barrier was employed. Chitosan substrates were clamped back-to-back in the LB dipper and submerged into the subphase. DMPC and DMPG stock solutions were prepared on the day of use, each at a concentration of 1 mg/mL in chloroform. With the substrates submerged in the subphase, 100 μL of the lipid solution was spread dropwise on the air/water interface and the chloroform given time to evaporate (∼30

minutes). The monolayer was subsequently compressed to 32 mN/m and maintained at pressure for 30 minutes, after which the LB deposition was performed at a speed of 4 mm/min. The LS deposition was performed with double sided tape adhering the back of the substrate to a stainless steel bracket held in the dipper clip. The samples were passed horizontally through the monolayer into the subphase and maintained in 18.2 MΩ·cm water while being transferred to a 6 well plate.

3.2.2 Translocation Assay

The following procedure was developed based upon the translocation assay detailed in Section 3.1.2. The 18.2 MΩ·cm water in the wells was replaced with transport assay buffer through multiple rinses. The substrates were moved to a humidity chamber (an enclosed container containing a moistened Kim wipe). Within the chamber, each substrate was placed on a glass slide supporting a previously applied nail polish barrier (a thick layer of nail polish encompassing a cover glass) to prevent movement and allow a small amount of liquid to be maintained on the cover glass. 94.7 μL of transport assay buffer with 10 μM GTP and protease inhibitor cocktail and 2 μg of FGF-1 were dispensed onto each of the substrates. The substrates were subsequently incubated for 4 hours at 37°C.

Following incubation, the substrates were transferred to a 6 well plate and rinsed 3 times with transport assay buffer to remove excess FGF-1 and other reaction components. FGF-1 translocation across the supported membrane was assessed by utilizing the protease and/or detergent scheme employed for the vesicle study (see Section 3.1.2). Trypsin and Triton X-100 (1% w/v in 50 mM Tris buffer) served as the protease and the detergent, respectively. It may be inferred from Section 3.1 that trypsin degrades FGF-1 in solution. Further, Triton X-100 renders the lipids of the membrane soluble in the aqueous buffer, ultimately breaking down the membrane and releasing its components into the buffer. The substrates were

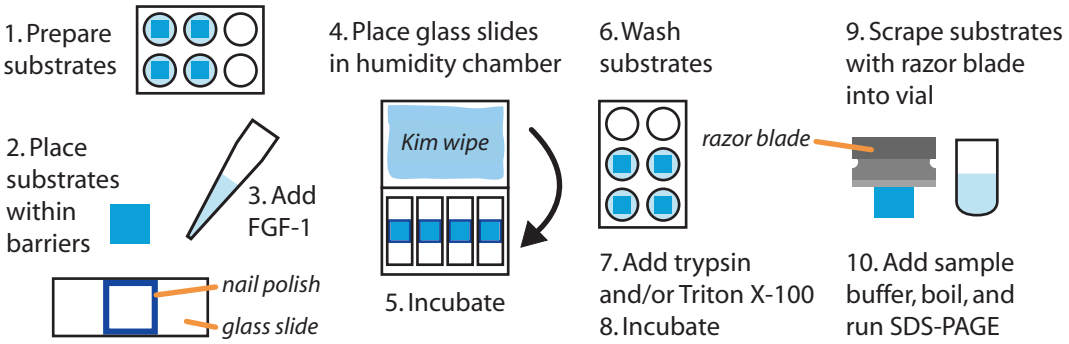

Figure 3.8. Schematic of the translocation assay. The assay was employed to study FGF-1 translocation with cushioned model membranes.

incubated with trypsin and/or Triton X-100 for 24 hours at 4°C on a rocker platform. It was determined that in order to run the incubated substrate on an SDS-PAGE gel, careful scraping across the cover glass surface with a clean razor blade was the most effective way to remove the chitosan and any residual membrane. Immediately after scraping the cover glass surface and transferring all material removed into a reaction tube, reactions were stopped by adding 100 μL of SDS-PAGE sample buffer and boiling the samples for 5 minutes. An aliquot of 100 μL of each boiled sample was subsequently run on the appropriate SDS-PAGE gel to separate the proteins present, and Western blot was employed to visualize the results. Figure 3.8 depicts the translocation assay employed in the present work.

3.2.3 Results of Translocation Assay

Initial assay results were inconclusive with regard to FGF-1 translocation across both DMPC and DMPG chitosan supported membranes. Based on the lack of apparent protected FGF-1, it was hypothesized that the washing step may have removed FGF-1 that had translocated during incubation. In order to increase the potential of protein retention within the chitosan, and therefore, detection in the Western blot, a chitosan solution containing 10 units/mL heparin (Sigma-Aldrich, St. Louis, MO) was prepared and spin cast onto cover glass as described in Section

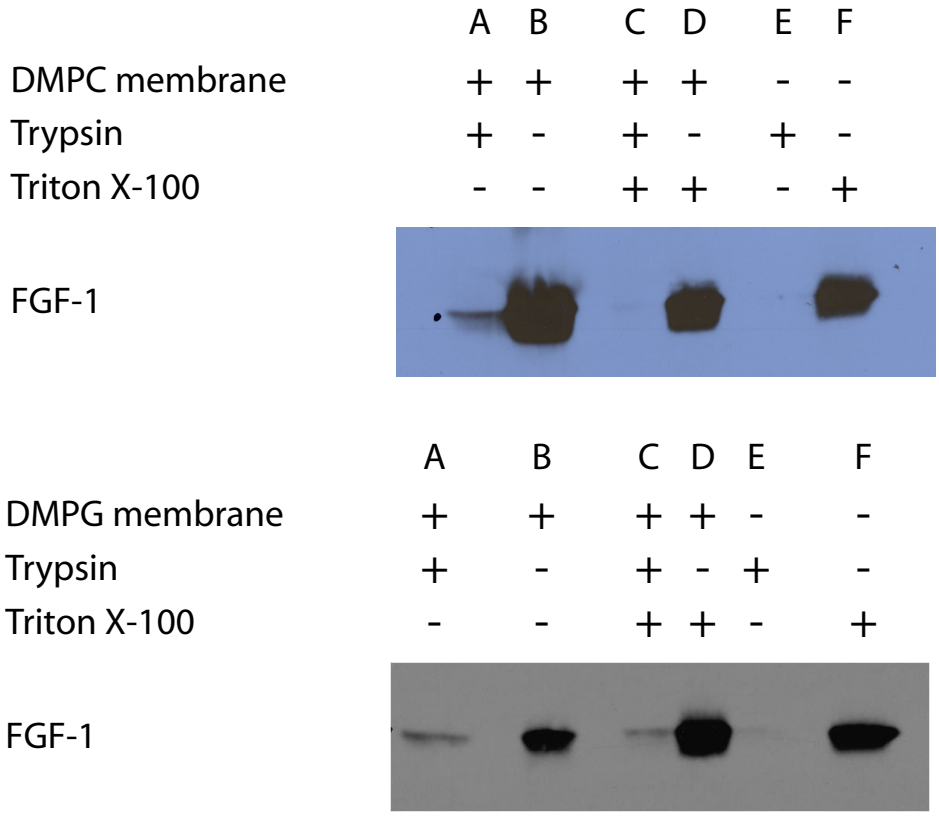

Figure 3.9. Western blot results of the FGF-1 translocation assay employing planar membranes supported on chitosan doped with heparin. FGF-1 was incubated with DMPC and DMPG membranes for 4 hours at 37°C followed by treatment with trypsin and/or Triton X-100. The "+" indicates presence of a membrane, trypsin or Triton X-100 and the "-" indicates no membrane was deposited or no trypsin or Triton X-100.

2.1.2. Heparin, a negatively charged glycosaminoglycan, has been shown to bind and stabilize FGF-1.[4,6] Inclusion of heparin in the chitosan cushion was hypothesized to aid retention of FGF-1 translocated across the membrane during the post-incubation rinses. The FGF-1 translocation assay was repeated as detailed in Section 3.2.2 with DMPC and DMPG membranes, each supported on the heparin-doped chitosan substrates. Assay results from the DMPC and DMPG membranes provided the first evidence of FGF-1 translocation and subsequent protection for planar chitosan cushioned membranes. The Western blot results are presented in Figure 3.9.

Comparison of the translocation assay results for the DMPC and DMPG membranes, indicates a similar degree of FGF-1 protection occurred for each lipid membrane. It is evident in Columns A, C, and E that the presence of trypsin greatly diminished the amount of FGF-1 retained when compared with Columns B, D, and F, where no trypsin was employed. In Columns A, where membranes were deposited and only trypsin treatment was employed, FGF-1 is present, indicating that a portion of the protein was protected from the action of the protease. A comparable protease was applied to Columns E, however, no membrane was deposited on the substrate, and no evidence of FGF-1 protection resulted. As such, comparison of Columns A to Columns E, indicates that the presence of a membrane had a notably positive effect on the protection of FGF-1 from trypsin degradation. In Columns D, where membranes were deposited and only Triton X-100 treatment was applied, and Columns F, which contained no membranes and only Triton X-100 treatment was employed, the strong bands of FGF-1 indicate the protein may have been bound to/in the membrane, or present in the chitosan post incubation.

Further examination of the cushioned membrane assay results (Columns A-D), indicate similar results to the vesicle translocation assay presented in Figure 3.3. Columns B, (membranes deposited with no post-FGF-1 trypsin or Triton X-100 treatments), provide evidence that FGF-1 was present in the cushioned membrane, however it is not clear whether the FGF-1 was bound to the membrane, or present within the chitosan. FGF-1 was also present in Columns D, although again, no definite location of FGF-1 is evident. Columns A reveal that a portion of FGF-1 was protected by the DMPC and separately, DMPG membrane. FGF-1 may have been bound in the membranes, or may have translocated into the chitosan. Columns C, (membranes deposited with post-FGF-1 trypsin and Triton X-100 treatments) provide conflicting results between DMPC and DMPG membranes. In Column C of Figure 3.9, the DMPC membrane results yield no evidence of FGF-1, a comparable

finding to that for the vesicle translocation assay of Figure 3.3. In the DMPG Column C of Figure 3.9, a band of FGF-1 is present in the Western blot, implying that protein was present post trypsin and Triton X-100 treatment. This finding strongly suggests that FGF-1 penetrated into the heparin doped hydrogel, an exciting and very significant finding.

3.2.4 Summary

As noted, the results presented for the cushioned membranes are the first evidence of FGF-1 translocation in a planar chitosan cushioned membrane. While the methodology was rudimentary, the preliminary study lends further support to the use of cushioned model membrane systems for investigating translocation of the non-classical FGF-1 release complex and its components.

Chapter 4
CUSHIONED MODEL MEMBRANE CHARACTERIZATION BY Z-SCAN FCS

The FGF-1 translocation assays with reconstituted vesicles and planar cushioned membranes, developed and detailed in Chapter 3, provide evidence that FGF-1 may translocate across such membranes. However, the assays did not yield insight into the dynamics or conformation of the lipids comprising the membranes prior to, during, or post FGF-1 translocation. As such, the present chapter details work performed to determine the lateral diffusion of a phospholipid bilayer supported on a chitosan cushion. As discussed in Section 1.4, the lateral diffusion of lipids comprising membranes may be measured by a variety of techniques; fluorescence recovery after photobleaching (FRAP), fluorescence correlation spectroscopy (FCS), or single particle tracking (SPT).[121,122] Of these techniques, FCS performed in the z-scan mode is the most facile since it is calibration-free and does not require large concentrations of fluorophore, and subsequently lowers the potential for membrane perturbation. The instrument and data analysis scheme employed for z-scan FCS measurements have been described in Section 2.3.2.

For the present work, 1,2-dimyristoyl-*sn*-glycero-3-phosphocholine (DMPC, Figure 3.6) membranes were deposited on the chitosan cushion via the LB/LS technique (see Section 2.1.3). In brief, LB deposition was performed first; the substrate was held vertically in the subphase, and was drawn through the monolayer at the subphase/air interface. LS deposition was performed on the substrate with the proximal leaflet already deposited; the substrate was held horizontally with the lipid facing toward the target monolayer at the subphase/air interface. The substrate was passed through the monolayer into the subphase, thus depositing the distal leaflet of the bi-

layer. The entire substrate was subsequently maintained in aqueous solution. Since each deposition took place separately, the lipid composition of each leaflet of the resultant bilayer was readily varied. Further, the process allowed each membrane leaflet to be labeled with fluorophore separately. Combining the low concentration of fluorophore required for FCS measurements, and the calibration-free nature of the z-scan FCS method, the resultant diffusion coefficients should be an excellent representation of the dynamics of the lipids comprising each leaflet of the bilayer.

4.1 Diffusion Behavior of Chitosan Supported DMPC Model Membranes

Bilayers prepared in the absence of a fluorophore were found to have very low background fluorescence. Consequently, the dynamics of each leaflet of the model membranes were able to be characterized independently by incorporating RhoPE in the phospholipid solution employed in the LB deposition of the proximal leaflet, or in the LS deposition of the distal leaflet. Employing the methods detailed in Chapter 2, chitosan supported DMPC model membranes were fabricated on cover glass (LB/LS deposition surface pressure was 35 mN/m) with the membrane leaflet of interest doped with RhoPE.

Samples were fabricated and mounted in the liquid cell (see Figure 2.7B). Diffusion of the fluorophore was then confirmed visually at room temperature for all samples employing the eyepiece of the FCS microscope. Subsequently, the sample temperature was reduced to 16°C and allowed to equilibrate. Data collection occurred over a temperature range of 16°C to 44°C, from low to high temperature, in increments of 1-2°C. Separate experiments revealed that data collected from high temperature to low temperature yielded comparable results. As detailed in Chapter 2, for each temperature, correlation curves were collected at 13 axial positions (cen-

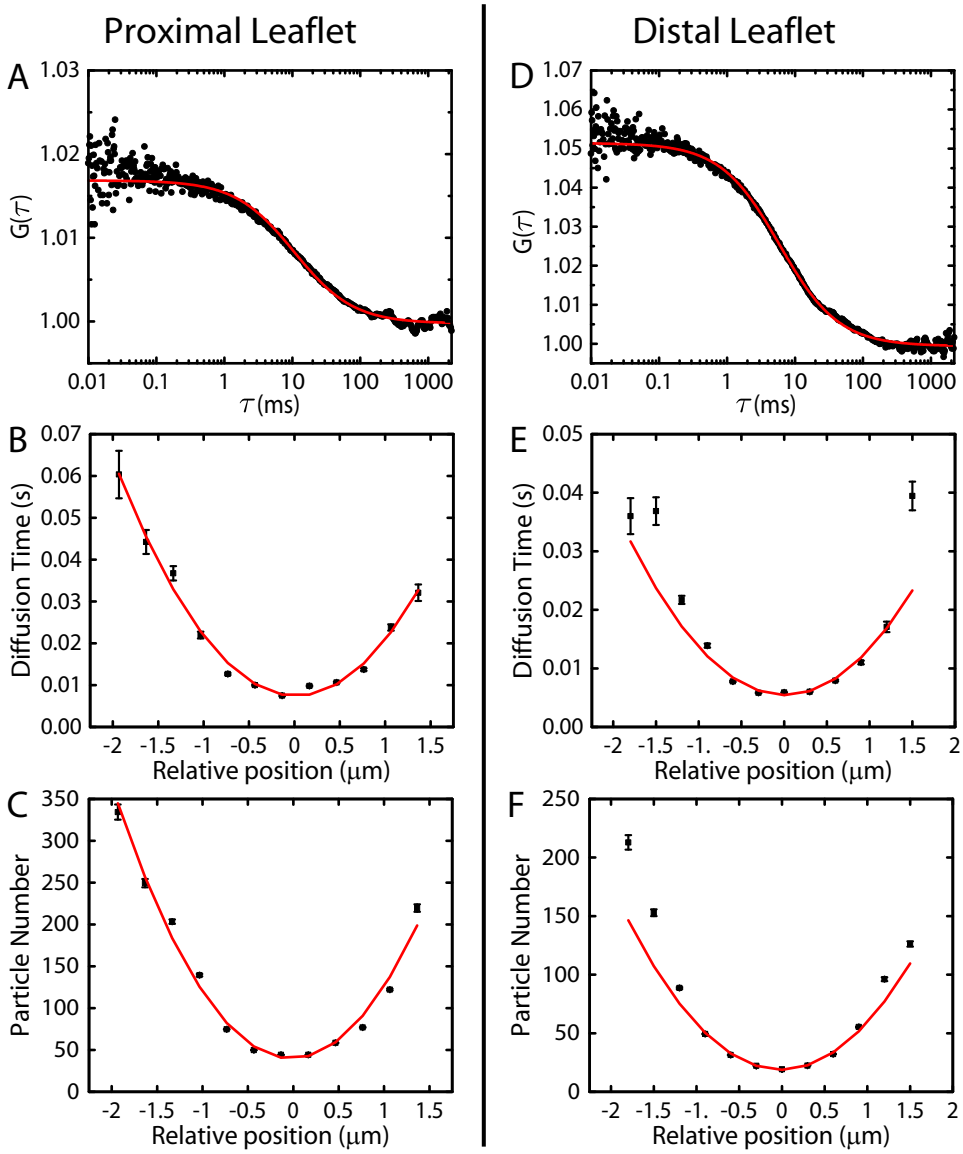

Figure 4.1. Representative z-scan FCS data and fits for DMPC supported on a chitosan substrate. **A** and **D** are the autocorrelation curves fit to the 2D diffusion model for the proximal and distal leaflets at 36°C, respectively. When combined with the other fitted autocorrelation curves at 36°C, **B** and **E** present the diffusion time vs. relative position, and **C** and **F** present the particle number vs. relative position. Each have been fit to the appropriate z-scan FCS equation to yield the diffusion coefficient (from **B** and **E**) and the effective concentration (from **C** and **F**).

tered around the $z = 0$ position with step sizes of 200-300 nm), averaged at each position, and fit with a weighted Levenberg-Marquardt fit routine, with the standard deviation serving as the fitted weight. Sample autocorrelation curves from a single axial position fit by this method for the proximal and distal leaflets of a DMPC bilayer supported on chitosan at 36°C are given in Figures 4.1A and D, respectively. The model employed in the fits was the 2D diffusion model presented in Equation 2.23. Employing the data from the fitted autocorrelation curves from the 13 axial positions, plots of diffusion time, and separately particle number, as a function of axial position were generated for each given temperature. Representative plots of the data collected at 36°C for the proximal and distal leaflets of a DMPC bilayer on chitosan are presented in Figures 4.1B and E (diffusion time vs. relative position), and Figures 4.1C and F (particle number vs. relative position). Equations 2.24 and 2.25 were used to fit the diffusion time and particle number z-scan FCS plots, respectively, in order to extract the diffusion coefficient.

Z-scan FCS measurements and analysis were performed on three separate DMPC bilayers over the temperature range stated. Plotting the resultant mean diffusion coefficients with respect to temperature generated a phase transition curve as presented in Figure 4.2. It is noted that since the fluorophore was incorporated into either the proximal or distal leaflet of the membranes, phase transition curves for the two leaflets were obtained independently. A weighted average was employed to compute the diffusion coefficient for each temperature while standard error propagation methods were used to determine the uncertainties.

The phase transition temperatures were determined via the sigmoidal fit method employed by other workers.[95,240] Specifically, the Boltzmann sigmoidal line shape is defined as

$$D(T) = \frac{D_0 - D_f}{1 + e^{(T - T_m)/\Delta T}} + D_f \tag{4.1}$$

where D_0 is the initial (lowest) diffusion coefficient value, D_f is the final (highest) diffusion coefficient value, T_m is the temperature at the center of the phase transition, and ΔT is the change in temperature over the range in which D varies the most. Employing Equation 4.1 yielded a proximal leaflet phase transition temperature, T_m, of 28.04±0.08°C and a distal leaflet phase transition temperature, T_m, of 28.10±0.07°C as shown by the dashed line in Figure 4.2. Separately, but not shown, the non-weighted mean and standard deviation of the diffusion coefficients were determined and fit to Equation 4.1 with the result yielding phase transition temperatures within error of those presented in Figure 4.2.

The diffusion coefficients determined in the present work are best compared to those reported by Baumgart and Offenhäusser for FRAP measurements of a chitosan supported DMPC bilayer.[171] Baumgart et al. report diffusion coefficients in the range of 0.004 $\mu m^2 s^{-1}$ to 1.02 $\mu m^2 s^{-1}$ over a temperature range of 14°C to 35°C. It is noted that these values are significantly lower than those determined in the present work of 0.825 $\mu m^2 s^{-1}$ to 3.98 $\mu m^2 s^{-1}$ over a comparable temperature range. The difference may potentially be attributed to the fact that two different measurement techniques were employed in the studies. Indeed, comparative measurements of diffusion coefficients via FRAP and FCS by Guo et al. revealed that FRAP derived values are often lower.[121] It is hypothesized that the source of the difference is the much greater degree of fluorophore doping employed for FRAP measurements and consequent perturbation of the membrane (1 mol% in each leaflet by Baumgart et al.[171]). Interestingly, the phase transition temperatures determined in the present work for the proximal and distal leaflets are within the range of values reported by Baumgart et al. (26.4-30.0°C),[171] although higher than the reported main phase transition temperature of 23°C.[241] It was postulated by Baumgart et al. that diffusion may be perturbed or hindered in this particular chitosan/phospholipid system by electrostatic interaction between the phosphate of the phospholipid head-

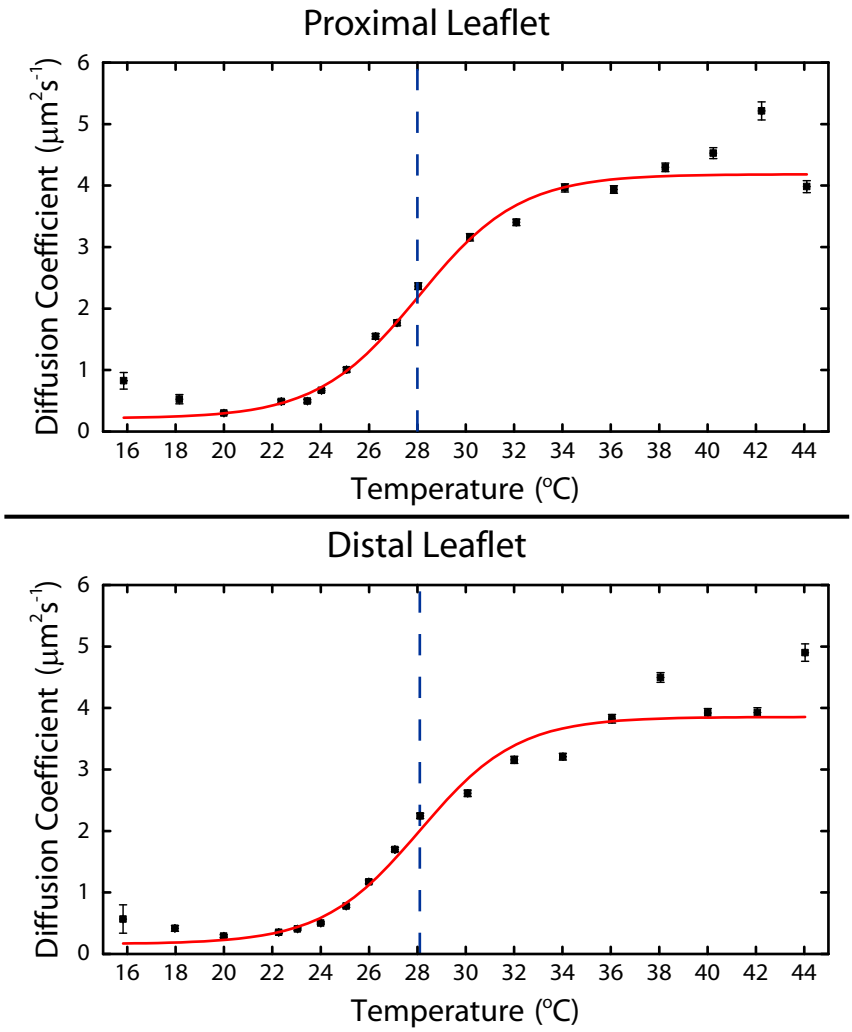

Figure 4.2. Phase transition curves for DMPC on chitosan substrates. The diffusion coefficients were plotted with respect to temperature. The mean diffusion coefficients were determined by a weighted average and the error bars were determined by propagation of errors from the weighted fitting and averaging. The phase transition temperatures, resulting from a Boltzmann sigmoidal line fit, were determined to be 28.04°C and 28.10°C for the proximal and distal leaflets, respectively. The values are indicated by the dashed lines.

group (negatively charged) and the amine of the chitosan (positively charged).[171] Indeed, it has been reported elsewhere that both the charge of a cushion and its surface roughness may affect diffusion of the bilayer it supports.[148,188,197] Interestingly, the fact that the diffusion coefficients of the proximal and distal leaflets determined in the present work are nearly identical suggests that either minimal perturbation exists, or both leaflets are affected to a similar extent.

Due to the observed difference between the main phase transition temperature of DMPC reported in the literature and the phase transition temperature obtained for DMPC in the present work, further analysis was undertaken regarding the type of perturbation that may be induced by chitosan on the individual phospholipid leaflets. Baumgart et al.[171] postulated that closer packed phospholipid headgroups, stemming from membrane dehydration caused by the chitosan/phospholipid interaction, may cause the increased phase transition temperature. That is to say, the chitosan may be acting as a mesh, and hindering the diffusion of the phospholipids. A similar phenomenon was reported by Wawrezinieck et al. for actin meshworks.[242] Indeed, Wawrezinieck et al. found that taking FCS measurements at various observation areas yielded different measured dynamic behavior. As a result, Wawrezinieck et al. developed a submicron confinement model of diffusion such that three types of diffusion were defined: free diffusion, diffusion within microdomains or so-called lipid rafts, and diffusion confined by a meshwork such as the actin cytoskeleton.

In order to account for the effect of crossing a spatial barrier (such as that posed by a microdomain boundary, or meshwork) on the measured diffusion coefficient, Wawrezinieck et al.[242] defined an apparent diffusion time, τ_D^{app}, as

$$\tau_D^{\text{app}} = t_0 + \frac{w_0^2}{4D_{\text{eff}}} \tag{4.2}$$

where D_{eff} is the apparent diffusion coefficient, w_0 is defined by Equations 2.24 and 2.25, and t_0 is a constant that is zero for free diffusion, positive for diffusion in

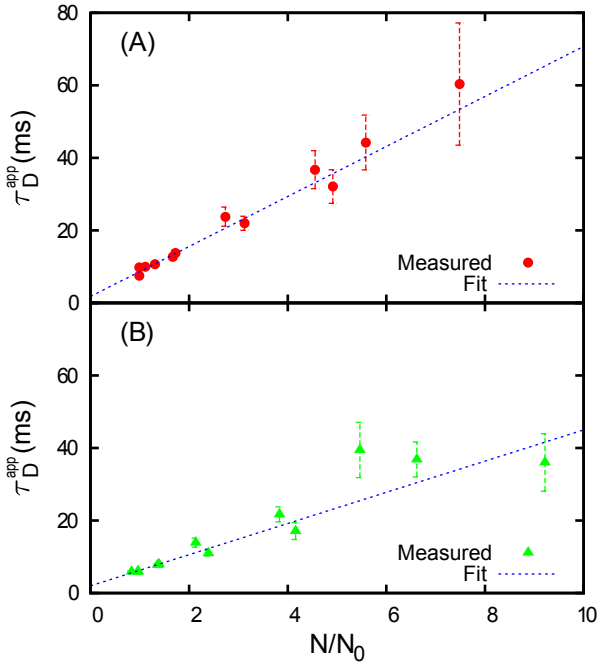

Figure 4.3. Representative confinement model data. The apparent diffusion time, τ_D^{app}, as a function of the ratio of the effective concentration, N, to the effective concentration at the minimum waist, N_0, is fit via a linear expression for the proximal (A) and distal (B) leaflets of a DMPC bilayer on a chitosan support at 36°C.

isolated microdomains/rafts and negative for diffusion in a meshwork. In addition, t_0 is proportional to the confinement time, or the average time required for a molecule within a domain to exit the domain.[242]

Humpolíčková et al.[156] recently demonstrated that data collected by the z-scan FCS technique may be readily analyzed via the methodology established by Wawrezinieck et al., by simply employing the effective fluorophore concentration as the measured change in the area probed. Specifically, Humpolíčková et al.[156] expressed the apparent diffusion time, τ_D^{app} as

$$\tau_D^{\text{app}} = t_0 + \frac{w_0^2}{4D_{\text{eff}}}\frac{N}{N_0} \tag{4.3}$$

where N_0 is the effective concentration at the minimum beam waist, and N is defined by Equation 2.25. It is evident from examination of Equation 4.3 that if one plots the measured diffusion time at each axial position as a function of N/N_0, the y intercept

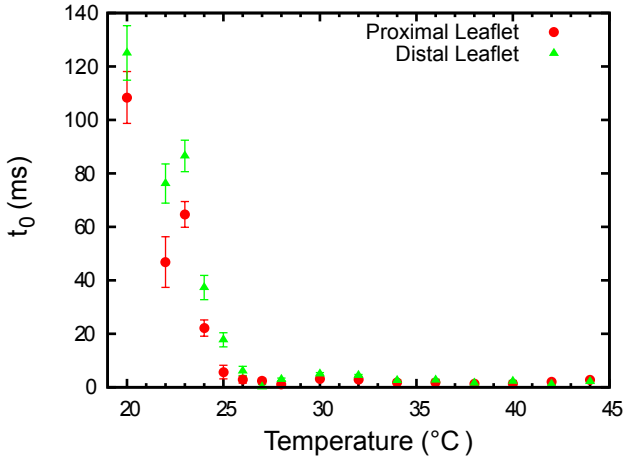

Figure 4.4. Confinement model data for DMPC on chitosan substrates. The y intercept values, t_0, of Figure 4.3 for each leaflet of a DMPC bilayer on a chitosan support as a function of temperature.

of a linear fit provides a value for t_0 and hence, a measure of the nature of diffusion. The submicron confinement model was applied to the z-scan FCS data collected in the present work to elucidate the nature of diffusion of each of the DMPC leaflets on the chitosan cushion as a function of temperature. Figure 4.3 presents the analysis for the proximal and distal leaflets of a DMPC bilayer on chitosan at 36°C.[243]

Figure 4.4 presents a plot of t_0 as a function of temperature for both the proximal and distal leaflets of a DMPC bilayer on chitosan.[243] It is evident from examination of Figure 4.4 that t_0 is greater than zero at temperatures less than approximately 27°C (approximately the phase transition temperature determined by fitting with the Boltzmann sigmoidal lineshape), indicating diffusion hindered by rafts. At temperatures equal to and greater than approximately 27°C, both leaflets have t_0 values near zero, indicative of free diffusion. These findings further support the diffusion coefficient results above, suggesting similar behavior for the two leaflets of the chitosan supported bilayer. It may also be concluded that the type of perturbation, if any, induced by the chitosan on the phospholipid leaflets may not be attributed directly to the meshwork of the chitosan since the resultant t_0 values are non-negative.

As reported in the literature, a variety of methods, (e.g. differential scanning calorimetry, electronic spin resonance, and fluorescence recovery after patterned photobleaching), and a variety of substrates (e.g. multilamellar vesicles, planar bilayers formed by vesicle fusion or LB/LS) have been employed to measure the phase transition temperature of DMPC membranes, yielding varying results.[188,241] The values reported in the present work (27-28°C) are within the range of values reported by Baumgart et al. (26.4-30.0°C),[171] both of which are higher than values reported in the same article for a substrate with no chitosan (glass supported planar DMPC bilayers). The results of the present work reinforce the conclusion that the substrate, specifically the chitosan cushion, is contributing to the higher phase transition temperature.[171]

4.2 Diffusion Behavior of Glass Supported DMPC Model Membranes

In an effort to assess the perturbative affect of the chitosan film, DMPC bilayers supported on glass were investigated via z-scan FCS. Solid supported membranes are a commonly employed model membrane system, as discussed in Section 1.5.4, where the membrane is supported on a hydrophilic substrate. Glass supported membranes are particularly amenable to the present work since the cover glass are compatible with the existing liquid cell. In addition, the negative surface charge of the cover glass in 18.2 MΩ·cm water, provides a contrast to the positive amine surface presented by chitosan.

Employing an identical bilayer fabrication procedure to that described for chitosan substrates (Section 2.1.3 with a surface deposition pressure of 35 mN/m), samples were prepared for examination of the proximal leaflet of a DMPC bilayer via z-scan FCS. With a glass supported DMPC bilayer mounted in the sample cell, diffusion of the fluorophores was confirmed visually. Z-scan FCS measurements were

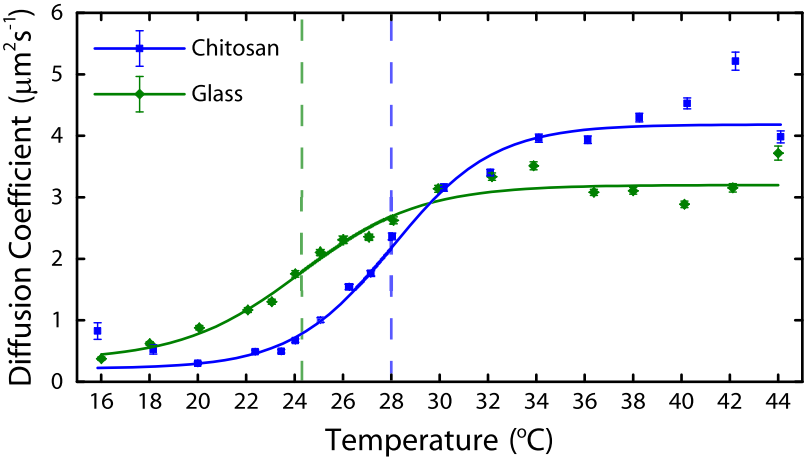

Figure 4.5. Comparison of glass and chitosan supported DMPC proximal leaflet phase transition curves. The diffusion coefficients were plotted with respect to temperature. There is a significant difference between the mobilities of proximal leaflets supported on chitosan and separately, glass as indicated by the Boltzmann sigmoidal line fit. The resultant phase transition temperature for the chitosan supported proximal is 28.04°C while the phase transition temperature for the glass supported proximal leaflet is 24.3°C as indicated by the dashed lines. The mean diffusion coefficients were determined by a weighted average and the error bars were determined by propagation of errors from the weighted fitting and averaging.

performed and analyzed in an analogous manner to that described in Chapter 2 and in Section 4.1. As such, a phase transition curve was obtained for the proximal leaflet of a DMPC bilayer supported on glass, as presented in Figure 4.5. To enable direct comparison, the phase transition curve of the proximal leaflet of the chitosan supported DMPC bilayer detailed in Section 4.1 is also presented in Figure 4.5. A weighted average was employed to compute the diffusion coefficient for each temperature and standard error propagation methods were employed to determine the uncertainties. The measured phase transition curve of the glass supported DMPC bilayer was fit with Equation 4.1 yielding a phase transition temperature of 24.3±0.1°C, a value significantly lower than the 28.04±0.08°C obtained for the chitosan supported membrane (shown by the dashed lines in Figure 4.5).

The diffusion coefficients determined for the proximal leaflet of glass supported DMPC bilayers in the present work may be readily compared to diffusion coefficients reported by Baumgart et al..[171] It is noted, however, that the values reported by Baumgart et al. are an average of the diffusion coefficients of the proximal and distal leaflets. Baumgart et al. report diffusion coefficients in the range of 0.007 $\mu m^2 s^{-1}$ to 1.56 $\mu m^2 s^{-1}$ over a temperature range of 14°C to 47°C.[171] Again, it is noted that these values are significantly lower than those determined in the present work of 0.376 $\mu m^2 s^{-1}$ to 3.71 $\mu m^2 s^{-1}$ over a comparable temperature range. In addition, the diffusion coefficients determined in the present work may be compared to those obtained via FRAPP (fluorescence recovery after patterned photobleaching) of glass supported, LB/LS DMPC bilayers by Scomparin et al..[188] Indeed, the diffusion coefficients reported by Scomparin et al. of 0.02 $\mu m^2 s^{-1}$ to 10 $\mu m^2 s^{-1}$ over a temperature range of 16°C to 47°C encompass the values obtained in the present work. It should be noted, however, that it is unclear whether the Scomparin et al. data are for membranes doped with fluorophore in one or both leaflets.[188] Finally, Forstner et al. employed a calibration-dependent FCS methodology to study DMPC bilayers formed by vesicle fusion on glass substrates in which both leaflets were labeled with a fluorophore.[244] Forstner et al. reported diffusion coefficients in the range of 0.08 $\mu m^2 s^{-1}$ to 4.8 $\mu m^2 s^{-1}$ over a temperature range of 19°C to 45°C.[244] It is noted that none of the reported studies employed identical bilayer fabrication and measurement methodologies, both of which have been shown to vary the resultant diffusion coefficients.[188,241] As such, it is perhaps not surprising that differences exist in reported values although it is noted that all are within an order of magnitude.

The phase transition temperature obtained in the present work for the glass supported DMPC membrane is within error of the range reported by Baumgart and Offenhäusser (20.4-24°C).[171] The phase transition temperature reported by Scomparin et al. (18±0.8°C) was determined by fitting their diffusion coefficient versus

temperature data with a power law, and by the authors own admission was an underestimation.[188] Forstner et al. did not report a measured phase transition temperature for their DMPC bilayers.[244] The data obtained in the present work was further analyzed to probe the nature of diffusion via application of the submicron confinement model (Equation 4.3) by Edward Allgeyer in his Ph.D. thesis. Examination of the data indicates that t_0 is greater than zero at temperatures less than approximately 23°C (within uncertainty of the reported main phase transition temperature of DMPC[241]), indicating diffusion hindered by rafts.[232] At temperatures greater than approximately 23°C, the proximal leaflet has t_0 values near zero, indicative of free diffusion.[232] It is further noted that the diffusion character determined by Dr. Allgeyer differed from that reported by Scomparin et al.; indeed, Scomparin et al. state that diffusion of DMPC bilayers on glass supports followed free diffusion at all temperatures investigated.[188,232] The change in the nature of diffusion of the glass supported DMPC bilayer proximal leaflet in the 23-24°C temperature range is consistent with the phase transition temperature value determined by fitting with the Boltzmann sigmoidal lineshape. While a marked difference in the phase transition temperature of the glass supported and chitosan supported DMPC bilayers of the present work exists, it does not negate the great potential chitosan has as a membrane support. Rather, it affirms the necessity of thorough characterization of model membrane systems via appropriate methods prior to further studies such as transmembrane protein insertion or protein translocation studies.

4.3 Diffusion Behavior of Supported Acidic Phospholipid Bilayers

With the diffusion behavior of zwitterionic DMPC bilayers supported on glass and chitosan films fully characterized, the study of comparable bilayers composed of acidic phospholipids commenced. Building upon the work of Doyle et al.,[101]

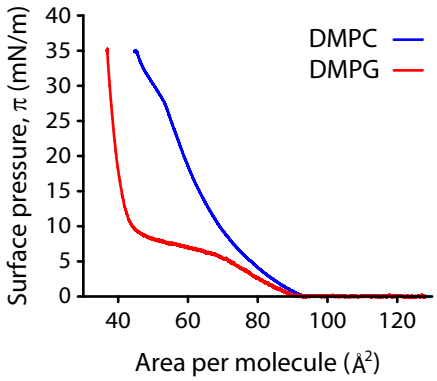

Figure 4.6. Compression isotherms of DMPC and DMPG on an 18.2 MΩ·cm water subphase. The isotherms were collected at 15°C and are shown to the deposition pressure of 35 mN/m.

1,2-dimyristoyl-*sn*-glycero-3-phospho-(1'-rac-glycerol) (sodium salt) (DMPG) was selected as a representative acidic phospholipid for the fabrication of chitosan supported bilayers; the molecular structure of DMPG is presented in Figure 3.7. DMPG is widely reported to have the same phase transition temperature as DMPC, making it an excellent candidate for comparison.[241,245,246]

Fabrication of DMPG bilayers was performed in a comparable manner to that detailed in Section 4.1. The proximal, chitosan supported, leaflet was studied first via z-scan FCS. The subphase employed in the LB trough was 18.2 MΩ·cm water, maintained at 15°C. Phospholipid solutions were prepared daily from stock solution at 1 mg/mL DMPG in chloroform and 0.0005 mol% RhoPE in 1 mg/mL DMPG in chloroform. As per recommendations of Avanti Polar Lipids,[247] DMPG was gently heated with a hot plate to ensure full solubility in chloroform. With the chitosan coated substrates submerged in the subphase, 50 μL of the respective phospholipid solutions were spread drop-wise on the appropriate trough compartment. Upon chloroform evaporation, the monolayers were compressed to 35 mN/m, decompressed, and finally compressed to, and maintained at, 35 mN/m. It is noted that the compression isotherms of DMPC and DMPG on 18.2 MΩ·cm water at 15°C differ greatly

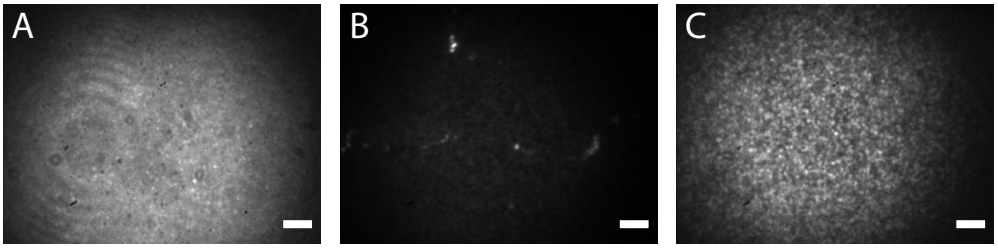

Figure 4.7. Fluorescence images of DMPC and DMPG bilayers. The bilayers were supported on chitosan with the proximal leaflets doped with 0.0005 mol% RhoPE. **A** presents a DMPC bilayer at 40.2°C, fabricated at a deposition surface pressure of 35 mN/m. **B** presents a DMPG bilayer at 44°C, fabricated at a deposition surface pressure of 35 mN/m. **C** presents a DMPG bilayer at 44.3°C, fabricated at a deposition surface pressure of 12 mN/m. The images were collected with an acquisition time of 1 second employing a 60X high NA water immersion objective and a 1.5X magnifying slider. The non-uniform lighting is a result of laser illumination, not sample preparation. The scale bars are 5μm.

as is evident in Figure 4.6. Indeed, the solid, gel-like, or tightly packed, phase of DMPG is reached at a much lower surface pressure ($\sim$10 mN/m) than DMPC ($\sim$30 mN/m) on 18.2 MΩ·cm water. After 30 minutes of equilibration, the LB deposition was performed at a speed of 4 mm/min. The LS deposition was performed immediately after the LB deposition, and the substrate was maintained in 18.2 MΩ·cm water while bring mounted in the sample cell.

Directly after fabrication, the DMPG bilayers were visualized through the microscope eyepiece; representative images of such a bilayer and a comparable DMPC bilayer are presented in Figure 4.7A and B. Investigation of the DMPG bilayer image of Figure 4.7B reveals that the fluorophore is clumped together in very dense, bright regions, leaving large areas with very little fluorophore. Additionally, no lateral movement was detectable by the eye. Conversely, the DMPC membrane of Figure 4.7A depicts good fluorophore dispersity and had obvious fluorophore mobility. Autocorrelation curves and resultant z-scan FCS plots of DMPG membranes could not be fit to Equations 2.23, and 2.24 and 2.25, respectively. The experiment

was repeated many times with comparable results. As such, work was performed to investigate the effect of deposition pressure on fluorophore distribution and mobility. Consequently, the deposition pressure was decreased from 35 mN/m to 12 mN/m while all other parameters were maintained at constant values. 12 mN/m was selected as the deposition pressure since it is approximately the surface pressure of the liquid-like to solid-like phase transition for DMPG monolayers on 18.2 MΩ·cm water at 15°C as determined by the isotherm of Figure 4.6. The fluorophore in the subsequent bilayer was not clumped into dense regions, however, it was unevenly distributed (see Figure 4.7C) and quantitative assessment via FCS indicated extensive fluorophore immobility (sticking) even at elevated temperatures (e.g. 44°C). In contrast, the DMPC bilayers presented in Section 4.1 displayed a uniform fluorophore distribution with slight movement detectable at low temperatures and rapid diffusion readily apparent at high temperatures. In order to determine if the poor fluorophore distribution and mobility were specific to the proximal leaflet, chitosan supported DMPG membranes were prepared with 0.0005 mol% RhoPE in the distal leaflet employing identical fabrication methods to those detailed for the 12 mN/m deposition pressure. Chitosan supported DMPG bilayers were subsequently mounted in the sample cell and observed via the eyepiece of the microscope. The bilayers doped in the distal leaflet demonstrated comparable poor fluorophore distribution and mobility to bilayers doped in the proximal leaflet, even at high temperatures. In order to determine if the source of the poor membrane was the chitosan, bilayers were fabricated directly on clean cover glass with the proximal leaflet doped with fluorophore. Observation of the bilayer yielded very little fluorescence, further the fluorescence that did exist was not replenished when the fluorophores were bleached in a given area, indicating very little to no movement of the phospholipid comprising the membrane.

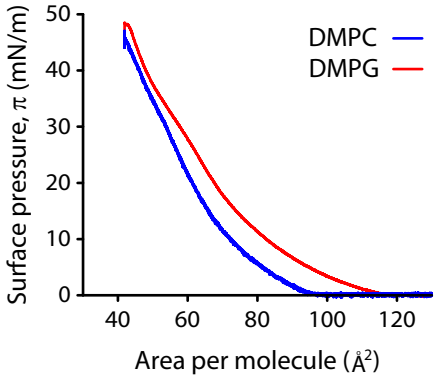

Figure 4.8. Compression isotherms of DMPC and DMPG on a PBS pH 7.0 subphase. The isotherms are shown to the collapse of the monolayers.

With little to no discernible lateral movement in the proximal or distal leaflets of the DMPG bilayers, even after lowering the deposition surface pressure and removing the chitosan support, the subphase was changed in an effort to improve phospholipid mobility. Subsquently, phosphate buffered saline (PBS), a buffer often used for biological studies including the vesicle preparation work detailed in Chapter 3, was employed as the subphase (at pH 7.0) in lieu of 18.2 MΩ·cm water. The subphase temperature was maintained at 15°C. A compression isotherm of DMPG on PBS (Figure 4.8) revealed a very different form to that obtained on 18.2 MΩ·cm water (Figure 4.6); interestingly, it bore great similarity to DMPC on PBS, as presented in Figure 4.8. Consequently, DMPG bilayers were fabricated on chitosan and separately, bare cover glass, with the proximal leaflet doped with 0.0005 mol% RhoPE at a deposition surface pressure of 35 mN/m from a PBS subphase. The DMPG bilayer supported on cover glass showed a non-uniform fluorophore distribution with areas of high fluorophore density and areas devoid of fluorophore. FCS was performed on areas with fluorophore; the autocorrelation curves and resultant z-scan FCS plots were fit very well by the 2D diffusion model and z-scan FCS equations, respectively. Although the results appeared promising, no two measurements on a given sample at a specific temperature gave consistent results. Subsequently,

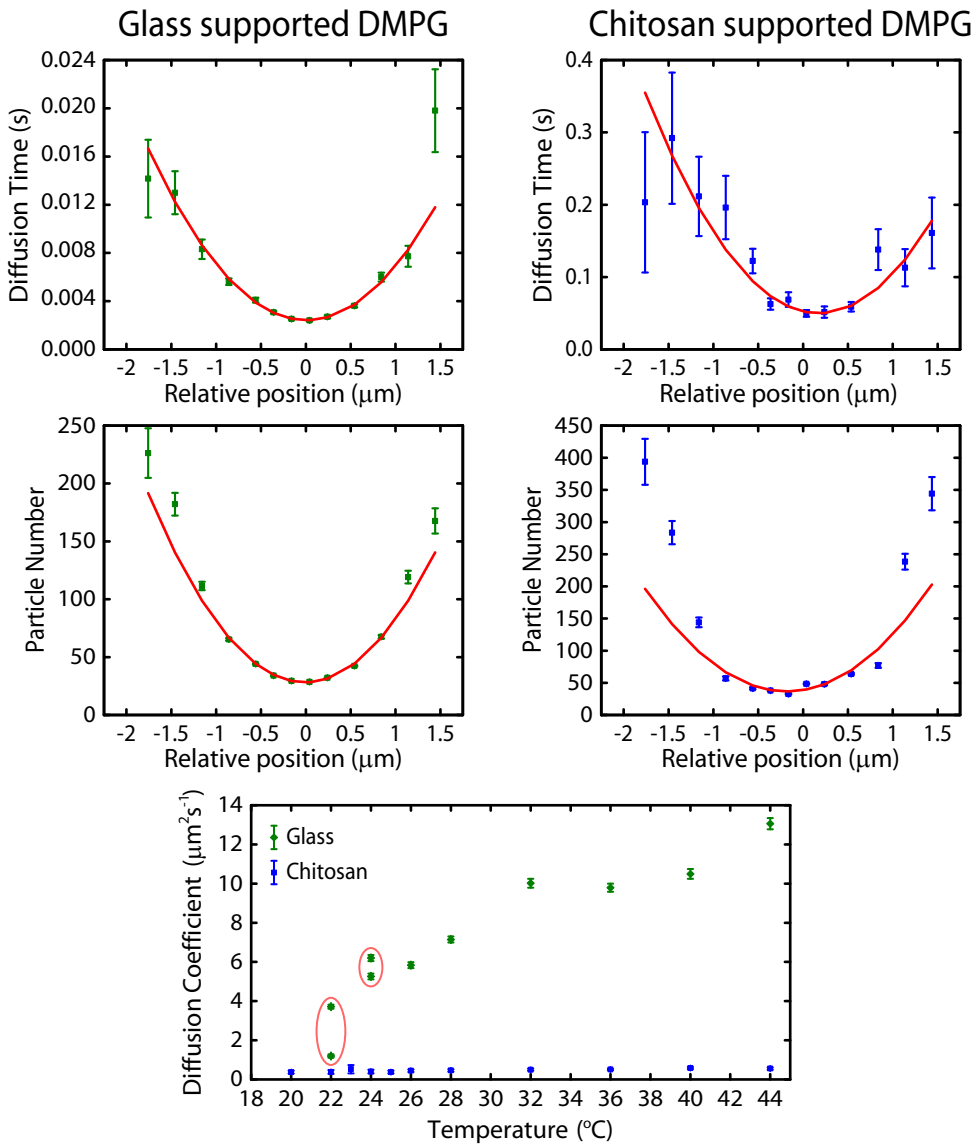

Figure 4.9. Z-scan FCS plots and phase transition curves of DMPG bilayers. The z-scan FCS plots of DMPG bilayers supported on bare cover glass, and separately chitosan, in which the proximal leaflet was doped with 0.0005 mol% RhoPE were collected at 36°C. Phase transition curves are plotted with diffusion coefficient versus temperature, and represent one bilayer supported on cover glass and one separate bilayer supported on chitosan. The data points in the ovals were collected at different points on the same bilayer at the same temperature. The error bars were propagated from the weighted averaging and fitting.

comparable bilayers were fabricated on chitosan coated substrates. Observation of the resultant bilayers indicated excellent fluorophore coverage, but poor apparent mobility. Indeed, z-scan FCS data collected over a range of temperatures indicated very little mobility in the chitosan supported bilayers when compared to the glass supported bilayers. Representative z-scan FCS plots collected at 36°C, in addition to phase transition curves measured for each of the glass and chitosan supported bilayers are presented in Figure 4.9. Given the somewhat positive results stemming from bilayers fabricated with RhoPE in the proximal leaflets, DMPG bilayers supported on chitosan with the distal leaflet containing 0.0005 mol% RhoPE were fabricated with a deposition surface pressure of 35 mN/m employing the PBS (pH 7.0) subphase. Unfortunately, no observable fluorescence was detected from the bilayers.

4.3.1 Hybrid Membranes

In order to have utility in the study of FGF-1 interactions with acidic phospholipid bilayers, it was considered necessary to employ a bilayer in which at least the distal leaflet of the bilayer was 1) composed of acidic phospholipids, 2) mobile, and 3) amenable to z-scan FCS. Since acidic phospholipids are negatively charged, it was considered possible that the lack of mobility observed in the chitosan supported DMPG bilayers stemmed from a stronger electrostatic interaction between the phospholipid and the positively charged amine groups of chitosan. Support for this hypothesis was the observation of potential success of glass supported DMPG bilayers, possibly due to the negative surface charge of the glass substrate. Thus, asymmetric bilayers with DMPC in the proximal leaflet and DMPG doped with 0.0005 mol% RhoPE in the distal leaflet were fabricated on chitosan coated substrates. The subphase employed initially was 18.2 MΩ·cm water maintained at 15°C, while deposition pressures of 35 mN/m and 12 mN/m were employed for DMPC

and DMPG, respectively. The bilayers fabricated employing these parameters displayed reasonable fluorescence but limited lateral mobility at elevated temperatures. Autocorrelation curves collected did not fit well to the 2D diffusion model, and the resultant z-scan FCS plots deviated significantly from the expected behavior. In addition, reproducibility was problematic with fabrication employing identical parameters, since bilayers exhibited widely variable fluorescence intensity.

A final attempt at modifying the experimental procedure to yield a viable hybrid DMPC/DMPG membrane was made via subphase modification. Specifically, in accordance with the findings of Lamy-Freund et al., who reported that the liquid-like to solid-like phase transition of DMPG in the presence of high ionic strength solutions was similar to that of DMPC,[245] a subphase of 10 mM HEPES (4-(2-Hydroxyethyl)piperazine-1-ethanesulfonic acid) at pH 7.4 with 100 mM NaCl was employed. Accordingly, a bilayer was fabricated on chitosan with the proximal leaflet composed of DMPC deposited at 35 mN/m surface pressure, and the distal leaflet composed of DMPG doped with 0.0005 mol% RhoPE also deposited at 35 mN/m surface pressure. When observed with the microscope, no visible fluorescence was evident from the bilayer.

4.3.2 Alternate Fluorophore

The bilayer fabrication parameters adjusted thus far had not lead to a reproducible means of fabricating a successful acidic phospholipid bilayer/hybrid bilayer. As such, attention was turned to a parameter that had not yet been manipulated, specifically, the fluorophore employed. RhoPE was employed as the fluorophore in the present work due to its strong fluorescence, the fact of its molecular structure is that of a phospholipid, and the fact that data collected with it was well fit by the 2D diffusion model. However, many alternatives exist. Indeed, preliminary work performed during initial instrument construction employed DiI C_{18}, a fluorescent

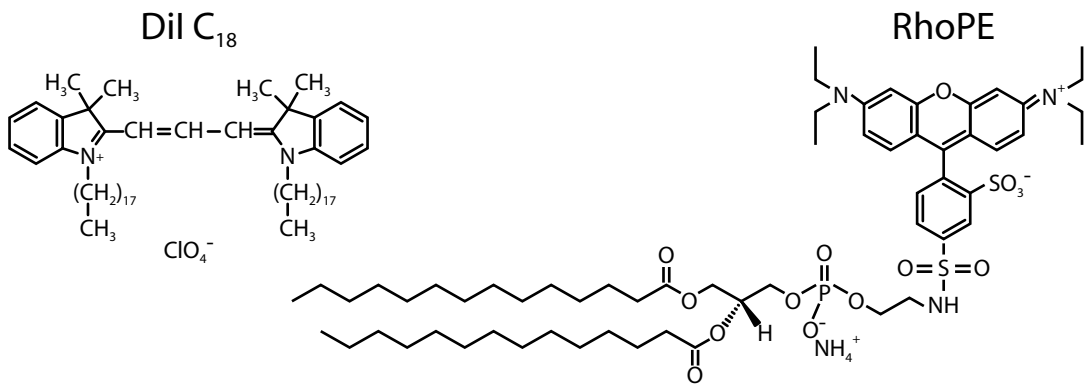

Figure 4.10. Molecular structures of 1,2-dimyristoyl-*sn*-glycero-3-phosphoethanolamine-N-(lissamine rhodamine B sulfonyl) (ammonium salt) (RhoPE) and 1,1'-dioctadecyl-3,3,3',3'-tetramethylindocarbocyanine perchlorate (DiI C_{18}). RhoPE is a phospholipid with a fluorophore covalently bound to the headgroup, while DiI C_{18} is a fluorescent lipid analog.

lipid analog with lower fluorescence emission than RhoPE. Importantly, DiI C_{18} is cationic as opposed to RhoPE's anionic nature (see Figure 4.10 for their respective molecular structures). As such, DiI C_{18} was tested as an alternate fluorophore.

A bilayer containing DiI C_{18} was fabricated employing a PBS (pH 7.0) subphase maintained at 15°C. The proximal leaflet comprised DMPC, while the distal leaflet comprised DMPG doped with 0.0005 mol% DiI C_{18}, both leaflets were deposited at 35 mN/m surface pressure. Visual observation of the bilayer revealed uniform fluorophore coverage and short range mobility. With good apparent stability, z-scan FCS data were collected and a phase transition curve generated as presented in Figure 4.11. Comparison of Figure 4.11 with the DMPC distal leaflet phase transition curves of Figure 4.2 reveals comparable behavior, as expected from the literature. However, two subsequent repetitions of the fabrication methodology resulted in bilayers that lacked fluorescence as measured by both the microscope eyepiece and the APD. As such, the methodology was deemed irreproducible and untenable.

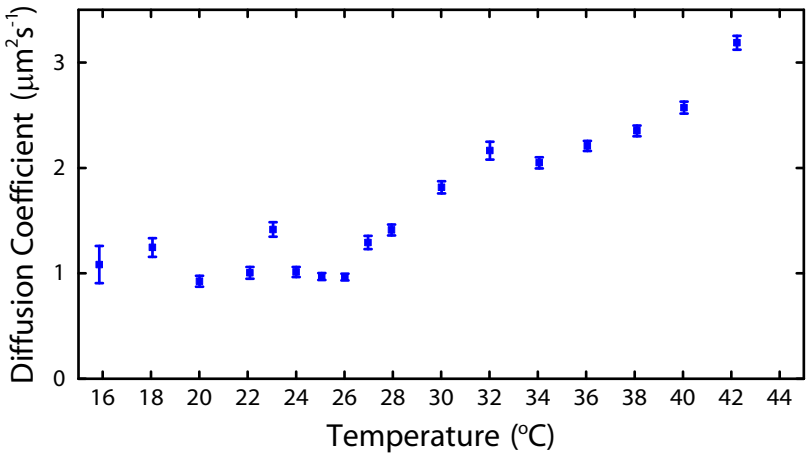

Figure 4.11. Phase transition curve of DMPG with DiI C_{18}. An asymmetric bilayer with DMPC in the proximal leaflet and DMPG doped with 0.0005 mol% DiI C_{18} in the distal leaflet was supported on chitosan and fabricated using a PBS pH 7.0 subphase and a deposition surface pressure of 35 mN/m for both leaflets. Data presented in the phase transition curve is for one bilayer, and the error bars were propagated from the weighted averaging and fitting.

4.3.3 Mixed Leaflet Composition

Given the difficulties encountered in fabricating acidic phospholipid monolayers and bilayers coupled with the relative ease of creating zwitterionic monolayers and bilayers, a procedure was developed to enable fabrication of mixed DMPC/DMPG leaflets.[248] Specifically, mixtures of DMPC and DMPG in 3:1 and 1:3 molar ratios were prepared each with 0.0005 mol% RhoPE. Monolayers were deposited from an 18.2 MΩ·cm water subphase on clean cover glass for initial assessment of the phospholipid:phospholipid:fluorophore interaction on the trough surface. The 3:1 DMPC:DMPG mixture was deposited at a surface pressure of 30 mN/m and the 1:3 DMPC:DMPG mixture was deposited at 18 mN/m based on the liquid-like to solid-like phase transitions of each monolayer determined from compression isotherms (not shown). Fluorescence images of the monolayers are presented in Figures 4.12A and B. Examination of Figures 4.12A and B indicates uneven fluorophore distribution with defined edges of apparent domains. Despite the non-uniform fluorophore

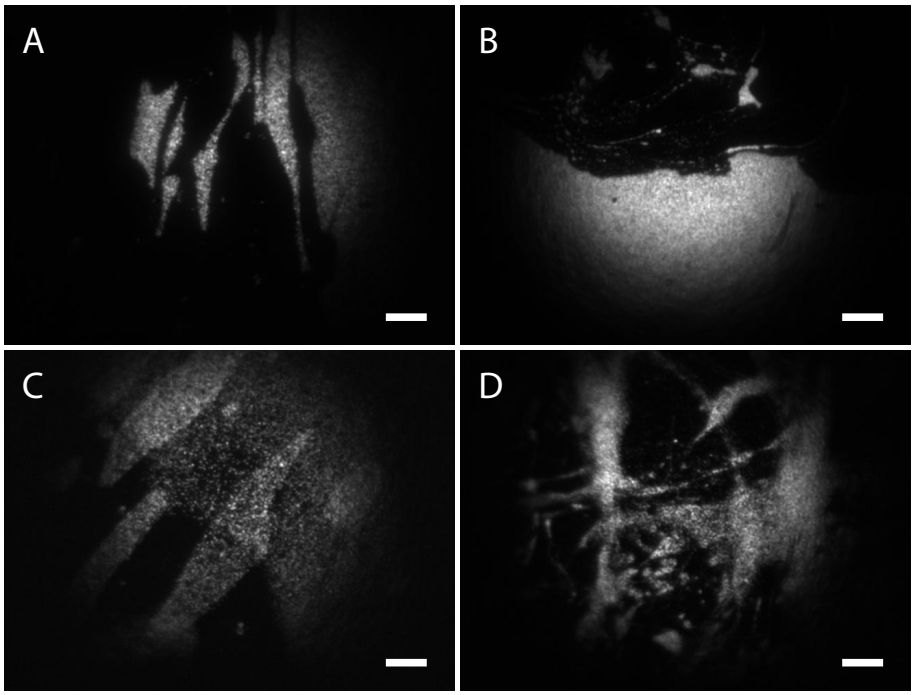

Figure 4.12. Fluorescence images of mixed DMPC and DMPG monolayers and bilayers. The monolayers and bilayers were supported on cover glass with all leaflets doped with 0.0005 mol% RhoPE. **A** and **B** correspond to monolayers with 1:3 and 3:1 ratios of DMPC:DMPG, respectively. **C** and **D** correspond to bilayers with 1:3 and 3:1 ratios of DMPC:DMPG, respectively. The images were collected employing a 60X high NA water immersion objective. The scale bars are 5μm.

distribution, distal leaflets were deposited on the monolayers from the same phospholipid mixtures to assess whether bilayers could be formed. Figures 4.12C and D present images of the resultant bilayers. The obvious presence of RhoPE in the resultant bilayers was encouraging and these systems proved to be the starting point for other phase separated monolayers that will be discussed in Chapter 5. In terms of the objectives of the present study, however, the non-uniform RhoPE labeling of the mixed phospholipid method was not suitable, and as such, was abandoned.

4.3.4 Investigation of Potential Phase Separation of Fluorophores

A small body of research suggests that RhoPE has a propensity to phase separate into disordered, fluid-like, phases when used in mixed monolayers, specifically, in

the presence of solid-like phospholipid domains (such as those that regularly exist at high surface pressures).[81,249–251] As such, work was undertaken to determine if a decrease in the deposition surface pressure would result in more uniform and mobile labeling of a distal DMPG leaflet. Employing 18.2 MΩ·cm water as the subphase, DMPC proximal leaflets were deposited on bare cover glass at 35 mN/m, and DMPG doped with 0.0005 mol% RhoPE was deposited at a surface pressure of 3 mN/m. As may be seen from investigation of the DMPG isotherm of Figure 4.6, at 3mN/m, the phospholipid exists in the liquid-like region. Visual observation of the bilayer indicated uniform fluorophore coverage, however there was no movement detected, visually or otherwise, even at temperatures well above the reported phase transition temperature of DMPG. Subsequently, bilayers were prepared using 10 mM HEPES buffer with 100 mM NaCl at pH 7.4. A DMPC proximal leaflet was deposited on bare cover glass at 35 mN/m followed by a distal leaflet of DMPG doped with 0.0005 mol% RhoPE at a surface pressure of 10 mM/m. Visual observation of the bilayer indicated uniform fluorophore coverage, and minimal movement at higher temperatures. Given the somewhat encouraging results on glass, an identical fabrication method was employed on chitosan coated substrates. Visual observation of the subsequent bilayers revealed no fluorescence whatsoever. It is noted that a LB monolayer of DMPG:RhoPE was deposited on cover glass from the same trough preparation as the chitosan supported bilayers, and fluorescence was visually observed, indicating that RhoPE was present on the LB trough.

In order to determine if the observed behavior was fluorophore dependent, bilayers were fabricated employing DiI C_{18} and 10mM HEPES, 100 mM NaCl at pH 7.0 as the subphase. DMPC proximal leaflets were prepared on glass and chitosan at 35 mN/m surface pressure, and DMPG:DiI C_{18} distal leaflets were deposited at a surface pressure of 10 mM/m. DiI C_{18} was found to be visually present in the membrane on the glass supported substrate and was mobile at temperatures well

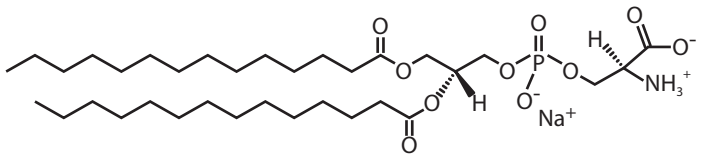

Figure 4.13. Molecular structure of 1,2-dimyristoyl-*sn*-glycero-3-phospho-L-serine (sodium salt) (DMPS), an acidic phospholipid.

above the reported phase transition temperature. No fluorescence was observed from the chitosan supported bilayer. Finally, monolayers of the DMPG:DiI C_{18} mixture were deposited at 35 mN/m surface pressure on cover glass and chitosan from the same trough preparation, and visual inspection of each indicated the presence of DiI C_{18}. From these findings two possibilities exist; first, that low surface pressure depositions do not yield consistent bilayers, at least for phospholipid/support combinations employed in the present studies, and second, that chitosan is simply not a suitable support for LB/LS deposited DMPG bilayers.

4.3.5 DMPS Membranes

In order to determine if the difficulty in fabricating an acidic phospholipid supported membranes stemmed from the use of DMPG, an alternate acidic phospholipid was investigated. Specifically, due to data supporting the mediative role of acidic PS in FGF-1 cellular secretion,[26] attention was turned to the phospholipid 1,2-dimyristoyl-*sn*-glycero-3-phospho-L-serine (DMPS). The molecular structure of DMPS is presented in Figure 4.13. Interesting, while it has the same alkyl chain tail length as DMPC, the phase transition temperature is reported as 35°C[252,253] vs. 23°C for DMPC; a fact attributed to an increased number of hydrogen binding sites due to the presence of phosphate, carboxyl, and amine groups.[254] The presence of these chemical moieties in the structure of DMPS presents the opportunity to adjust the overall charge characteristics of the phospholipid by adjusting the pH

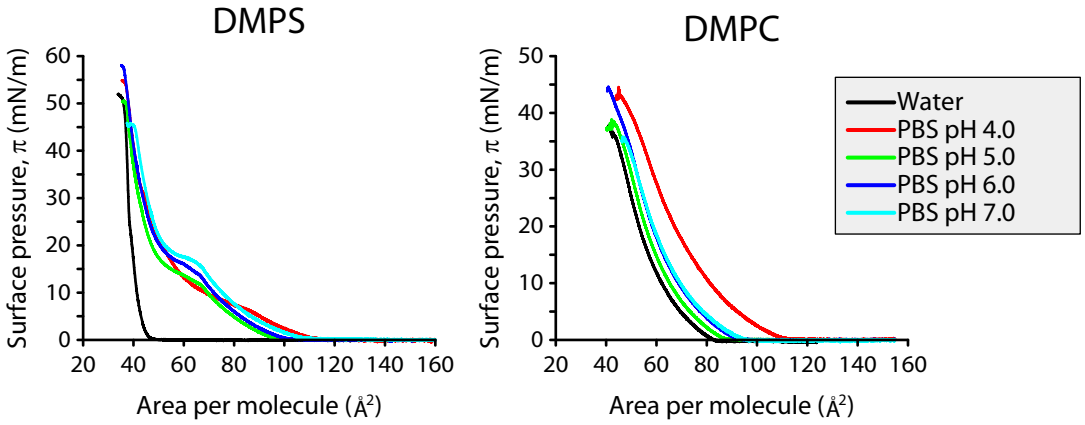

Figure 4.14. Compression isotherms of DMPC and DMPS at various pH values. The isotherms, collected on PBS and 18.2 MΩ·cm water subphases, are shown to collapse of the monolayers.

of the subphase; the pK_as of the phosphate, carboxyl, and amine groups are 2.6, 5.5, and 11.55, respectively.[255] Compression isotherms of DMPS and DMPC were measured on pH adjusted PBS buffer and 18.2 MΩ·cm water (Figure 4.14). Investigation of Figure 4.14 reveals that while the DMPC monolayers were only minimally affected by the type of subphase and its pH, very dramatic differences were evident for the DMPS monolayers when changing from 18.2 MΩ·cm water to PBS, and further upon raising the pH from 4.0 to 5.0. It is likely that at pH 4.0, DMPS has a nearly net neutral charge with the carboxyl groups of the phospholipid protonated, while conversely at pH 5.5, approximately 50% of the carbonyl groups are likely deprotonated.

Initial DMPS hybrid bilayers were fabricated from a PBS subphase at pH 7.0, maintained at 15°C. DMPC proximal leaflets were deposited at 35 mN/m surface pressure on glass and separately, chitosan substrates and DMPS, doped with 0.0005 mol% DiI C_{18}, distal leaflets were deposited at 10 mN/m surface pressure. Visual observation of the glass supported bilayer indicated a small amount of fluorescence, while the chitosan supported bilayer displayed none. To confirm the presence of the fluorophore on the trough, monolayers of DMPS:DiI C_{18} were deposited at 10 mN/m

on glass and separately, chitosan substrates. Visual observation of each monolayer indicated the presence of the fluorophore. Consequently, comparable bilayers were fabricated but the subphase and pH were modified in light of the findings of Figure 4.14. Specifically, a subphase of PBS at pH 4.0 was employed. Additionally, the deposition surface pressure for the DMPS:DiI C_{18} was reduced to 3 mN/m in order to deposit the monolayer in the liquid-like phase. Visual observation of the bilayers on both glass and chitosan did not yield any fluorescence. It is noted, however, that DMPS:DiI C_{18} monolayers on cover glass and chitosan were fluorescent.

As is evident from the work presented in this section, the creation of acidic phospholipid supported bilayers is extremely challenging. Further study regarding subphase and substrate interactions will be required to determine a functional method for reproducibly creating such bilayers.

4.4 Actin Supported Membrane Development

While Section 4.1 demonstrated successful creation of a cushioned DMPC bilayer on a chitosan film, the physiologic relevance of chitosan is non-ideal. As such preliminary work was performed to develop a cushioned membrane system of greater physiologic relevance. The work presented in this section was performed in collaboration with Dr. Sharon Ashworth's laboratory and an undergraduate honors student, Ryan Dawes.

The underlying cellular cytoskeleton shapes and orders membrane constituents which, in part, define cellular membrane function.[256] The cytoskeleton is largely composed of the dynamic protein found in all eukaryotic cells, actin. Actin is a 42 kDa cytosolic protein capable of dynamic and reversible polymerization from its globular, monomeric "G-actin" state, to its filamentous "F-actin" state through the binding and subsequent hydrolysis of ATP.[257] This dual-conformational character

allows actin to play many critical roles in a cell. Specifically, actin has been implicated in protein and vesicle trafficking,[258,259] cell motility[260] and shape,[261] and has also been shown to interact indirectly with membranes via lipid-binding proteins.[262,263] These interactions allow for the actin cytoskeleton to coordinate membrane domains,[264,265] form critical cellular structures,[266–268] and transport various factors to and from the membrane proximal leaflet.[11,269] Further understanding of membrane structure and function, as related to actin, promises to provide greater insight into specific physiological and pathophysiological cellular events.[270,271]

Biological cellular membranes are supported on the proximal leaflet by the cell's actin cytoskeleton network while the distal leaflet is exposed to varying aqueous environments or the extracellular matrix mesh. As such, a planar membrane system with the proximal leaflet supported by an actin cushion and the distal leaflet exposed to an aqueous environment would be a highly physiologically relevant system. Previous work has investigated actin binding with lipid monolayers,[272] biofunctionalized monolayers,[273] and bilayers.[274] Actin has been encapsulated inside giant unilamellar vesicles for the study of mechanical influence[275] and membrane organization.[276] Additionally, F-actin has been investigated as an inducer of single ionic channels[277] and further, the binding affinity of actin to phospholipid monolayers has been studied.[272,273,278]

Although a wealth of cushioned and solid supported planar membrane systems have been developed (reviewed by Kiessling et al.[279]) actin has not yet, to the author's knowledge, been employed as a support for a phospholipid membrane. Thus, presented below is the first realization of an actin supported planar phospholipid membrane. The actin support was fabricated via a novel self assembly procedure, and characterized using surface immunochemistry and ellipsometry. Phospholipid bilayers were deposited by the LB/LS technique as detailed in Section 2.1.3, and the lateral mobility was determined as a function of temperature via z-scan FCS.

4.4.1 Actin Purification

Actin was extracted from acetonic powder, prepared from rabbit skeletal muscle, following the protocol of Pardee and Spudich.[280] In brief, rabbit hind leg and back muscle were removed, ground and washed with successive buffer solutions. The resulting muscle mince was then rinsed in acetone and allowed to dry before storage at -80°C. Purified actin concentration was evaluated by a Bradford protein assay[281] on a BioTek Synergy 2 Microplate Reader (Winooski, VT) and subsequently diluted to 30 μg/mL in G-buffer (5 mM tris(hydroxymethyl)aminomethane, 0.2 mM calcium chloride, 0.2 mM adenosine triphosphate, 0.5 mM dithiothreitol, pH 7.9).[280] Prior to use, actin solutions were dialyzed against G-buffer for 48 hours. A final dialysis was performed against phosphate buffered saline (PBS) (137 mM sodium chloride, 2.7 mM potassium chloride, 8.1mM sodium phosphate, 1.76 mM potassium phosphate, pH 7.8) for 24 hours, to remove residual G-buffer components from the protein solution. Isolated actin was used within one week of initial purification.

4.4.2 Surface Functionalization

The same cover glass employed for chitosan substrates was used as the substrate for actin functionalization, and was cleaned as detailed in Section 2.1.1. Actin surface functionalization was accomplished using a modified procedure reported by Okada et al.[282] and An et al..[283] Cover glass substrates were incubated for three hours at 24°C in 5 mM (3-aminopropyl)trimethoxy silane (APTMS) (Gelest, Inc., Morrisville, PA), dissolved in a 5:1 v/v solution of ACS Certified acetone (Fisher Scientific, Suwanee, GA) and 18.2 MΩ·cm water. After incubation, APTMS functionalized cover glass substrates were rinsed in a 5:1 v/v acetone/18.2 MΩ·cm water solution and dried under nitrogen flow. Directly before use, APTMS functionalized cover glass substrates were incubated for one hour in 10% v/v glutaraldehyde (Sigma-Aldrich, St. Louis, MO) in 18.2 MΩ·cm water. Functionalized cover glass

were rinsed with excess amounts of 18.2 MΩ·cm water, and immersed for two hours in a 30 μg/mL G-actin solution. Actin modified cover glass substrates were subsequently rinsed with excess amounts of 18.2 MΩ·cm water before use.

4.4.3 Surface Characterization

Actin modified cover glass substrates were investigated using immunochemical staining. Cover glass samples were incubated for 8 hours at 24°C in 1:200 v/v anti-C4 actin antibody (Millipore, Billerica, MA) in G-buffer with 2% v/v bovine serum albumin (BSA) (Sigma-Aldrich, St. Louis, MO), followed by rinsing with excess G-buffer. Control cover glass substrates were incubated solely in G-buffer. The substrates were then incubated overnight at 24°C in 1:200 v/v FITC-conjugated goat-anti-mouse antibody (Jackson ImmunoResearch Laboratories, Inc., West Grove, PA) in G-buffer with 2% BSA. Following secondary antibody incubation, cover glass substrates were rinsed with excess G-buffer and mounted on a glass microscope slide using a 1:1 v/v solution of Certified ACS glycerol (Fisher Scientific, Suwanee, GA) and PBS containing 1% by volume 1,4-diazabicyclo[2.2.2]octane (Sigma-Aldrich, St. Louis, MO). Cover glass substrates were viewed on an Olympus FluoView laser scanning confocal microscope using a 40x objective and images were collected. Separately, ellipsometry was performed to assess the thickness of the actin layer on the functionalized substrate. The substrates employed were polished, monocrystalline silicon wafers prepared using the method described above for cover glass. The substrates were measured using a J.A. Woollam M-2000V spectroscopic ellipsometer (Lincoln, NE) at an incident angle of 75° in 18.2 MΩ·cm water within a 5 mL liquid cell.

Assessment of the actin functionalized substrates was performed prior to bilayer deposition. Figure 4.15A presents a confocal fluorescence image of an actin functionalized cover glass substrate exposed to immunochemical staining. As indicated

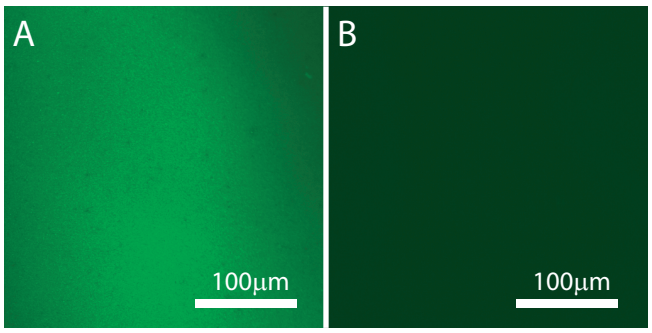

Figure 4.15. Confocal fluorescence images of actin functionalized substrates. Specifically, laser scanning confocal fluorescence images of **A** immunochemical stained actin functionalized cover glass and **B** a no-primary antibody control were collected. The mean count rate per pixel for the actin and control were 11.1 and 3.5 MHz respectively which corresponds to greater than a factor of 3 increase in count rate for the actin functionalized samples over the control, strongly suggesting the presence of actin. Additionally, imaging over multiple sample regions (data not shown) shows uniform intensity for the actin functionalized cover glass suggesting excellent surface coverage and a lack of large scale surface defects above the resolvable limit of confocal microscopy (for the excitation wavelength employed here, 488 nm, features below approximately 250 nm would not be visible).

by the uniformity of the staining, the surface of the cover glass substrate was evenly coated with actin monomers. The lack of fluorescence in the no-primary antibody control (Figure 4.15B) confirmed the specificity of the staining and confirmed the high purity of actin achieved via the Pardee and Spudich method. These representative images indicate that the functionalization method is highly effective in adsorbing actin onto the substrate. Additionally, the staining uniformity demonstrates that there are no local defects perceptible at the optical level. The ellipsometric measurements performed in parallel with the immunochemical staining confirmed that a layer of actin was adsorbed on the substrate. Ellipsometry measurements were performed for each step of the functionalization procedure for a series of samples, showing progressive film thickness increases. Additional measurements indicated uniform thickness of actin across individual substrates. The mean thickness for the actin functionalized substrates was $\sim$45 Å.[284] As stated in Section 4.1, the surface

roughness of the cushion supporting a membrane is critical, as defects present in the supporting substrate can exert direct topological effects on the membrane,[221,285] as well as affect membrane structural integrity and fluidity.[197,205] As such, the actin functionalized substrates were likely very good cushions for subsequent phospholipid depositions.

4.5 Actin Supported Membrane Results

With confirmation of uniform actin coverage on the cover glass, DMPC bilayers were successfully deposited via the LB/LS technique, as determined by the transfer ratio and visual observation with the microscope. The proximal leaflet was studied by z-scan FCS to assess the lateral diffusion of the lipids. The LB trough was prepared with an 18.2 MΩ·cm water subphase maintained at 15°, and 1 mg/mL DMPC and 0.0005 mol% RhoPE in 1 mg/mL DMPC in chloroform were prepared on the day of use. With the actin modified substrates held in the subphase, the LB and LS depositions were performed in the same manner as described for the chitosan coated substrates (Section 4.1). The completed bilayer was mounted in the sample cell, and diffusion of the lipids confirmed visually. Autocorrelation curves were measured over the same temperature range and analyzed as detailed in Section 4.1 for 3 separate, actin supported, proximal leaflet doped, DMPC membranes. The resultant mean diffusion coefficients were plotted with respect to temperature to produce the phase transition curve presented in Figure 4.16. The phase transition curves from the chitosan and glass supported DMPC membranes of Sections 4.1 and 4.2 have been included to aid comparison. The actin supported membrane phase transition curve was fit with Equation 4.1 to yield a phase transition temperature of 32.7±0.5°C, a value significantly higher than determined for DMPC proximal leaflets on chitosan (28.04°C) and glass (24.3°C). The distal leaflet of a DMPC

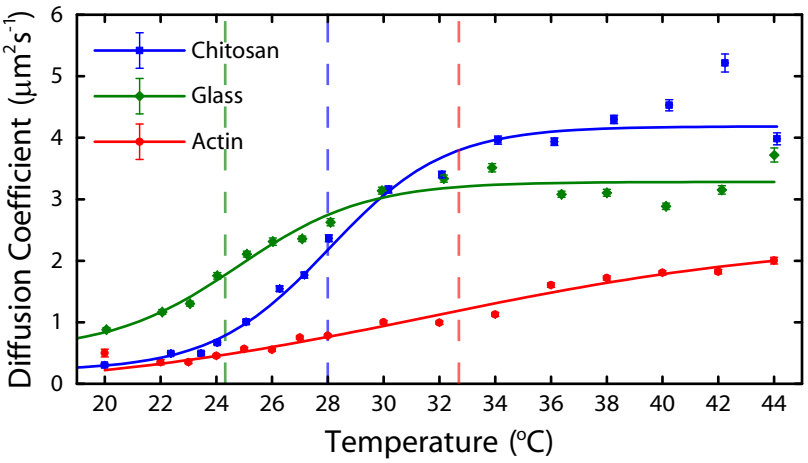

Figure 4.16. Comparison of actin, chitosan, and glass supported DMPC proximal leaflet phase transition curves. The diffusion coefficients are plotted with respect to temperature. There is a significant difference between the leaflet mobilities supported on the three substrates as indicated by the Boltzmann sigmoidal line fits. The resultant phase transition temperatures are 28.04°C, 24.3°C, and 32.7°C for the chitosan, glass, and actin substrates, respectively, as indicated by the dashed lines. The mean diffusion coefficients were determined by a weighted average and the error bars were determined by propagation of errors from the weighted fitting and averaging.

bilayer supported on actin was also studied by z-scan FCS, and the resultant phase transition temperature for the single bilayer was found to be within error of the proximal leaflet value.

The elevated phase transition temperature for DMPC proximal leaflets on actin substrates may be a result of the high anionic charge density of the actin layer. Actin is an anionic protein which has been shown to interact with charged lipids, in both the monomeric (G-actin) and polymeric forms (F-actin).[286–289] Additionally, liposomes have been shown to induce G-actin to form F-actin, a process that is charge dependent.[290] However, Le Bihan et al.[288] and separately, Bouchard et al.[287] have found that zwitterionic lipids, specifically DMPC, have very little interaction with actin *in situ*. Interaction between zwitterionic phospholipids and actin has been shown to be mediated by the presence of Mg^{2+}, resulting in binding of actin

to the phospholipids.[291,292] It is noted that in the present work, no Mg^{2+} was used in the preparation of the supports or phospholipids, however, Mg^{2+} was employed to polymerize the actin during preparation.[284] Mg^{2+} was removed by G-buffer and subsequent PBS washes of the actin solution, therefore, any phospholipid:actin interactions stemming from Mg^{2+} mediation should have been significantly decreased. Alternatively, the physical surface features of the actin substrate may potentially contribute to the elevated phase transition temperature. It is noted that while the ellipsometric results indicated a relatively uniform thickness, they do not provide detailed rms roughness values. As mentioned previously, surface roughness is strongly correlated with membrane mobility. Indeed, if there are chains of F-actin on the surface, the fluidity of the membrane may potentially be interrupted by penetration of F-actin filaments through the membrane.[277] The data obtained in the present work was further analyzed to probe the nature of diffusion via application of the submicron confinement model (Equation 4.3) by Dr. Edward Allgeyer in his Ph.D. thesis. Examination of the data indicates that t_0 is greater than zero at temperatures less than approximately 31°C, indicating diffusion hindered by rafts.[232] At temperatures greater than approximately 31°C, the proximal leaflet has t_0 values near zero, indicative of free diffusion.[232] The change in the phospholipid diffusion mode, that occurred at the measured phase transition temperature, for the actin supported membrane is similar to the results reported for the DMPC proximal leaflets on chitosan and glass (Sections 4.1 and 4.2). Indeed, the actin cushioned model membrane system reported in the present work is the first of its kind, and the diffusion of the phospholipids, hindered or not, lends ample support to its use in further studies.

4.6 Summary

The diffusion dynamics of three different planar supported DMPC membranes have been investigated via z-scan FCS, and their phase transition temperatures assessed. It was determined that the diffusion coefficients of each leaflet of the chitosan supported DMPC membranes, as a function of temperature, were comparable. The diffusion coefficients of the membrane leaflets were found to be higher than reported by similar studies, although it is noted that the measurements performed in the present work were made at a much lower fluorophore concentration and, as such, were likely of a less perturbed membrane system. The phase transition temperatures of the proximal and distal phospholipid leaflets were found to be nearly identical ($\sim$28°C) and within range of values reported in the literature for a similar chitosan supported DMPC membrane. Separately, the phase transition temperature of glass supported DMPC proximal leaflets were determined ($\sim$24°C) and found to be within range of values reported in the literature for similar glass supported DMPC membranes. The chitosan and glass substrates were employed to prepare supported acidic phospholipid membranes, an investigation which assessed a variety of fabrication variables. Specifically, the surface deposition pressure, hybrid membranes, mixed leaflet composition, alternate fluorophores, and multiple acidic phospholipids were investigated. Separately, a novel, physiologically relevant, actin supported DMPC membrane was developed and characterized. As with the chitosan and glass supported DMPC membranes, proximal leaflet diffusion dynamics were assessed with z-scan FCS, and the phase transition temperature was determined ($\sim$32°C). It is noted that the actin supported DMPC proximal leaflet phase transition temperature was extremely elevated relative to the chitosan and glass supported DMPC membranes. Finally, additional analysis of the diffusion mode as a function of temperature was performed for each of the supported DMPC proximal leaflets

and the chitosan supported distal leaflet. The analysis of each leaflet revealed that phospholipid diffusion changes from raft-like to free diffusion as the temperature approaches the phase transition temperature.

Chapter 5
SUM FREQUENCY SPECTROSCOPY OF CUSHIONED MODEL MEMBRANES

The z-scan FCS study of Chapter 4 provided detailed information regarding the dynamics of cushioned model membranes. The ability to correlate such data with the conformation of the phospholipids comprising the individual membrane leaflets would provide an unprecedented level of molecular characterization. Further, conducting FCS and SFS of model membranes would enable detailed investigation of FGF-1 translocation, furthering the work of Doyle et al.,[101] who demonstrated that FGF-1 induces *gauche* defects in hybrid bilayer membranes utilizing sum frequency spectroscopy (Section 1.5.3). To facilitate such capabilities, it was necessary to first reconfigure the Neivandt SF spectrometer for in-solution measurements, and to design and build a custom, temperature controlled, liquid flow cell. In addition to the spectrometer reconfiguration, a hybrid sum frequency spectral imaging and confocal fluorescence microscope was constructed. The novel microscope combines standard confocal fluorescence techniques with spatially correlated sum frequency spectroscopy spectral imaging.

5.1 Preliminary Sum Frequency Spectroscopy of Chitosan Supported Model Membranes

The following sum frequency spectroscopy work (Section 5.1) was performed at Hokkaido University's Catalysis Research Center in the laboratory of Dr. Shen Ye with the assistance of Dr. Yujin Tong. The objective of the collaboration was to establish the protocols and methods best suited for probing planar supported phospholipid membrane systems prior to reconfiguring the Neivandt SF spectrometer.

5.1.1 Sample Preparation

Spin cast chitosan films were created on gold coated slide glass and CaF_2 hemicylinder prisms. The slide glass (2.5 cm by 7.5 cm) was cut by etching and snapping into 2.5 cm by 1 cm pieces, and cleaned employing the protocol presented in Section 2.1.1, substituting Deconex (Borer Chemie AG, Switzerland) for Contrad 70. The slide glass was primed with an adhesive titanium layer, and then coated with $\sim$200 nm of gold (both deposited via evaporation in Dr. Ye's laboratory). The surface was functionalized by submerging the substrate in a 5 mM solution of carboxylic acid terminated thiol (3,3'-Dithiodipropionic acid, prepared in Dr. Ye's laboratory) in absolute ethanol (Wako, Osaka, Japan) (degassed by bubbling with N_2 for an hour) for at least 18 hours. The substrates were rinsed in ethanol and dried with N_2.

CaF_2 hemicylinder prisms employed as substrates for chitosan film deposition were cleaned according to the procedure described in Section 2.1.1. For selected experiments, the prism was coated with a thin SiO_2 film employing a sol-gel method[92] prior to bilayer deposition. Separately, chitosan films were prepared on CaF_2 prisms following the procedure outlined in Section 2.1.2 employing a Mikasa Spincoater (Tokyo, Japan).

All monolayers and bilayers prepared in the Ye laboratory were fabricated with perprotonated 1,2-dipalmitoyl-*sn*-glycero-3-phosphocholine (DPPC) and/or perdeuterated 1,2-dipalmitoyl-d62-*sn*-glycero-3-phosphocholine-1,1,2,2-d4 (d-DPPC) (Figure 5.1). DPPC was purchased from Sigma-Aldrich and d-DPPC was purchased from Avanti Polar Lipids. Both phospholipids were stored at -20°C until used. Stock solutions (4-10 mg/mL) were prepared with HPLC grade chloroform (Wako) which were subsequently diluted to a concentration of 1 mg/mL on the day of use. LB/LS deposition was employed to fabricate bilayers (LB for monolayers) utilizing

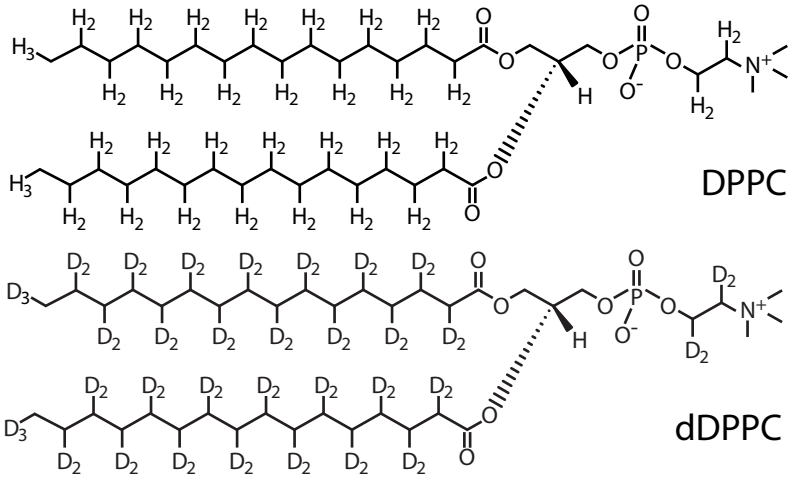

Figure 5.1. Molecular structures of perprotonated 1,2-dipalmitoyl-*sn*-glycero-3-phosphocholine (DPPC) and perdeuterated 1,2-dipalmitoyl-d62-*sn*-glycero-3-phosphocholine-1,1,2,2-d4 (d-DPPC).

a Langmuir-Blodgett trough (FSD-500, USI System, Japan). The trough contained a single Wilhelmy balance sensor, a mechanical dipper, and a single computer controlled barrier. Depositions were performed as described in Section 2.1.3 employing 18.2 MΩ·cm water maintained at 15°C as the subphase. The monolayer on the subphase surface was compressed to 32 mM/m. After 30 minutes of equilibration, LB depositions were performed at a dipper speed of 4 mm/min. LS depositions were performed utilizing a Teflon clamp, after thorough cleaning of the subphase surface, and spreading, compression, and equilibration of the second phospholipid solution. The resultant bilayer was maintained in the subphase until the time of use. Transfer ratios for the LB depositions were routinely unity (within error).

5.1.2 Instrumentation

The Ye SF spectrometer is a broadband system consisting of a tunable (nominally 800 nm), pulsed, 800 mW seed beam produced by a Ti:Sapphire oscillator (Mai Tai, Spectra Physics, Mountain View, CA) and a fixed, 527 nm, pulsed, 30 W pump beam produced by a frequency doubled Nd:YLF laser (Empower 30, Spectra

Physics, Mountain View, CA). Both beams enter a regenerative amplifier (Spitfire-Pro, Spectra-Physics, Mountain View, CA) that produces a pulsed (pulse width of approximately 120 fs), ∼2.25 mJ beam at a 1 kHz repetition rate. The output of the amplifier is split with approximately half delivered to a home-built spectral shaper[293] (TII, Tokyo, Japan) that employs a variable slit which narrows the spectral width while stretching the temporal pulse width into the picosecond regime. Standard output (Vis) from the spectral shaper is approximately 5 cm^{-1} (full width half maximum), or less, and the pulse width is ∼8 ps. Alternatively, a flip mounted mirror may be employed to divert this portion of the amplifier output to a tunable optical parametric amplifier (OPA) (TOPAS-white-NB, Light Conversion, Vilnius, Lithuania) to generate a narrow-band, tunable visible beam in the range of 250 to 1000 nm.[294] The remaining output from the amplifier is directed to a tunable OPA (TOPAS, Light Conversion) where it is converted to a tunable infrared pulse train (IR) (tunable from 2.5 to 10 μm wavelength). The IR and Vis beams were employed in a co-propagating geometry with input angles of 70° and 50° to the surface normal, respectively. The SF collection optics were aligned based on the emission angle predicted by conservation of momentum detailed in Equation 2.14, and the type of sample employed (e.g. flat gold coated substrate or hemicylinder prism). All emitted SF signal is focused into a monochromator (MS350li, Solar-TII, Minsk, Belarus) and collected by a CCD camera (DU420-BV, Andor Technology, Belfast, UK). Appropriate polarizers and halfwave plates are employed for each beam to manipulate the polarization as required. Figure 5.2 presents a schematic of the Ye spectrometer.

5.1.3 TIR-SFS of Phospholipid Monolayers and Bilayers

A DPPC monolayer deposited on a CaF_2 hemicylinder prism was employed to optimize the acquisition of total internal reflection (TIR) SF spectra. The SF spec-

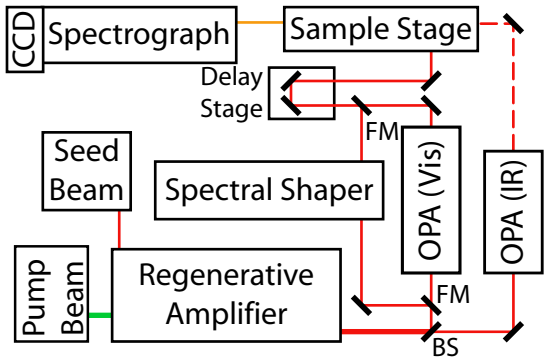

Figure 5.2. Schematic of the Ye spectrometer. BS indicates a 50/50 beamsplitter and FM indicates a flip mounted mirror.

trometer was aligned with the IR beam tuned to the C-H stretching region (2800-3100 cm^{-1}), and SF measurements were performed employing three polarization combinations, *ppp*, *ssp*, and *sps* (detailed in Section 2.2). The resultant spectra (presented in Figure 5.3) were normalized by the IR beam energy profile obtained by measuring the non-resonant background of a gold coated CaF_2 hemicylinder prism in the relevant wavenumber region (detailed in Section 2.2.3). It is noted that the peaks present in the spectra arose solely from the methyl group resonances of the phospholipid tails, a fact attributable to the DPPC monolayer being highly ordered. The spectra were fit (not shown) employing the custom LabView program detailed in Section 2.2.3.[232] The three peaks present in the *ppp* spectrum may be attributed to the symmetric methyl stretching mode (r^+, 2883 cm^{-1}), a Fermi resonance of the symmetric methyl stretching mode (r^+_{FR}, 2942 cm^{-1}), and the asymmetric methyl stretching mode (r^-, 2975 cm^{-1}). In contrast, the *ssp* spectrum is dominated by two peaks which are assigned as the r^+ (2889 cm^{-1}) and r^+_{FR} (2950 cm^{-1}) modes. The sole peak in the *sps* spectrum is assigned to the r^- mode (2975 cm^{-1}). As is clearly demonstrated by the spectra of Figure 5.3, select vibrational modes are enhanced when various polarization combinations are employed.[30]

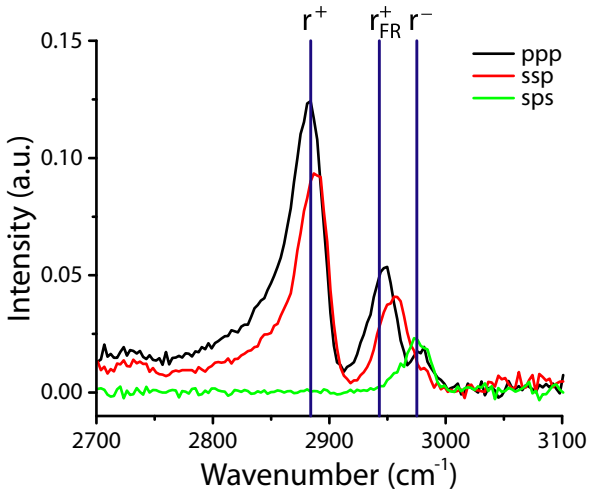

Figure 5.3. TIR-SF spectra of a DPPC monolayer. The monolayer was deposited on a CaF_2 hemicylinder prism. TIR-SF spectra were collected employing the *ppp*, *ssp*, and *sps* beam polarization combinations, and were normalized to the IR beam energy profile. The SF intensity has arbitrary units (a.u.).

Having demonstrated the capability of measuring SF spectra of phospholipid monolayers, the work was extended to an asymmetric bilayer. Specifically, an asymmetric d-DPPC/DPPC bilayer was fabricated on a silica coated CaF_2 hemicylinder prism (the silica was employed to create a surface amenable to bilayer deposition).[85] A d-DPPC monolayer was deposited via the LB method, subsequently a DPPC was deposited via LS deposition. The substrate was maintained in the subphase while it was mounted in a custom temperature-controlled liquid cell. SF spectra were collected in the C-H stretching region and separately, in the C-D stretching region (2000-2300 cm^{-1}). It is noted that the SF excitation beam angles were not adjusted for the bilayer SF measurements, therefore the Vis excitation beam was not in a TIR geometry and was refracted into solution. It is noted that it has been reported that TIR-SF spectra may still be collected employing a geometry in which the IR excitation beam is close to the critical angle and the Vis excitation beam is far from the critical angle and therefore refracting.[231] The two spectral regions were probed by changing the wavelength of the IR beam (via adjustment of the output of the

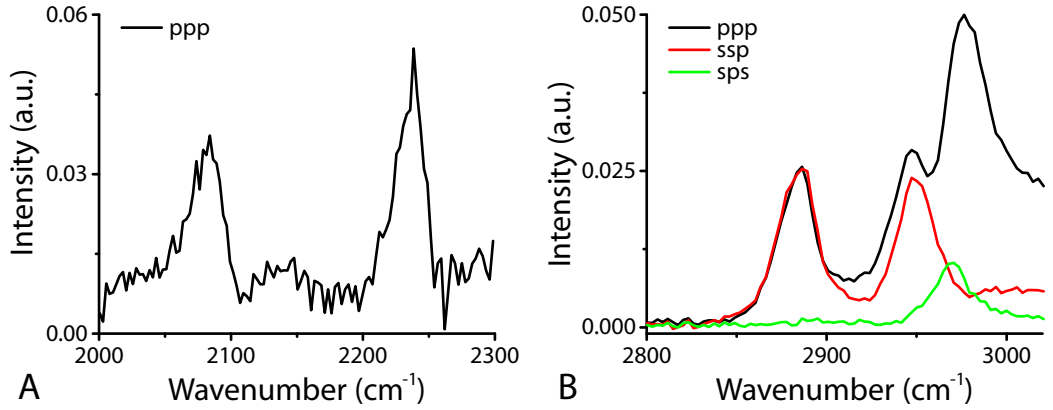

Figure 5.4. TIR-SF spectra of an asymmetric bilayer. The proximal and distal leaflets, deposited by the LB/LS technique on a CaF_2 hemicylinder prism, were d-DPPC and DPPC, respectively. **A** was collected in the C-D stretching region employing the *ppp* beam polarization combination. **B** was collected in the C-H stretching region employing the *ppp*, *ssp*, and *sps* beam polarization combinations. Spectra were normalized to the IR beam energy profile for their respective stretching regions. The SF intensity has arbitrary units (a.u.).

OPA). Figure 5.4 presents the relevant spectra, normalized to the IR beam energy profile. The acquisition time for the C-D stretching region spectrum (Figure 5.4A) was approximately 5 minutes versus that for the C-H stretching region spectrum (1 minute) due to the weaker OPA output in the C-D stretching region. Additional spectra in the *ssp* and *sps* beam polarization combinations were collected in the C-H stretching region (Figure 5.4B).

In order to determine the sensitivity of the SF spectra to membrane perturbation, the effect of temperature was explored by collecting short (20 second), consecutive SF spectra as the temperature was increased from 24°C to 40°C. Selected non-normalized *ppp* beam polarization combination spectra are presented in Figure 5.5. Shading has been added to indicate the spectral regions associated with methyl and methylene resonances.[30,85,232] It is evident from investigation of Figure 5.5 that spectra collected at low temperatures display strong methyl resonances arising from the proximal DPPC leaflet. As the temperature increased, the methyl resonances weakened, and methylene resonances became apparent. The change in the relative

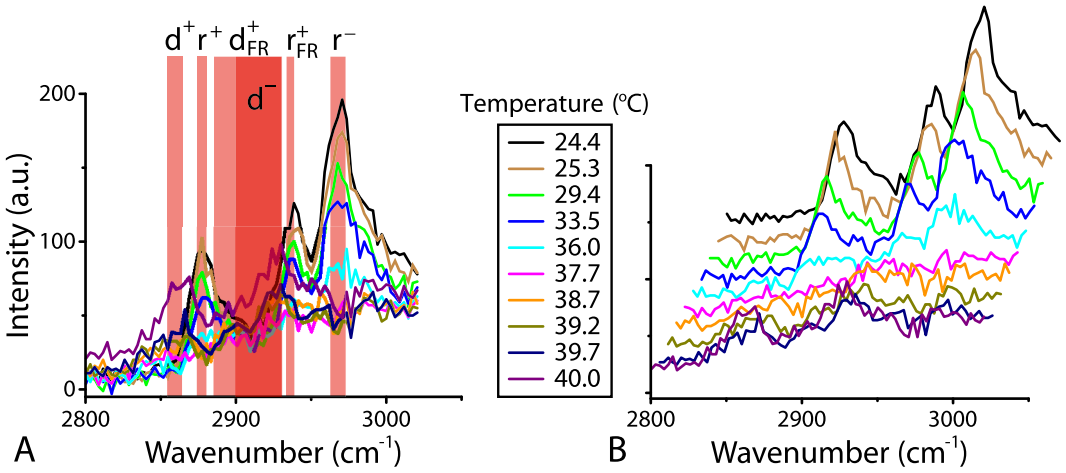

Figure 5.5. Temperature dependence of TIR-SF spectra of asymmetric bilayers. The bilayers were deposited on CaF_2 hemicylinder prisms. **A** and **B** contain the same data (non-normalized); **B** is offset for clarity. Shading in **A** indicates the range of peak assignments found in selected literature.

peak intensities of the methyl and methylene resonances with temperature implies the introduction of *gauche* defects into the alkyl chains of the phospholipids[97] as the temperature was increased.[81,85] The sensitivity of the SF spectra to moderate temperature changes demonstrates the utility of SFS in the study of membrane structure and conformation.

5.1.4 TIR-SFS of Chitosan and Phospholipids

Since chitosan contains methylene groups in its molecular structure, its use as a bilayer support required characterization of its SF activity. As such, chitosan films were spin cast on CaF_2 hemicylinder prisms following the procedure outlined in Section 2.1.2. TIR-SF spectra were subsequently recorded in air in the C-H stretching region, employing the *ppp*, *ssp*, and *sps* beam polarization combinations (Figure 5.6A). The normalized *ppp* and *ssp* spectra were fit with 2 peaks (not shown).[295] For the *ppp* spectrum, the symmetric methylene stretching mode (d^+) appeared at 2861 cm^{-1}, while the symmetric methylene stretching Fermi resonance mode (d^+_{FR}) occurred at 2929 cm^{-1}. The two peaks in the *ssp* spectrum may also be assigned

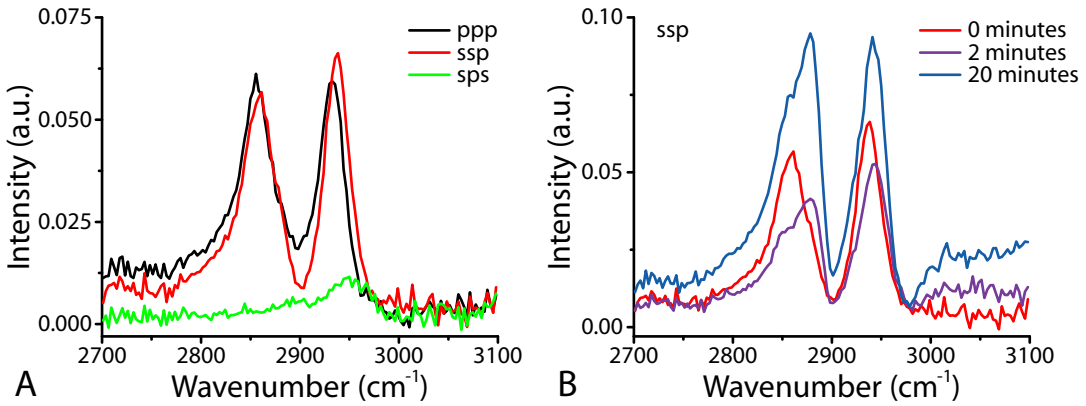

Figure 5.6. TIR-SF spectra of chitosan films. The chitosan films were spin cast on CaF_2 hemicylinder prisms. TIR-SF spectra were collected employing the *ppp*, *ssp*, and *sps* beam polarization combinations in **A**. **B** presents *ssp* spectra collected in air after soaking the prism in 18.2 MΩ·cm water for 2 minutes and 20 minutes. The spectra were normalized to the IR beam energy profile. The SF intensity has arbitrary units (a.u.).

to the d^+ (2863 cm^{-1}) and d^+_{FR} (2934 cm^{-1}) modes, while the sole peak in the *sps* spectrum may be assigned to the d^- mode (2950 cm^{-1}). In order to assess the affect of hydrating the chitosan film, the prism was immersed in 18.2 MΩ·cm water for 2 minutes, and separately, for 20 minutes, each time period followed by collection of an *ssp* beam polarization combination spectrum of the film in air (Figure 5.6B). It is noted that while little affect on intensity occurred with short duration hydration, a subsequent increase occurred on extended hydration. Further, while the d^+_{FR} peak remained in the same position for each spectrum, there was either a resonance shift or shoulder that occurred for the d^+ mode. The blue-shift/shoulder may potentially be attributed to rearrangement of the polymer chains as the film changed from the dry to the swollen state, possibly creating multiple interfaces. Alternatively, frequency shifts occurring upon changes in the medium (e.g. air to water) are expected from the literature, although such changes typically occur to various extents for all resonances.[70,296]

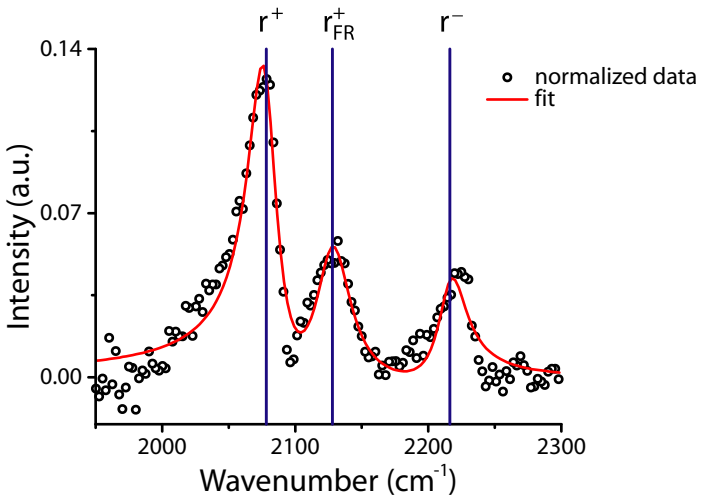

Figure 5.7. TIR-SF spectra of a d-DPPC monolayer on chitosan in air. The monolayer was deposited via the LB technique onto a chitosan coated CaF_2 hemicylinder prism. The *ppp* beam polarization combination spectrum was normalized to the IR beam energy profile in the C-D stretching region.

Subsequently, chitosan coated CaF_2 hemicylinder prisms were employed for LB deposition of d-DPPC monolayers. The substrates were mounted in a custom liquid cell permitting fluid flow across the sample. Figure 5.7 presents a normalized *ppp* beam polarization combination TIR-SF spectrum of a d-DPPC monolayer in air supported on a chitosan coated CaF_2 hemicylinder prism collected in the C-D stretching region. Investigation of Figure 5.7 reveals that the spectrum contains three peaks attributable to the vibrational modes of the perdeuterated methyl groups of d-DPPC. It is noted that chitosan does not have SF active components in the C-D stretching region, and therefore does not contribute to the spectrum of Figure 5.7. Specifically, the three resonances at 2078 cm^{-1}, 2128 cm^{-1}, and 2216 cm^{-1} correspond to the r^+, r^+_{FR}, and r^- vibrational modes of the perdeuterated methyl resonances of the d-DPPC, respectively.[66]

Finally, preliminary measurements of an asymmetric d-DPPC/DPPC bilayer were attempted on a chitosan coated CaF_2 hemicylinder prism in water. The proximal and distal leaflets were composed of d-DPPC and DPPC, respectively. The

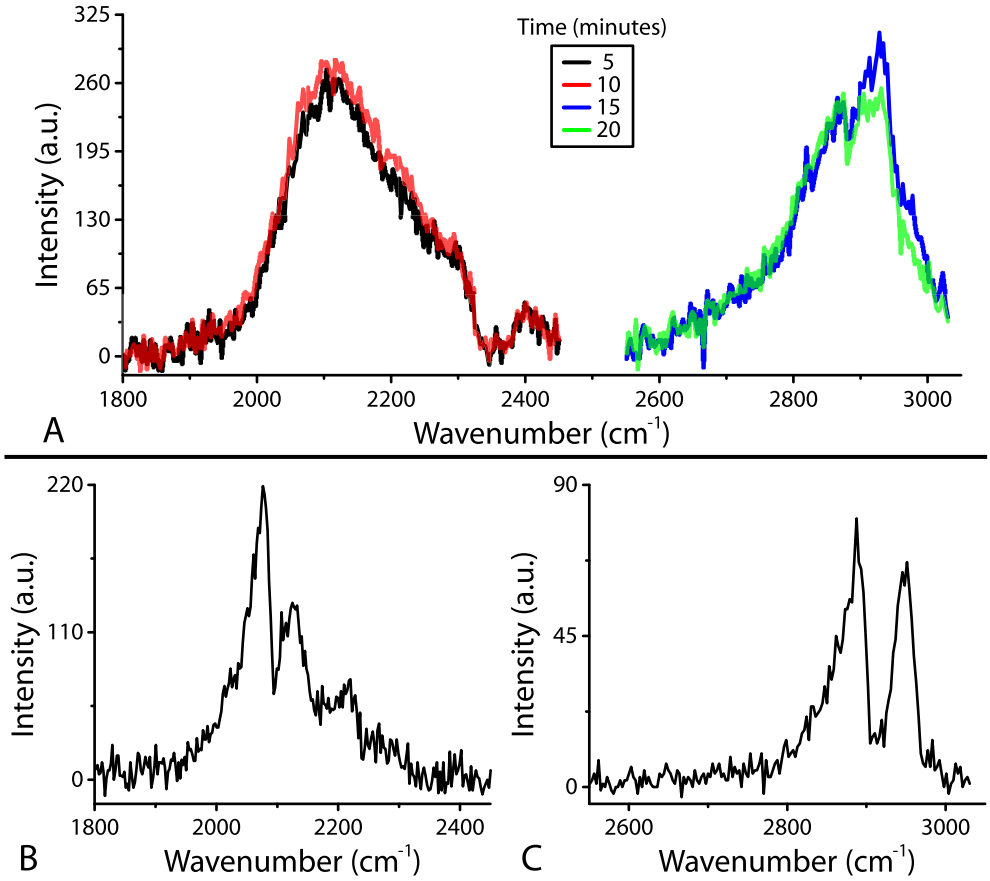

Figure 5.8. TIR-SF spectra of an asymmetric bilayer on chitosan. The bilayer was deposited via the LB/LS technique onto a chitosan coated CaF_2 hemicylinder prism. **A** presents non-normalized *ppp* beam polarization combination spectra collected in water in the C-D and C-H stretching regions over the course of 20 minutes (5 minute acquisition time for each spectrum). Post-drying (48 hours) spectra were collected in air in the C-D (**B**) and C-H (**C**) stretching regions.

substrate was maintained in the subphase as it was mounted into the liquid cell. SF spectra were recorded, in both the C-D and C-H stretching regions, the non-normalized *ppp* beam polarization combination spectra are presented in Figure 5.8A. The sample proved to be relatively SF inactive, with individual resonances being indistinguishable due to an unknown background signal. Although the SF measurements were recorded at a temperature (23°) well below the phase transition temperature of DPPC (41°C[241]), it was believed at the time, that the bilayer may have undergone the 'flip-flop' phenomenon described by Liu and Conboy.[85] The

'flip-flop' phenomenon is the movement of phospholipids from one membrane leaflet to the other.[85] For the asymmetric bilayers in the present work, redistribution of the perdeuterated and perprotonated phospholipids by 'flip-flop', such that each leaflet contained both phospholipids, would have created inversion symmetry and therefore, the individual phospholipid leaflets would no longer have been SF active.

Subsequently, the substrate was removed from the liquid cell, permitted to dry for 48 hours, and SF measurements in air were then recorded. The resultant *ppp* beam polarization combination SF spectra, collected in the C-D and C-H stretching regions, are presented in Figure 5.8B and C. Spectra in the C-D stretching region (Figure 5.8B) displayed strong resonances at 2076 cm^{-1}, 2124 cm^{-1}, and 2216 cm^{-1}, attributed to the r^+, r^+_{FR}, and r^- modes, respectively. The SF active modes in the C-H stretching region (Figure 5.8C) are likely attributed to the SF active methylene resonances (d^+ and d^+_{FR}) of chitosan as previously detailed. It is noted that the observation of methyl resonances in Figure 5.8B suggests that the d-DPPC leaflet distribution remained relatively intact, and hence, the 'flip-flop' phenomenon was not the source of the indistinguishable resonances in the aqueous phase (Figure 5.8A).

5.2 The Neivandt Sum Frequency Spectrometer

The work of Section 5.1 determined the SF spectrometer infrastructure required at the University of Maine for measurements of phospholipid bilayers. Rather than simply replicating existing SF spectrometers, the Neivandt SF spectrometer was rebuilt to facilitate the development of a custom hybrid sum frequency spectral imaging and confocal fluorescence microscope (detailed in Section 5.4), the first such instrument constructed. The SF spectrometer base infrastructure was already in existence, and with the purchase of a new tunable optical parametric amplifier

(OPA) (Topas-C), reconstruction of the Neivandt system commenced. The components and layout of the Neivandt spectrometer have been described in Section 2.2.2. An extensive presentation of the Neivandt spectrometer reconstruction may be found in the Ph.D. thesis of Edward S. Allgeyer.[232] As such, the overview presented herein will focus on methods to facilitate SF measurements of phospholipid bilayers and critical maintenance and alignment procedures determined during the course of the reconstruction and optimization.

5.2.1 Alignment Procedure

With the SF spectrometer infrastructure in place, achievement of spatial and temporal overlap of the two excitation beams was essential for the collection of SF spectra. The spatial overlap of the excitation beams was assessed first, and for safety reasons, was achieved with three visible alignment lasers (depicted in Figure 5.9). To employ the visible alignment lasers, the Vis and IR beams were aligned to their respective sets of reference irises (denoted by A in Figure 5.9) and the outputs from the spectral shaper and OPA were subsequently blocked. Subsequently, two Helium-Neon (HeNe) lasers, at wavelengths of 633 nm and 542 nm, were aligned to the Vis and IR beam iris sets, respectively. Alignment to the sample stage was achieved solely with the alignment lasers. The Vis and IR beams were aligned to input angles of 60° and 65° to the surface normal, respectively, in accordance with previous values.[223,296] The SF emission collection optics were aligned employing a 473 nm diode alignment laser. The SF alignment laser was configured to mimic the SF beam emitted from the sample at an angle predicted by conservation of momentum (Equation 2.14). Variation of the alignment procedure occurred due to changes in the input angles, and the type of substrate employed (e.g. flat gold coated silicon or hemicylinder prism). A detailed alignment procedure is provided in the standard operating procedure of the Neivandt SF spectrometer, Appendix B.

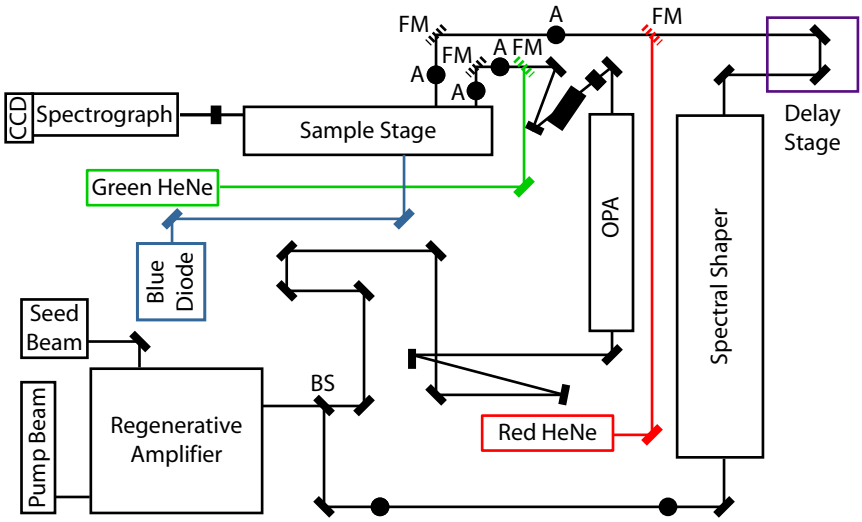

Figure 5.9. Schematic of the Neivandt SF spectrometer. The schematic presents the visible alignment lasers (Green and Red HeNe lasers and a blue diode laser). BS indicates the 70/30 beamsplitter and FM indicates flip mounted mirrors. The schematic is not to scale.

Temporal overlap of the excitation beam pulses required that the optical path length from the beamsplitter at the output of the regenerative amplifier to the sample stage was identical for the two beams. The path length within the spectral shaper is considerably longer than that of the OPA, therefore the input beam to the OPA was passed through a delay line. Fine tuning of the temporal overlap was performed by adjusting the Vis beam path length via a computer controlled delay line composed of two mirrors on a translation stage (NRT100, Thorlabs, Newton, NJ).

5.2.2 Standard SFS Sample Preparation

To assess the spatial and temporal alignment of the SF spectrometer, short (acquisition ~1 second), consecutive SF spectra from a gold coated silicon wafer were monitored as final alignment was performed. As stated in Section 2.2, a large non-resonant signal is generated from a gold substrate, such substrates consequently serve as excellent alignment tools. In addition, an SF spectrum of a gold substrate

is employed to normalize spectra for the IR beam energy profile during spectral processing, and as such, must be measured. To ensure that the OPA is tuned to the spectral region of interest (e.g. C-H or C-D stretching region), SF spectra of robust, tightly-packed, self assembled monolayers (SAMs) of octadecane thiol are typically collected. Monolayers of 1-octadecanethiol (ODT) (Sigma-Aldrich, St. Louis, MO) and separately, 1-octadecane-d37-thiol (d-ODT) (C/D/N Isotopes, Pointe-Claire, Quebec, Canada) were prepared on separate gold coated silicon wafers. Specifically, 5 mM solutions of each thiol were prepared in ethanol (200 proof, Sigma-Aldrich), and clean (procedure of Section 2.1.1), gold coated silicon wafers were submerged in the ODT and d-ODT solutions for at least 24 hours. Substrates were subsequently rinsed with, and stored in, ethanol. Immediately prior to SF measurements, substrates were removed from ethanol storage, and dried with N_2. Figure 5.10 presents raw and normalized *ppp* beam polarization combination SF spectra of ODT and d-ODT on gold coated silicon wafers in their respective regions of interest. The normalized spectra were fit as discussed in Section 2.2.3. Each spectrum was fit with 3 peaks corresponding to the r^+, r^+_{FR}, and r^- methyl stretching modes as indicated in Figure 5.10C and D. The specific peak assignments were 2067 cm^{-1} (r^+), 2126 cm^{-1} (r^+_{FR}), and 2214 cm^{-1} (r^-) for the d-ODT spectrum, and 2874 cm^{-1} (r^+), 2934 cm^{-1} (r^+_{FR}), and 2961 cm^{-1} (r^-) for the ODT spectrum.

5.2.3 General Spectrometer Maintenance

There are a variety of nuances associated with the maintenance of an SF spectrometer, and the Neivandt spectrometer is no exception. The temperature and humidity of the room containing the spectrometer should be monitored on a daily basis, as should the fluid level, temperature, flow rate and/or pressure of the chillers. Fluctuations in temperature and humidity may lead to alignment issues and clouding of optics such as diffraction gratings, while changes in chiller settings may lead

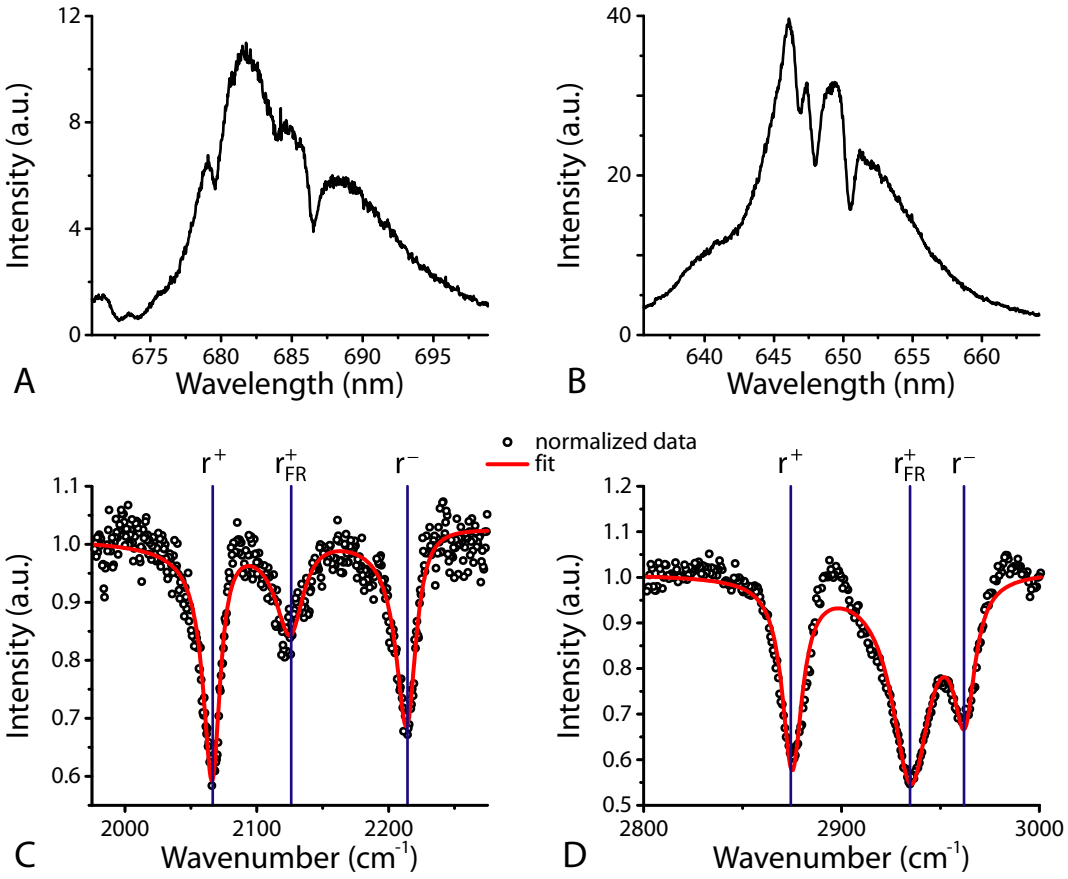

Figure 5.10. Raw and normalized SF spectra of ODT and d-ODT. ODT and d-ODT self assembled monolayers were prepared on gold coated silicon wafers. Spectra were collected in the *ppp* beam polarization combination. **A** and **B** are the raw spectra of d-ODT and ODT, respectively. **C** and **D** are the normalized and fit spectra of d-ODT and ODT, respectively. Peak assignments are presented in the text.

to leaks or overheating of components. Additionally, the fluid in the chillers should be changed periodically to reduce build-up of debris and/or undesired algal growth. This is of particular importance for the Empower laser since the chiller solution flows around the lasing medium. As such, turbidity of the chiller solution will reduce the pump efficiency and possibly lead to overheating and irreversible damage.

General alignment issues of the SF spectrometer components may be remedied by procedures outlined in the relevant user manuals, under the guidance of a technician in some cases. Alignment of optical components on the table may be addressed

by employing the standard operating procedure provided in Appendix B. Most optics of the SF spectrometer may be cleaned by blowing with an inert gas. For more rigorous cleaning, a lens paper saturated with acetone, methanol, or isopropyl alcohol may be wiped across the surface to remove particulates. The solvent selection depends upon the optic surface or coating, however, for the dielectric mirrors and protected metallic (gold or silver) mirrors of the Neivandt SF spectrometer, each solvent is appropriate for cleaning. Other optics, such as diffraction gratings, require a passive cleaning method that should only be employed after consultation with a technician. Specifically, diffraction gratings may be cleaned by soaking in a dilute sodium dodecyl sulfate (SDS) (Sigma-Aldrich) solution in distilled water. In order to perform such a cleaning, a 1 mM solution of SDS in distilled water is prepared. The diffraction grating should subsequently be placed in a clean vessel, submerged in distilled water, and one drop of the 1 mM SDS solution added for each 150 mL of distilled water employed. The vessel should be gently swirled and the diffraction grating left to soak for 1-24 hours. The diffraction grating should be rinsed by flowing distilled water into the vessel until no SDS bubbles form, and the grating should subsequently be dried with N_2.

5.3 Sample Stage Reconstruction

To facilitate the study of cushioned phospholipid bilayers via SFS, modification of the Neivandt SF spectrometer sample stage was necessary in order to accommodate a hemicylinder prism. Further, the hemicylinderical prism was required to be maintained in a liquid flow cell with temperature control capabilities. In addition, the prism, flow cell, and temperature control apparatus had to be mounted on x, y, and z translation stages fit with a goniometer, to achieve accurate sample position-

ing and ready manipulation at the center of rotation. The fabrication described in the following sections was performed by Mr. Amos Cline.

5.3.1 Temperature Control Stage

A custom temperature control stage was designed and fabricated. The base of the temperature control stage comprised a 100x65 mm stainless steel (SS) plate. A dovetail mount consisting of two pins and one tail, compatible with the goniometer, was affixed to the bottom of the base plate. Six clearance holes were drilled in the base plate to accommodate two sets of three 6-32 SS screws to attach the SS dovetail pins. One pin was the same thickness as the tail of the dovetail mount, while the second pin was thinner and wider to allow for a locking mechanism. The SS tail of the dovetail mount was drilled with three clearance holes to match the M6 mounting holes of the goniometer. With the tail attached to the goniometer and the pins attached to the base plate, the stage was slid into place on the goniometer. To lock the base plate onto the goniometer, a bar was tightened on the side of the base plate to hold the dovetail mount flush. Figure 5.11A presents the base of the temperature control stage affixed to the goniometer, with the asymmetric pins and locking bar.

A SS leveling plate (75x65 mm) was fabricated to adjust the tilt and height of the stage to match the goniometer center of rotation. Four clearance holes were drilled in the leveling plate to mount it to the top of the base plate. A second set of four clearance holes were drilled in the leveling plate to accommodate low profile SS 6-32 screws for attachment of four nylon washers and spacing posts to the top of the leveling plate. A third set of four adjacent holes were drilled and tapped in the leveling plate for four additional SS screws to act as adjustment points. To adjust the tilt or height of the stage, the leveling plate mounting screws were loosened to allow manipulation of the adjustment screws and hence, control the leveling plate

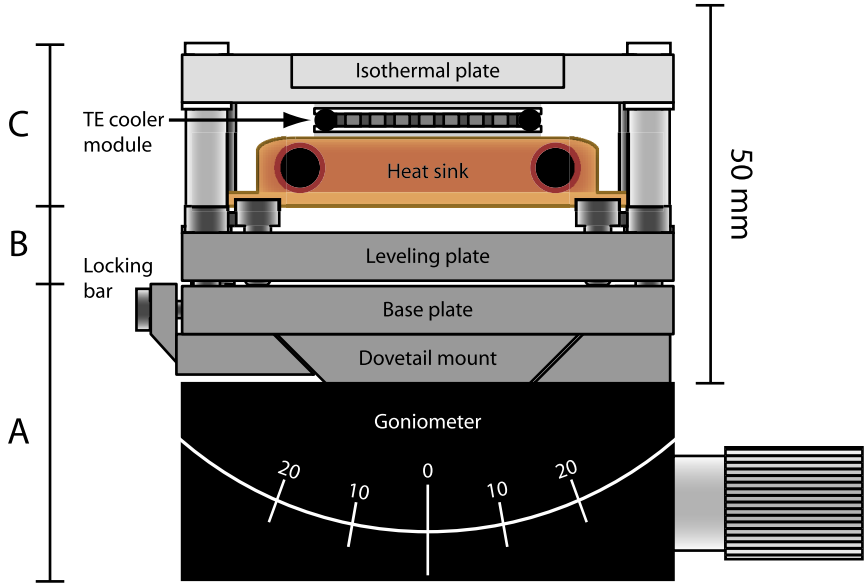

Figure 5.11. Temperature control stage schematic, front view. **A** presents the base plate mounted and secured on the goniometer with the dovetail mount and locking bar. **B** presents the leveling plate and adjustment screws. **C** presents the spacing posts, the isothermal plate, TE cooler module, and heat sink. The mounted thermistor is obscured by the heat sink in the front view. The insulation, tubing, and wire connections have been omitted for clarity.

position. The leveling plate mounting screws were subsequently tightened to set the stage position. Figure 5.11B presents the leveling plate attached to the base plate.

Spacing posts between the leveling plate and the isothermal plate accommodate a Peltier-thermoelectric (TE) cooler module, in addition to a heat sink. The TE cooler module (HP-127-1.0-0.8, TE Technology, Traverse City, MI) was sandwiched between a copper, liquid heat sink (CL-W0088, Thermaltake Technology, Taipai, Taiwan) and an aluminum (65x65 mm) isothermal plate (Figure 5.11C). Conductive thermal pads (Intermark Inc., San Jose, CA) were employed to fill air gaps between each component, thereby increasing the efficiency of heat transfer from the TE cooler module to the heat sink and the isothermal plate. The heat sink/TE cooler module was mounted to the base of the isothermal plate with nylon washers and SS screws. A thermistor (MP-2996), with a conductive thermal pad, was mounted to the base

of the isothermal plate to monitor and provided feedback regarding the temperature of the plate. Exposed portions of the TE cooler module, thermistor, and base of the isothermal plate were covered with insulation (omitted from Figure 5.11 for clarity) to reduce temperature fluctuations induced by the heat sink. Finally, employing four clearance holes, the isothermal plate was mounted to the four spacing posts with nylon screws to reduce heat transfer between the isothermal plate and the base of the unit.

The liquid heat sink was connected to a circulating liquid cooler (BigWater 780e ESA, Thermaltake Technology) via chemical-resistant clear Tygon tubing with in-line quick-disconnect tube couplings. Thermaltake's Coolant 1000 (CL-W0148), which consists primarily of water and propylene glycol, served as the circulating liquid. The cooling unit was packaged in a computer tower case which served as a power supply and protection unit. The computer case also housed a proportional-integral-derivative (PID) controller (TC-36-25 RS232, TE Technology) to regulate the temperature of the TE cooler module and isothermal plate. The TE cooler module and thermistor were wired to a connector mounted on a circuit board attached to the base plate of the temperature control stage. The connector was wired to the PID controller and subsequentially to a laboratory computer. Software provided by TE Technology was utilized to adjust the PID settings and hence control the isothermal plate to a given temperature within a tenth of a degree Celsius. Accuracy of the temperature was confirmed by adjusting the set point over a wide temperature range (14-44°C), and independently measuring the temperature of the isothermal plate with a thermocouple and separately, a thermometer in a beaker of water on the isothermal plate.

5.3.2 Hemicylinderical Prism Liquid Flow Cell

All components of the liquid flow cell were fabricated from stainless steel (SS) and corrosive resistant materials to allow for thorough cleaning as detailed in Section 2.1.1. The liquid cell consisted of a SS base (40x40x6.5 mm) with a 22 mm diameter pocket milled in the center. The depth of the pocket was such that a fluorinated ethylene propylene (FEP)-encapsulated Viton o-ring (19 mm inner diameter, 22 mm outer diameter, 93445K018, McMaster-Carr, Robbinsville, NJ) was compressed by $\sim$5% when the hemicylinder prism was secured. FEP is a pliable and corrosion resistant alternative to PTFE (polytetrafluoroethylene, Teflon). The top, hemicylinder clamping, portion of the liquid cell was a custom machined SS piece designed to secure the ends of the prism while providing the maximum possible area for SF excitation and emission beams. The top portion of the sample cell attached to the base utilizing four 4-40 SS screws. The entire sample cell was secured to the isothermal plate of the temperature control stage via two additional 4-40 SS screws through two clearance holes. Figure 5.12 presents an exploded diagram of the liquid flow cell. It is noted that the corners of the top and base are notched to facilitate registration and hence, correct assembly of the flow cell.

To enable liquid flow across the face of the hemicylinder prism, two ports were drilled into the base of the liquid cell. Two holes adjoining the ports were drilled and tapped in the side of the base to accommodate two chlorotrifluoroethylene (CTFE) internal 10-32 nuts and PTFE ferrules (VICI Valco Instruments, Houston, TX). The internal nut and ferrule were selected to accommodate 1.6 mm (1/16") outer diameter PTFE tubing (VICI Valco Instruments, Houston, TX). The tubing could be connected to an adapter with a Luer lock port to enable syringe injection into the liquid cell. Alternatively, the tubing could be coupled to a peristaltic pump for continuous liquid flow. If desired, the ports could be closed off by connecting the

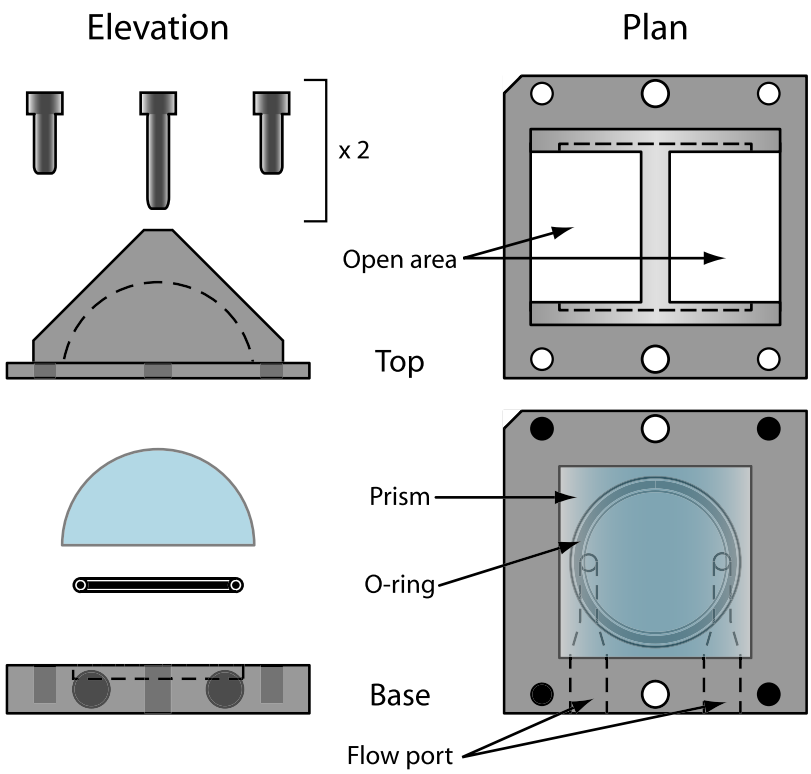

Figure 5.12. Liquid flow cell schematic, elevation and plan views. Elevation view: An o-ring sits in a pocket of the base, indicated by a dashed line, and a hemicylinder prism sits on the o-ring. The top slides down over the prism, and is secured to the base with 4-40 screws. Plan view: The top of the liquid cell has open areas to allow the SF beams to pass through, the dashed lines indicate the prism position. The base has two ports (indicated by dashed lines) to permit liquid flow across the prism face. Both the top and base have clearance holes to allow for rotation of the liquid cell on the temperature control stage.

tubing to stainless steel caps, or by replacing the internal nut, ferrule and tubing with 10-32 plugs (VICI Valco Instruments).

5.3.3 TIR-SFS of Phospholipid Monolayers and Bilayers

The performance of the temperature control stage and the liquid flow cell were evaluated by the collection of SF spectra of phospholipids deposited on the prism face. SF measurements of monolayers deposited directly on the prism surface were collected in air in the TIR geometry with the Vis and IR excitation beams set to input angles to the surface normal of 60° and 65°, respectively. The input angles

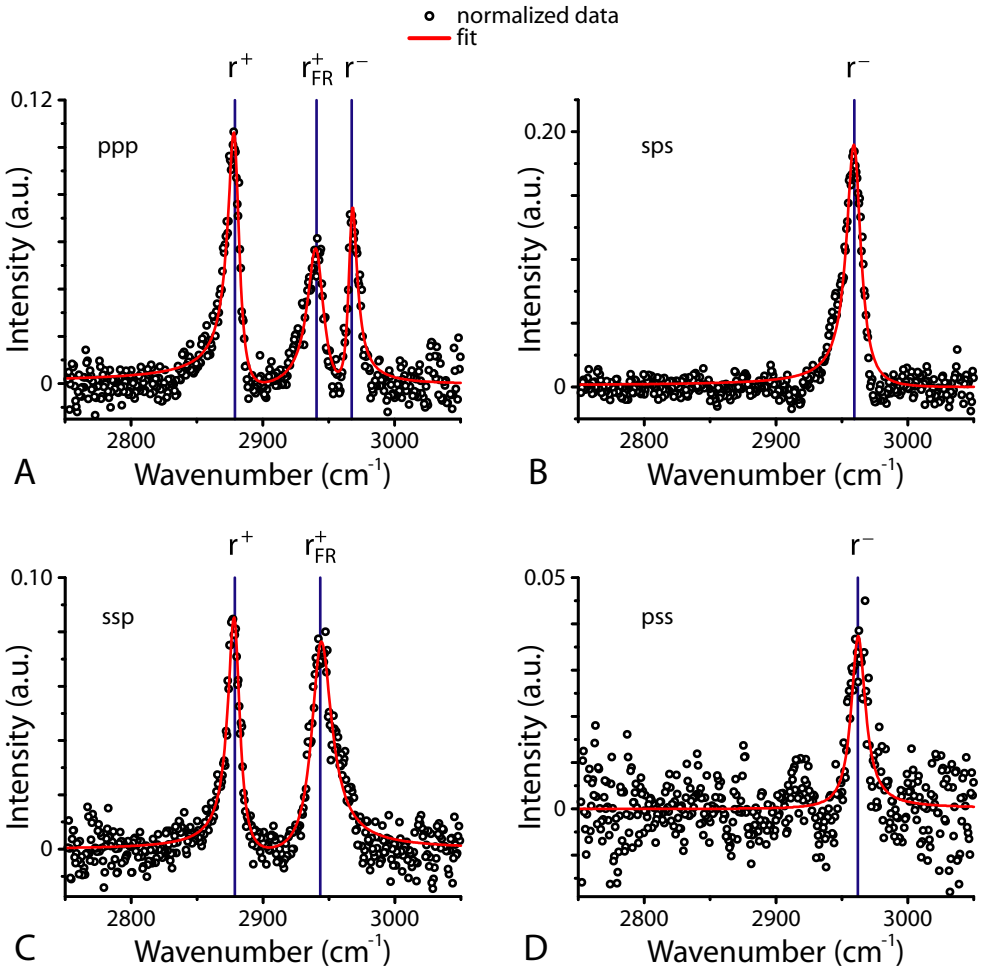

Figure 5.13. TIR-SF spectra of a DMPC monolayer in air. The monolayer was deposited via the LB technique onto a CaF_2 hemicylinder prism. Spectra were collected for the *ppp*, *ssp*, *sps*, and *pss* beam polarization combinations (**A**, **C**, **B**, and **D**, respectively), and were normalized to the IR beam energy profile. The peaks in the spectra have been assigned to their corresponding methyl resonances.

selected were greater than the critical angles calculated for each excitation beam incidental upon the CaF_2/air interface (Vis: $\theta_C = 44°$, IR: $\theta_C = 45°$). As such, each beam reflected from the face of the prism, generating an evanescent wave in the optically rarer medium (air), thus probing the phospholipids at the interface (detailed in Section 2.2.2).

A DMPC monolayer was deposited on a CaF_2 hemicylinderical prism following the procedure outlined in Section 2.1.3. TIR-SF spectra, presented in Figure 5.13,

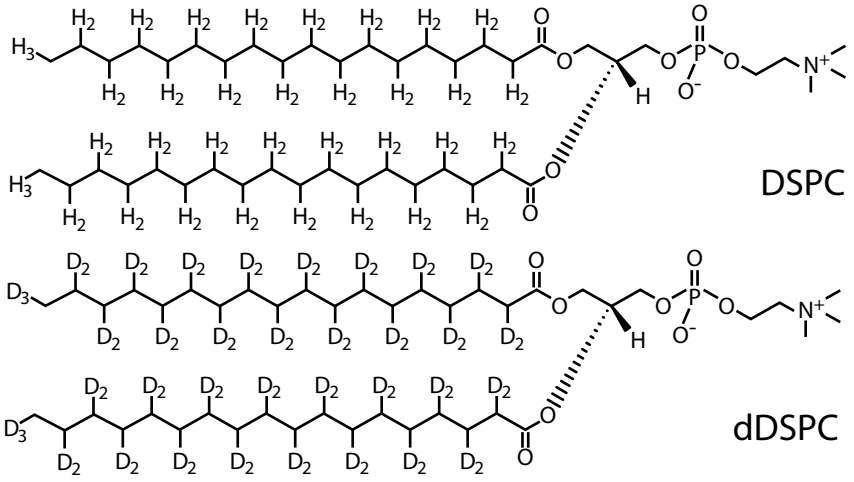

Figure 5.14. Molecular structures of 1,2-distearoyl-*sn*-glycero-3-phosphocholine (DSPC) and perdeuterated 1,2-distearoyl-d70-*sn*-glycero-3-phosphocholine (d-DSPC).

were collected in the C-H stretching region employing the *ppp*, *ssp*, *sps*, and *pss* beam polarization combinations. The peaks in the spectra may be assigned solely to the methyl groups terminating the alkyl chains of phospholipids comprising the monolayer. Specifically, the three peaks at 2875 cm^{-1}, 2936 cm^{-1}, and 2962 cm^{-1} in the *ppp* spectrum may be assigned to the r^+, r^+_{FR}, and r^- modes, respectively. The *ssp* spectrum has two resonances assigned to the r^+ and r^+_{FR} modes. A single peak is present in the *sps* and *pss* spectra, and is assigned to the r^- resonance.

The fact that solely methyl resonances were evident in the spectra of Figure 5.13 indicates that the methylene groups of the alkyl chains were highly ordered and therefore in a centrosymmetric and non-SF active environment. This finding implies that a highly ordered DMPC monolayer was deposited on the prism face. Clearly, the quality of the SF spectra also infers that the alignment of the SF spectrometer in the TIR geometry was correct and well optimized. It is noted that alignment of the hemicylinder prism requires more precision than that necessary for a reflective sample (e.g. a gold coated silicon wafer) as there is no strong non-resonant background to guide optimization of the alignment. To ensure that the

prism is properly positioned, the back reflection of the IR alignment beam may be employed as follows: with the prism set on the sample stage, a portion of the IR alignment beam is reflected from the curved surface of the prism, the back reflection of the IR alignment beam may be observed by blocking part of the input beam with an index card. The IR alignment input beam and back reflection should be overlapped by adjusting the position of the prism. The clearance holes on the sides of the liquid cell (Figure 5.12) allow for slight rotation to aid the back reflection alignment.

For SF measurements of the prism/water interface (required for measuring a phospholipid bilayer on the prism surface), the excitation beam angles required adjustment from those employed for the prism/air interface, due to modification of the critical angles (Vis: $\theta_C = 69°$, IR: $\theta_C = 68.5°$). Rather than changing the excitation geometry of the SF spectrometer, the goniometer was simply adjusted by 10° to accomplish the change; such a method maintained spatial overlap of the excitation beams and was rigid and effective. It is noted, however, that the SF emission pathway required adjustment. In order to demonstrate that successful bilayer fabrication was not specific to the phospholipid pair selected, asymmetric bilayers were fabricated employing perprotonated and perdeuterated phospholipids with longer alkyl chains. Specifically, 1,2-distearoyl-d70-*sn*-glycero-3-phosphocholine (d-DSPC) and 1,2-distearoyl-*sn*-glycero-3-phosphocholine (DSPC) were deposited (at 35 mN/m deposition pressure) on the prism surface as detailed in Section 2.1.3 with d-DSPC serving as the proximal leaflet and DSPC as the distal leaflet (molecular structures presented in Figure 5.14). TIR-SF spectra were collected in the C-D and C-H stretching regions for each of the *ppp*, *ssp*, *sps*, and *pss* beam polarization combinations; the normalized spectra are presented in Figure 5.15. The three peaks in each of the *ppp* spectra are assigned to their respective r^+, r^+_{FR}, and r^- perpro-

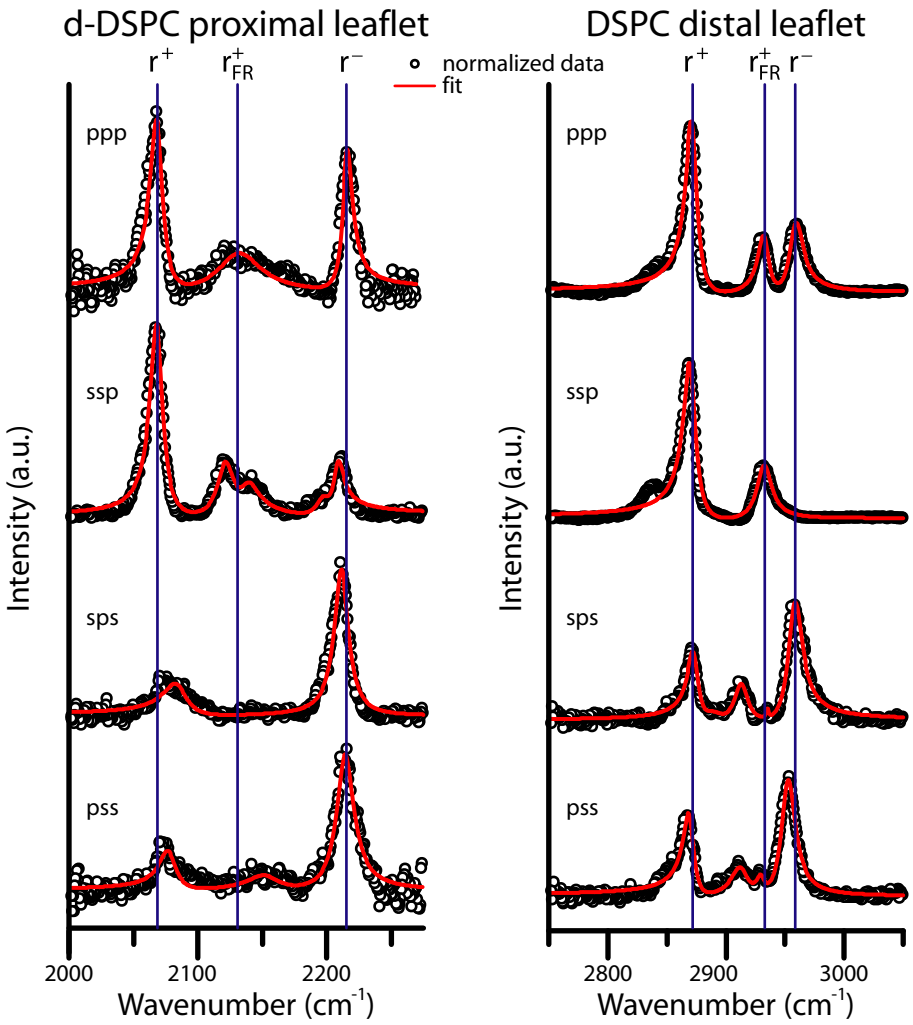

Figure 5.15. TIR-SF spectra of an asymmetric bilayer. The proximal and distal leaflets, deposited by the LB/LS technique on a CaF_2 hemicylinder prism, were d-DSPC and DSPC, respectively. The C-D and C-H stretching regions were each probed employing the *ppp*, *ssp*, *sps*, and *pss* beam polarization combinations. The spectra have been vertically offset for clarity.

tonated or perdeuterated methyl resonances; variants of these resonances occur in the other beam polarization combination spectra, as indicated.

The SF spectra of Figure 5.15 indicate that a highly ordered asymmetric bilayer was successfully deposited and maintained on the prism face (for a period of ∼5 hours). Clearly, mounting and manipulation of the prism in the sample holder did

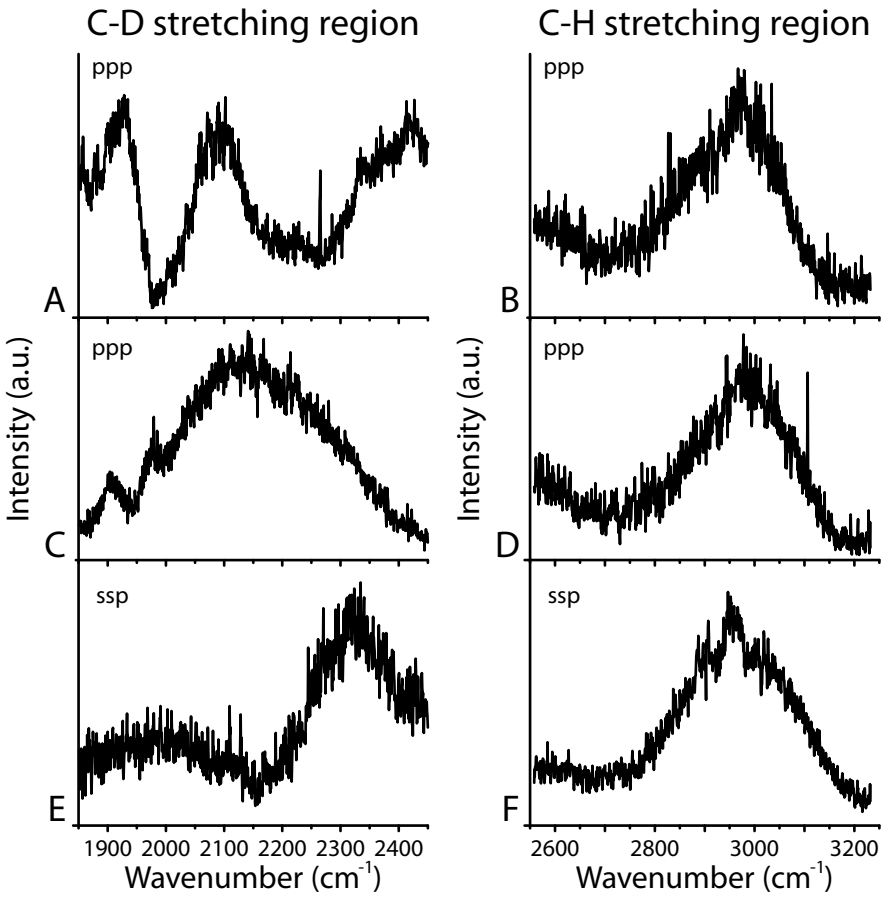

Figure 5.16. Non-normalized TIR-SF spectra of a chitosan supported asymmetric bilayer. The bilayer was deposited via the LB/LS technique onto a chitosan coated CaF_2 hemicylinder prism. The proximal and distal leaflets were d-DSPC and DSPC, respectively. The C-D and C-H stretching regions were probed for each bilayer. **A** and **B** are *ppp* spectra of a bilayer supported on a standard chitosan film (fully hydrated thickness ∼130 nm). **C** and **D** are *ppp* spectra of a bilayer supported on a thinner chitosan film (fully hydrated thickness ∼9nm). **E** and **F** are *ssp* spectra of the chitosan supported bilayer of spectra **C** and **D**.

not disrupt the bilayer on the prism surface. These results confirm the utility of the liquid cell and the bilayer fabrication technique.

5.3.4 TIR-SFS of Chitosan Supported Phospholipid Bilayers

A chitosan supported asymmetric bilayer was prepared on a CaF_2 hemicylinder prism employing the methods detailed in Section 2.1. The proximal and distal leaflets were d-DSPC and DSPC, respectively. Figures 5.16A and B present non-

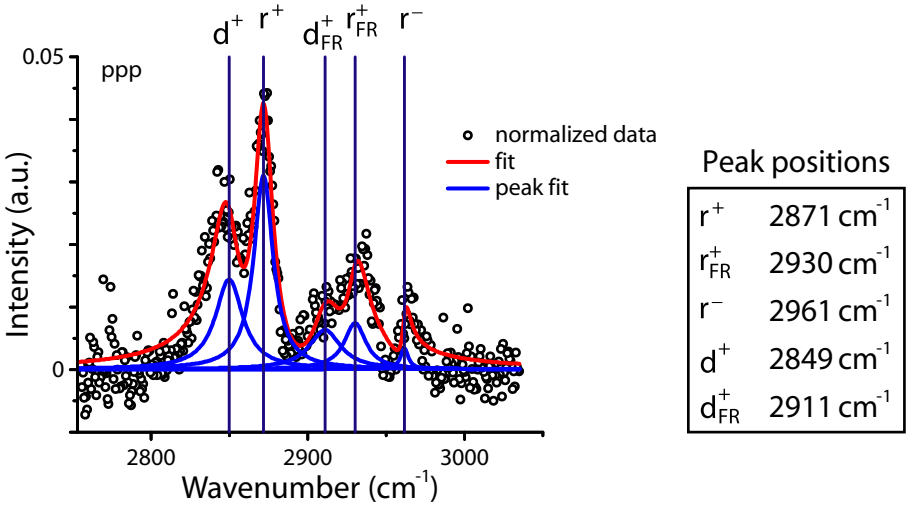

Figure 5.17. TIR-SF spectra of a chitosan cushioned asymmetric bilayer dried in air for 24 hours. A *ppp* spectrum was collected in the C-H stretching region, normalized, and fit with five peaks. The SF intensity has arbitrary units (a.u.). The peak positions are listed in the inset.

normalized *ppp* spectra collected in the C-D and C-H stretching regions, respectively. It is evident from observation of Figure 5.16 that while peaks are present, they are almost indistinguishable from an unknown background signal. It is noted that the background signal is similar to that observed in the non-normalized spectra collected at Hokkaido University (see Figures 5.8A and B).

To assess if the intensity of the background signal was proportional to the thickness of the chitosan support, and if the chitosan thickness would prove problematic for SF measurements in the TIR geometry, a second asymmetric bilayer was fabricated employing on a thinner chitosan film. The 1% w/w chitosan solution detailed in Section 2.1.2 was diluted 10x in a 1% v/v glacial acetic acid solution in 18.2 MΩ·cm water. The resulting solution was mixed by hand, and subsequently centrifuged, neutralized, and spread on the prism face as detailed in Section 2.1.2. Independent ellipsometric measurements of the same solution spread on a silicon wafer revealed the thickness to be ∼3.9 nm in the dry state. Figures 5.16C-F present non-normalized *ppp* and *ssp* TIR-SF spectra collected in the C-D and C-H stretching

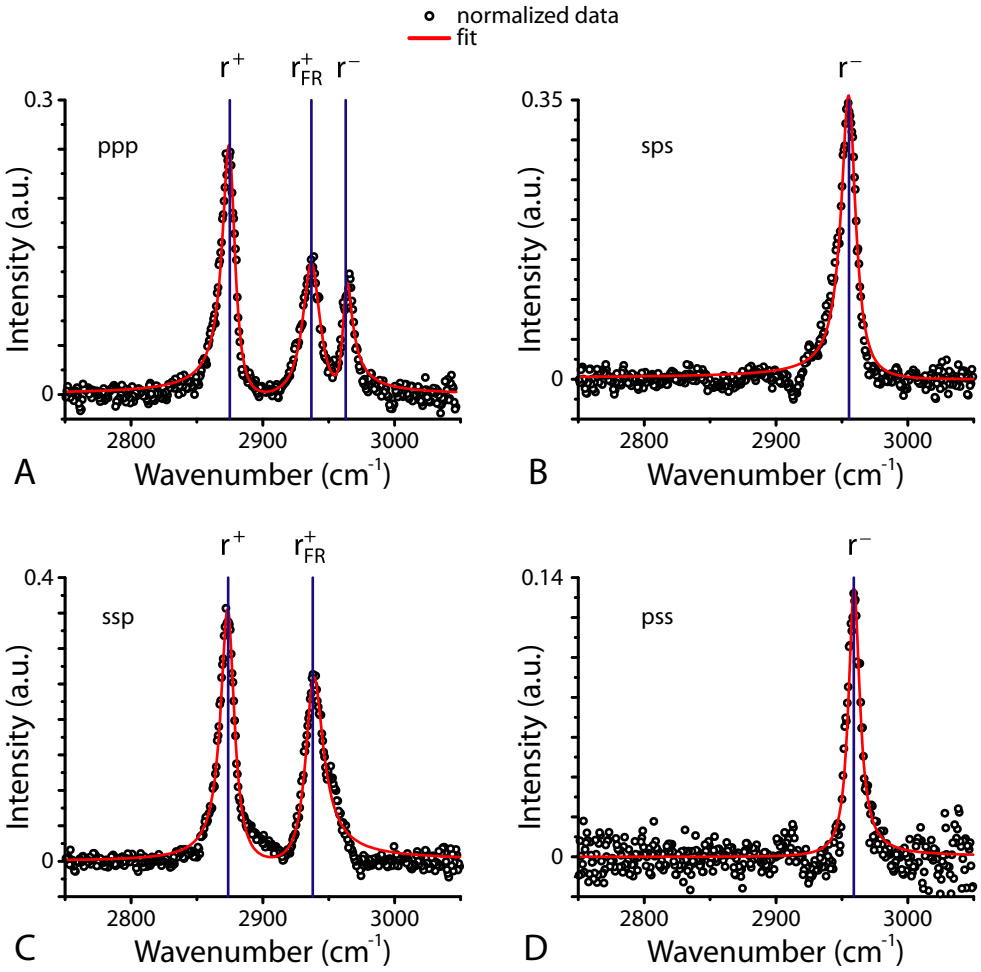

Figure 5.18. TIR-SF spectra of a chitosan supported DSPC monolayer. The chitosan, spin cast on a CaF_2 hemicylinder prism, was a 10x dilution in a 1% v/v glacial acetic acid in 18.2 MΩ·cm water solution. Spectra were collected in air for the *ppp*, *ssp*, *sps*, and *pss* beam polarization combinations, and normalized to the IR beam energy profile. The peaks in the spectra have been assigned to their corresponding methyl resonances.

regions. It is evident from investigation of Figure 5.16 that the background signal is present in each spectra, although some features are potentially present, superimposed on the background (Figures 5.16E and F). It is noted that the background signal occurs only when chitosan is present; the background was not evident in the bilayer spectra of Figure 5.15.

In order to ascertain if the bilayer was in fact present and intact, the bilayer supported on the thin chitosan film was permitted to dry for ∼24 hours while still mounted in the liquid cell. The goniometer was subsequently adjusted such that the Vis and IR excitation beam input angles were 60° and 65°, respectively, and TIR-SF *ppp* spectra were collected in air in the C-H stretching region. The normalized spectrum is presented in Figure 5.17. The spectrum was fit with five peaks, three of which were assigned to the r^+, r^+_{FR}, and r^- methyl resonances of the DSPC alkyl chains. The remaining two resonances were determined to be contributions from the methylene groups of chitosan or to arise from *gauche* defects of the DSPC alkyl chains, and were assigned to d^+ and d^+_{FR} resonances. It is noted that the only potential source of methyl resonances in the spectrum was the DSPC present in the distal leaflet of the bilayer. Therefore it may be concluded that a bilayer was indeed deposited on the chitosan film, and further, that it was undisturbed while the prism was mounted in the liquid cell. Additionally, the background signal seen in the hydrated state is not evident in Figure 5.17.

Confirmation of the presence of the background signal solely in hydrated chitosan supported films was determined by the collection of TIR-SF spectra of a DSPC monolayer on a thin chitosan film in air. TIR-SF spectra were collected in the C-H stretching region employing the *ppp*, *ssp*, *sps*, and *pss* beam polarization combinations. The raw spectra did not contain any appreciable background signal; the normalized spectra are presented in Figure 5.18. The peaks in each spectra were fit to the r^+, r^+_{FR}, and r^- methyl resonances. No methylene resonances are evident in the spectra, signifying that the DSPC monolayer highly ordered and that the dry thin chitosan film is SF inactive. It is concluded that chitosan is not a suitable polymer to employ as a hydrogel forming material for *in situ* SF measurements. Future work should focus on exploring alternate polymers.

5.4 Hybrid Sum Frequency Spectral Imaging and Confocal Fluorescence Microscope

SFS has proven to be a powerful tool for determining the orientation and conformation of phospholipid monolayers and bilayers, in both the present work and the literature at large. However, such work has largely been limited to the study of spatially homogeneous (model) surfaces. Spatially heterogeneous surfaces, such as the mixed monolayers presented in Figure 4.12, are problematic in that without knowledge of the location of the sample region being probed, spectral interpretation may be misleading. Several workers have successfully addressed this issue by constructing sum frequency microscopes.[120,297–299] An alternate approach to collecting SF images of heterogeneous surfaces is to utilize a secondary technique such as fluorescence microscopy to map surface heterogeneities. A major advantage of this approach is that information collected from the secondary technique would be complementary to that obtained via SFS. To this end, the author, Dr. Edward S. Allgeyer and Drs Michael Mason, David Neivandt, and Samuel Hess, constructed a hybrid sum frequency spectral imaging and confocal fluorescence microscope. In the following section an overview of construction will be given, along with a description of its capabilities and results from its application to phospholipid monolayers. For further detail regarding instrument development, design, and operation, the Ph.D. thesis of Dr. Edward S. Allgeyer should be consulted.[232]

5.4.1 Instrumentation

The Neivandt SF spectrometer was adapted to facilitate the development of the custom hybrid sum frequency spectral imaging and confocal fluorescence (SF/FL) microscope (Figure 5.19). The Vis and IR excitation beams were directed, when required, to an adjacent optical table containing the microscope base via use of two

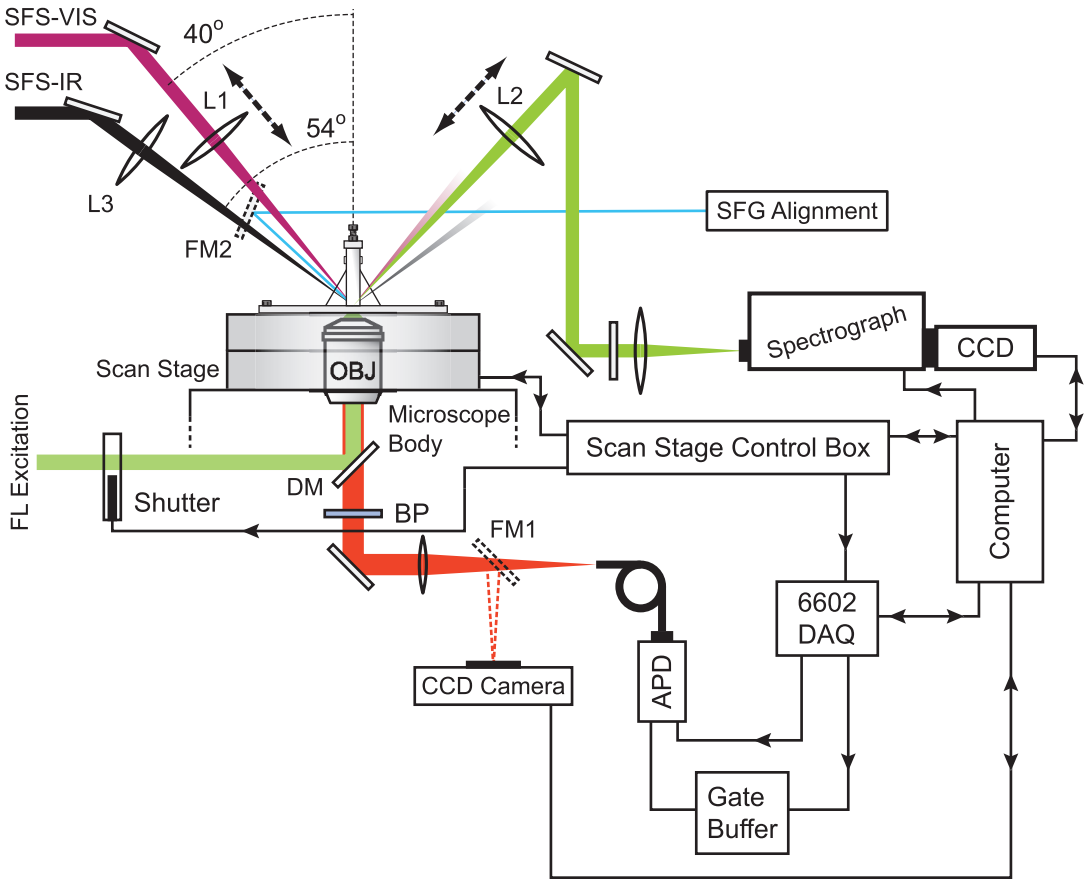

Figure 5.19. Schematic of the hybrid SF/FL microscope.[232] L1-3 are the SF excitation and collection lenses, FM1-2 are flip mounted mirrors, OBJ is the objective, DM is the dichroic mirror, and BP is the bandpass filter.

flip mounted mirrors (depicted by black dashed lines labeled FM in Figure 5.9). The inverted microscope base employed was that utilized for the z-scan FCS measurements, described in Section 2.3.2. A co-propagating TIR geometry was employed in conjunction with the XYZ piezo scan stage described in Section 2.3.2. The resultant SF signal was collected, polarization selected, and focused into a spectrograph (2300, Princeton Instruments) for imaging on a CCD camera (1024 ProEM, Princeton Instruments). The inverted microscope base permitted fluorescence excitation of the sample from below. The fluorescence excitation beam entered the back port of the microscope base, where a dichroic mirror directed the beam to the objective

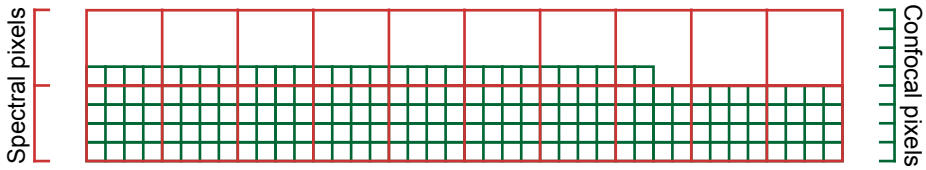

Figure 5.20. Schematic of the hybrid SF/FL microscope image collection. When both confocal fluorescence and SF spectral imaging are selected (not to scale), a line of SF spectral pixels are read followed by the confocal FL pixels. A subsequent line of SF spectral pixels is collected, and so on until the images are complete.

lens (40X, 0.65NA, PLAN N infinity corrected, Olympus). Fluorescence emission was collected by the same objective, and directed through the dichroic mirror and a bandpass filter before exiting the side port of the microscope. The fiber and APD described in Section 2.3.2 and a separate CCD camera were mounted adjacent to the microscope base (a flip mounted mirror directed the output) for collection of the fluorescence emission.

The SF/FL microscope is controlled by a custom built LabView control program.[232] The elegantly designed, user-friendly interface permits 1) adjustment of SF spectral and confocal fluorescence images and SF spectral acquisition parameters with real time viewing, 2) control of the spectrograph and CCD camera collecting the SF signal, and 3) stage positioning, sample focusing, and live APD count rates. Additionally, a series of indicators have been included to indicate the status of the various instrument components. Confocal FL and SF spectral imaging may be performed separately, or in tandem. When both confocal FL and SF spectral imaging are selected, the two images are collected line by line, sequentially (see Figure 5.20 for a visual example of the process). Sequential acquisition continues until both images have been completed. It is noted that the hybrid SF/FL microscope may be returned to points of interest on the sample to collect further SF spectra or FL time courses.

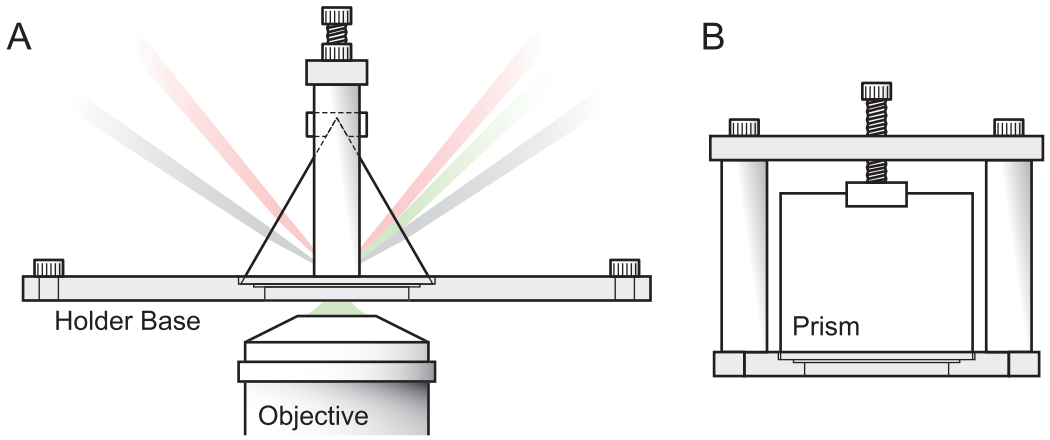

Figure 5.21. Schematic of the equilateral prism/substrate and its sample holder.[232] **A** and **B** present the front and side views of the sample holder, respectively.

With the microscope hardware requiring the sample to be placed between the two imaging capabilities (top down SF, bottom up FL), a TIR-SF geometry (detailed in Section 2.2.2) was chosen to provide SF signal enhancement while permitting FL imaging. Due to its curved surface, the hemicylinder prism geometry employed in Sections 5.1-5.3 would not permit the sample scanning required to collect an image, as such an alternate geometry was selected. Specifically, a 25.4x25.4 mm CaF_2 equilateral prism (ISP Optics, Irvington, NY) served as the prism/substrate for the TIR-SF measurements. As the position of the equilateral prism is changed in the process of scanning to collect an image, the SF excitation and emission beam angles remained fixed. A custom sample holder was designed and fabricated to mount the prism (presented in Figure 5.21). The sample holder consists of a SS base with a stepped aperture to allow a cover glass and the prism to be mounted in close proximity ($\sim$215 μm vertical separation) as required by the FL objective. The prism is straddled by two metal rods with a connecting cross bar mounted to a base plate. The cross bar is fitted with a notched Teflon block to secure the prism to the base when lowered into contact with the prism via an attached screw. The entire sample holder is mounted to the piezo scan stage for imaging.

Spatial alignment of the SF and FL excitation beams is essential for correlating the resultant images. Just as the Vis and IR alignment beams were spatially aligned on the Neivandt SF spectrometer sample stage, the same beams are aligned to the FL excitation spot viewed through the SF/FL microscope eyepiece. The SF alignment beams are subsequently turned off, and the FL excitation spot is imaged with the CCD camera. The Vis excitation beam position is confirmed by monitoring the scattered laser light with respect to the FL excitation spot previously recorded.

5.4.2 Phase Separated Monolayer Investigation

Due to the observation of cellular membrane spatial heterogeneity and the formation of distinct lipid domains (lipid rafts), the fabrication of heterogeneous monolayers and bilayers has become a highly active research area.[300–302] Equimolar mixtures of membrane constituents (cholesterol, sphingomyelin, and dioleoylphosphatidylcholine) known as the 'raft mixture'[301,302] have been used to create domains while other groups have employed simple binary mixtures of phospholipids for the same purpose.[303] In the present work, binary PC phospholipid mixtures were employed to create heterogeneous monolayers via phase separation.[303,304] Phase separated monolayers may be fabricated by mixing two immiscible phospholipids such as DSPC (Figure 5.14) and 1,2-dilauroyl-*sn*-glycero-3-phosphocholine (DLPC, Avanti Polar Lipids) (Figure 5.22) at an appropriate temperature. Since the main phase transition temperatures of DSPC and DLPC are 55°C and -1°C, respectively,[241] maintaining the mixture at an intermediate temperature results in phospholipid phase separation. Specifically, for the DSPC and DLPC combination, solid-like DSPC domains are formed within liquid-like DLPC monolayers. To create phase separated monolayers and bilayers amenable to FL imaging, a variety of fluorescent lipid analogs and fluorescently tagged phospholipids have been shown to selectively phase separate into the liquid-like phase of the leaflets.[305,306]

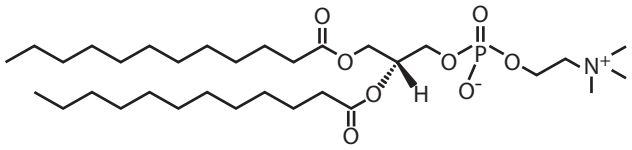

Figure 5.22. Molecular structure of 1,2-dilauroyl-*sn*-glycero-3-phosphocholine (DLPC).

In order to fabricate substrates that would serve as a useful means of characterizing the SF spectral and FL imaging capabilities of the hybrid microscope, the work on homogeneous phospholipid monolayers detailed in Section 5.3.3, as well as the mixed phospholipid bilayer work presented in Section 4.3.3, was built upon. To develop suitable protocols, work commenced on cover glass for confocal FL imaging. Once optimized, heterogeneous monolayers were deposited on the CaF_2 equilateral prism. Following the methods detailed in Chapter 2, 1:1 DSPC/DLPC monolayers with 0.0005mol% RhoPE were deposited on clean cover glass via LB deposition. The deposition surface pressure and subphase temperature were the primary parameters varied to investigate the effect of each on the size and morphology of the resultant domains. The phospholipid ratio and addition of various concentrations of cholesterol were also investigated, however such monolayers did not yield amenable phase separated domains or indeed, domains at all. Figure 5.23 presents a series of confocal FL images of phase separated monolayers with their respective deposition parameters. The effect of deposition surface pressure on the size and morphology of the domains is evident when comparing Figure 5.23A with B, and Figure 5.23D with E. Specifically, the domain morphology becomes more irregular and the domain size increases with the elevated deposition surface pressure in Figures 5.23B and E. Additionally, the domain distribution appears more uneven (domains are packed together) in Figures 5.23B and E when compared to Figures 5.23A and D. The effect of subphase temperature is evident when comparing Figure 5.23B with C and E, and

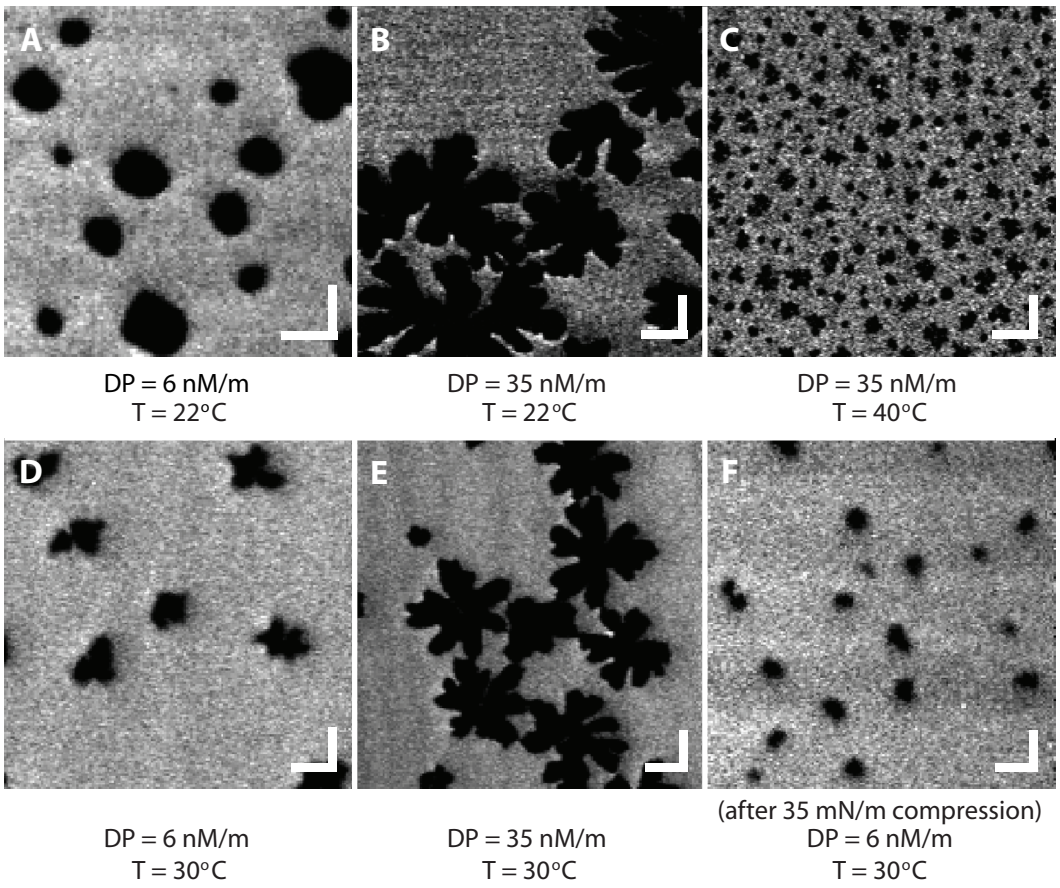

Figure 5.23. Confocal FL images of phase separated phospholipid monolayers.[232] Specifically, 1:1 DSPC/DLPC (with 0.0005 mol% RhoPE) was deposited via the LB technique on cover glass. DP is the deposition surface pressure and T is the temperature employed for each monolayer. All scale bars are 10 μm.

Figure 5.23A with D. Specifically, as the temperature increases, the domain morphology becomes more irregular and the domain size decreases. In addition, Figure 5.23F indicates that compression and subsequent decompression of a monolayer on the trough prior to deposition has a dramatic affect on domain characteristics.

As a result of the investigation detailed above, the deposition parameters chosen for phase separated monolayer preparation on the CaF_2 prism, were a surface pressure of 35 mN/m and a subphase temperature of 26°C. RhoPE served as the fluorophore required for confocal FL imaging. To create corresponding contrast for SF spectral imaging, DSPC was replaced with d-DSPC (Figure 5.14). Fabrication

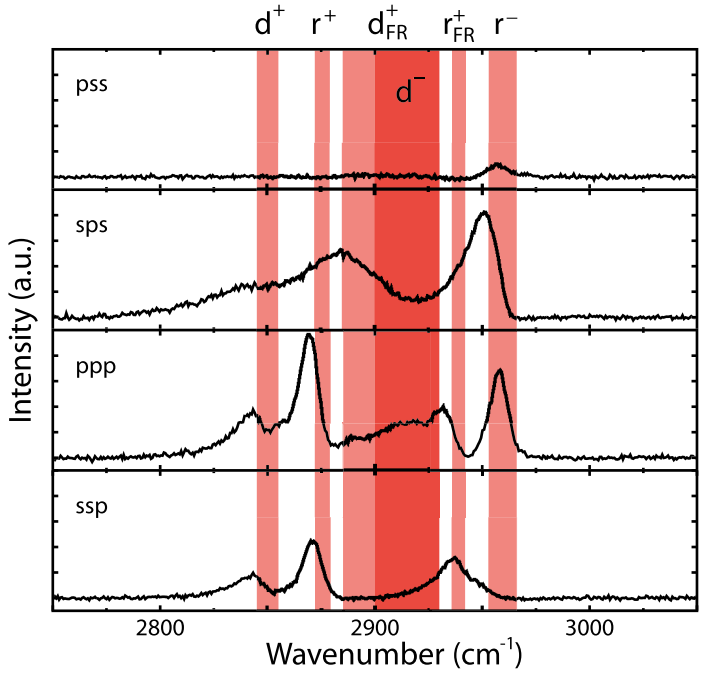

Figure 5.24. TIR-SF spectra of a phase separated monolayer in the C-H stretching region.[232] The deposition parameters for the d-DSPC/DLPC monolayer preparation were a deposition pressure of 35 mN/m and a subphase temperature of 26°C. Background subtraction and wavenumber calibration via polystyrene was performed on each spectrum. Shading indicates the range of peak assignments found in selected literature.

of phase separated monolayers employing these conditions yielded domains with a size and distribution amenable to SF spectral imaging and confocal FL imaging.

5.4.3 TIR-SF/FL Imaging Results

Initial TIR-SF spectra of phase separated d-DSPC/DLPC monolayers were collected in the C-H stretching region, employing the *ppp*, *ssp*, *sps*, and *pss* beam polarization combinations. Figure 5.24 presents the resultant TIR-SF spectra and their relative peak assignments determined by spectral fitting (Section 2.2.3). It is noted that the spectra contain both methyl and methylene resonances indicating that the DLPC is not present in a highly ordered state in the monolayer. The disorder likely stems from the fact that the DLPC is well above its phase transi-

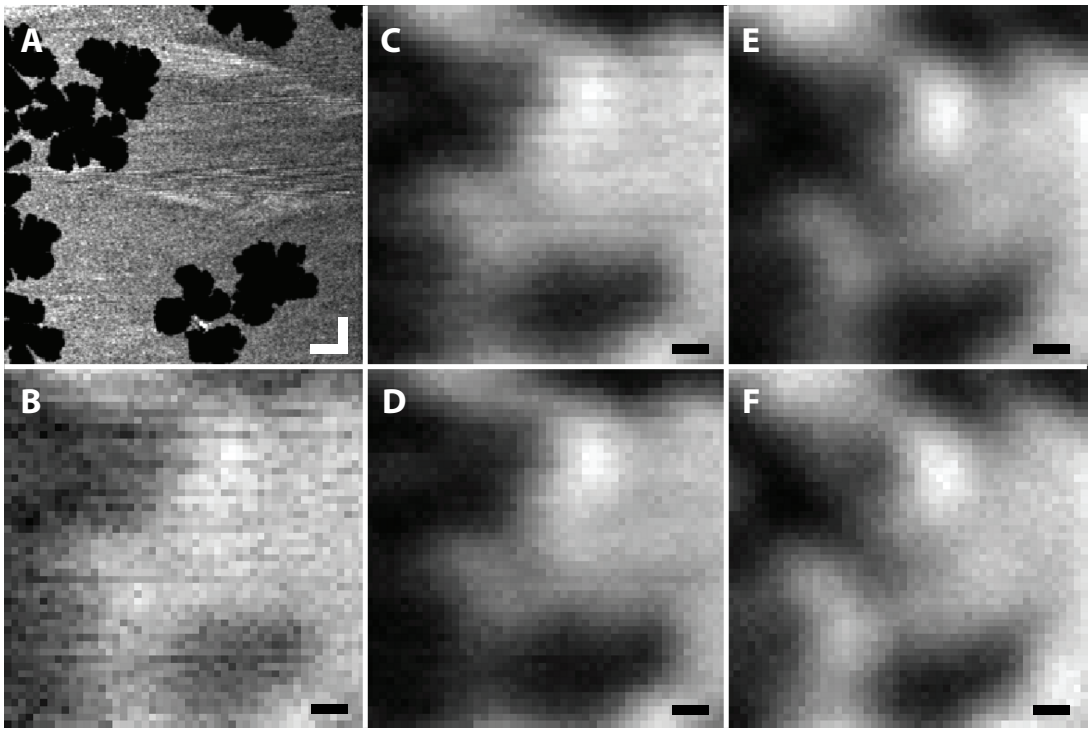

Figure 5.25. Confocal FL and SF spectral images of phase separated phospholipid monolayers.[232] **A** is a confocal FL image and **B-F** are SF spectra images of a 1:1 d-DSPC/DLPC (with 0.0005 mol% RhoPE) monolayer. SF spectral images were collected in the C-H stretching region employing the *ppp* and *ssp* beam polarization combinations. **B** presents the integrated intensity of the entire *ppp* spectrum. **C** and **D** present the intensity of the r^+ mode of the *ppp* spectrum. **E** and **F** present the intensity of the r^- mode of the *ssp* spectrum. All scale bars are 10 μm.

tion temperature of -1°C and hence, is in a liquid-like phase. The peak assignments (labeled by the shaded areas of Figure 5.24) serve as calibration for the TIR-SF spectrum collected at each pixel of the SF spectral image. The resultant SF spectral image may subsequently be tailored to represent specific spectral features.

TIR-SF and confocal FL images of the monolayer described above are presented in Figures 5.25 and 5.26. TIR-SF images were collected employing the *ppp* (Figures 5.25B, C, and E) and *ssp* (Figures 5.25D and F) beam polarization combinations. Visual comparison of the images indicates that the FL active features in the confocal FL image (Figure 5.25A) are well matched by SF active areas of the SF spectral images (Figure 5.25B-F). The SF spectral images have been tailored to reflect in-

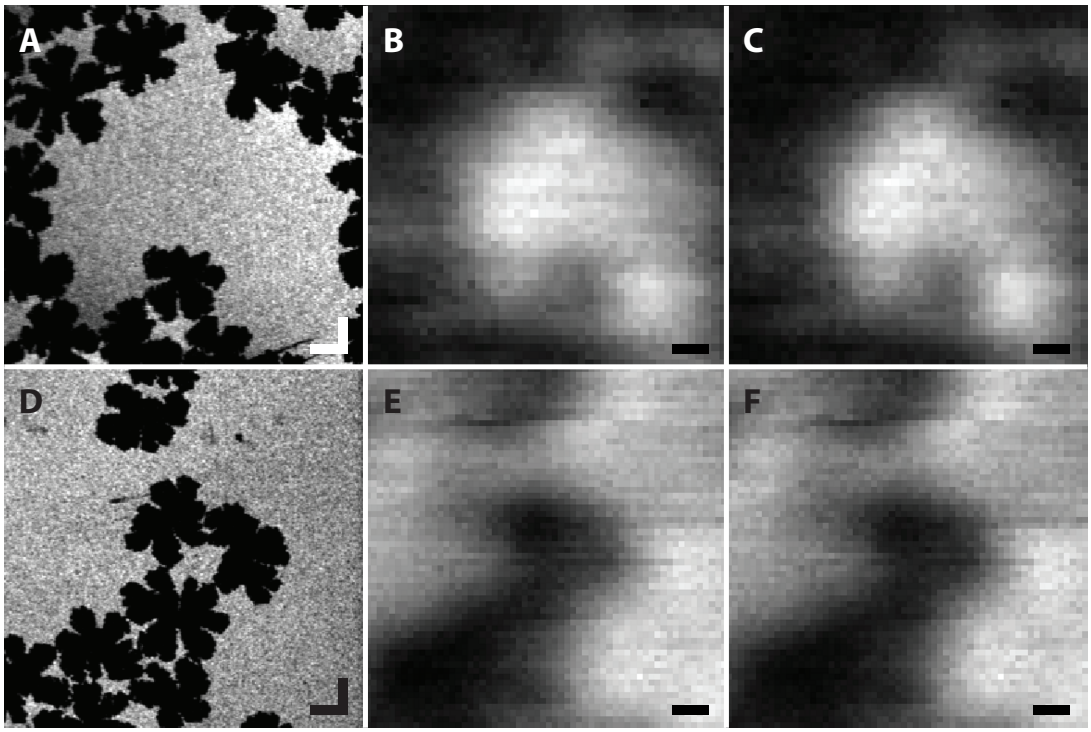

Figure 5.26. Confocal FL and SF spectral images of phase separated phospholipid monolayers.[232] **A** and **D** are confocal FL images and **B**, **C**, **E**, and **F** are SF spectral images of a 1:1 d-DSPC/DLPC (with 0.0005 mol% RhoPE) monolayer. SF spectral images were collected in the C-H stretching region employing the *ppp* beam polarization combination. **B** and **E** present the intensity of the r^+ mode while **C** and **F** present the intensity of the r^- mode. All scale bars are 10 μm.

dividual resonances in the acquired spectra. The pixel intensity in Figures 5.25C and D represents the intensity of the methyl symmetric stretching mode (r^+), while the pixel intensity in Figures 5.25E and F represents the intensity of the methyl asymmetric stretching mode (r^-). For Figure 5.25B, the pixel intensity reflects the integrated intensity of the entire *ppp* spectrum collected; it is notably more challenging to distinguish the features corresponding to the confocal FL image when compared to the other SF spectral images.

Figure 5.26 presents TIR-SF and confocal FL images of two different areas of the phase separated monolayer. The SF spectral images were collected employing the *ppp* beam polarization combination. Visual comparison of the FL active features in

the confocal FL images (Figures 5.26A and D) closely match the SF active area in the SF spectral images (Figures 5.26B, C, E, and F). The SF spectral images have been tailored to represent the r^+ mode in Figure 5.26B and E, while Figure 5.26C and F represent the r^- mode.

The images of Figures 5.25 and 5.26 confirm that DSPC (or d-DSPC) and DLPC do indeed phase separate forming DSPC domains, and that RhoPE does preferentially separate into the liquid-like phase of the DLPC. More importantly, the sample SF spectral and confocal FL images of Figures 5.25 and 5.26 show a very strong spatial correlation and demonstrate that direct chemical identification and visualization of interfacial species in heterogeneous samples is in fact achieved with the hybrid SF/FL microscope.

5.5 Summary

The work presented in Chapter 5 has detailed the reconstruction of the Neivandt SF spectrometer to enable TIR-SF spectroscopy, and the design, fabrication, and optimization of a temperature control stage and hemicylinder prism liquid flow cell to facilitate such measurements. Extensive work was subsequently performed to characterize solid supported and cushioned phospholipid monolayers and bilayers via SFS. It was determined that employing chitosan as a hydrogel cushion is not amenable to SF measurements *in situ* and an alternative polymer should be explored. Finally, an overview of the hardware and capabilities of a novel hybrid SF/FL microscope has been presented. An investigation of phase separated monolayers yielded a reproducible and tunable means of fabricating such monolayers. SF spectral and confocal FL images of the resultant monolayers confirmed the capability of the SF/FL microscope to proved complementary interfacial information from these two powerful modalities.

Chapter 6
CONCLUSIONS AND FUTURE DIRECTIONS

6.1 Summary

The cellular membrane has been established as a key component in the multi-protein FGF-1 release complex mechanism.[26] The present work has furthered understanding of this complicated and important process via application of a range of advanced techniques. Employing the method developed by Schäfer et al.,[161] reconstituted vesicles were prepared from NIH 3T3 cell membranes. FGF-1 translocation assays revealed that FGF-1 was able to translocate across vesicle membranes, and be protected from protease degradation, in a cell-free system. This work was a significant advance from previous studies which had determined that the presence of FGF-1 lead to the destabilization of acidic phospholipid liposomes (also a cell-free system).[27] It was hypothesized that the multicomponent membranes of the reconstituted vesicles may provide a more stable environment than the single component liposomes employed by Graziani et al.,[27] thereby yielding a stable, protective environment for FGF-1.

Additionally, FGF-1 translocation studies in the present work determined that a correlation exists between incubation temperature and the amount of FGF-1 translocated into vesicles. This finding is consistent with previous work which demonstrated that FGF-1 may be released from cells due solely to heat shock.[7] However, it was demonstrated in the present work that detectable amounts of FGF-1 translocated at, and below, 37°C; a finding not previously reported in the literature.[7] Since the reconstituted vesicles employed in the present work are a cell-free system that lacks native organelles and signal pathways present in the cellular system, it was hypoth-

esized that some of the absent organelles and signal pathways may act to hinder FGF-1 translocation under normal cellular conditions. Indeed, the degree of FGF-1 translocation and protection observed with the reconstituted vesicles likely stemmed primarily from changes in lipid fluidity with respect to temperature. Specifically, at low temperatures, the fluidity of the lipids comprising the vesicles is expected to be low, thereby yielding more rigid and potentially impenetrable membranes. Conversely, at elevated temperatures, more fluid and easily penetrable membranes are expected.

Finally, the osteopontin (OPN) translocation assay results emphasize the difference between classically (OPN) and non-classically (FGF-1) secreted proteins. No OPN translocation, and subsequent protection from degradation, was detected after incubation with the reconstituted vesicles. The lack of OPN translocation highlights the potential role of protein structure in the transmembrane translocation process. Indeed, OPN lacks extensive secondary structure,[239] while FGF-1 has a β-barrel structure comparable to that found in many transmembrane proteins. Further FGF-1 exhibits a molten globule state at physiologically relevant temperatures.[5]

To further probe the role of the cellular membrane in FGF-1 transmembrane translocation, a planar chitosan cushioned model membrane system amenable to study by a range of microscopic and spectroscopic techniques, was developed. Ellipsometry, atomic force microscopy, and fluorescence microscopy were employed to characterize the chitosan films. The films were found to be relatively featureless and smooth, with rms roughness values of 1.1 nm *in situ*. The swelling ratio from the dry to hydrated states of the chitosan films was determined as 2.3, as such, the average film thickness employed *in situ* was 125-140 nm. Zwitterionic (DMPC) phospholipid bilayers were reproducibly deposited on the chitosan films employing the Langmuir-

Blodgett/Langmuir Schaefer technique with Langmuir-Blodgett transfer ratios of unity within uncertainty.

Chitosan supported model membranes were initially employed in an FGF-1 translocation assay, comparable to that performed with the reconstituted vesicles. Zwitterionic (DMPC) and separately, acidic (DMPG) phospholipid bilayers were deposited on chitosan films, which were subsequently incubated with FGF-1. Western blot analysis indicated that a similar degree of FGF-1 translocation, and protection from protease degradation, occurred for each type of chitosan supported membrane. However, when the respective membranes were subjected to protease and detergent (membrane degradation) treatment, the DMPG membranes demonstrated a higher degree of FGF-1 protection. It was hypothesized that the presence of FGF-1 post protease and detergent incubation, may arise from FGF-1 penetration into the chitosan film.

To establish a stronger basis for utilizing chitosan supported membranes in FGF-1 translocation studies, diffusion dynamics of the proximal and separately, distal leaflet of the phospholipid membranes were determined employing z-scan fluorescence correlation spectroscopy (FCS). Z-scan FCS is a calibration-free method that yields the diffusion coefficient and the fluorophore concentration of fluorescently labeled thin planar systems. In the present work, z-scan FCS was employed for the first time to determined diffusion dynamics of individual phospholipid leaflets of cushioned bilayers. Specifically, phospholipid diffusion coefficients were collected over a range of temperatures for chitosan supported DMPC membranes doped with RhoPE, and the DMPC phase transition temperature was characterized for each leaflet. The phase transition temperatures of the proximal and distal phospholipid leaflets were found to be nearly identical ($\sim$28°C for each leaflet) and to agree well with literature values for similar chitosan supported DMPC membranes.[171]

To determine the extent of potential perturbative effects of the supporting substrate on membrane fluidity, comparable DMPC membranes were deposited on glass substrates, and the diffusion dynamics of the proximal leaflet assessed by z-scan FCS. The phase transition temperature was determined to be $\sim$24°C, a value consistent with literature reports for glass supported DMPC membranes.[171] It is noted that the phase transition temperature of the chitosan supported DMPC membrane determined in the present work, is elevated by $\sim$4°C relative to that of the glass supported DMPC membrane. The difference in phase transition temperature values, attributed to the nature of the substrate, affirms the necessity of thorough characterization of model membranes systems via appropriate methods prior to studies of phenomena such as transmembrane protein insertion or protein translocation.

With the zwitterionic DMPC membranes well characterized, attention was turned to the creation and characterization of acidic phospholipid membranes. Exhaustive work was performed utilizing the acidic phospholipid DMPG. It was determined that membranes composed of DMPG were recalcitrant and far more challenging to prepare compared to DMPC. Indeed, it was shown that the interaction of DMPG with various subphases employed in the Langmuir-Blodgett trough must be taken into careful consideration. To ascertain if the difficulties encountered were specific to DMPG, a second acidic phospholipid, DMPS, was employed; comparable results were found to those of DMPG.

While chitosan supported zwitterionic phospholipid membranes provide an excellent model membrane system for protein translocation studies, the physiologic relevance of chitosan is non-ideal. As such, preliminary work was performed to develop a cushioned model membrane system composed of the dynamic protein found in the cytoskeleton of all eukaryotic cells, actin. Cover glass was successfully functionalized with actin monomers, yielding relatively smooth, uniform films as determined via confocal fluorescence and ellipsometric measurements. DMPC

membranes were successfully deposited on the actin films via LB/LS deposition. As with the chitosan and glass supported DMPC membranes, proximal leaflet diffusion dynamics were assessed via z-scan FCS as function of temperature. The phase transition temperature of the actin supported DMPC proximal leaflet was significantly elevated relative to the chitosan supported membranes ($\sim$32°C vs. $\sim$28°C). Interestingly, actin has been reported to have very little interaction with zwitterionic phospholipids such as DMPC,[287,288] as such, a strong perturbative effect was not expected. It was hypothesized that the negatively charged actin molecules[287] or potential actin filaments on the surface[277] may have acted to hinder the diffusion of DMPC phospholipids. The actin cushioned model membrane system reported in the present work is the first of its kind, and the diffusion of the phospholipids, hindered or not, lends ample support to its use in further studies.

For each of the supported DMPC proximal leaflets and the distal leaflet of the chitosan supported DMPC membrane, additional analysis of the diffusion mode as a function of temperature was performed. Specifically, application of the submicron confinement model of diffusion (the so-called FCS diffusion laws[156,242]) revealed that phospholipid diffusion changes from raft-like to free diffusion as the temperature approaches the phase transition temperature for each of the leaflets. The results indicate the elevated phase transition temperatures of the chitosan and actin supported leaflets relative to the glass supported membranes, may not be attributed to hindrance by the meshwork of the cushion constituents. It is noted that a different property of each cushion must be inducing more sustained raft formation (based on the calculated phase transition temperatures) of the membrane leaflets than assessed for the glass supported membrane.

To complement the dynamic diffusion characterization performed via z-scan FCS, SF spectroscopy was utilized to elucidate the phospholipid conformation of supported model membranes and build on the FGF-1/hybrid bilayer membrane study

of Doyle et al..[101] The SF work represents a major extension to a previous study[101] of the interaction between FGF-1 and phospholipid membranes. The work of Doyle et al. employed a hybrid bilayer membrane (HBM) of octadecanethiol and phospholipid on a gold surface, a model membrane that was not a true phospholipid bilayer and could not facilitate FGF-1 translocation. As such, it was necessary to reconfigure the Neivandt SF spectrometer to accommodate measurements of cushioned model membrane systems. In addition, the reconfigured SF spectrometer provided the basis for development of a novel hybrid sum frequency spectral imaging and confocal fluorescence (SF/FL) microscope. To facilitate solution-based total internal reflection SF measurements, a liquid flow cell and temperature control stage were designed, fabricated, and implemented.

A variety of CaF_2 supported phospholipid systems were investigated employing the Neivandt SF spectrometer and the hybrid SF/FL microscope. The Neivandt SF spectrometer was employed to study homogeneous phospholipid systems in both air and solution. Perprotonated and perdeuterated phospholipids were employed to create SF spectral asymmetry and hence, facilitate measurements in the C-H and C-D stretching regions in the *ppp*, *ssp*, *sps*, and *pss* beam polarization combinations. It is noted that the *pss* beam polarization combination, which was consistently probed with the Neivandt SF spectrometer, is not often employed due to its inherently extremely low SF signal level,[226] thus demonstrating the excellent sensitivity of the instrument.

The hybrid SF/FL microscope was employed to study heterogeneous phospholipid systems in air, specifically, phase separated zwitterionic phospholipid monolayers. A confocal fluorescence imaging investigation of phase separated monolayers yielded a reproducible and tunable method for fabricating such monolayers. Two primary parameters were identified that permitted manipulatioin of the size and

morphology of the domains within the monolayers; the deposition surface pressure and the subphase temperature.

In addition to CaF_2 supported heterogeneous phospholipid monolayers, preliminary SF spectra were collected of chitosan supported monolayers and bilayers. SF spectra of chitosan films (55-60nm) in air confirmed that strong methylene modes are present in the C-H stretching region, a factor that must be considered when probing phospholipids deposited on such films. To facilitate spectral analysis of such bilayers, it was necessary to employ perdeuterated phospholipids in the leaflet of interest, thereby removing chitosan spectral interference. Interestingly, however, it was demonstrated that SF spectra of perprotonated phospholipids on chitosan films could be measured in air and interpreted providing the chitosan film was $\sim$3.9 nm thick in the dry state. Finally, chitosan supported asymmetric phospholipid bilayers were probed in the C-H and C-D stretching regions *in situ*. Unfortunately, a large background signal obscured the spectral features. SF spectra of dried bilayers indicated that phospholipids were indeed present on the chitosan film and that the lack of a clear spectrum was not due to the lack of a bilayer.

6.2 Future Work

Clearly work should be performed to address the poor signal level and high background signal when performing SFS of asymmetric bilayers on chitosan. Specifically, the SF excitation beam angles employed may require adjustment to yield results comparable to the CaF_2 supported bilayers. To guide selection of appropriate excitation angles, further ellipsometric studies should be performed to provide a more accurate value for the refractive index of hydrated chitosan films and hence facilitate accurate determination of the critical angle required for total internal reflection. It is possible that broad methylene stretching modes of hydrated chitosan may be con-

tributing to the background signal observed when probing the C-H stretching region, while the presence of carbon dioxide in the water may be contributing to the background signal observed when probing the C-D stretching region.[307] Based on the results of the present work, chitosan may not be the optimal hydrogel for use in SFS studies of cushioned phospholipid bilayers. In contrast, poly(*L*-lactic acid) cushioned phospholipid bilayers have recently been probed via TIR-SFS, and spectral features stemming from the phospholipids were clearly observed.[109] By performing an experimental survey of potential SF background signals of various hydrogels in solution, an optimal hydrogel could be chosen to meet all criteria in the present work as well as provide the scientific community with detailed interfacial information regarding hydrogels not currently present in the literature.

Once SF spectral acquisition from cushioned asymmetric bilayers on is optimized, SF spectra of perdeuterated phospholipid leaflets comprising cushioned supported membranes should be investigated over a range of temperatures. Determining the ratio of the amplitude of the symmetric methylene stretching mode (d^+) to the amplitude of the symmetric methyl stretching mode (r^+), will permit assessment of the phase transition temperature of the phospholipid leaflet.[95] Such data would provide valuable complementary information to the z-scan FCS measurements of the phase transition temperatures. Subsequent SF studies probing the interaction of FGF-1 with cushioned phospholipid bilayers should be performed to elucidate the molecular conformational changes undergone by the bilayer during translocation. Additionally, the hybrid SF/FL microscope sample holder could be modified to make it amenable to liquid samples. The microscope could then be employed to provide spatially correlated FL and SF data of FGF-1:phospholipid interactions.

The z-scan FCS study of supported DMPC bilayers yielded a well characterized chitosan supported model membrane system, in addition to a novel actin supported model membrane system. The actin model membrane system should undergo fur-

ther characterization including rms roughness determination prior to its application. Further FCS work should be performed in a configuration that enables liquid flow and thus a new liquid cell with flow capabilities should be fabricated. While a preliminary FCS study with fluorescently tagged FGF-1 was performed by Dr. Andrew Doyle,[164] the integrity of the membranes employed in that study, specifically the chitosan cushioned acidic phospholipid membranes, may not have been ideal. Indeed, as the present work has demonstrated, further development of planar acidic phospholipid bilayers is required. Fabrication of a bilayer composed of an acidic phospholipid leaflet may require alternate deposition techniques such as vesicle fusion, or Langmuir-Blodgett deposition in place of the Langmuir Schaefer deposition employed in the present work.[308] Other avenues yet to be fully explored include employing a fluorophore with a net neutral charge to minimize interaction with the phospholipids[249] and separately, adjusting the ionic strength and pH of the subphase to manipulate the packing of the phospholipids, and hence, membrane fluidity.[288]

While successful fabrication of homogeneous acidic phospholipid bilayers would yield a simple model membrane system amenable to study via SFS and FCS, it is noted that neat systems of acidic phospholipids are not physiologically relevant. Rather, native plasma membranes (proximal and distal leaflets combined) generally consist of sphingomyelin (SM, ~25%), phosphatidylcholine (PC, ~25%), phosphatidylethanolamine (PE, ~30%), and phosphatidylserine (PS, ~10%) with the remaining percentage composed of phosphatidylinositol (PI), phosphatidylinositol 4-phosphate (PIP), phosphatidylinositol 4,5-phosphate (PIP_2), and phosphatidic acid (PA).[309,310] Cholesterol, another plasma membrane component, has been reported to have a 8:1 molar ratio with total PS present in the plasma membrane.[311] The membrane constituents are asymmetrically distributed in each of the plasma membrane leaflets; SM, PC, and PE dominate the distal leaflet (~40%, ~40%, and ~15%, respectively), while PE, PS, and PC dominate the proximal leaflet (~50%,

$\sim$30%, and $\sim$15%, respectively).[309] Based on the lipid ratios presented for native plasma membranes, homogeneous phospholipid bilayers are far from being physiologically relevant. Subsequent monolayers and bilayers should be fabricated employing the ratios described herein. Based on fluorescence images of bilayers fabricated with 1:3 and 3:1 PC:PG molar ratios in Section 4.3.3, selection of appropriate fluorophore(s) may also be necessary for probing either the liquid-like or solid-like regions of the fabricated bilayers.[249] Establishing a heterogeneous phospholipid planar cushioned model membrane system would be a valuable tool, and would ideally permit FGF-1 translocation to be investigated by FCS and SFS. To provide a metric for acidic phospholipid diffusion in model membrane systems, further investigation of acidic phospholipid fluidity in domains of native plasma membranes would be advantageous. Recently, Kay et al. employed a genetically encoded PS biosensor and separately, a synthetic PS fluorescent analog to determine diffusion coefficients of PS in model membrane systems and live cells via FCS, FRAP, and SPT.[310] The breadth of results reported by Kay et al. were the first determination of PS dynamics in the proximal leaflet of the plasma membrane, establishing a metric for further PS membrane diffusion behavior studies.[310]

With respect to the reconstituted vesicle study, further translocation assays should be performed with other non-classical transport complex members, individually, and in combination. Additionally, the reconstituted vesicles should be characterized more thoroughly with respect to their orientation ('inside-out' and 'right side-out') and their size. Assessing and potentially manipulating the size of the vesicles may provide information regarding the role of membrane curvature in the translocation of FGF-1. The FGF-1 translocation assays performed in the present work on chitosan supported membranes were conducted under rudimentary conditions; such measurements should be executed after fabrication of a sample holder capable of maintaining fluid on the membrane. Assessment of the translo-

cation assay by Western blot analysis is not readily achieved for planar chitosan supported bilayers (due to the method required to move the sample from a flat glass substrate to a vial). Alternate non-invasive methods, such as employing chitosanase, a chitinolytic enzyme that hydrolyzes chitosan, to degrade the chitosan and remove it from the substrate, should be investigated.

REFERENCES

[1] Alberts, B.; Johnson, A.; Lewis, J.; Raff, M.; Roberts, K.; Walter, P. *Molecular Biology of the Cell*, 5th ed.; Garland Science, Taylor & Francis Group: New York, 2008.

[2] Blobel, G. Nobel Prize in Physiology or Medicine for 1999 - Press Release. 1999; `http://www.nobelprize.org/nobel_prizes/medicine/laureates/1999/press.html`.

[3] Blobel, G. *Chembiochem* **2000**, *1*, 86–102.

[4] Burgess, W.; Maciag, T. *Annu. Rev. Biochem.* **1989**, *58*, 575–606.

[5] Prudovsky, I.; Mandinova, A.; Soldi, R.; Bagalá, C.; Graziani, I.; Landriscina, M.; Tarantini, F.; Duarte, M.; Bellum, S.; Doherty, H.; Maciag, T. *J. Cell Sci.* **2003**, *116*, 4871–4881.

[6] Mach, H.; Middaugh, C. R. *Biochemistry* **1995**, *34*, 9913–9920.

[7] Jackson, A.; Friedman, S.; Zhan, X.; Engleka, K. A.; Forough, R.; Maciag, T. *Proc. Natl. Acad. Sci. USA* **1992**, *89*, 10691–10695.

[8] Shin, J. T.; Opalenik, S. R.; Wehby, J. N.; Mahesh, V. K.; Jackson, A.; Tarantini, F.; Maciag, T.; Thompson, J. A. *Biochim. Biophys. Acta* **1996**, *1312*, 27–38.

[9] Kuwabara, K.; Ogawa, S.; Matsumoto, M.; Koga, S.; Clauss, M.; Pinsky, D.; Lyn, P.; Leavy, J.; Witte, L.; Joseph-Silverstein, J. *Proc. Natl. Acad. Sci. USA* **1995**, *92*, 4606–4610.

[10] Ananyeva, N.; Tjurmin, A.; Berliner, J.; Chisolm, G.; Liau, G.; Winkles, J.; Haudenschild, C. *Arterioscler. Thromb. Vasc. Biol.* **1997**, *17*, 453–455.

[11] Prudovsky, I.; Bagalá, C.; Tarantini, F.; Mandinova, A.; Soldi, R.; Bellum, S.; Maciag, T. *J. Cell Biol.* **2002**, *158*, 201–208.

[12] LaVallee, T.; Tarantini, F.; Gamble, S.; Carreira, C.; Jackson, A.; Maciag, T. *J. Biol. Chem.* **1998**, *273*, 22217–22223.

[13] Prudovsky, I.; Tarantini, F.; Landriscina, M.; Neivandt, D.; Soldi, R.; Kirov, A.; Small, D.; Kathir, K. M.; Rajalingam, D.; Kumar, T. K. S. *J. Cell. Biochem.* **2008**, *103*, 1327–43.

[14] Landriscina, M.; Soldi, R.; Bagalá, C.; Micucci, I.; Bellum, S.; Tarantini, F.; Prudovsky, I.; Maciag, T. *J. Biol. Chem.* **2001**, *276*, 22544–22552.

[15] Mouta Carreira, C.; LaVallee, T. M.; Tarantini, F.; Jackson, A.; Lathrop, J. T.; Hampton, B.; Burgess, W. H.; Maciag, T. *J. Biol. Chem.* **1998**, *273*, 22224–22231.

[16] Bagalá, C.; Kolev, V.; Mandinova, A.; Soldi, R.; Mouta Carreira, C.; Graziani, I.; Prudovsky, I.; Maciag, T. *Biochem. Biophys. Res. Commun.* **2003**, *310*, 1041–1047.

[17] Landriscina, M.; Bagalá, C.; Mandinova, A.; Soldi, R.; Micucci, I.; Bellum, S.; Prudovsky, I.; Maciag, T. *J. Biol. Chem.* **2001**, *276*, 25549–25557.

[18] Sivaraja, V.; Kumar, T. K. S.; Rajalingam, D.; Graziani, I.; Prudovsky, I.; Yu, C. *Biophys. J.* **2006**, *91*, 1832–1843.

[19] Mandinova, A.; Soldi, R.; Graziani, I.; Bagalá, C.; Bellum, S.; Landriscina, M.; Tarantini, F.; Prudovsky, I.; Maciag, T. *J. Cell Sci.* **2003**, *116*, 2687–2696.

[20] Soldi, R.; Mandinova, A.; Venkataraman, K.; Hla, T.; Vadas, M.; Pitson, S.; Duarte, M.; Graziani, I.; Kolev, V.; Kacer, D.; Kirov, A.; Maciag, T.; Prudovsky, I. *Exp. Cell. Res.* **2007**, *313*, 3308–3318.

[21] Ancellin, N.; Colmont, C.; Su, J.; Li, Q.; Mittereder, N.; Chae, S.-S.; Stefansson, S.; Liau, G.; Hla, T. *J. Biol. Chem.* **2002**, *277*, 6667–6675.

[22] Peterson, E. A.; Sutherland, M. R.; Nesheim, M. E.; Pryzdial, E. L. G. *J. Cell Sci.* **2003**, *116*, 2399–2408.

[23] Pomorski, T.; Hrafnsdóttir, S.; Devaux, P. F.; van Meer, G. *Semin. Cell Dev. Biol.* **2001**, *12*, 139–148.

[24] Tarantini, F.; Gamble, S.; Jackson, A.; Maciag, T. *J. Biol. Chem.* **1995**, *270*, 29039–29042.

[25] Mandinov, L.; Mandinova, A.; Kyurkchiev, S.; Kyurkchiev, D.; Kehayov, I.; Kolev, V.; Soldi, R.; Bagala, C.; de Muinck, E. D.; Lindner, V.; Post, M. J.; Simons, M.; Bellum, S.; Prudovsky, I.; Maciag, T. *Proc. Natl. Acad. Sci. USA* **2003**, *100*, 6700–6705.

[26] Kirov, A.; Al-Hashimi, H.; Solomon, P.; Mazur, C.; Thorpe, P. E.; Sims, P. J.; Tarantini, F.; Kumar, T. K. S.; Prudovsky, I. *J. Cell. Biochem.* **2012**, *113*, 956–966.

[27] Graziani, I.; Bagalá, C.; Duarte, M.; Soldi, R.; Kolev, V.; Tarantini, F.; Kumar, T. K. S.; Doyle, A.; Neivandt, D.; Yu, C.; Maciag, T.; Prudovsky, I. *Biochem. Biophys. Res. Commun.* **2006**, *349*, 192–199.

[28] Sanz, J. M.; Jiménez, M. A.; Giménez-Gallego, G. *Biochemistry* **2002**, *41*, 1923–1933.

[29] Graziani, I.; Doyle, A.; Sterling, S.; Kirov, A.; Tarantini, F.; Landriscina, M.; Kumar, T. K. S.; Neivandt, D.; Prudovsky, I. *Biochem. Biophys. Res. Commun.* **2009**, *381*, 350–354.

[30] Lambert, A.; Davies, P.; Neivandt, D. *Appl. Spectrosc. Rev.* **2005**, *40*, 103–145.

[31] Shen, Y. *Nature* **1989**, *337*, 519–525.

[32] Adamson, A.; Gast, A. *Physical Chemistry of Surfaces*, 6th ed.; Wiley: New York, 1997.

[33] Walker, R. A.; Conboy, J. C.; Richmond, G. L. *Langmuir* **1997**, *13*, 3070–3073.

[34] Zhu, X.; Suhr, H.; Shen, Y. *Phys. Rev. B* **1987**, *35*, 3047–3050.

[35] Harris, A.; Chidsey, C.; Levinos, N.; Loiacono, D. *Chem. Phys. Lett.* **1987**, *141*, 350–356.

[36] Hunt, J. H.; Guyot-Sionnest, P.; Shen, Y. R. *Chem. Phys. Lett.* **1987**, *133*, 189–192.

[37] Watry, M. R.; Richmond, G. L. *J. Am. Chem. Soc.* **2000**, *122*, 875–883.

[38] Conboy, J. C.; Messmer, M. C.; Richmond, G. L. *J. Phys. Chem.* **1996**, *100*, 7617–7622.

[39] Conboy, J. C.; Messmer, M. C.; Richmond, G. L. *J. Phys. Chem. B* **1997**, *101*, 6724–6733.

[40] Walker, R.; Gragson, D.; Richmond, G. *Colloids Surf. A Physicochem. Eng. Asp.* **1999**, *154*, 175–185.

[41] Smiley, B.; Richmond, G. *Biopolymers* **2000**, *57*, 117–125.

[42] Watry, M. R.; Richmond, G. L. *Langmuir* **2002**, *18*, 8881–8887.

[43] Watry, M. R.; Tarbuck, T. L.; Richmond, G. L. *J. Phys. Chem. B* **2003**, *107*, 512–518.

[44] Pohle, W.; Saβ, M.; Selle, C.; Wolfrum, K.; Löbau, J. *Vib. Spectrosc.* **1999**, *19*, 321–327.

[45] Löbau, J.; Sass, M.; Pohle, W.; Selle, C.; Koch, M.; Wolfrum, K. *J. Mol. Struct.* **1999**, *480-481*, 407–411.

[46] Roke, S.; Schins, J.; Müller, M.; Bonn, M. *Phys. Rev. Lett.* **2003**, *90*, 128101.

[47] Smits, M.; Sovago, M.; Wurpel, G.; Kim, D.; Muller, M.; Bonn, M. *J. Phys. Chem. C* **2007**, *111*, 8878–8883.

[48] Sovago, M.; Wurpel, G. W. H.; Smits, M.; Müller, M.; Bonn, M. *J. Am. Chem. Soc.* **2007**, *129*, 11079–11084.

[49] Campen, R. K.; Ngo, T. T. M.; Sovago, M.; Ruysschaert, J.-M.; Bonn, M. *J. Am. Chem. Soc.* **2010**, *132*, 8037–8047.

[50] Rzeźnicka, I. I.; Sovago, M.; Backus, E. H. G.; Bonn, M.; Yamada, T.; Kobayashi, T.; Kawai, M. *Langmuir* **2010**, *26*, 16055–16062.

[51] Wurpel, G. W. H.; Sovago, M.; Bonn, M. *J. Am. Chem. Soc.* **2007**, *129*, 8420–8421.

[52] Smits, M.; Ghosh, A.; Bredenbeck, J.; Yamamoto, S.; Müller, M.; Bonn, M. *New J. Phys.* **2007**, *9*, 390.

[53] Sovago, M.; Vartiainen, E.; Bonn, M. *J. Chem. Phys.* **2009**, *131*, 161107.

[54] Bonn, M.; Bakker, H. J.; Ghosh, A.; Yamamoto, S.; Sovago, M.; Campen, R. K. *J. Am. Chem. Soc.* **2010**, *132*, 14971–14978.

[55] Zhang, Z.; Piatkowski, L.; Bakker, H. J.; Bonn, M. *J. Chem. Phys.* **2011**, *135*, 021101.

[56] Bonn, M.; Roke, S.; Berg, O.; Juurlink, L. B.; Stamouli, A.; Müller, M. *J. Phys. Chem. B* **2004**, *108*, 19083–19085.

[57] Ohe, C.; Sasaki, T.; Noi, M.; Goto, Y.; Itoh, K. *Anal. Biolanal. Chem.* **2007**, *388*, 73–79.

[58] Ohe, C.; Ida, Y.; Matsumoto, S.; Sasaki, T.; Goto, Y.; Noi, M.; Tsurumaru, T.; Itoh, K. *J. Phys. Chem. B* **2004**, *108*, 18081–18087.

[59] Ohe, C.; Goto, Y.; Noi, M.; Arai, M.; Kamijo, H.; Itoh, K. *J. Phys. Chem. B* **2007**, *111*, 1693–1700.

[60] Ma, G.; Liu, J.; Fu, L.; Yan, E. C. Y. *Appl. Spectrosc.* **2009**, *63*, 528–537.

[61] Fu, L.; Liu, J.; Yan, E. C. Y. *J. Am. Chem. Soc.* **2011**, *133*, 8094–8097.

[62] Fu, L.; Ma, G.; Yan, E. C. Y. *J. Am. Chem. Soc.* **2010**, *132*, 5405–5412.

[63] Viswanath, P.; Aroti, A.; Motschmann, H.; Leontidis, E. *J. Phys. Chem. B* **2009**, *113*, 14816–14823.

[64] Hill, K.; Pénzes, C. B.; Schnöller, D.; Horváti, K.; Bősze, S.; Hudecz, F.; Keszthelyi, T.; Kiss, E. *Phys. Chem. Chem. Phys.* **2010**, *12*, 11498–11506.

[65] Liljeblad, J. F. D.; Bulone, V.; Tyrode, E.; Rutland, M. W.; Johnson, C. M. *Biophys. J.* **2010**, *98*, L50–L52.

[66] Liljeblad, J. F. D.; Bulone, V.; Rutland, M. W.; Johnson, C. M. *J. Phys. Chem. C* **2011**, *115*, 10617–10629.

[67] Ma, G.; Allen, H. C. *Langmuir* **2006**, *22*, 11267–11274.

[68] Ma, G.; Allen, H. C. *Photochem. Photobiol.* **2006**, *82*, 1517–1529.

[69] Ma, G.; Allen, H. C. *Langmuir* **2007**, *23*, 589–597.

[70] Ma, G.; Allen, H. C. *Langmuir* **2006**, *22*, 5341–5349.

[71] Chen, X.; Hua, W.; Huang, Z.; Allen, H. C. *J. Am. Chem. Soc.* **2010**, *132*, 11336–11342.

[72] Casillas-Ituarte, N. N.; Chen, X.; Castada, H.; Allen, H. C. *J. Phys. Chem. B* **2010**, *114*, 9485–9495.

[73] Chen, X.; Allen, H. C. *J. Phys. Chem. A* **2009**, *113*, 12655–12662.

[74] Harper, K. L.; Allen, H. C. *Langmuir* **2007**, *23*, 8925–8931.

[75] Can, S. Z.; Chang, C. F.; Walker, R. A. *Biochim. Biophys. Acta* **2008**, *1778*, 2368–2377.

[76] Nickolov, Z. S.; Britt, D. W.; Miller, J. D. *J. Phys. Chem. B* **2006**, *110*, 15506–15513.

[77] Mondal, J. A.; Nihonyanagi, S.; Yamaguchi, S.; Tahara, T. *J. Am. Chem. Soc.* **2010**, *132*, 10656–10657.

[78] Sung, W.; Seok, S.; Kim, D.; Tian, C. S.; Shen, Y. R. *Langmuir* **2010**, *26*, 18266–18272.

[79] Liu, J.; Conboy, J. C. *Langmuir* **2005**, *21*, 9091–9097.

[80] Liu, J.; Conboy, J. C. *J. Am. Chem. Soc.* **2004**, *126*, 8894–8895.

[81] Liu, J.; Conboy, J. C. *J. Phys. Chem. C* **2007**, *111*, 8988–8999.

[82] Liu, J.; Conboy, J. C. *Vib. Spectrosc.* **2009**, *50*, 106–115.

[83] Nguyen, T. T.; Rembert, K.; Conboy, J. C. *J. Am. Chem. Soc.* **2009**, *131*, 1401–1403.

[84] Liu, J.; Conboy, J. C. *J. Am. Chem. Soc.* **2004**, *126*, 8376–8377.

[85] Liu, J.; Conboy, J. C. *Biophys. J.* **2005**, *89*, 2522–2532.

[86] Anglin, T. C.; Conboy, J. C. *Biophys. J.* **2008**, *95*, 186–193.

[87] Anglin, T. C.; Conboy, J. C. *Biochemistry* **2009**, *48*, 10220–10234.

[88] Anglin, T. C.; Cooper, M. P.; Li, H.; Chandler, K.; Conboy, J. C. *J. Phys. Chem. B* **2010**, *114*, 1903–1914.

[89] Anglin, T. C.; Liu, J.; Conboy, J. C. *Biophys. J.* **2007**, *92*, L01–L03.

[90] Anglin, T. C.; Brown, K. L.; Conboy, J. C. *J. Struct. Biol.* **2009**, *168*, 37–52.

[91] Brown, K. L.; Conboy, J. C. *J. Am. Chem. Soc.* **2011**, *133*, 8794–8797.

[92] Tong, Y.; Li, N.; Liu, H.; Ge, A.; Osawa, M.; Ye, S. *Angew. Chem. Int. Ed. Engl.* **2010**, *49*, 2319–2323.

[93] Kim, J.; Kim, G.; Cremer, P. *Langmuir* **2001**, *17*, 7255–7260.

[94] Petralli-Mallow, T. P.; Briggman, K. A.; Richter, L. J.; Stephenson, J. C.; Plant, A. L. *Proc. SPIE* **1999**, *3858*, 25–31.

[95] Anderson, N. A.; Richter, L. J.; Stephenson, J. C.; Briggman, K. A. *Langmuir* **2006**, *22*, 8333–8336.

[96] Anderson, N. A.; Richter, L. J.; Stephenson, J. C.; Briggman, K. A. *J. Am. Chem. Soc.* **2007**, *129*, 2094–2100.

[97] Levy, D.; Briggman, K. A. *Langmuir* **2007**, *23*, 7155–7161.

[98] Kett, P. J. N.; Casford, M. T. L.; Davies, P. B. *Langmuir* **2010**, *26*, 9710–9719.

[99] Kett, P. J. N.; Casford, M. T. L.; Davies, P. B. *J. Phys. Chem. B* **2011**, *115*, 6465–6473.

[100] Lis, D.; Guthmuller, J.; Champagne, B.; Humbert, C.; Busson, B.; Tadjeddine, A.; Peremans, A.; Cecchet, F. *Chem. Phys. Lett.* **2010**, *489*, 12–15.

[101] Doyle, A. W.; Fick, J.; Himmelhaus, M.; Eck, W.; Graziani, I.; Prudovsky, I.; Grunze, M.; Maciag, T.; Neivandt, D. J. *Langmuir* **2004**, *20*, 8961–8965.

[102] Chen, X.; Tang, H.; Even, M. A.; Wang, J.; Tew, G. N.; Chen, Z. *J. Am. Chem. Soc.* **2006**, *128*, 2711–2714.

[103] Chen, X.; Chen, Z. *Biochim. Biophys. Acta* **2006**, *1758*, 1257–1273.

[104] Avery, C. W.; Som, A.; Xu, Y.; Tew, G. N.; Chen, Z. *Anal. Chem.* **2009**, *81*, 8365–8372.

[105] Yang, P.; Ramamoorthy, A.; Chen, Z. *Langmuir* **2011**, *27*, 7760–7767.

[106] Avery, C. W.; Palermo, E. F.; McLaughlin, A.; Kuroda, K.; Chen, Z. *Anal. Chem.* **2011**, *83*, 1342–1349.

[107] Chen, X.; Wang, J.; Kristalyn, C. B.; Chen, Z. *Biophys. J.* **2007**, *93*, 866–875.

[108] Nguyen, K. T.; Le Clair, S. V.; Ye, S.; Chen, Z. *J. Phys. Chem. B* **2009**, *113*, 12358–12363.

[109] Wang, T.; Li, D.; Lu, X.; Khmaladze, A.; Han, X.; Ye, S.; Yang, P.; Xue, G.; He, N.; Chen, Z. *J. Phys. Chem. C* **2011**, *115*, 7613–7620.

[110] Chen, X.; Boughton, A. P.; Tesmer, J. J. G.; Chen, Z. *J. Am. Chem. Soc.* **2007**, *129*, 12658–12659.

[111] Chen, X.; Wang, J.; Boughton, A. P.; Kristalyn, C. B.; Chen, Z. *J. Am. Chem. Soc.* **2007**, *129*, 1420–1427.

[112] Thennarasu, S.; Huang, R.; Lee, D.-K.; Yang, P.; Maloy, L.; Chen, Z.; Ramamoorthy, A. *Biochemistry* **2010**, *49*, 10595–10605.

[113] Ye, S.; Nguyen, K. T.; Boughton, A. P.; Mello, C. M.; Chen, Z. *Langmuir* **2010**, *26*, 6471–6477.

[114] Ye, S.; Nguyen, K. T.; Chen, Z. *J. Phys. Chem. B* **2010**, *114*, 3334–3340.

[115] Nguyen, K. T.; King, J. T.; Chen, Z. *J. Phys. Chem. B* **2010**, *114*, 8291–8300.

[116] Nguyen, K. T.; Soong, R.; Lm, S.-C.; Waskell, L.; Ramamoorthy, A.; Chen, Z. *J. Am. Chem. Soc.* **2010**, *132*, 15112–15115.

[117] Pavinatto, F. J.; Caseli, L.; Pavinatto, A.; dos Santos, D. S.; Nobre, T. M.; Zaniquelli, M. E. D.; Silva, H. S.; Miranda, P. B.; de Oliveira, O. N. *Langmuir* **2007**, *23*, 7666–7671.

[118] Pavinatto, F. J.; Pacholatti, C. P.; Montanha, E. A.; Caseli, L.; Silva, H. S.; Miranda, P. B.; Viitala, T.; Oliveira, O. N. *Langmuir* **2009**, *25*, 10051–10061.

[119] Nobre, T. M.; de Sousa e Silva, H.; Furriel, R. P. M.; Leone, F. A.; Miranda, P. B.; Zaniquelli, M. E. D. *J. Phys. Chem. B* **2009**, *113*, 7491–7497.

[120] Inoue, K.; Fujii, M.; Sakai, M. *Appl. Spectrosc.* **2010**, *64*, 275–281.

[121] Guo, L.; Har, J. Y.; Sankaran, J.; Hong, Y.; Kannan, B.; Wohland, T. *Chemphyschem* **2008**, *9*, 721–728.

[122] Chen, Y.; Lagerholm, B. C.; Yang, B.; Jacobson, K. *Methods* **2006**, *39*, 147–153.

[123] Zhang, L.; Granick, S. *J. Chem. Phys.* **2005**, *123*, 211104.

[124] Magde, D.; Elson, E.; Webb, W. *Phys. Rev. Lett.* **1972**, *29*, 705–708.

[125] García-Sáez, A. J.; Schwille, P. *Methods* **2008**, *46*, 116–122.

[126] Schwille, P.; Haustein, E. *Biophysics Textbook Online*; 2001; pp 1–33.

[127] Haustein, E.; Schwille, P. *Annu. Rev. Biophys. Biomol. Struct.* **2007**, *36*, 151–169.

[128] Hess, S.; Huang, S.; Heikal, A.; Webb, W. *Biochemistry* **2002**, *41*, 697–705.

[129] Rochira, J.; Gudheti, M.; Gould, T.; Laughlin, R.; Nadeau, J.; Hess, S. *J. Phys. Chem. C* **2007**, *111*, 1695–1708.

[130] Schwille, P.; Korlach, J.; Webb, W. *Cytometry* **1999**, *36*, 176–182.

[131] Burns, A.; Frankel, D.; Buranda, T. *Biophys. J.* **2005**, *89*, 1081–1093.

[132] Krichevsky, O.; Bonnet, G. *Rep. Prog. Phys.* **2002**, *65*, 251–297.

[133] Chiantia, S.; Ries, J.; Schwille, P. *Biochim. Biophys. Acta* **2009**, *1788*, 225–233.

[134] Elliott, J. T.; Burden, D. L.; Woodward, J. T.; Sehgal, A.; Douglas, J. F. *Langmuir* **2003**, *19*, 2275–2283.

[135] Bacia, K.; Majoul, I. V.; Schwille, P. *Biophys. J.* **2002**, *83*, 1184–1193.

[136] Kahya, N.; Scherfeld, D.; Bacia, K.; Poolman, B.; Schwille, P. *J. Biol. Chem.* **2003**, *278*, 28109–28115.

[137] Kahya, N.; Schwille, P. *Mol. Membr. Biol.* **2006**, *23*, 29–39.

[138] Kahya, N.; Schwille, P. *J. Fluoresc.* **2006**, *16*, 671–678.

[139] Korlach, J.; Schwille, P.; Webb, W. W.; Feigenson, G. W. *Proc. Natl. Acad. Sci. USA* **1999**, *96*, 8461–8466.

[140] Fahey, P. F.; Webb, W. W. *Biochemistry* **1978**, *17*, 3046–3053.

[141] Zhang, L.; Granick, S. *Proc. Natl. Acad. Sci. USA* **2005**, *102*, 9118–9121.

[142] Takakuwa, Y.; Pack, C. G.; An, X. L.; Manno, S.; Ito, E.; Kinjo, M. *Biophys. Chem.* **1999**, *82*, 149–155.

[143] Campbell, A. S.; Yu, Y.; Granick, S.; Gewirth, A. A. *Environ. Sci. Technol.* **2008**, *42*, 7496–7501.

[144] Dertinger, T.; Pacheco, V.; von der Hocht, I.; Hartmann, R.; Gregor, I.; Enderlein, J. *Chemphyschem* **2007**, *8*, 433–443.

[145] Benda, A.; Beneš, M.; Mareček, V.; Lhotský, A.; Hermens, W. T.; Hof, M. *Langmuir* **2003**, *19*, 4120–4126.

[146] Dertinger, T.; von der Hocht, I.; Benda, A.; Hof, M.; Enderlein, J. *Langmuir* **2006**, *22*, 9339–9344.

[147] Miszta, A.; Machán, R.; Benda, A.; Ouellette, A. J.; Hermens, W. T.; Hof, M. *J. Pept. Sci.* **2008**, *14*, 503–509.

[148] Renner, L.; Osaki, T.; Chiantia, S.; Schwille, P.; Pompe, T.; Werner, C. *J. Phys. Chem. B* **2008**, *112*, 6373–6378.

[149] Štefl, M.; Kułlakowska, A.; Hof, M. *Biophys. J.* **2009**, *97*, L01–L03.

[150] Beranova, L.; Cwiklik, L.; Jurkiewicz, P.; Hof, M.; Jungwirth, P. *Langmuir* **2010**, *26*, 6140–6144.

[151] Machán, R.; Miszta, A.; Hermens, W.; Hof, M. *Chem. Phys. Lipids* **2010**, *163*, 200–206.

[152] Macháň, R.; Hof, M.; Chernovets, T.; Zhmak, M. N.; Ovchinnikova, T. V.; Sýkora, J. *Anal. Biolanal. Chem.* **2011**, *399*, 3547–3554.

[153] Przybylo, M.; Sýkora, J.; Humpolíckova, J.; Benda, A.; Zan, A.; Hof, M. *Langmuir* **2006**, *22*, 9096–9099.

[154] Kriegsmann, J.; Gregor, I.; von der Hocht, I.; Klare, J.; Engelhard, M.; Enderlein, J.; Fitter, J. *Chembiochem* **2009**, *10*, 1823–1829.

[155] Gielen, E.; VandeVen, M.; Margineanu, A.; Dedecker, P.; Auweraer, M. V. D.; Engelborghs, Y.; Hofkens, J.; Ameloot, M. *Chem. Phys. Lett.* **2009**, *469*, 110–114.

[156] Humpolíčková, J.; Gielen, E.; Benda, A.; Fagulova, V.; Vercammen, J.; VandeVen, M.; Hof, M.; Ameloot, M.; Engelborghs, Y. *Biophys. J.* **2006**, *91*, L23–L25.

[157] Ganguly, S.; Chattopadhyay, A. *Biophys. J.* **2010**, *99*, 1397–1407.

[158] Šegota, S.; Težak, u. *Adv. Colloid Interface Sci.* **2006**, *121*, 51–75.

[159] Kleinfeld, A. M.; Chu, P.; Romero, C. *Biochemistry* **1997**, *36*, 14146–14158.

[160] Wong, J. Y.; Majewski, J.; Seitz, M.; Park, C. K.; Israelachvili, J. N.; Smith, G. S. *Biophys. J.* **1999**, *77*, 1445–1457.

[161] Schäfer, T.; Zentgraf, H.; Zehe, C.; Brügger, B.; Bernhagen, J.; Nickel, W. *J. Biol. Chem.* **2004**, *279*, 6244–6251.

[162] Uchiyama-Kokubu, N.; Naito, M.; Nakajima, M.; Tsuruo, T. *FEBS Lett.* **2004**, *574*, 55–61.

[163] Stegmayer, C.; Kehlenbach, A.; Tournaviti, S.; Wegehingel, S.; Zehe, C.; Denny, P.; Smith, D. F.; Schwappach, B.; Nickel, W. *J. Cell Sci.* **2005**, *118*, 517–527.

[164] Doyle, A. W. Non-classical export of signal peptide-less proteins studied via sum frequency spectroscopy and biochemical techniques. Ph.D. Thesis, University of Maine, 2008.

[165] Yang, Y.; Hu, L.; Chen, X.; Ottow, E. A.; Polle, A.; Jiang, X. *Biochim. Biophys. Acta* **2007**, *1768*, 2078–2088.

[166] de Beer, A.; de Aguiar, H.; Nijsen, J.; Roke, S. *Phys. Rev. Lett.* **2009**, *102*, 095502.

[167] de Beer, A.; Roke, S. *Phys. Rev. B* **2007**, *75*, 245438.

[168] Tien, H. T.; Ottova, A. L. *J. Memb. Sci.* **2001**, *189*, 83–117.

[169] Castellana, E.; Cremer, P. *Surf. Sci. Rep.* **2006**, *61*, 429–444.

[170] Römer, W.; Lam, Y. H.; Fischer, D.; Watts, A.; Fischer, W. B.; Göring, P.; Wehrspohn, R. B.; Gösele, U.; Steinem, C. *J. Am. Chem. Soc.* **2004**, *126*, 16267–16274.

[171] Baumgart, T.; Offenhäusser, A. *Langmuir* **2003**, *19*, 1730–1737.

[172] Duschl, C.; Liley, M.; Lang, H.; Ghandi, A.; Zakeeruddin, S. M.; Stahlberg, H.; Dubochet, J.; Nemetz, A.; Knoll, W.; Vogel, H. *Mat. Sci. Eng. C* **1996**, *4*, 7–18.

[173] Plant, A. *Langmuir* **1999**, *15*, 5128–5135.

[174] Dubois, L. H.; Nuzzo, R. G. *Annu. Rev. Phys. Chem.* **1992**, *43*, 437–463.

[175] Roberts, G. *Contemp. Phys.* **1984**, *25*, 109–128.

[176] Rao, N. M.; Silin, V.; Ridge, K. D.; Woodward, J. T.; Plant, A. L. *Anal. Biochem.* **2002**, *307*, 117–130.

[177] Zhang, L.; Vidu, R.; Waring, A.; Lehrer, R.; Longo, M.; Stroeve, P. *Langmuir* **2002**, *18*, 1318–1331.

[178] Tien, H. T.; Ottova, A. L. *Colloids Surf. A Physicochem. Eng. Asp.* **1999**, *149*, 217–233.

[179] Tien, H. T.; Wurster, S. H.; Ottova, A. L. *Bioelectrochem. Bioenerg.* **1997**, *42*, 77–94.

[180] Ottova, A.; Tvarozek, V.; Racek, J.; Sabo, J.; Ziegler, W.; Hianik, T.; Tien, H. T. *Supramol. Sci.* **1997**, *4*, 101–112.

[181] Ottova, A. L.; Tien, H. T. *Bioelectrochem. Bioenerg.* **1997**, *42*, 141–152.

[182] Ottova, A.; Tien, H. T. *Bioelectrochemistry* **2002**, *56*, 171–173.

[183] Asaka, K.; Ottova, A.; Tien, H. T. *Thin Solid Films* **1999**, *354*, 201–207.

[184] Asaka, K.; Tien, H. T.; Ottova, A. *J. Biochem. Biophys. Methods* **1999**, *40*, 27–37.

[185] Tamm, L.; McConnell, H. *Biophys. J.* **1985**, *47*, 105–113.

[186] Hinterdorfer, P.; Baber, G.; Tamm, L. *J. Biol. Chem.* **1994**, *269*, 20360–20368.

[187] Salafsky, J.; Groves, J.; Boxer, S. *Biochemistry* **1996**, *35*, 14773–14781.

[188] Scomparin, C.; Lecuyer, S.; Ferreira, M.; Charitat, T.; Tinland, B. *Eur. Phys. J. E* **2009**, *220*, 211–220.

[189] Chi, L. F.; Johnston, R. R.; Ringsdorf, H.; Kimizuka, N.; Kunitake, T. *Langmuir* **1992**, *8*, 1360–1365.

[190] Sackmann, E. *Science* **1996**, *271*, 43–48.

[191] Tanaka, M.; Sackmann, E. *Nature* **2005**, *437*, 656–663.

[192] Purrucker, O.; Förtig, A.; Jordan, R.; Tanaka, M. *Chemphyschem* **2004**, *5*, 327–335.

[193] Albertorio, F.; Diaz, A. J.; Yang, T.; Chapa, V. A.; Kataoka, S.; Castellana, E. T.; Cremer, P. S. *Langmuir* **2005**, *21*, 7476–7482.

[194] Albertorio, F.; Daniel, S.; Cremer, P. S. *J. Am. Chem. Soc.* **2006**, *128*, 7168–7169.

[195] Cremer, P. S.; Yang, T. *J. Am. Chem. Soc.* **1999**, *121*, 8130–8131.

[196] Holden, M. A.; Jung, S.-Y.; Yang, T.; Castellana, E. T.; Cremer, P. S. *J. Am. Chem. Soc.* **2004**, *126*, 6512–6513.

[197] Smith, E. A.; Coym, J. W.; Cowell, S. M.; Tokimoto, T.; Hruby, V. J.; Yamamura, H. I.; Wirth, M. J. *Langmuir* **2005**, *21*, 9644–9650.

[198] Atanasov, V.; Knorr, N.; Duran, R. S.; Ingebrandt, S.; Offenhäusser, A.; Knoll, W.; Köper, I. *Biophys. J.* **2005**, *89*, 1780–1788.

[199] Knoll, W.; Köper, I.; Naumann, R.; Sinner, E. *Electrochim. Acta* **2008**, *53*, 6680–6689.

[200] Kügler, R.; Knoll, W. *Bioelectrochemistry* **2002**, *56*, 175–178.

[201] Naumann, R.; Schiller, S.; Giess, F.; Grohe, B.; Hartman, K.; Kärcher, I.; Köper, I.; Lübben, J.; Vasilev, K.; Knoll, W. *Langmuir* **2003**, *19*, 5435–5443.

[202] Shen, W. W.; Boxer, S. G.; Knoll, W.; Frank, C. W. *Biomacromolecules* **2001**, *2*, 70–79.

[203] Spinke, J.; Yang, J.; Wolf, H.; Liley, M.; Ringsdorf, H.; Knoll, W. *Biophys. J.* **1992**, *63*, 1667–1671.

[204] Munro, J. C.; Frank, C. W. *Langmuir* **2004**, *20*, 10567–10575.

[205] Weng, K. C.; Stålgren, J. J.; Duval, D. J.; Risbud, S. H.; Frank, C. W. *Langmuir* **2004**, *20*, 7232–7239.

[206] Luo, G.; Liu, T.; Zhao, X. S.; Huang, Y.; Huang, C.; Cao, W. *Langmuir* **2001**, *17*, 4074–4080.

[207] Kühner, M.; Tampé, R.; Sackmann, E. *Biophys. J.* **1994**, *67*, 217–226.

[208] Arya, A.; Krull, U. J.; Thompson, M.; Wong, H. *Anal. Chim. Acta* **1985**, *173*, 331–336.

[209] Wiegand, G.; Jaworek, T.; Wegner, G.; Sackmann, E. *Langmuir* **1997**, *13*, 3563–3569.

[210] Nissen, J.; Gritsch, S.; Wiegand, G.; Rädler, J. *Eur. Phys. J. B* **1999**, *10*, 335–344.

[211] Györvary, E.; Wetzer, B.; Sleytr, U. B.; Sinner, A.; Offenhäusser, A.; Knoll, W. *Langmuir* **1999**, *15*, 1337–1347.

[212] Elender, G.; Kühner, M.; Sackmann, E. *Biosens. Bioelectron.* **1996**, *11*, 565–577.

[213] Hillebrandt, H.; Wiegand, G.; Tanaka, M.; Sackmann, E. *Langmuir* **1999**, *15*, 8451–8459.

[214] Baumgart, T.; Offenhäusser, A. *Langmuir* **2002**, *18*, 5899–5908.

[215] Naumann, C. A.; Prucker, O.; Lehmann, T.; Rühe, J.; Knoll, W.; Frank, C. W. *Biomacromolecules* **2002**, *3*, 27–35.

[216] Smith, H.; Jablin, M.; Vidyasagar, A.; Saiz, J.; Watkins, E.; Toomey, R.; Hurd, A.; Majewski, J. *Phys. Rev. Lett.* **2009**, *102*, 228102.

[217] Rohindra, D.; Nand, A.; Khurma, J. *S. Pac. J. Nat. Sci.* **2004**, *22*, 32–35.

[218] Deng, T.; Wang, H.; Li, J.; Shen, G.; Yu, R. *Anal. Chim. Acta* **2005**, *532*, 137–144.

[219] Allgeyer, E. S.; Pongan, A.; Browne, M.; Mason, M. D. *Nano Lett.* **2009**, *9*, 3816–3819.

[220] Lee, T.-H.; Heng, C.; Swann, M. J.; Gehman, J. D.; Separovic, F.; Aguilar, M.-I. *Biochim. Biophys. Acta* **2010**, *1798*, 1977–1986.

[221] Richter, R. P.; Brisson, A. R. *Langmuir* **2003**, *19*, 1632–1640.

[222] Martin and Szablewski, M., P. *Langmuir-Blodgett troughs operating manual*; NIMA Technology: Coventry, England, 1989.

[223] Lambert, A. G. Resonantly Enhanced Sum Frequency Spectroscopy of Adsorption on Hydrophilic Mica Substrates. Ph.D. Thesis, University of Cambridge, 2001.

[224] Ye, S.; Uosaki, K. Sum frequency generation (SFG) evaluation of the chemically modified solid surface. 2007.

[225] Hirose, C.; Akamatsu, N.; Domen, K. *Appl. Spectrosc.* **1992**, *46*, 1051–1072.

[226] Richmond, G. *Annu. Rev. Phys. Chem.* **2001**, *52*, 357–389.

[227] Dreesen, L.; Sartenaer, Y.; Humbert, C.; Mani, a.; Lemaire, J.; Methivier, C.; Pradier, C.; Thiry, P.; Peremans, a. *Thin Solid Films* **2004**, *464-465*, 373–378.

[228] Löbau, J.; Wolfrum, K. *J. Opt. Soc. Am. B* **1997**, *14*, 2505–2512.

[229] Zappe, H. *Fundamentals of Micro-Optics*; Cambridge University: Cambridge, 2010; p 647.

[230] Williams, C. T.; Yang, Y.; Bain, C. D. *Langmuir* **2000**, *16*, 2343–2350.

[231] York, R. L.; Li, Y.; Holinga, G. J.; Somorjai, G. A. *J. Phys. Chem. A* **2009**, *113*, 2768–2774.

[232] Allgeyer, E. S. Development of instrumentation for sum frequency spectral imaging combined with confocal fluorescence imaging and additional topics. Ph.D. Thesis, University of Maine, 2011.

[233] Rüttinger, S.; Buschmann, V.; Krämer, B.; Erdmann, R.; Macdonald, R.; Koberling, F. *J. Microsc.* **2008**, *232*, 343–352.

[234] Müller, C. B.; Loman, A.; Pacheco, V.; Koberling, F.; Willbold, D.; Richtering, W.; Enderlein, J. *Europhys. Lett.* **2008**, *83*, 46001.

[235] Allgeyer, E. S.; Sterling, S. M.; Neivandt, D. J.; Mason, M. D. *Rev. Sci. Instrum.* **2011**, *82*, 053708.

[236] Ries, J.; Bayer, M.; Csúcs, G.; Dirkx, R.; Solimena, M.; Ewers, H.; Schwille, P. *Opt. Express* **2010**, *18*, 11073–11082.

[237] Rajalingam, D.; Graziani, I.; Prudovsky, I.; Yu, C.; Kumar, T. K. S. *Biochemistry* **2007**, *46*, 9225–9238.

[238] Sodek, J.; Ganss, B.; McKee, M. *Crit. Rev. Oral. Biol. Med.* **2000**, *11*, 279–303.

[239] Wang, K. X.; Denhardt, D. T. *Cytokine Growth Factor Rev.* **2008**, *19*, 333–345.

[240] Lee, C.; Bain, C. D. *Biochim. Biophys. Acta* **2005**, *1711*, 59–71.

[241] Silvius, J. R. In *Lipid-Protein Interactions*; Jost, P. C., Griffith, O. H., Eds.; Wiley: New York, 1982; pp 239–281.

[242] Wawrezinieck, L.; Rigneault, H.; Marguet, D.; Lenne, P.-F. *Biophys. J.* **2005**, *89*, 4029–4042.

[243] Sterling, S. M.; Allgeyer, E. S.; Fick, J.; Prudovsky, I.; Mason, M. D.; Neivandt, D. J. *Langmuir* **2013**, *Manuscript in review*.

[244] Forstner, M. B.; Yee, C. K.; Parikh, A. N.; Groves, J. T. *J. Am. Chem. Soc.* **2006**, *128*, 15221–15227.

[245] Lamy-Freund, M. T.; Riske, K. A. *Chem. Phys. Lipids* **2003**, *122*, 19–32.

[246] Spinozzi, F.; Paccamiccio, L.; Mariani, P.; Amaral, L. Q. *Langmuir* **2010**, *26*, 6484–6493.

[247] Verbal communication, Avanti Polar Lipids, Inc., 2006.

[248] Contreras, L. M.; de Almeida, Rodrigo, F.; Villalaín, J.; Fedorov, A.; Prieto, M. *Biophys. J.* **2001**, *80*, 2273–2283.

[249] Baumgart, T.; Hunt, G.; Farkas, E. R.; Webb, W. W.; Feigenson, G. W. *Biochim. Biophys. Acta* **2007**, *1768*, 2182–2194.

[250] Bagatolli, L.; Gratton, E. *Biophys. J.* **2000**, *78*, 290–305.

[251] Gudmand, M.; Fidorra, M.; Bjørnholm, T.; Heimburg, T. *Biophys. J.* **2009**, *96*, 4598–4609.

[252] Cevc, G.; Watts, A.; Marsh, D. *Biochemistry* **1981**, *20*, 4955–4965.

[253] Lefèvre, T.; Subirade, M. *Int. J. Biol. Macromol.* **2000**, *28*, 59–67.

[254] Petrache, H. I.; Tristram-Nagle, S.; Gawrisch, K.; Harries, D.; Parsegian, V. A.; Nagle, J. F. *Biophys. J.* **2004**, *86*, 1574–1586.

[255] Marsh, D. *CRC Handbook of Lipid Bilayers*; CRC Press: Boca Raton, 1990.

[256] Van Aelst, L.; Symons, M. *Genes Dev.* **2002**, *16*, 1032–1054.

[257] Carlsson, A. E. *Annu. Rev. Biophys.* **2010**, *39*, 91–110.

[258] Landriscina, M.; Prudovsky, I.; Mouta Carreira, C.; Soldi, R.; Tarantini, F.; Maciag, T. *J. Biol. Chem.* **2000**, *275*, 32753–32762.

[259] Mehta, A.; Rock, R.; Rief, M.; Spudich, J.; Mooseker, M.; Cheney, R. *Nature* **1999**, *400*, 590–596.

[260] Doherty, G. J.; McMahon, H. T. *Annu. Rev. Biophys.* **2008**, *37*, 65–95.

[261] Yu, J. H.; Crevenna, A. H.; Bettenbühl, M.; Freisinger, T.; Wedlich-Söldner, R. *J. Cell Sci.* **2011**, *124*, 1533–1541.

[262] Bosk, S.; Braunger, J. A.; Gerke, V.; Steinem, C. *Biophys. J.* **2011**, *100*, 1708–1717.

[263] Harder, T.; Kellner, R.; Parton, R.; Gruenberg, J. *Mol. Biol. Cell* **1997**, *8*, 533–545.

[264] Pato, C.; Stetzkowski-Marden, F.; Gaus, K.; Recouvreur, M.; Cartaud, A.; Cartaud, J. *Chem. Biol. Interact.* **2008**, *175*, 64–67.

[265] Viola, A.; Gupta, N. *Nat. Rev. Immunol.* **2007**, *7*, 889–896.

[266] Saotome, I.; Curto, M.; McClatchey, A. I. *Dev. Cell* **2004**, *6*, 855–864.

[267] Ruiz-Cañada, C.; Budnik, V. *Int. Rev. Neurobiol.* **2006**, *75*, 217–236.

[268] Svitkina, T. M.; Bulanova, E. A.; Chaga, O. Y.; Vignjevic, D. M.; Kojima, S.-i.; Vasiliev, J. M.; Borisy, G. G. *J. Cell Biol.* **2003**, *160*, 409–421.

[269] DePina, A. S.; Wöllert, T.; Langford, G. M. *Cell Motil. Cytoskeleton* **2007**, *64*, 739–755.

[270] Vicente-Manzanares, M.; Sánchez-Madrid, F. *Nat. Rev. Immunol.* **2004**, *4*, 110–122.

[271] Chandrasekar, I.; Stradal, T. E. B.; Holt, M. R.; Entschladen, F.; Jockusch, B. M.; Ziegler, W. H. *J. Cell Sci.* **2005**, *118*, 1461–1472.

[272] Demé, B.; Hess, D.; Tristl, M.; Lee, L.-T.; Sackmann, E. *Eur. Phys. J. E* **2000**, *2*, 125–136.

[273] Sengupta, K.; Limozin, L.; Tristl, M.; Haase, I.; Fischer, M.; Sackmann, E. *Langmuir* **2006**, *22*, 5776–5785.

[274] Barfoot, R. J.; Sheikh, K. H.; Johnson, B. R. G.; Colyer, J.; Miles, R. E.; Jeuken, L. J. C.; Bushby, R. J.; Evans, S. D. *Langmuir* **2008**, *24*, 6827–6836.

[275] Zhang, Y.; Cheng, C.-m.; Cusick, B.; LeDuc, P. R. *Langmuir* **2007**, *23*, 8129–8134.

[276] Liu, A. P.; Fletcher, D. A. *Biophys. J.* **2006**, *91*, 4064–4070.

[277] Grigoriev, P. A.; Tarahovsky, Y. S.; Pavlik, L. L.; Udaltsov, S. N.; Moshkov, D. A. *IUBMB Life* **2000**, *50*, 227–233.

[278] Isanta, S.; Espinosa, G.; Rodríguez-García, R.; Natale, P.; López-Montero, I.; Langevin, D.; Monroy, F. *Soft Matter* **2011**, *7*, 3100.

[279] Kiessling, V.; Domanska, M. K.; Murray, D.; Wan, C.; Tamm, L. K. *Wiley Encyclopedia of Chemical Biology*; John Wiley & Sons: Hoboken, 2008; pp 411–422.

[280] Pardee, J.; Spudich, J. *Methods Enzymol.* **1982**, *85*, 164–181.

[281] Bradford, M. *Anal. Biochem.* **1976**, *72*, 248–254.

[282] Okada, T.; Yamamoto, Y.; Sano, M.; Muramatsu, H. *Ultramicroscopy* **2009**, *109*, 1299–303.

[283] An, Y.; Chen, M.; Xue, Q.; Liu, W. *J. Colloid Interface Sci.* **2007**, *311*, 507–513.

[284] Dawes, R. P. Development of an actin hydrogel substrate for fluorescence correlation spectroscopy of FGF protein transfer across a model membrane. Honors Thesis, University of Maine, 2011.

[285] Hennesthal, C.; Steinem, C. *J. Am. Chem. Soc.* **2000**, *122*, 8085–8086.

[286] Renault, A.; Lenne, P. F.; Zakri, C.; Aradian, A.; Vénien-Bryan, C.; Amblard, F. *Biophys. J.* **1999**, *76*, 1580–1590.

[287] Bouchard, M.; Pare, C.; Dutasta, J. P.; Chauvet, J. P.; Gicquaud, C.; Auger, M. *Biochemistry* **1998**, *37*, 3149–3155.

[288] Le Bihan, T.; Pelletier, D.; Tancrède, P.; Heppell, B.; Chauvet, J. P.; Gicquaud, C. R. *J. Colloid Interface Sci.* **2005**, *288*, 88–96.

[289] Li, A.-X.; Cui, X.-Q.; Yang, F.; Yang, X.-R. *Chinese J. Anal. Chem.* **2009**, *37*, 25–29.

[290] Laliberte, A.; Gicquaud, C. *J. Cell Biol.* **1988**, *106*, 1221–1227.

[291] Limozin, L.; Bärmann, M.; Sackmann, E. *Eur. Phys. J. E* **2003**, *10*, 319–330.

[292] Gicquaud, C. *Biochem. Biophys. Res. Commun.* **1995**, *208*, 1154–1158.

[293] Ye, S.; Noda, H.; Morita, S.; Uosaki, K.; Osawa, M. *Langmuir* **2003**, *19*, 2238–2242.

[294] Tong, Y.; Zhao, Y.; Li, N.; Ma, Y.; Osawa, M.; Davies, P. B.; Ye, S. *J. Chem. Phys.* **2010**, *133*, 034705.

[295] Li, L. Cellulose Model Surfaces Studied by Femtosecond Sum Frequency Spectroscopy. Ph.D. Thesis, University of Maine, 2012.

[296] Ong, T. H.; Davies, P. B.; Bain, C. D. *Langmuir* **1993**, *9*, 1836–1845.

[297] Cimatu, K.; Baldelli, S. *J. Phys. Chem. B* **2006**, *110*, 1807–1813.

[298] Hoffmann, D. M. P.; Kuhnke, K.; Kern, K. *Rev. Sci. Instrum.* **2002**, *73*, 3221.

[299] Mizutani, G.; Miyauchi, Y. *Surf. Interface Anal.* **2010**, *42*, 1675–1679.

[300] Miersch, S.; Mutus, B. *Curr. Anal. Chem.* **2007**, *3*, 81–92.

[301] Dietrich, C.; Bagatolli, L. A.; Volovyk, Z. N.; Thompson, N. L.; Levi, M.; Jacobson, K.; Gratton, E. *Biophys. J.* **2001**, *80*, 1417–1428.

[302] Hammond, A.; Heberle, F.; Baumgart, T.; Holowka, D.; Baird, B.; Feigenson, G. W. *Proc. Natl. Acad. Sci. USA* **2005**, *102*, 6320–6325.

[303] Ratto, T.; Longo, M. *Biophys. J.* **2002**, *83*, 3380–3392.

[304] Lin, W.-C.; Blanchette, C. D.; Ratto, T. V.; Longo, M. L. *Biophys. J.* **2006**, *90*, 228–237.

[305] Crane, J. M.; Tamm, L. K. *Biophys. J.* **2004**, *86*, 2965–2979.

[306] Crane, J. M.; Kiessling, V.; Tamm, L. K. *Langmuir* **2005**, *21*, 1377–1388.

[307] Brugnerotto, J.; Lizardi, J.; Goycoolea, F. M.; Argüelles-Monal, W.; Desbrières, J.; Rinaudo, M. *Polymer* **2001**, *42*, 3569–3580.

[308] Rinia, H.; Demel, R.; van der Eerden, J.; de Kruijff, B. *Biophys. J.* **1999**, *77*, 1683–1693.

[309] Zachowski, A. *Biochem. J.* **1993**, *294*, 1–14.

[310] Kay, J. G.; Koivusalo, M.; Ma, X.; Wohland, T.; Grinstein, S. *Mol. Biol. Cell* **2012**, *23*, 2198–2212.

[311] Leventis, P. A.; Grinstein, S. *Annu. Rev. Biophys.* **2010**, *39*, 407–427.

Appendix A

INFRARED SPECTRUM OF POLYSTYRENE

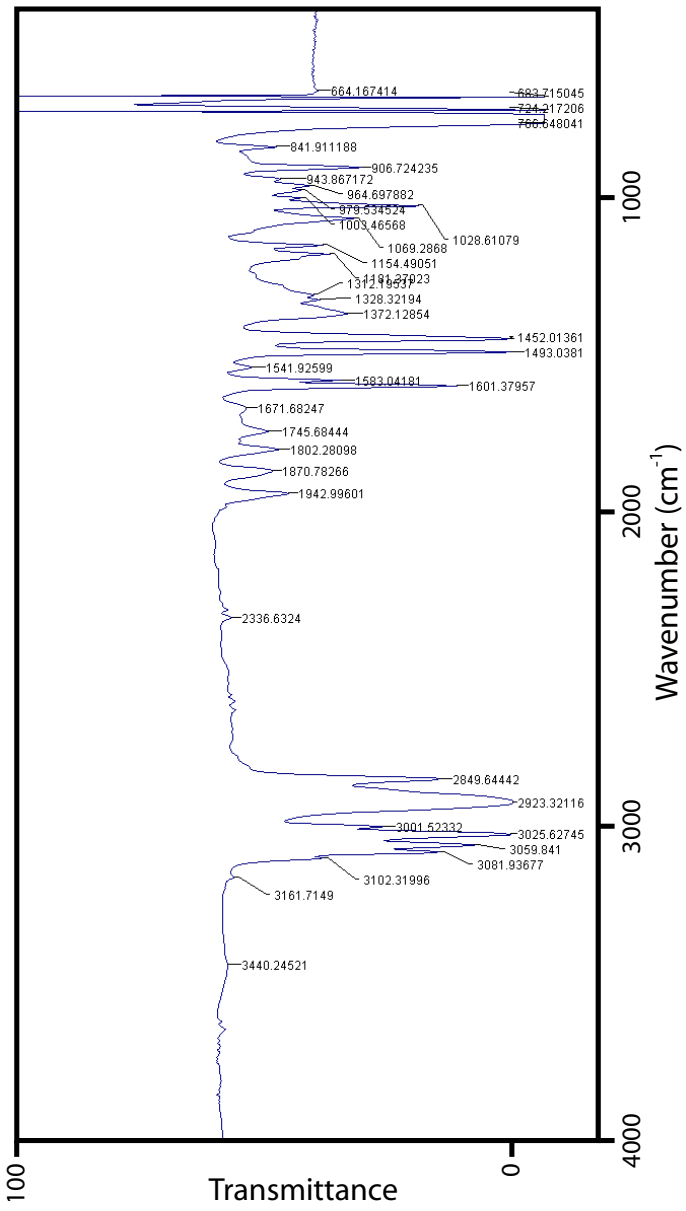

Figure A.1. IR spectrum of a polystyrene film employed as a calibration standard for the Neivandt sum frequency spectrometer.

Appendix B

STANDARD OPERATING PROCEDURE FOR THE NEIVANDT SF SPECTROMETER

Start up:

1. Turn laser warning light on
2. Switch laser warning sign on lab door
3. Turn key on the Empower power supply to reset
4. Fill in required information on the SFS Daily Log (room and laser conditions)
5. Place beam blocks in Spitfire output
6. Put on laser goggles
7. Start the Mai Tai:
   (a) Open the Mai Tai control program on the black laptop (COM-Port 1)
   (b) Confirm that the Set Wavelength is 800 nm
   (c) Hold On/Off Button until EMISSION appears
   (d) Wait until Output power rises to approximately the previous day's Output power and confirm that the laser starts pulsing (green indicator light)
      - Should the pulsing light not turn on, deviate the wavelength from 800 nm until the light comes on, and then move back to 800 nm
   (e) Push and hold Shutter button until red indicator light turns on
8. Start the Empower:

(a) Open the Empower software on the gray laptop

(b) Check that the "COM" has a green light in the program. If the program displays a red light for "FAULT", open the Fault Menu and press the "Reset Faults" button. If this does not resolve the issue, turn the power supply key to the "Off" position and then to the "On" position. Press the "Reset Faults" button again, and close this window

(c) Confirm that the Set Current is set to the previous day's current (via Setup Menu)

(d) Press and hold the green "RUN" button until EMISSION appears

9. Press the "Reset" button on the High Speed Driver, taking care not to touch any knobs

10. Turn on Pockels Cell 1 only

    (a) If the Pockels Cells do not turn on, confirm the Mai Tai shutter is open

11. Wait 45-60 minutes for warm up

12. Turn on Pockels Cell 2

13. Wait 30 minutes for warm up

14. Remove the beam blocks from the Spitfire output

15. Start the TOPAS-C:

    (a) Open TOPAS program on laser table laptop

    (b) Set the desired wavelength and open the shutter

    (c) Consult blue section of TOPAS-C manual if there are programmatic issues

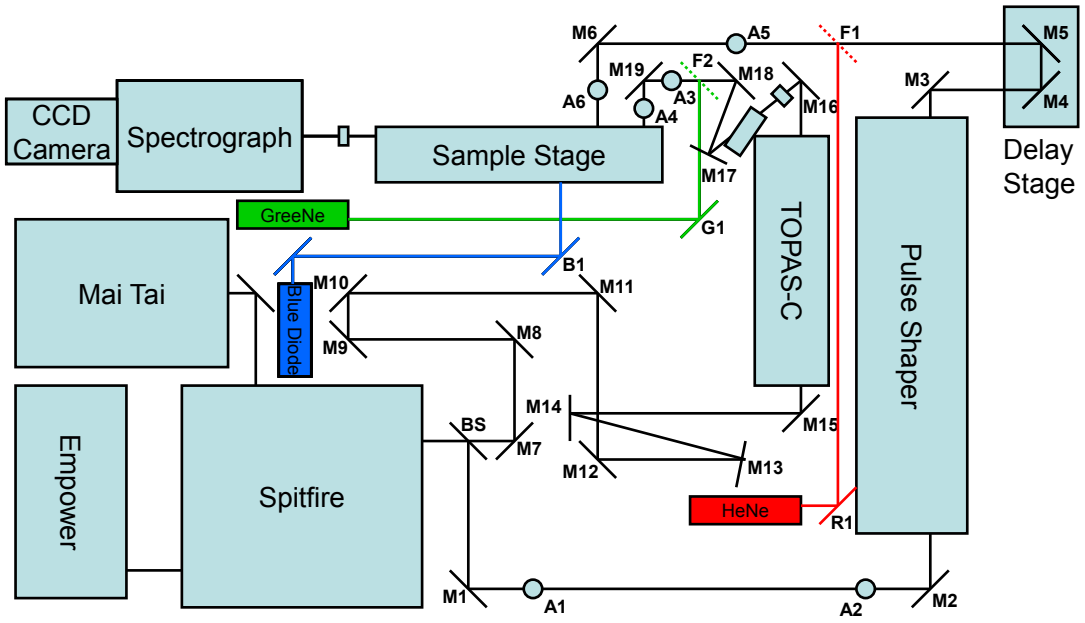

Figure B.1. Schematic of the Neivandt SF spectrometer (not to scale).

16. Wait at least 30 minutes for warm up (may start alignment of visible beam)

Equipment Alignment:

1. Mai Tai and Empower: Please consult a technician *before* opening the cases

2. Pump laser in the amplifier: Alignment is performed following the Spitfire manual *after* consulting technician regarding the issues

3. Spitfire to the TOPAS-C: Alignment of M7 through M15 is performed *after* consulting the technician regarding the issues

4. OPA (TOPAS-C): Alignment is performed following Chapter 4 of the Light Conversion, TOPAS-C manual *after* consulting technician regarding the issues

5. Spitfire to Pulse shaper to Sample stage (Figure B.1):

   (a) Adjust reflected beam from the beam splitter (BS) to the center of mirror M1 using alignment irises A1 and A2

(b) Employ mirrors M1 and M2 to center the beam on M3 and confirm that the beam is not clipped in the pulse shaper

(c) Measure the energy of the beam after the pulse shaper. If it is significantly lower than 10 μJ open the shaper and check the slit width (0.43 mm) and try to optimize the energy by moving the slit. If this doesn't help, realign the shaper (see CDP SS-800 user manual)

(d) Align the 800 nm beam from the pulse shaper using irises A5 and A6

- Use M5 for A5 and use M6 for A6

(e) Block the 800 nm beam at the pulse shaper

(f) Turn on the red HeNe (key switch near TOPAS laptop)

(g) Flip the F1 mirror into the 800 nm beam path

(h) Proceed to align the HeNe through A5 and A6

- Use R1 for A5 and use F1 for A6

6. Mid IR beam to Sample stage (Figure B.1):

(a) Optional: Place the power meter in the path of the beam coming out of the TOPAS and optimize the power by pressing on the corners of M15. Only adjust the mirror the slightest bit if required to optimize

(b) Use the heat sensitive paper to track the mid IR beam. Due to the fact that the paper has a smooth surface and is therefore reflecting part of the beam, make sure to wear the laser safety goggles at all times

(c) Note that the beam should be optimized through the two filters to the center of M17 and M18. If it is not, block the beam and replace M17 with a power meter and optimize power. Then replace the power meter with M17 and use the heat sensitive paper to direct the beam to center of M17 and M18

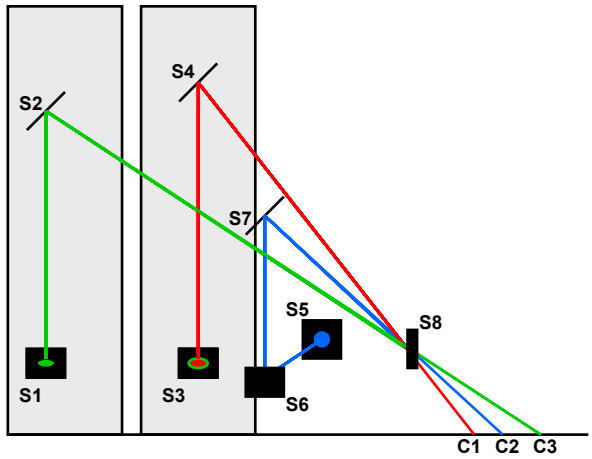

Figure B.2. Schematic of the sample stage for the SF excitation beam alignment (not to scale).

(d) Align the Mid IR beam from the TOPAS using irises A3 and A4

- Use M18 for A3 and use M19 for A4

(e) Block the Mid IR beam at the TOPAS

(f) Turn on the GreeNe (key switch near the Sample stage)

(g) Flip the F2 mirror into the Mid IR beam path

(h) Proceed to align the GreeNe through A3 and A4

- Use G1 for A3 and use F2 for A4

7. Sample stage - first part (Figure B.2):

(a) Block all the beams and remove the sample stage from its specified location

(b) Screw the standard alignment post with iris into the hole marked with arrows (noted as S8)

(c) Determine angles to be used for measurement and find the corresponding cross-hatch markings on the table (noted as C1, C2, and C3 for the visible, SF, and mid IR beams, respectively)

(d) Alignment of GreeNe

- Use mirror S1 to align the beam through the center of S8
- Use mirror S2 to center the beam on C3

(e) Alignment of HeNe

- Use mirror S3 to align the beam through the center of S8
- Use mirror S4 to center the beam on C1

(f) Alignment of the Blue diode

- Turn on the blue diode by plugging the power cord into the power supply
- Note that S7 is a flipping ND filter and will allow some light to pass, so be sure to have on laser safety goggles
- Block the beam, flip S7 into the beam path, and then unblock the beam
- Use mirror S5 to align the beam through the center of S8
- Use mirror S6 to center the beam on C2

8. Sample stage - second part (Figure B.3)

(a) Block all the beams

(b) Replace S8 with the sample stage, confirm that it is center in the beam path, and verify the height of the stage (and sample) with a ruler (166 mm)

(c) With a reflective sample on the stage (eg: gold coated silicon), continue to align the blue diode

- Unblock the beam
- Confirm that the beam is nearly centered on the S9 iris

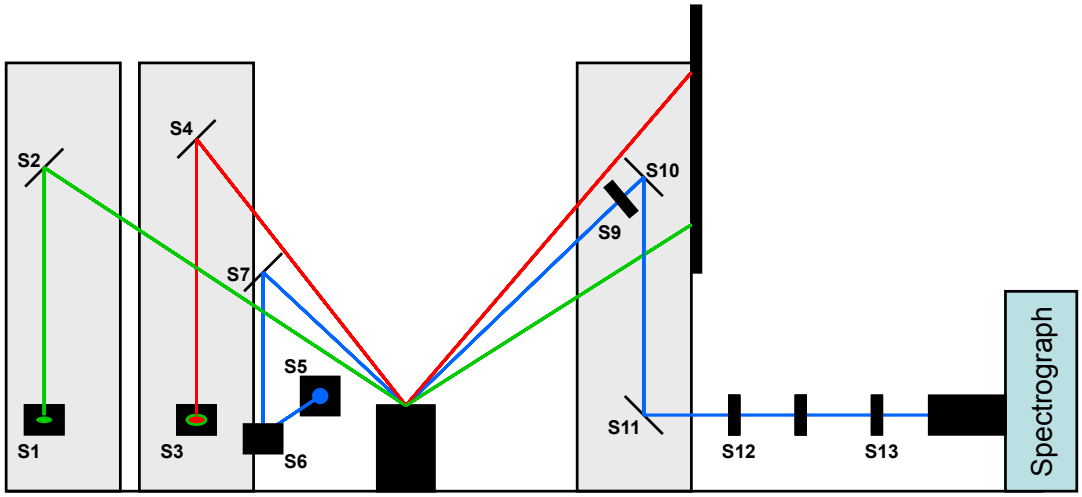

Figure B.3. Schematic of the sample stage for the SF emission beam alignment (not to scale).

- Use mirror S10 to align the beam through the center of iris S12
- Use mirror S11 to align the beam through the center of iris S13

(d) Turn off the HeNe, GreeNe, and Blue diode, flip F1, F2, and S7 out of the beam paths, and remove or open any irises in the beam path. Be sure that the 800 nm and Mid IR beams are still blocked

Taking a measurement:

1. Verify that the 800 nm and Mid IR beams are blocked
2. Turn off all lights in the room
3. Verify that the Spectrograph and CCD camera power supplies are turned on
4. Open WinSpec32 software on main computer hub
5. Confirm that the CCD camera is in Safe Mode
6. Verify the Detector Temperature is -20°C (Setup menu)

   (a) If it is not, enter -20°C and click Set Temp.

7. Choose the appropriate Spectrograph wavelength based on the TOPAS-C wavelength already chosen
    (a) Under Spectrograph, click Move
        - Choose the proper grating and Move to the wavelength desired
8. Place sample on the sample stage
9. Confirm that all lights are off and light from the computers is blocked where possible
10. Turn on the CCD camera via the switch on the back
    (a) Do not lean on the Spitfire cover at any point
11. Remove cap from detection pathway (found after iris S13)
12. Click on Experiment Setup button
    (a) Under the Main tab
        - CCD Readout - Choose Full chip or Region of Interest (ROI)
        - Accumulations - Amount of times the camera will read
        - Intensifier - Set Gain to 220 for gold coated samples
    (b) Under the ROI setup tab
        - Based on a Full chip read, use the mouse to set the Region of Interest (draw a box around the signal)
        - Click on Mouse, then the Main tab, and confirm all pop-up boxes
13. Click on Pulse button
    (a) Confirm Gate width is 250 μs and Gate Delay is 265 ns

(b) Set Gates Per Exposure (GPE) based on a 1000 gates per second time frame (1000 gates = 1 s exposure)

(c) Click Apply and click Close

14. Click on either Acquire or Focus based on the desired measurement

15. Unblock the beams confirming that the camera is not saturated immediately

16. For optimization of signal

(a) Choose Full Chip read and Focus measurement

(b) Locate signal and choose ROI

(c) Start a Focus measurement

(d) Open the delay controller program called APT User and adjust delay position to optimize the temporal overlap

(e) Adjust mirror S2 to optimize the spatial overlap of the 800 nm and Mid IR beams

(f) Adjust mirror S11 slightly to optimize the intensity of the signal

17. Always block the beams when not taking measurements and while switching samples

18. For the use of the CCD camera software and the spectrograph refer to the manuals

Troubleshooting: When power levels drop to below previously established levels and cannot be re-established, consult instructors, technicians, and manuals for guidance.

Shut down:

1. Before turning on the lights, turn off the CCD camera and recap the Spectrograph
2. Confirm the CCD camera is in Safe Mode, and close the WinSpec32 program
3. Measure 800 nm and Mid IR beams with the power meter, blocking the beams again after completion, and record in the SFS Daily Log
4. Measure Spitfire output with Spectra-Physics power meter (set to 3) and record in the SFS Daily Log
5. Record the room and laser conditions in the SFS Daily Log
6. Close the shutter on the TOPAS, close the program, and turn off the computer
7. Turn off the Empower
   (a) Press the red "STOP" button and confirm the laser is off
   (b) Close the program and turn off the computer
8. Turn off the Mai Tai
   (a) Press the button to close the shutter
   (b) Press the On/Off button and confirm the laser is off
9. Turn off the laser warning light and switch the laser warning sign

BIOGRAPHY OF THE AUTHOR

Sarah Marie Sterling was born in Johnson City, New York on September 13, 1982. She was raised, along with her younger brother, Adam, by two loving parents, Scott and Antoinette Sterling in East Maine, New York. Sarah played basketball and softball, and was an accomplished bassoonist, performing at the local and state levels. She graduated from Maine-Endwell Senior High in 2001, and received a B.S. in Chemistry from Russell Sage College in Troy, New York in May of 2005.

At Russell Sage, Sarah was actively involved in student government and served as Rally Overall for the annual fundraiser her senior year. She also worked on two astrochemistry research projects during her tenure involving the design and construction of a high vacuum line for use in planetary science research and separately, searching for methanol masers in areas of star formation. In September of 2005, Sarah began graduate studies at the University of Maine in the Department of Chemical and Biological Engineering, and in 2006, she became the second student to work toward a joint Ph.D., concentrating in Biomedical Engineering, for which the present work was performed. During her time at the University of Maine, she was a teaching assistant in a variety of classes and taught high school students during summer research experiences. Sarah is a member of the American Chemical Society. In 2011, she married her long time friend, Dr. Jonathan Purnell, who has been a loving support throughout the years.

Sarah M. Sterling is a candidate for the Doctor of Philosophy degree in Biomedical Sciences and Chemical Engineering from The University of Maine in May, 2013.